ANNUAL REPORT
2013

and list of publications

Bayerisches Forschungsinstitut
für Experimentelle Geochemie und Geophysik
Universität Bayreuth

Bayerisches Geoinstitut
Universität Bayreuth
D-95440 Bayreuth
Germany

Telephone: +49-(0)921-55-3700
Telefax: +49-(0)921-55-3769
e-mail: bayerisches.geoinstitut@uni-bayreuth.de
www: http://www.bgi.uni-bayreuth.de

Editorial compilation by: Stefan Keyssner and Petra Buchert
Section editors: Andreas Audétat, Tiziana Boffa Ballaran, Leonid Dubrovinsky,
Robert Farla, Dan Frost, Florian Heidelbach, Tomoo Katsura,
Takaaki Kawazoe, Hans Keppler, Catherine McCammon,
Nobuyoshi Miyajima, Dave Rubie, Gerd Steinle-Neumann

Staff and guests of the Bayerisches Geoinstitut in **July 2013**:

Die Mitarbeiter und Gäste des Bayerischen Geoinstituts im **Juli 2013**:

First row, from left (1. Reihe, v. links) Anastasia Zakharchenko, Ana Cernok, Anja Rosenthal, Fanny Sorbadere, Martha Pamato, Gertrud Gollner, Kanchana Kularatne, Xochilt Gutiérrez, Ahmed El Goresy, Corinne Frigo, Caroline Bollinger

Second row, from left (2. Reihe, v. links) Anna Spivak, Ryosuke Sinmyo, Catherine McCammon, Tiziana Boffa Ballaran, Antje Vogel, Mattia Giannini, Takaaki Kawazoe, Huiyang Gou, Oles Savchuk, Hongzhan Fei, Lydia Kison-Herzing

Third row, from left (3. Reihe, v. links) Petra Buchert, Florian Heidelbach, Tomoo Katsura, Sven Linhardt, Christopher Beyer, Lin Wang, Dave Rubie, Hoda Mohseni, Jellie de Vries, Esther Posner, Ulrike Trenz

Fourth row, from left (4. Reihe, v. links) Stefan Keyssner, Vera Laurenz, Hubert Schulze, Raphael Njul, Dan Frost, Kurt Klasinski, Nobuyoshi Miyajima, Heinz Fischer, Valerio Cerantola, Sylvain Petitgirard, Vincent Soustelle

Fifth row, from left (5. Reihe, v. links) Dmytro Trots, Davide Novella, Reidar Trønnes, Rebecca Fischer, Luca Ziberna, Egor Zakharchenko, Alexander Kurnosov, Detlef Krauße, Stefan Übelhack, Stephan Blaha

Sixth row, from left (6. Reihe v. links) Bob Myhill, Andreas Audétat, Hans Keppler, Robert Farla, Ganna Dinius, Joseph Premier, Sergey Ovsyannikov, Leonid Dubrovinsky, Svyatoslav Shcheka

Absent (Es fehlten) Ulrich Böhm, Holger Kriegl, Yuan Li, Matteo Masotta, Gerd Ramming, Oliver Rausch, Gerd Steinle-Neumann, Natalia Solopova, Vojtech Vlcek, Nico Walte

Contents

Foreword

The principal research objective of the Bayerisches Geoinstitut is to provide insight into the structure, dynamics and evolution of the Earth and planetary interiors. This is achieved through the use of state-of-the-art high-pressure and high-temperature experiments on geo- and cosmo-materials and through the use of atomistic and geodynamic computer modelling. In this yearbook the achievements made at the Geoinstitut in 2013 towards this objective are reported. These results have been obtained through the exploration of highly original ideas and reflect the tremendous efforts made by research scientists at the Geoinstitut. The atmosphere of the institute – one of open-minded discussion and freedom to pursue independent research – is highly conducive to such high quality research. The research achievements also reflect the excellent support provided by the technical and administrative staff at the Geoinstitut. The continuing support of the State of Bavaria and the various funding programs in Germany and the European Union are also extremely important.

In order to promote further scientific exchange and cooperation with external scientists, a "Core Facility" proposal was submitted to the DFG in 2012, and successfully approved in spring 2013. As a result of this program, a significant number of external researchers are now visiting the Geoinstitut to utilize its facilities and will continue to conduct collaborative high-pressure research with Geoinstitut scientists over the next three years.

Two new pieces of major equipment were installed at the institute in the past year; a new 200 keV transmission electron microscope and a numerically controlled ultrasonic milling machine. The transmission electron microscope has a spatial resolution of 0.16 nm in STEM mode, and is capable of chemical analysis at the atomic-scale. It is able, for example, to image and identify individual cation sites in a mineral structure. The milling machine can manufacture ceramic parts for multianvil assemblies in complex forms. It gives researchers a high level of freedom in the design of unique experimental configurations, enabling a wider and even more innovative range of experiments.

The characterization and measurement of physical properties of materials relevant to the Earth's deep interior should, in principal, be conducted *in situ* under high-pressure and high-temperature conditions. However, high-pressure devices hinder direct analytical access to the sample materials, and the tiny sample volumes make *in situ* analysis difficult. For these reasons, utilization of high-energy X-ray and neutron beamlines has become increasingly important over the last few years. In 2013, the Geoinstitut successfully obtained more than five million Euros of funding through the BMBF for three programs to develop high-pressure experimental stations at large facilities. The first program is to perform an up-grade of the high-pressure neutron diffraction system at FRM-II in Garching. The second program is to construct a large-volume high-P-T X-ray observation system at a damping-wiggler beamline at DESY in Hamburg. The third is to develop time-dependent nuclear resonance spectroscopy within laser-heated diamond anvil cells at the ESRF in Grenoble. These programs will run over the next three years and the resulting infrastructure will not only facilitate academic research by Geoinstitut scientists, but will be a long term benefit for the global high-pressure research community.

The ERC project "ACCRETE" has produced remarkable new results in the understanding of the early evolution of terrestrial planetary bodies by combining numerical N-body accretion simulations with geochemical modelling of core-mantle differentiation. A recent result has established that the Moon was formed by a giant impact at a relatively late stage in early Solar System history, i.e. ~ 100 Ma after the formation of the first Solar System solids. Another result predicts that planetary bodies that formed near the Sun have highly reduced compositions, but that compositions were more oxidized with increasing distance from the Sun. CI chondrite parent bodies likely formed beyond 6-8 astronomical units, which enabled them to supply sufficient water to the Earth.

The institute also produced a range of further interesting and important results. For example, experiments on the isotopic fractionation of nitrogen between liquid iron and silicate melt indicate that isotopically light nitrogen would have segregated into the core during early Earth differentiation. This can explain the present nitrogen isotopic enrichment in the silicate Earth. Another example concerns the measurement of grain-boundary silicon self-diffusion as a function of pressure, temperature and water content, which, in contradiction of conventional wisdom, implies a transition with depth in the upper mantle from diffusion creep to dislocation creep. One more example involves *in situ* observations of olivine crystallization from a basaltic melt, where results raise fundamental questions concerning the widely accepted CSD (crystal size distribution) theory.

As in previous years, and also on behalf of my colleagues, I would like to thank the *Free State of Bavaria* as represented by the *Ministry of Education and Culture, Science and Art* as well as the *Commission for High-Pressure Research in Geoscience* for their continuing support and strong commitment to the Bayerisches Geoinstitut. We also gratefully acknowledge generous support from external funding agencies, in particular the *Alexander von Humboldt Foundation*, the *European Union*, the *German Science Foundation* and the *Federal Ministry of Education and Research*, which have also contributed greatly to the development and success of the Geoinstitute.

Bayreuth, March 2014 Tomoo Katsura

Vorwort

Das zentrale Forschungsziel des Bayerischen Geoinstituts (BGI) ist es, die Struktur, Dynamik und Entwicklung des Erdinneren und erdähnlicher Planeten zu untersuchen. Modernste Hochdruck-/Hochtemperatur-Experimente an Geo- und Kosmomaterialien werden von computergestützten physikalischen Berechnungen und geodynamischer Modellierung begleitet. Dieser Bericht dokumentiert die Aktivitäten des Instituts im vergangenen Jahr und unsere Fortschritte auf diesem Weg. Die Erfolge wurden hauptsächlich durch die originellen Ideen und enormen Anstrengungen der BGI-Wissenschaftler ermöglicht. Das hohe Forschungsniveau wird durch die aufgeschlossene Atmosphäre und die wissenschaftliche Freiheit am Institut gefördert. Die Ergebnisse sind nicht zuletzt der hervorragenden Unterstützung durch die technischen und administrativen Mitarbeiter des Institutes zu verdanken, sowie der Förderung durch den Freistaat Bayern und durch nationale und europäische Einrichtungen.

Um den weiteren wissenschaftlichen Austausch und Forschungskooperationen zu fördern, beantragte das Institut 2012 bei der DFG den Status einer „Core Facility", was im Frühjahr 2013 bewilligt wurde. Zahlreichen Wissenschaftlern ermöglicht dieses Programm in den nächsten drei Jahren, die experimentellen Möglichkeiten des Geoinstituts zu nutzen und/oder verschiedene Projekte in der Hochdruckforschung zusammen mit Mitarbeitern des Instituts durchzuführen.

Die experimentellen und analytischen Einrichtungen des BGI wurden im vergangenen Jahr um ein neues 200-keV Transmissionselektronenmikroskop und eine computergesteuerte Ultraschall-Fräsmaschine erweitert. Das Transmissionselektronenmikroskop hat eine räumliche Auflösung von 0,16 nm in STEM-Mode, und ermöglicht chemische Analysen im atomaren Maßstab. Dadurch wird es zum Beispiel ermöglicht, einzelne Kationen-Stellen in einer Mineralstruktur abzubilden und zu identifizieren. Keramikteile mit komplexen Formen für „*state-of-the-art*" Multianvil-Experimente können nun mit Hilfe dieser Fräsmaschine angefertigt werden und ermöglichen dadurch ein noch weiteres innovatives Spektrum experimenteller Forschungsarbeiten.

Zur präzisen Bestimmung der physikalischen und chemischen Eigenschaften von Materialien des tiefen Erdinneren sollten Messungen im Prinzip unter Hochdruck- und Hochtemperaturbedingungen durchgeführt werden. Derartige Messungen sind oft durch die Konstruktion der Hochdruckapparaturen eingeschränkt, die zum Beispiel den Zugang einer Messsonde zur Probe behindern. Eine weitere Herausforderung für *in situ* Analysen stellen die äußerst geringen Probenmengen dar. Daher wird der Einsatz hochenergetischer Röntgen- und Neutronenstrahlung in den letzten Jahren zunehmend wichtiger. In 2013 war das BGI mit drei Anträgen über insgesamt mehr als fünf Millionen Euro Forschungsförderung beim BMBF erfolgreich. Die Mittel werden zur Entwicklung von Hochdruckexperimenten an Großforschungseinrichtungen verwendet, wie zum Beispiel für eine Erweiterung des Hochdruck-Neutronenbeugungssystems am FRM II in Garching. Des Weiteren wird eine großvolumige Presse für *in situ*-Röntgenbeugungsmessungen bei hohen Drücken und Temperaturen an der Damping-Wiggler-Beamline am DESY in Hamburg errichtet. Ebenso finanziert wird die

Entwicklung zeitabhängiger Kernresonanz-Experimente mit lasergeheizten Diamantstempelzellen am ESRF in Grenoble. Diese Programme haben eine Laufzeit von drei Jahren. Die durch diese Programme geförderten Einrichtungen werden nicht nur die institutseigene Forschungsaktivität beflügeln, sondern auch zur globalen Weiterentwicklung der Hochdruckforschung beitragen.

Das ERC-Projekt „ACCRETE“ hat bemerkenswerte Beiträge für das Verständnis der frühen Evolution der terrestrischen Planeten durch die Kombination numerischer N-Körper-Simulationen mit geochemischen Analysen geleistet. Ein Ergebnis ist, dass sich der Mond durch ein gewaltiges Kollisionsereignis („Giant-Impact“) in einer relativ späten Phase der Geschichte des Sonnensystems bildete. Ein weiteres Ergebnis sagt vorher, dass die planetaren Körper in der Nähe der Sonne sehr reduzierte Zusammensetzungen haben sollten, während mit zunehmender Entfernung von der Sonne der Oxidationsgrad steigt. CI-Chondrite sollten sich bei einer Entfernung > 9 AU (Astronomischen Einheiten) von der Sonne gebildet und später Wasser auf die Erde geliefert haben.

Zu den vielen anderen Forschungsergebnissen des Institutes zählen die Erkenntnisse aus Experimenten zur Stickstoffverteilung und Isotopenfraktionierung zwischen geschmolzenem Eisen und Silikatsschmelzen. Danach kann zum Beispiel Stickstoff aus dem terrestrischen Magmenozean durch Isotopenfraktionierung im Erdkern angereichert worden sein, was die heutige Stickstoffisotopenverteilung in der Silikat-Erde erklären würde. Messungen der Eigendiffusionskoeffizienten für Silizium an Korngrenzen bei variierenden Druck-, Temperaturbedingungen sowie als Funktion des Wassergehaltes lassen annehmen, dass mit steigendem Druck ein Übergang im Deformationsmechanismus von Diffusions- zu Versetzungskriechen im oberen Erdmantel stattfindet, was im Gegensatz zur klassischen Lehrmeinung steht. *In situ*-Beobachtungen bei der Kristallisation von Olivin in basaltischer Schmelze stellen die weithin akzeptierte CSD-Theorie der Korngrößenverteilung in Frage.

Wie bereits in vergangenen Jahren möchte ich auch im Namen meiner Kollegen dem *Freistaat Bayern*, vertreten durch das *Staatsministerium für Wissenschaft, Forschung und Kunst*, und der *Kommission für Geowissenschaftliche Hochdruckforschung* meinen Dank für ihre fortwährende Unterstützung und die enge Verbundenheit mit dem Bayerischen Geoinstitut aussprechen. Wir sind auch für die großzügige Förderung durch externe Geldgeber, insbesondere durch die *Alexander von Humboldt-Stiftung*, die *Europäische Union* und das *Bundesministerium für Bildung und Forschung* sowie die *Deutsche Forschungsgemeinschaft*, die ebenfalls wesentlich zur Entwicklung und zum Erfolg des Bayerischen Geoinstituts beigetragen haben, sehr dankbar.

Bayreuth, im März 2014 Tomoo Katsura

1. Advisory Board and Directorship

1.1 Advisory Board

The *Kommission für Geowissenschaftliche Hochdruckforschung der Bayerischen Akademie der Wissenschaften* advises on the organisation and scientific activities of the institute. Members of this board are:

Prof. Dr. G. BREY	Institut für Geowissenschaften der Johann Wolfgang Goethe-Universität, Frankfurt am Main
Prof. Dr. U. CHRISTENSEN	Max-Planck-Institut für Sonnensystemforschung, Katlenburg-Lindau
Prof. Dr. R. KNIEP	Institut für Chemische Physik fester Stoffe der Max-Planck-Gesellschaft, Dresden
Prof. Dr. H. PALME	Institut für Mineralogie und Geochemie der Universität zu Köln
Prof. Dr. M. RIEDERER (Chairman)	Julius-von-Sachs-Institut für Biowissenschaften, Würzburg
Prof. Dr. R. RUMMEL (Vice Chairman)	Institut für Astronomische und Physikalische Geodäsie der TU München
Prof. Dr. E. SALJE, FRS, FRSA	Department of Earth Sciences, University of Cambridge
Prof. Dr. H. SOFFEL	Emeritus, Institut für Allgemeine und Angewandte Geophysik der Universität München

The Advisory Board held meetings in Bayreuth (26.04.2013) and in Munich (15.11.2013).

1.2 Leadership

Prof. Dr. Tomoo KATSURA (Director)
Prof. Dr. Dan FROST (Deputy Director)
Prof. Dr. Hans KEPPLER

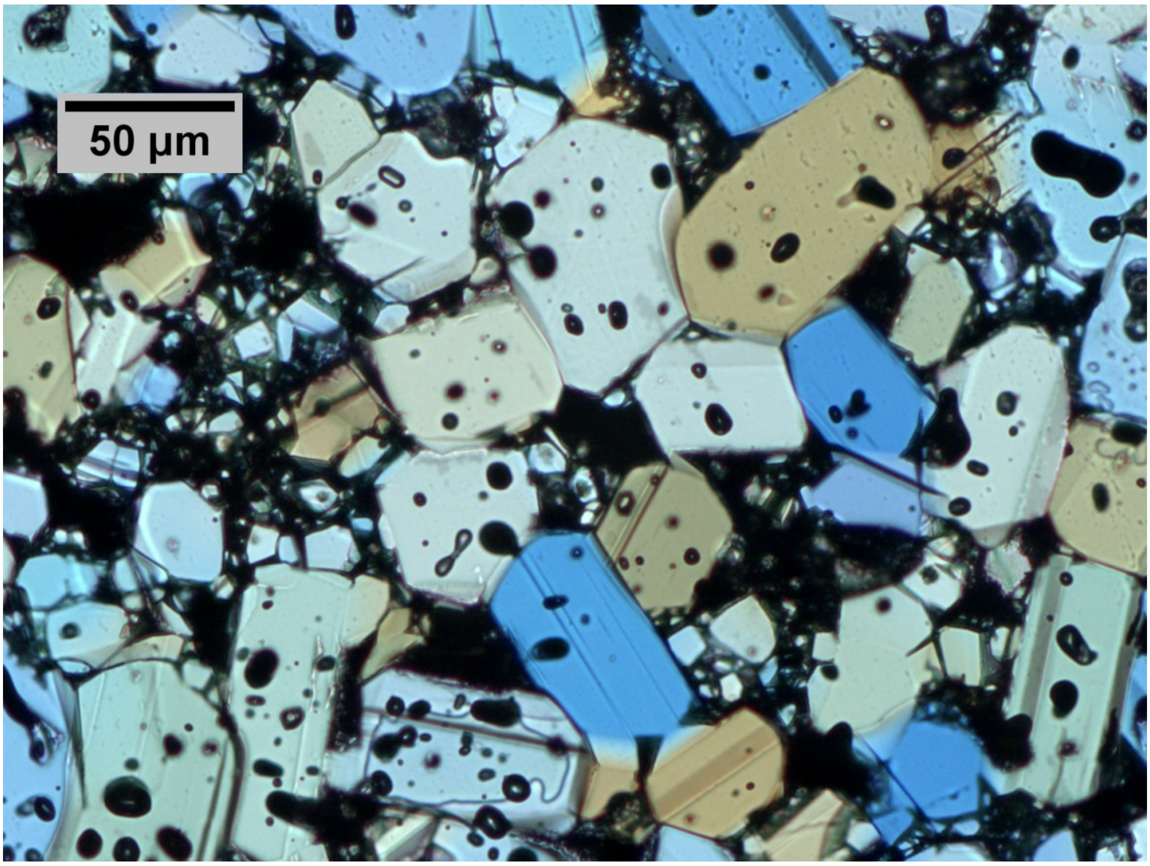

Large single crystals of Ti-Mg-bearing hibonite synthesised at 1500 °C under reducing conditions (log fO_2 = -11, 1 bar). This image was taken with transmitted light and nearly parallel polarizers. Blue color and intense pleochroism are due to Ti^{3+}. Hibonite coexists with Ca-Ti-perovskite (small light grains), similar to what has been observed in Ca-Al-rich inclusions (CAIs) of Chondritic meteorites. CAIs are considered to be the oldest solid materials of our Solar system, formed 4.568 billion years ago. Spectroscopic measurements on polycrystalline hibonite (*i.e.*, grain size smaller than a few microns) have been previously correlated with the oxygen fugacity conditions at the time of its formation. This is the first time that large Ti-Mg-bearing single crystals of hibonite have been synthesised, providing better constraints on the crystal chemistry and hence the structure-property relationships of this mineral. (Photo by Mattia Giannini/BGI)

Große Einkristalle von Ti-Mg-führendem Hibonit, die bei 1500 °C unter reduzierten Bedingungen (log fO_2 = -11, 1 bar) synthetisiert wurden. Das Bild wurde im Durchlicht mit nahezu parallelen Polarisatoren aufgenommen. Die blaue Farbe und der starke Pleochroismus werden durch Ti^{3+} verursacht. Hibonit koexistiert mit Ca-Ti-Perowskit (kleine, helle Körner) in ähnlicher Weise, wie in Ca-Al-reichen Einschlüssen (CAIs) in chondritischen Meteoriten beobachtet wurde. Chondrite werden als die älteste feste Materie unseres Sonnensystems mit einem Alter von 4,568 Mrd. Jahren angesehen. Spektroskopische Messungen an polykristallinem Hibonit (mit Korngrößen von wenigen Mikrometern) wurden kürzlich mit den Bedingungen der Sauerstofffugazität zur Zeit seiner Entstehung korreliert. Es ist zum ersten Mal gelungen, größere Ti-Mg-haltige Einkristalle aus Hibonit zu erzeugen, mit der Möglichkeit, genauere Aussagen über seine Kristallchemie und somit über Struktur-/Eigenschaftsbeziehungen zu treffen. (Foto: Mattia Giannini/BGI)

2. Staff, Funding and Facilities

2.1 Staff

At the end of 2013 the following staff positions existed in the Institute:

- Scientific staff: **12**
- Technical staff: **13**
- Administrative staff: **2**
- Administrative officer: **1**

During 2013, 31 scientific positions (294 months) were funded by grants raised externally by staff members of the institute. In addition 8 long-term scientific positions (60 months) were funded by the resources of the BGI Visiting Scientists' Programme (see Sect. 7) which also supported short-term visits for discussing future projects or presenting research results (see Sect. 5). 8 scientists (68 months) were supported by personal grants (stipends).

2.2 Funding

In 2013, the following financial resources were available from the Free State of Bavaria:

- Visiting Scientists' Programme: 194.000 €
- Consumables: 460.000 €
- Investment Funding: 1.572.000 €

The total amount of national/international external funding (*"Drittmittel"*) used for ongoing research projects in 2013 was 6.731.000 € (Positions: 1.418.000 €; equipment, consumables and travel grants: 5.313.000 €).

	positions	**equipment, consumables, travel grants**	**total**
• AvH	141.000 €	5.000 €	146.000 €
• BMBF	169.000 €	5.127.000 €	5.296.000 €
• DFG	484.000 €	90.000 €	574.000 €
• EU	600.000 €	87.000 €	687.000 €
• Stifterverband	3.000 €	- €	3.000 €
• Others	21.000 €	4.000 €	25.000 €
			6.731.000 €

(AvH = Alexander von Humboldt Foundation; DFG = German Science Foundation; EU = European Union; BMBF = Federal Ministry of Education and Research; Stifterverband = Stifterverband für die Deutsche Wissenschaft; Others: DAAD, University of Bayreuth, Universitaet Bayern e.V.)

In the following list only the BGI part of the funding is listed in cases where joint projects involved other research institutions. Principal investigators and duration of the grants are listed in brackets. Total project funding refers to the funding over the entire duration of this project.

Funding institution	Project, Funding	Total Project Funding
BMBF - DESY	05K10WC1 (L.S. Dubrovinsky – 7.10 - 6.13) "Verbundprojekt: Kernresonante Streutechniken: Entwicklung von Messplätzen zur Charakterisierung von Nanostrukturen, molekularen Schaltern, biologischen Mikroproben und Materie unter extremen Bedingungen mit kernresonanten Streutechniken. Teilprojekt 1" Total funding:	529.670 €
BMBF	05K12WC1 (L.S. Dubrovinsky – 8.12 - 7.15) "Single crystal crystallography at extreme pressures and variable temperatures" Total funding:	448.000 €
BMBF	056K13WC4 (L.S. Dubrovinsky – 7.13 - 6.16) "NANORES: Nanofokussierende Röntgenoptiken und Probenumgebungen für die resonante Kernstreuung zum Studium von schnellen Prozessen in Chemie, Biologie und in Materie unter extremen Bedingungen" Total funding:	475.300 €
BMBF	KEI0500009612 (T. Katsura – 7.13 - 6.16) "Aufbau einer experimentellen Station mit einer großvolumigen Hochdruckapparatur an der Damping-Wiggler-Beamline des Deutschen Elektronen Synchrotron (DESY)" Total funding:	1.186.000 €
BMBF	05K10WC2 (H. Keppler – 7.10 - 6.13) "Aufbau einer Hochdruckpresse vom Multi-Anvil-Typ für TOF-Neutronenbeugung und Neutronen-Radiographie am FRM II" Total funding:	2.050.078 €
BMBF	05K13WC2 (H. Keppler – 7.13 - 6.16) "Aufbau einer Hochdruckpresse vom Multi-Anvil-Typ an der Forschungs-Neutronenquelle FRM II in Garching" Total funding:	3.499.590 €
DFG	BO 2550/4-2 (T. Boffa Ballaran, F. Langenhorst – 2.12 - 1.14) "Crystal chemistry of hibonite as indicator for oxygen fugacities during solar nebula condensation" Positions: E 13/2, 24 months 57.300 € Consumables and travel funding: 25.000 € Overhead: 16.300 €	98.600 €

DFG	BO 2550/7-1 (T. Boffa Ballaran, A. Woodland – 8.13 - 7.16) "Crystal chemistry of ferric iron in the deep upper mantle and transition zone" Position: student assistant 5.000 € Consumables and travel funding: 9.500 € Overhead: 2.900 €	17.400 €
DFG	DU 393/7-1 (L.S. Dubrovinsky, N.A. Dubrovinskaia – 6.09 - 5.12 – extended to 07.13) "Elasticity of iron and iron-based alloys at conditions of the Earth's and planetary cores" Positions: student assistant (80 h/month), 36 months 23.895 € Consumables and travel funding 42.017 € Publication costs 1.500 € Overhead: 18.600 €	86.012 €
DFG	EV 166/1-1 (M. Evonuk – 11.10 - 10.13) "Core formation in Terrestrial planets via global Rayleigh-Taylor destabilization" 1 position: E 13, 36 months 186.300 € Consumables and travel funding: 6.727 € Publication costs 2.250 € Overhead: 37.100 €	232.377 €
DFG	GO 315/21-1 (A. El Goresy, L. Dubrovinsky – 11.12 - 10.14) "Mineralogical, REE and ^{146}Sm-^{142}Nd isotopic systematics of the earliest solar condensates in unequilibrated enstatite chondrites" Consumables and travel funding: 3.000 € Publication costs 1.500 € Overhead: 900 €	5.400 €
DFG	HE 3285/2-1 (F. Heidelbach – 4.13 - 3.16) "Reaction kinetics and plastic deformation in mantle rocks" 1 position: 36 months 188.900 € Consumables and travel funding: 21.500 € Overhead: 42.100 €	252.500 €
DFG	KA 3434/3 (T. Katsura – 4.13 – 3.16) "Dislocation recovery experiment of hydrous olivine as a function of water content and crystallographic orientation" 1 position: E 13, 36 months 186.300 € Consumables and travel funding: 20.000 € Overhead: 43.000 €	249.300 €
DFG	Forschungsgroßgeräte (T. Katsura) INST 91/291 "Ultrahochdruck-Vielstempelapparatur"	371.000 €
DFG	Forschungsgroßgeräte (T. Katsura) INST 91/302 "Fräsmaschiene für Keramikteile"	241.000 €

DFG	KE 501/8-2 (H. Keppler – 2013 - 2016) "*In situ* Beobachtung der Kristallisationskinetik und Gefügeentwicklung von Basalten" Total funding	174.000 €
DFG	KE 501/9-1 (H. Keppler – 2010 - 2013) "Noble gases in silicate perovskite: Solubility, dissolution mechanism and influence on the equation of state" 1 position: E 13, 36 months 186.300 € Consumables and travel funding: 15.000 € Overhead: 38.300 € 38.300 €	239.600 €
DFG	KE 501/10-1 (H. Keppler – 7.13 - 6.16) "DFG Core Facility: High-pressure laboratories of Bayerisches Geoinstitut" Total funding:	544.600 €
DFG	KE 501/11-1 (H. Keppler – 2013 - 2016) "Electrical conductivity and dissociation of fluids in crust and mantle" Total funding:	267.800 €
DFG	KO 3958/1-1 (N. de Koker, D.C. Rubie, D.J. Frost – 12.10 - 11.13) "Combining experimental and computational approaches to determine high P and T thermal conductivity of $CaGeO_3$ and $MgSiO_3$ perovskite" Positions: E 13, 20 months 103.500 € student assistant (57 h/month) 6 months 4.760 € Consumables and travel funding: 6.000 € Overhead: 22.000 €	136.260 €
DFG	KO 3958/2-1 (N. de Koker, G. Steinle-Neumann – 2.11 - 3.16) "Thermal and electrical conductivity of iron at planetary core conditions from ab initio computations" Positions: E 13, 36 months 186.300 € student assistant (79 h/month) 12 months 7.965 € Consumables and travel funding: 9.000 € Publication costs: 2.250 € Overhead: 41.100 €	246.615 €
DFG	MC 3/18-1 (C.A. McCammon, L.S. Dubrovinsky, D.J. Frost – 7.13 - 6.16) "The effect of pressure, temperature and oxygen fugacity on the stability of subducted carbonates and implications for the deep carbon cycle" Positions: E 13/2, 36 months 85.950 € student assistant 5.000 € Equipment, consumables and travel funding: 31.650 € Overhead: 24.900 €	147.500 €

DFG	MC 3/19-2 (C.A. McCammon, S. Gilder – 9.13 - 8.16) "How pressure influences the magnetic properties of titanomagnetite and iron with implications for magnetic anomalies and core fields" Equipment, consumables and travel funding: 6.400 € Overhead: 1.300 €	7.700 €
DFG	OV 110/1-1 (S.V. Ovsyannikov – 7.11 - 6.13) "Structural and electronic properties of sesquioxides at high pressures and temperatures: new forms, new insights and new possible applications" Positions: E 13, 24 months 124.200 € Consumables and travel funding: 14.000 € Overhead: 26.500 €	164.700 €
DFG	OV 110/1-2 (S.V. Ovsyannikov – 9.13 - 8.15) "Structural and electronic properties of sesquioxides at high pressures and temperatures: new forms, new insights and new possible applications" Positions: E 13, 24 months 124.200 € Consumables and travel funding: 20.000 € Overhead: 29.200 €	173.400 €
DFG	RU 1323/2-2 (D.C. Rubie, D.J. Frost, H. Palme – 6.12 - 5.14) "Conditions, timescales and cosmochemical evolution during the early accretion of terrestrial planets" Positions: E 13/2, 24 months 57.300 € Consumables and travel funding: 40.000 € Publication costs: 1.500 € Overhead: 19.600 €	118.400 €
DFG	STE 1105/6-2 (G. Steinle-Neumann, H.-P. Bunge – 9.10 - 8.13) DFG SPP 1375 (SAMPLE) "Mineralogical and Dynamic Origin of the South African Superplume" Positions: ¾ E13, 36 months 128.925 € Consumables and travel funding: 7.200 €	136.125 €
DFG	STE 1105/8-1 (S. Gilder/LMU München, G. Steinle-Neumann, R. Egli and N. Petersen/LMU München – 2.11 - 1.14) DFG SPP 1488 (PlanetMag) "How pressure influences the magnetic properties of titanomagnetite and iron with implications for magnetic anomalies and core fields" Budget (G. Steinle-Neumann): Positions: ¾ E13, 36 months 128.925 € Travel funding: 9.250 €	BGI funding: 138.175 €

EU	European Research Council (ERC) Advanced Grant No. 227893 (D.J. Frost – 2.09 - 1.14) "Deep Earth elastic properties and a universal pressure scale DEEP" Positions, equipment, consumables and travel funding maximum EU contribution:	2.079.888 €
EU	European Research Council (ERC) Advanced Grant No. 290568 (D.C. Rubie - 5.12 - 4.17) "Accretion and Early Differentiation of the Earth and Terrestrial Planets" ("ACCRETE") Positions, consumables and travel funding:	1.826.200 €
EU	Marie Curie – International Incoming Fellowship Grant No. 302637 (A. Rosenthal – 10.12 - 10.14) FATEMANTLE Fellowship, consumables and travel funding	167.370 €

2.3 Laboratory and office facilities

The institute occupies an area of

ca. 1350 m^2	laboratory space
ca. 480 m^2	infrastructural areas (machine shops, computer facilities, seminar room, library)
ca. 460 m^2	office space

in a building which was completed in 1994.

2.4 Experimental and analytical equipment

The following major equipment is available at the Bayerisches Geoinstitut:

I. High-pressure apparatus
6x800 tonne independently acting-anvil press (25 GPa, 3000 K)
5000 tonne multianvil press (25 GPa, 3000 K)
1200 tonne multianvil press (25 GPa, 3000 K)
1000 tonne multianvil press (25 GPa, 3000 K)
500 tonne multianvil press (20 GPa, 3000 K)
500 tonne press with a deformation DIA apparatus
4 piston-cylinder presses (4 GPa, 2100 K)
Cold-seal vessels (700 MPa, 1100 K, H2O), TZM vessels (300 MPa, 1400 K, gas), rapid-quench device
Internally-heated autoclave (1 GPa, 1600 K)
High-pressure gas loading apparatus for DAC

II. Structural and chemical analysis
1 X-ray powder diffractometer
1 X-ray powder micro-diffractometer
1 X-ray powder diffractometer with furnace and cryostat
2 automated single-crystal X-ray diffractometers
High-brilliance X-ray system
Single crystal X-ray diffraction with super-bright source
1 Mössbauer spectrometer (1.5 - 1300 K)
3 Mössbauer microspectrometers
2 FTIR spectrometers with IR microscope
FEG transmission electron microscope, 200 kV analytical, with EDS and PEELS
FEG scanning TEM, 80-200 kV analytical, with 4-SDDs EDS and post-column energy filter (EFTEM/EELS)
FEG scanning electron microscope with BSE detector, EDS, EBSD and CL
3 Micro-Raman spectrometers with ultraviolet and visible lasers
Tandem-multipass Fabry-Perot interferometer for Brillouin scattering spectroscopy
JEOL JXA-8200 electron microprobe; fully-automated with 14 crystals, 5 spectrometer configuration, EDX, capability for light elements

193 nm Excimer Laser-Ablation ICP-MS
ICP-AES sequential spectrometer
Water content determination by Karl-Fischer titration
GC/MS-MS for organic analyses
Confocal 3D surface measurement system

III. *In situ* determination of properties
Diamond anvil cells for powder and single crystal X-ray diffraction, Mössbauer, IR, Raman, optical spectroscopy, Brillouin scattering and electrical resistivity measurements up to at least 100 GPa
Facility for *in situ* hydrothermal studies in DAC
Externally heated DACs for in situ studies at pressures to 100 GPa and 1200 K
1-atm furnaces to 1950 K, gas mixing to 1600 K, zirconia fO_2 probes
1-atm high-temperature creep apparatus
Gigahertz ultrasonic interferometer with interface to resistance-heated diamond-anvil cells
Heating stage for fluid inclusion studies
Impedance/gain-phase analyser for electrical conductivity studies
Apparatus for in situ measurements of thermal diffusivity at high P and T
Laser-heating facility for DAC

IV. Computational facilities
9 node linux cluster (2x3.0 GHz Xeon Woodcrest Dual Core, 8 Gb memory), InfiniBand
8 node linux cluster (16x2.83 GHz Xeon 5440 Quad Core, 64 Gb memory), InfiniBand
32 TB mass storage

The Geoinstitut is provided with well equipped machine shops, an electronic workshop and sample preparation laboratories. It has also access to the university computer centre.

3. Forschungsprojekte

3.1 Struktur und Dynamik der Erde und Planeten

Die frühe Entwicklung der erdähnlichen Planeten in unserem Sonnensystem ist durch Akkretion und Differenzierung geprägt. Während der Akkretion erhalten die Planeten durch Kollision von Embryo-Planeten und Planetesimalen ihre endgültige Größe, während sie durch die Differentiation ihre typische interne Struktur erhalten, mit einem metallischen Kern in ihrem Zentrum, umgeben von einem silikatischen Mantel. Diese beiden Prozesse stehen im Zentrum des Projekts ACCRETE, das vom *European Research Council* (ERC) am Bayerischen Geoinstitut gefördert wird. Drei Beiträge in diesem Kapitel widmen sich diesen Prozessen.

Mit einer Halbwertzeit von 9 Millionen Jahren ist das Hafnium-Wolfram (Hf-W)-System sehr empfindlich für Prozesse, die im jungen Sonnensystem ablaufen; es kann folglich dazu genutzt werden, Ähnlichkeiten und Unterschiede im Ursprung verschiedener Planeten zu verstehen, zumindest wenn von diesen Planeten Gesteinsproben verfügbar sind. Außer für die Erde trifft dies für den Mond (der hier nicht weiter betrachtet werden soll) und den Mars (durch Meteoritenfall) zu. Auf der Basis von N-Körper-Simulationen, in denen der Akkretionsprozess modelliert wird, argumentiert der erste Beitrag des Kapitels, dass zu Beginn der Planetenbildung eine relativ große Masse an Planetenembryos (im Gegensatz zu den größeren Planetesimalen) vorhanden gewesen sein müssen, um den Hf-W-Werten von Erde und Mars gerecht zu werden. In solchen Simulationen kann Mars am besten als unvollendeter Embryo-Planet aufgefasst werden, der im Verlauf der jüngeren Geschichte mit gewaltigen Impaktereignissen auf unserem Planetensystem nicht beteiligt war. Im Gegensatz dazu erfordern die Simulationen, dass der Mond-bildende Impakt auf der Erde relativ spät in der Entwicklung des Planetensystems stattgefunden hat, d. h. erst nach ca. 100 Mio. Jahren.

Derartige Impaktereignisse sind für Schmelzprozesse auf Planetenembryos/Planetesimalen verantwortlich, die im Extremfall zu Magmaozeanen, d. h. globalen Aufschmelzungen, führen können. Der Umfang und die zeitliche Taktung der Schmelzprozesse hängt natürlich von der Größe und der Frequenz der Einschläge ab, wie sie in den N-Körper-Simulationen berechnet werden. Bisher wurde angenommen, dass der Zeitraum zwischen zwei Einschlägen groß genug ist, dass die Schmelzen vollständig kristallisieren. Diese Hypothese ist zumindest für große Einschläge fraglich und wird im zweiten Beitrag untersucht. Die Autoren finden, dass diese Annahme während der frühen Akkretion – solange die Projektile relativ klein sind – zutrifft. Im späteren Stadium der großen Impaktereignisse hängt die Kristallisation von der Wärmestrahlung des Planeten in das Weltall ab. Falls eine dichte Atmosphäre vorhanden ist, die sich zum Beispiel aus der Verdampfung von Teilen des Magmaozeans entwickelt hat, kann es vorkommen, dass der Magmaozean noch nicht vollständig kristallisiert ist und weitere Einschläge auf eine flüssige äußere Planetenschicht treffen, was zu einer sehr unterschiedlichen Einschlagsdynamik führen kann.

Weitere N-Körper-Simulationen, die bezüglich Masse und Abstand zur Sonne zu einem erdähnlichen Planeten führen, werden im dritten Beitrag vorgestellt. Dabei wird die chemische Zusammensetzung des primitiven Erdmantels aus der Zusammensetzung der ursprünglichen Planeten-Embryos und Planetesimalen berechnet. Aus diesen Simulationen ergibt sich, dass im Sonnensystem ein Gradient im Oxidationszustand vorliegen muss: Ursprungskörper im inneren Sonnensystem (< 1 astronomische Einheit, AU) müssen im reduzierten Zustand sein, während solche außerhalb 4 AU vollständig oxidiert sind. Dazwischen muss der Oxidationszustand mit dem Abstand zunehmen. Wenn außerdem eine chondritische (CI) Zusammensetzung für Ursprungskörper ab 9 AU angenommen wird, ergibt sich allein aus der Akkretion der Wassergehalt der Erde.

Die abschließenden zwei Beiträge in diesem Kapitel widmen sich im Gegensatz zu den vorhergehenden dem Zustand der heutigen Erde. Der erste dieser Beiträge stellt ein thermoelastisches Modell für Minerale des Erdmantels vor, mit dessen Hilfe der physikalische Zustand des Mantels bezüglich Temperatur und chemischer Zusammensetzung untersucht werden kann. Darüber hinaus ermöglicht ein solches Modell die Integration thermodynamischer und elastischer Information in rechnergestützte geodynamische und seismologische Studien über das Erdinnere.

Subduktionszonen stellen die wichtigste Ausgangsgebiete für Auftriebsprozesse im Erdmantel und Materialtransport von der Oberfläche der Erde in ihr Inneres dar. Während zahlreiche Aspekte der Subduktion bezogen auf den Temperaturzustand des Erdmantels bereits untersucht wurden, hat man in bisherigen Modellen die Produktion und Reduktion von Wärme als Folge von metamorphen Reaktionen nicht ausreichend berücksichtigt. Im letzten Beitrag des Kapitels wird der Einfluss von Phasenübergängen und der Verlust von Volatilen auf den Wärmehaushalt der subduzierten Lithosphäre mit Hilfe von berechneten Phasengleichgewichten untersucht. Der daraus resultierende Temperaturunterschied in der Subduktionszone ist dabei auf 70 °C beschränkt, jedoch erfahren unterschiedliche Schichten der Lithosphäre (Sedimente, Basalt und serpentinisierter Harzburgit) eine stark unterschiedliche thermische Entwicklung, was zu einer Entkopplung der verschiedenen Lagen führen kann.

3.2 Geochemie

Geochemische Austauschreaktionen im Verlauf der Akkretion der Erde waren wahrscheinlich Teil eines dynamischen Prozesses, bei dem sich metallisches Eisen aus dem Impaktkörper abtrennte und rasch durch den silikatischen Erdmantel hindurch weiter ins Erdinnere abtauchte. Das Ausmaß der abgeschiedenen Metallmenge und die Sinkgeschwindigkeit könnten dazu geführt haben, dass sich für bedeutende Teile der Metallschmelze unter den vorhandenen hohen Druck- und Temperaturbedingungen beim Abtauchen in den Erdkern kein Gleichgewicht mit dem umgebenden Mantel einstellen konnte. Diesem Thema widmet sich der erste Beitrag dieses Kapitels mit Untersuchungen über die chemische Diffusion von Silizium – eines der potentiellen leichten Elemente im Erdkern – in metallischem Eisen zu. Quantitative Diffusionsgeschwindigkeiten liefern uns neue Erkenntnisse über die Dynamik bei der Bildung des Erdkerns.

In den nächsten beiden Projekten wird untersucht, wie abgeschiedenes Metall während des Absinkens mit dem tiefen unteren Erdmantel reagiert haben könnte. Diese Untersuchungen stellen eine große technische Herausforderung dar, weil Experimente unter diesen Druckbedingungen in laserbeheizten Diamantstempelzellen durchgeführt werden müssen. Die Präparation und Analyse der nur Mikrometer großen Proben ist sehr anspruchsvoll und erfordert innovative Methoden und Technik. Ein Hauptergebnis dieser Studien ist, dass unter Bedingungen eines tiefen Magmaozeans mit Ausdehnung bis in den unteren Mantel große Anteile der leichten Elemente Silizium und Sauerstoff von der Schmelze aus metallischem Eisen aufgenommen werden.

In den folgenden vier Beiträgen wird die Erdkernbildung, anhand der relativen Verarmung des silikatischen Erdmantels an siderophilen („metallfreundlichen") Elementen untersucht. Eine Studie prüft, ob die Metall/Silikat-Verteilung von der Zusammensetzung der Silikatschmelze beeinflusst wird. Daraus ließe sich erkennen, ob Veränderungen in der Schmelzzusammensetzung, welche im Verlauf von Experimenten auftreten können, die Elementverteilung beeinflussen. Die drei im Anschluss beschriebenen Projekte befassen sich mit dem Einfluss von Schwefel auf die Metall-Silikat-Verteilung siderophiler, hochsiderophiler und volatil-siderophiler Elemente. Alle Studien weisen ähnliche Ergebnisse auf, in der Hinsicht, dass die Metall-Silikat-Verteilungskoeffizienten sich bei der Präsenz von Schwefel jenen Werten nähern, mit denen sich die Konzentration dieser Elemente im heutigen Erdmantel erklären lässt. Eine weitere Studie zur Erdkernbildung befasst sich mit Verteilung und Fraktionierung stabiler Stickstoffisotope zwischen Metall- und Silikatschmelze. Neben den überwiegenden Stickstoffisotopen mit der Massenzahl 14 findet sich ein stabiles Isotop mit der Massenzahl 15. Experimente haben gezeigt, dass Stickstoff mäßig siderophil ist und dass das leichtere Isotop eine stärkere Affinität zur Metallschmelze aufweist. Möglicherweise helfen diese Ergebnisse dabei, die Anreicherung des schwereren Isotops in äußeren Bereichen unseres Planeten zu erklären.

Die drei folgenden Beiträge befassen sich mit dem Einfluss von dreiwertigem Eisen auf Schmelzbeziehungen und Mineralstabilitäten im Erdmantel. Die Untersuchungen von Sorbadère *et al.* konzentrieren sich auf das sogenannte „$Fe^{3+}/\Sigma Fe$-Paradoxon" in MORB-Magmen (*Mid-Ocean Ridge Basalts*), das sich auf die $Fe^{3+}/\Sigma Fe$-Verhältnisse bezieht, die trotz deutlicher Schwankungen im Grad der Teilaufschmelzung überraschend konstant bleiben. Eine mögliche Erklärung für dieses Phänomen könnte sein, dass die Mineral/Schmelze-Koeffizienten von Fe^{3+} mit dem Grad der Teilaufschmelzung größer werden. Diese Hypothese wird experimentell untersucht. Myhill *et al.* überprüfen anhand eines synthetischen Peridotit-Analogons den Einfluss des Oxidationszustands von Eisen auf die

Solidustemperatur. Während bereits bekannt ist, dass bei niedrigen Drücken der Peridotit-Solidus sinkt, wenn vermehrt Eisen in einen höheren Oxidationszustand versetzt wird, sind bis heute keine systematischen Daten für Drücke oberhalb von 4 GPa verfügbar. Erste Ergebnisse deuten an, dass Fe^{3+} auch bei Bedingungen des unteren Mantels einen starken Einfluss auf den Solidus hat. Der nächste Beitrag behandelt den Einfluss des Oxidationszustands von Eisen auf die Mineralstabilitäten im oberen und unteren Erdmantel. Durch die Einbindung experimentell gewonnener Daten an eisenführenden Hochdruck-Mineralphasen in bekannte thermodynamische Modelle, wird es möglich, Phasenbeziehungen präzise vorherzusagen und Fe^{3+}-Aktivitäten sogar für Bedingungen des unteren Mantels zu berechnen.

Die Beziehungen wasserhaltiger Phasen im oberen Mantel sind Thema zweier weiterer Beiträge. Im ersten Artikel wird eine neue Methode eingesetzt, bei der unter Zugabe von Wasser in Form von festem $H_2Pt(OH)_6$ die bisher unzugänglichen H_2O-reichen Bereiche im MgO-SiO_2-H_2O-System erkundet werden sollen. Im Folgebeitrag werden die Phasenbeziehungen in hydratisierter Ozeankruste während der Umwandlung wasserführender Minerale im Verlauf der Subduktion untersucht. Die Ergebnisse legen nahe, dass sich das Stabilitätsfeld kaliumreicher Glimmer als Funktion des Wassergehalts der abtauchenden Kruste stark verändert.

In einer Untersuchung zum Speichern und Recycling von Halogenen im Erdmantel haben Roberge *et al.* die Löslichkeit von Fluor in Olivin, Wadsleyit und Ringwoodit unter Bedingungen der Übergangszone bestimmt. Sie fanden heraus, dass die ersteren beiden Minerale bis zu ~ 0.1 Gew.% F einbauen können, was bedeutet, dass die Übergangszone alleine bereits mehr Fluor speichern könnte, als man allgemein für die gesamte silikatreiche Zone der Erde annimmt. Der Beitrag von Beyer und Frost zielt auf die Verfeinerung des Granat-Klinopyroxen-Geobarometers, d. h. auf eine Gleichung, mit der anhand von chemischen Analysen dieser beiden Minerale der während der Gesteinsbildung herrschende Druck bestimmt werden kann. Ein derartiges Geobarometer ist besonders wertvoll, da es für Eklogit-Xenolithe anwendbar ist, die in Kimberliten gefunden werden, und somit Einblicke in die Entstehung kratonischer Lithosphäre sowie Diamanten ermöglicht. Der sich anschließende Artikel von Liu *et al.* behandelt das Verhalten von Kupfer bei Schmelzvorgängen im Erdmantel und der nachfolgenden fraktionierten Kristallisation der primären Magmen. Experimente zur Elementverteilung, die bei 0.75-3.5 GPa und 850-1300 °C mit Schmelzen von komatiitischer bis haplogranitischer Zusammensetzung durchgeführt wurden, lassen erkennen, dass Cu während der fraktionierten Kristallisation zunehmend kompatibler in Silikat- und Oxidmineralen wird, aber nicht soweit, dass es in der verbleibenden silikatischen Restschmelze vollständig abgereichert wird.

Die beiden abschließenden Beiträge befassen sich mit Prozessen, die während der Vermischung von Schmelzen in Magmenkammern der oberen Erdkruste ablaufen. Gutiérrez und Audétat führten Kristallisationsexperimente mit wasserführenden Alkalibasalten durch und fingen dabei abgeschiedene Fluide in Form synthetischer Flüssigkeitseinschlüsse ein. Sie bestimmten, welche Haupt- und Spurenelemente dazu tendieren, von in zonierte Magmenkammern eindringenden Basalten in die darüber liegenden, höher entwickelten Magmen transportiert zu werden. Die im letzten Beitrag von Audétat beschriebenen Untersuchungen an natürlichen Quarz-Phänokristallen aus der Bandelier Tuffserie, New Mexico/USA, zeigen, dass das Auftreten Ti-reicher Quarzsäume auf Ti-armen Quarzkernen hauptsächlich auf Veränderungen der Temperatur und der TiO_2-Aktivität nach Magmenvermischung beruht und weniger auf Unterschieden in den Druckverhältnissen.

3.3 Mineralogie, Kristallchemie und Phasenübergänge

Untersuchungen zur Kristallstruktur von Mineralen und ihrer Veränderung mit ansteigendem Druck und Temperatur sind Voraussetzung für das Verständnis des Erdinneren; sie verbessern unseren Kenntnisstand über Prozesse, die sich tief in der Erde vollziehen und dennoch Vorgänge an der Erdoberfläche stark beeinflussen. Scheinbar kleine Veränderungen in der Kristallstruktur der Materie, zum Beispiel des Neigungsgrads polyedrischer Struktureinheiten, können einen grundlegenden Einfluss auf physikalische Eigenschaften wie Elastizität und Stabilität ausüben. Einkristallbestimmungen an $CaIrO_3$-Perowskit haben gezeigt, dass die Kompression der Struktur im Wesentlichen durch die Deformation der B-Stellen-Oktaeder erreicht wird anstatt durch einfaches Verkippen der Oktaeder, was zur höheren Festigkeit des $CaIrO_3$-Perowskit im Vergleich zu anderen *Pbnm* Ca-Oxid-Perowskiten beiträgt. Der Grad der Oktaederverkippung in *Pbnm*-Perowskiten kann anhand der mit Pulver-Röntgenbeugungsmethoden bestimmten Zellparameter recht einfach abgeleitet werden, wenn die Oktaeder undeformiert geblieben sind; Einkristallbestimmungen an $(Mg,Fe)(Si,Al)O_3$-Perowskit haben jedoch gezeigt, dass die Kippwinkel unterbewertet werden, wenn man Daten von Pulverdiffraktometrie verwendet und dass Übergänge im Valenzzustand von Fe die elastischen Eigenschaften beeinflussen. Ein weiterer wichtiger Parameter ist der Spin-Zustand der Eisenatome. *In situ*-Bestimmungen an $(Mg,Fe)(Si,Al)O_3$-Perowskit bei Druck- und Temperaturbedingungen des unteren Erdmantels haben bestätigt, dass Fe^{2+} in einen intermediären Spin-Zustand übergeht, wohingegen Fe^{3+} im Hoch-Spin-Zustand verbleibt.

Der Einbau volatiler Elemente in die Kristallstruktur von Mineralphasen des Erdmantels kann zu starken Veränderungen ihrer elastischen und rheologischen Eigenschaften führen. Hochdruck-Experimente, bei denen $(Mg,Fe)(Si,Al)O_3$-Perowskit untersucht wurde, haben Änderungen der Löslichkeit von Wasser als Funktion von Druck und Temperatur ergeben, während ähnliche Experimente für keramische Perowskite eine hohe Ar-Löslichkeit zeigen, die an die Bildung von Sauerstoff-Leerstellen gekoppelt ist. Letztere Ergebnisse zeigen eindeutig, dass neutrale Edelgase sehr leicht Leerstellen von geeigneter Größe in Kristallgittern besetzen können. Sie bestätigen weiterhin, dass Silikatperowskit bedeutende Mengen von Argon im unteren Erdmantel aufnehmen kann. Sauerstoff-Leerstellen wurden auch im System $CaTiO_3$-$CaFeO_{2.5}$ identifiziert; dabei wurde eine neuartige Methode verwendet, bei der sich mit Hilfe der Transmissionselektronenmikroskopie feststellen ließ, dass Fe^{3+} bevorzugt die Oktaederstellen besetzt. Die Position von Wasserstoff in Kristallgittern lässt sich mit Neutronenbeugung bestimmen; Messungen an der super-hydrierten Phase B, einer potentiell wichtigen Phase im unteren Teil der Übergangszone, die in Verbindung mit relativ kalten Erdplatten steht, zeigt Gitterplätze innerhalb ausgedehnter Kanäle, die für das hohe Wasseraufnahmevermögen des Gefüges verantwortlich sind und durch die wahrscheinlich eine schnelle Diffusion von Wasser durch die Struktur hindurch ermöglicht wird.

Einkristalle liefern detaillierte Informationen zu Kristallstruktur und Symmetrie, die man häufig nicht durch Experimente mit polykristallinem Material erzielen kann. Einkristalle aus $NaNiF_3$-Perowskit, der teilweise in eine Post-Perowskitstruktur umgewandelt wurde, zeigen starke topotaktische Beziehungen, die auf einen martensitischen Umwandlungsmechanismus deuten; dieser könnte eine Erklärung für die bekannte seismische Anisotropie an der Basis des unteren Erdmantels liefern. Granat, ein wichtiger Bestandteil des oberen Mantels und der Übergangszone, kann als komplexer Mischkristall einer Vielzahl von Endgliedern beschrieben werden; Einkristalluntersuchungen sowohl von unvermischten Phasen als auch von Mischkristallen werden dafür verwendet, um von der Granat-Kristallchemie auf physikalische und chemische Eigenschaften zu schließen. Mit Hilfe von $Fe_3Fe_2Si_3O_{12}$ (“Skiagit”)-Einkristallen wurde der Oxidationszustands von Eisen als Funktion des Drucks untersucht. Einkristalle aus $Ca_3Al_2Si_3O_{12}$ (Grossular), $Ca_3Cr_2Si_3O_{12}$ (Uvarovit) und ihre Mischkristalle wurden synthetisiert, um ihre thermoelastischen Parameter zu bestimmen. Mit den Ergebnissen können Modelle erstellt werden, die zur Bestimmung des internen Drucks von Granateinschlüssen in natürlichem Diamant dienen.

Schon in einfachen Oxiden erweisen sich Phasenübergänge oft als sehr komplex. So sind zum Beispiel von SiO_2 mehr als 30 stabile oder metastabile natürliche Phasen bekannt. Die Mechanismen der Strukturübergänge zu den Hochdruck-Polymorphen sind bisher noch nicht vollständig bekannt. Deswegen wurden Einkristall-Untersuchungen an einer Zwischenphase innerhalb der Übergangsreihe von SiO_2, die für Cristobalit X-1 einen breiten Stabilitätsbereich zeigt, begonnen und für die die Strukturverfeinerung noch andauert. Eisenoxide unterlaufen ebenfalls zahlreiche Hochdruck-Phasenübergänge, begleitet von Wechseln in der Fe-Valenz und der Phasen-Stoichiometrie. Ergebnisse aus Hochdruck-Experimenten mit der kürzlich entdeckten Fe_4O_5-Phase, in Kombination mit thermodynamischen Berechnungen der Phasengrenzen, zeigen, dass Fe_4O_5 über einen weiten Druck- und Temperaturbereich stabil ist. Damit wird die Bedeutung dieser Phase bei der Bewertung thermodynamischer Kenngrößen, der Sauerstofffugazität und der Beziehungen eisenhaltiger Phasen im Erdmantel unterstrichen. Mit Hilfe von Röntgenbeugungs-untersuchungen an Einkristallen wurde ein neues Polymorph von Fe_2O_3 gefunden, das eine doppelte Perowskitstruktur aufweist. Bei höheren Drücken wandelt sich diese Phase in eine Phase mit Post-Perowskit-Struktur um und erklärt damit bisherige Kontroversen hinsichtlich des Verhaltens im Druckbereich von 40-60 GPa. Untersuchungen an natürlichen Proben aus hydrothermal alteriertem Gangmaterial unter atmosphärischem Druck lassen deutlich verschiedene Fe_2O_3-Generationen erkennen. Diese sind im nano-Maßstab auskristallisiert und liefern Erkenntnisse zur Stabilität von Phasen, die für die Endlagerung radioaktiver Abfälle genutzt werden könnten.

Fragen zum Schicksal von Kohlenstoff und zur Natur des tief ins Erdinnere reichenden Kohlenstoffkreislaufs haben Untersuchungen zu Kristallchemie und Phasenübergängen in Karbonaten unter Temperatur- und Druckbedingungen des Erdmantels veranlasst. Innovative Messmethoden in einer Diamantstempelzelle ermöglichten Bestimmungen der Schmelztemperaturen von $MgCO_3$ bis zu Drücken von 84 GPa, wobei *post mortem*-Analysen deutlich machen, dass zumindest eines dieser Experimente von einer Dekarbonatisierung betroffen war. Durch Einkristallmessungen an eisenführenden Karbonaten konnte der Übergangsdruck von *high-spin* nach *low-spin* Fe festgelegt werden sowie seine Verschiebung zu höheren Drücken bei steigender Temperatur. Die lasergesteuerte Aufheizung der Proben erzeugte einen Übergang zu einer oder mehreren neuen, chromreichen Phasen, für die sowohl mit der XANES-Methode als auch mit Synchrotron-Mössbauerspektroskopie ein signifikanter Fe^{3+}-Anteil nachgewiesen wurde. Eine neue Methodik zur Untersuchung von Phasenübergängen und kristallographischen Beziehungen wird mit Hilfe des Transmissionselektronenmikroskops installiert. Die dabei eingesetzten Verfahren der bildgebenden Raster-Transmissionselektronenmikroskopie sowie der Präzessionselektronen-beugung liefern Ansätze, diese und zahlreiche weitere Phasenübergänge und kristallo-graphische Verhältnisse im sub-Nanometer-Maßstab zu untersuchen.

3.4 Physikalische Eigenschaften von Mineralen

Die Beziehung zwischen Struktur und physikalischen Eigenschaften von Materialien steht im Fokus der Forschung in verschiedenen wissenschaftlichen Disziplinen. Insbesondere sind präzisere Kenntnisse über die physikalischen Eigenschaften von Mineralen wichtig, da vor allem durch sie sich geophysikalische und seismologische Beobachtungen sinnvoll interpretieren lassen. So wie immer detailliertere Informationen über Grösse und Verteilung von radialen und lateralen Änderungen der akustischen Wellengeschwindigkeiten, elektrischen Leitfähigkeit und der Magnetisierung innerhalb der Erde erzielt werden, so sind genauere Kenntnisse über die elastischen, elektrischen und magnetischen Eigenschaften der Minerale des tiefen Erdinneren nötig, um diese Beobachtungen als Ausdruck von Temperatur, chemischer Heterogenität, Massen- und Wärmefluss, Phasenübergängen und anderen Prozessen zu erklären.

Labormessungen von Kompressions- und Scherwellengeschwindigkeiten in Mineralen des Erdmantels spielen eine fundamentale Rolle bei der Konstruktion seismischer Modelle des Erdinneren. In diesem Zusammenhang ist die Nutzung der Brillouin-Spektroskopie von Einkristallen zur Methode der Wahl am BGI geworden, da sie die Bestimmung des kompletten Elastizitätstensor von niedrigsymmetrischen Mineralen erlaubt. In den ersten drei

Beiträgen dieses Kapitels wird über die Ermittlung longitudinaler und transversaler Wellengeschwindigkeiten in Einkristallen von majoritischen Granaten, NAL (Al-reichen) Phasen und reinen sowie Fe-haltigen $MgSiO_3$-Perowskiten berichtet. Diese Resultate zeigen, wie solche Experimente – wenn auch schwieriger and zeitaufwendiger als solche mit Pulverproben – bessere Daten über die Auswirkungen von Temperatur und chemischer Substitution auf das elastische Verhalten von Mineralen liefern.

Messungen der elektrischen Leitfähigkeit von Mineralen und Gesteinen stellen eine weitere Möglichkeit dar, den Chemismus und die Struktur des Erdinneren besser zu verstehen. Der vierte und fünfte Beitrag dieses Kapitels beschreiben zwei komplementäre Methoden zur Untersuchung der elektrischen Eigenschaften von Mineralen. Eine Vielstempelpresse wurde eingesetzt, um Experimente zur elektrischen Leitfähigkeits an vorher deformierten Mineralaggregaten durchzuführen. Diese Daten werden in Leitfähigkeitsmodellen verwendet, um ungewöhnliche Leitfähigkeitskontraste in verschiedenen Bereichen der Astenosphäre zu erklären. Eine Diamantstempelpresse mit Laser-Heizung wurde stattdessen zur Untersuchung der elektrischen Leitfähigkeit von Al,Fe-haltigem $MgSiO_3$-Perowskit unter Druck- und Temperaturbedingungen des unteren Erdmantels genutzt.

Minerale sind nicht nur Ziel von Untersuchungen, da sie das Material darstellen, aus dem die Erde geformt ist und daher die dynamischen Prozesse im Erdinneren kontrollieren; sie können auch als Blaupausen für oxidische Verbindungen dienen, die für die angewandte Materialforschung interessant sind, wie im Falle von Quarz, der am besten untersuchten Form von SiO_2, oder Hibonit ($CaAl_{12}O_{19}$), der in der Zementherstellung breite Anwendung findet. In dem vorletzten Beitrag dieses Kapitels wurde das elastische Verhalten von Quarz unter hohem Druck nochmals mithilfe der Brillouin-Spektroskopie an Einkristallen untersucht, um eine fortdauernde Kontroverse zwischen verschiedenen Publikationen in der Literatur zu lösen. Im letzten Beitrag wurde der Oxidationszustand von Al substituierendem Ti in Hibonit durch Energieverlust-Spektroskopie und UV/Vis-Absorptionsspektroskopie bestimmt.

3.5 Fluide, Schmelzen und ihre Wechselwirkung mit Mineralen

Die Gefüge magmatischer Gesteine speichern Informationen über die Entwicklung und Kristallisation von Magmen. Prinzipiell sollten die Zeitskalen magmatischer Prozesse aus den Gefügen ablesbar sein, ähnlich wie man Druck und Temperatur aus der Zusammensetzung koexistierender Phasen bestimmen kann. Alle verfügbaren Methoden und Modelle leiden aber darunter, dass sie nicht direkt gegen experimentelle Daten kalibriert sind, da die direkte Beobachtung der Kristallisation von Magmen bisher extrem schwierig oder unmöglich war. Der Beitrag zu Beginn dieses Kapitels beschreibt die erste direkte Beobachtung der Kristallisation von Olivin aus einer Basaltschmelze, einschließlich Keimbildung, Kristallwachstum und Texturentwicklung. Die Daten zeigen, dass die CSD-Theorie (*crystal size distribution theory*), die oft verwendet wird um kinetische Daten aus Texturen von magmatischen Gesteinen zu extrahieren, fundamental falsch ist. Keimbildung und Kristallwachstum laufen nicht gleichzeitig nebeneinander ab, wie in der CSD-Theorie angenommen und Kristallwachstumsgeschwindigkeiten sind nicht konstant. In Wirklichkeit steigt die Kristallwachstumsgeschwindigkeit mit der Größe der Kristalle; dieser Effekt bestimmt zum größten Teil die Form der beobachteten CSD-Kurven. Dieser Effekt von „proportionalem Wachstum“ wurde bereits in Modellsystemen bei tiefer Temperatur beobachtet, aber die hier vorgestellten Daten zeigen erstmals, dass proportionales Wachstum auch während der Kristallisation natürlicher Magmen auftritt.

Das Verhalten von Schwefel in Magmen beeinflusst die Auswirkungen von Vulkaneruptionen auf das Klima sowie die Entstehung hydrothermaler Erzlagerstätten. Unter oxidierenden Bedingungen kann ein großer Teil des Schwefels in Form von kristallinem Anhydrit $CaSO_4$ vorliegen, so dass die Menge an Schwefel, die als Gas freigesetzt werden kann, begrenzt ist. Die Stabilität und Löslichkeit von Anhydrit in Silikatschmelzen ist jedoch bisher noch kaum untersucht worden. Der zweite Beitrag in diesem Kapitel beschreibt eine neue experimentelle Kalibrierung der Löslichkeit von Anhydrit über einen weiten Bereich von Schmelzzusammensetzungen. Der folgende Beitrag beschäftigt sich mit der Löslichkeit von Zirkon in SiO_2-reichen Schmelzen; diese Löslichkeit kann als Geothermometer verwendet werden. Eine neue experimentelle Strategie wird beschrieben, mit der vorhandene Daten zur Löslichkeit von Zirkon ergänzt werden konnten.

Schmelzbildung im tieferen Mantel ist nur in Gegenwart von flüchtigen Bestandteilen, wie H_2O oder CO_2 möglich, da ansonsten die Solidustemperatur weit über einer normalen Geotherme liegt. Bisher haben sich aber nur wenige Studien mit der möglichen Wechselwirkung von H_2O und CO_2 in Silikatschmelzen beschäftigt. Daten über die Verteilung von Wasser zwischen einer Basaltschmelze und Forsterit bei 13 GPa und 1500 bis 1700 ˚C in einem weiteren Beitrag dieses Kapitels deuten darauf hin, dass die Zugabe von CO_2 zu einer stärkeren Anreicherung von Wasser in der Schmelze führt. Dies würde bedeuten, dass die Wechselwirkung mit CO_2 die durch Wasser verursachte Erniedrigung des Schmelzpunktes noch verstärkt. Dieser Effekt könnte wichtig sein für die Stabilisierung von Silikatschmelzen in den tieferen Teilen des oberen Mantels. Karbonat-Schmelzen treten ebenfalls in Teilen des Erdmantels auf und sie könnten eine wichtige Rolle bei der Kristallisation von Diamant spielen. Der letzte Beitrag in diesem Kapitel enthält daher neue Daten zu Schmelzgleichgewichten in Mehrkomponenten-Karbonat-Systemen bei 12 bis 23 GPa.

3.6 Rheologie

Kenntnisse über die rheologischen Eigenschaften der erdbildenden Minerale ist unabdinglich, um die dynamische Entwicklung der Erde zu verstehen. Deshalb werden große Anstrengungen darauf verwendet, die Rheologie von Mineralen und Gesteinen unter den hohen Druck- und Temperaturbedingungen des Erdinneren zu verstehen. Experimentell sind solche Untersuchungen besonders schwierig, da es nicht nur nötig ist, stabile Druck- und

Temperatur-Bedingungen (p,T) sowie Probenumgebungen zu erzeugen, sondern auch deviatorische Spannungen und Deformationen des Probenvolumens über relativ lange Zeiträume stabil zu halten. Natürliche plastische Deformationsraten im Erdmantel liegen ungefähr bei 10^{-12}/sec oder darunter, während Deformationsraten in Laborexperimenten im Bereich von 10^{-7}/sec oder höher liegen. Das bedeutet, dass experimentelle Resultate immer um mindestens 5-6 Grössenordnungen extrapoliert werden müssen. Die Deformationsprozesse werden jedoch durch verschiedene Gitterdefekte (Punktdefekte, Versetzungen, (Sub-)Korngrenzen) erzeugt, und das Verhalten dieser Defekte kann experimentell quantifiziert werden, ohne dass natürliche Deformationsraten kopiert werden müssen. Darüberhinaus gibt es eine große Anzahl intrinsischer und extrinsischer Faktoren, die das rheologische Verhalten eines Materials beeinflussen und während eines Deformationsexperiments kontolliert oder konstant gehalten werden müssen.

Zur Überwindung dieser Schwierigkeiten hat das Bayerische Geoinstitut (BGI) zwei verschiedene Strategien entwickelt, um die Rheologie von Mineralen und Gesteinen zu verstehen. Die erste Strategie besteht darin, direkte Deformationsexperimente mit den fortgeschrittensten Technologien durchzuführen. Das BGI hat dazu kürzlich eine 6-Achsen-Vielstempelpresse eingeführt, die es ermöglicht, kontrollierte Deformationsexperimente über einen sehr weiten p,T-Bereich hinweg durchzuführen. Der erste Beitrag dieses Kapitels konzentriert sich auf die kristallographische Vorzugsorientierung (Textur) von Lawsonit und darauf, inwieweit solche Texturen die seismisch beobachteten Niedriggeschwindigkeitsschichten in Subduktionszonen erklären können. Die Resultate der Studie sprechen bisher allerdings gegen eine solche Erklärung. Der zweite Beitrag zielt darauf ab, die Wechselwirkungen von Festkörper (Dunit) und Schmelze unter Scherbedingungen zu verstehen. Bisherige Ergebnisse deuten darauf hin, dass ein positiver Zusammenhang zwischen Scherrate und dem Orthopyroxengehalt besteht. Dies ist wahrscheinlich darauf zurückzuführen, dass die höhere Scherrate die reaktive Oberfläche erhöht, so dass sich mehr Orthopyroxen bilden kann. In der dritten Studie wird die Wechselwirkung zwischen Deformation und dem Phasenübergang von Spinell- nach Granatlherzolith untersucht. Vorläufige Ergebnisse zeigen, dass unter dynamischen Bedingungen die Granatbildung deutlich schneller vonstatten geht, d. h. dass deviatorische Spannungen die Reaktionsrate direkt beeinflussen. Über diese Projekte am BGI hinaus wurde auch eine Studie zur Deformation von Wadsleyit in seinem Stabilitätsfeld durchgeführt, wobei eine rotationale Drickamerpresse in Kombination mit *in situ*-Röntgenmessungen an einer Synchrotroneinrichtung (NSL-II/New Haven, USA) eingesetzt wurde. Vorläufige Ergebnisse deuten auf eine relativ niedrige Aktivierungsenergie und ein sehr hohes Aktivierungsvolumen für dieses wichtige Mineral der Übergangszone des Erdmantels hin.

Die zweite Strategie ist darauf ausgerichtet, die grundlegenden Prozesse des Mineralkriechens zu verstehen, so wie z. B. Punktdefekt- oder Versetzungsmobilität in verschiedenen Mineralen. Im fünften Projekt wurden die Koeffizienten der Si-Selbstdiffusion in Korngrenzen gemessen, da dieser Prozess als entscheidend für die Deformationsrate des sog.

Coble-Kriechens angesehen wird. Die Studie zeigt, dass die Abhängigkeit von Temperatur, Druck und Wassergehalt von *Coble*-Kriechen in Olivin nur sehr gering ist, und postuliert, dass sich daher der Übergang des Deformationsmechanismus von Diffusions- zu Versetzungskriechen im oberen Erdmantel mit grösserer Tiefe ereignet. Die letzten beiden Beitäge berichten über Resultate von Experimenten, in denen die Erholungsrate von Versetzungen gemessen wurde. Die Resultate sind die unterschiedlichen Mobilitäten verschiedener Versetzungstypen in Olivin, die einen essentiellen Beitrag zum Versetzungskriechen und den resultierenden Texturen leisten. Es wurde herausgefunden, dass die Versetzungsmobilitäten für die Systeme [100](010) und [001](010) unter den untersuchten p,T-Bedingungen äquivalent sind, obwohl das [100](010) System in natürlich deformiertem Olivin viel häufiger beobachtet wird.

3.7 Materialwissenschaften

Ein Hauptziel der Experimentellen Geowissenschaften ist die Modellierung von Prozessen und des Verhaltens von Mineralen im Erdinneren. Bei der Hochdruckforschung in den Material- und Ingenieurswissenschaften kommen die gleichen Methoden zur Anwendung wie in den experimentellen Geowissenschaften; das Anwendungsspektrum ist jedoch deutlich breiter. Am Bayerischen Geoinstitut ist eine einzigartige Hochdruck-Ausstattung mit der Möglichkeit von *in situ*-Bestimmungen verfügbar, die anspruchsvolle und herausfordernde Forschungsarbeiten über physikalische und chemische Eigenschaften von Materie unter extremen Bedingungen erlaubt. In diesem Jahresbericht des Instituts werden Ergebnisse aus materialwissenschaftlichen Untersuchungen von Feststoffen – Metallen, Legierungen, Boriden, einfachen und komplexen Oxiden, Oxy-Chloriden – vorgestellt.

Obwohl die Supraleitfähigkeit bereits vor über 100 Jahren entdeckt wurde, bleibt die Synthese neuer Supraleiter auf der Basis theoretischer Prognosen weiterhin schwierig. Für die neu entdeckte Verbindung Eisentetraborid (FeB_4) mit einer bisher völlig unbekannten Kristallstruktur wurde schon im Jahr 2010 Supraleitfähigkeit vorhergesagt. Dieses neue Material aus handelsüblichem, preiswertem Eisen und Bor konnte jetzt erfolgreich bei hohem Druck und hoher Temperatur synthetisiert werden. Röntgenbeugungsanalysen an Einkristallen bestätigten die vorausgesagte Kristallstruktur. Darüber hinaus erwies sich das Material in der Tat nicht nur als Supraleiter sondern auch als unerwartet hart. Eisen- und Mangan-Tetraboride (weitere Verbindungen, deren Struktur und Eigenschaften in diesem Bericht vorgestellt werden) stellen eine neue Klasse äußerst attraktiver Materialien mit einer ungewöhnlichen Kombination von mechanischen, elektronischen und magnetischen Eigenschaften dar.

Perowskite, mit der allgemeinen Formel ABO_3, bilden eine sehr weit verbreitete Gruppe von Oxidmaterialen, die in fast allen Bereichen menschlicher Aktivitäten Verwendung findet. Sie weisen eine enorme Spannbreite in Zusammensetzung und Struktur auf, sowie eine große Vielfalt hinsichtlich ihrer physikalischen Eigenschaften, wie z. B. Ferroelektrizität, Supraleitfähigkeit, übergroße Magnetoresistenz und Multiferroizität. Die Perowskitstruktur hält zwei verschiedene Gitterplätze für Metallkationen bereit: Oktaedrisch koordinierte *B*-Stellen sowie *A*-Plätze mit variabler Koordinationzahl. Bei der weit überwiegenden Mehrheit der Perowskite weisen *A*- und *B*-Stellen unterschiedliche Materialeigenschaften auf: Oktaedrisch koordinierte Kationen der Übergangsmetalle (*B*) sind an Ladungsübertragung und magnetischen Wechseleinflüssen beteiligt, die *A*-Kationen hingegen bleiben elektronisch inaktiv. Mitglieder einer der wichtigsten industrierelevanten Untergruppe der Perowskite sind zum Beispiel Mangan-Perowskite, $A\mathrm{MnO}_3$, bei dem Mn-Ionen ausschließlich die *B*-Plätze in der Kristallstruktur besetzen. Zwei neue $\mathrm{Mn}_2\mathrm{O}_3$-Phasen, vom Korund- und vom Perowskit-Typ, wurden unter Hochdruck-/Hochtemperatur-Bedingungen synthetisiert. Die Entdeckung einer Perowskitstruktur in einfachem $\mathrm{Mn}_2\mathrm{O}_3$ lässt an der bestehenden Annahme in der Perowskit-Forschung und -Verwendung Zweifel aufkommen; bisher wurde von einer strikten Trennung der *A*- und *B*-Plätze in der Kristallstruktur ausgegangen, wobei die *A*-Plätze durch elektronisch inaktive Metalle (Alkali, Erdalkali, Seltene Erden), die *B*-Plätze durch Übergangsmetalle besetzt werden.

Multiferroische Materialien sind ein Feld intensiver Forschung in der modernen Festkörperphysik und -chemie. Diese Materialien veranschaulichen die Koppelung elektrischer und magnetischer Eigenschaften; sie ist für die Entwicklung neuer elektronischer Bauteile, in denen Magnetismus durch ein elektrisches Feld beeinflusst wird, von großer Bedeutung. Die Hochdruckforschung an der neuartigen multiferroischen Verbindung $\mathrm{PbFe}_{0.5}\mathrm{Nb}_{0.5}\mathrm{O}_3$ am Bayerischen Geoinstitut konnte ein komplexes Verhalten dieses Materials aufzeigen und deutet die Möglichkeit an, neue Polymorphe unter erhöhtem Druck zu erzeugen.

3.8 Methodische Entwicklungen

Ein Hauptziel der experimentellen Geo- und Materialwissenschaften besteht darin, neue experimentelle Ansätze und Methoden zu entwickeln und bestehende zu verbessern. Um Materialeigenschaften und Materialverhalten unter Bedingungen zu bestimmen, die im tiefen Erdmantel oder Erdkern herrschen, muss ein primäres Ziel sein, die experimentell bisher einstellbaren Druck- und Temperaturbereiche für Experimente mit Vielstempel-Pressen (Multianvil) oder Diamantstempel-Pressen über die bestehenden Obergrenzen hinaus zu verschieben. Verformungsexperimente bei hohen Drücken dienen der Bestimmung der Rheologie des Erdmantels, die einen wichtigen Parameter für die Konvektion im Erdmantel darstellt. Derartige Experimente dienen auch stets der Verfeinerung der Bestimmungsmethoden für deviatorische Spannungen und Verformungen, sowie der Genauigkeit bei der Einstellung von Druck und Temperatur. Weiterhin wird bei Hochdruck-/Hochtemperatur-Experimenten die Optimierung der Messmethoden bei *in situ*-Bestimmungen von physikalischen und chemischen Eigenschaften des Probenmaterials angestrebt.

Der erste Artikel stellt Bestrebungen vor, für Experimente mit Multianvil-Pressen in Druckbereiche vorzustoßen, die jenseits von 25 GPa, der bisherigen Druckobergrenze für Standardexperimente, liegen. Deutlich höhere Drücke könnten bei Verwendung von Druckstempeln aus gesinterten Diamanten erzeugt werden, jedoch ist dieser Ansatz extrem teuer. Zudem brechen gesinterte Diamantstempel sehr leicht und das Erreichen hoher Temperaturen wird durch die ausgezeichnete Wärmeleitfähigkeit von Diamant erschwert. Der daher gewählte Ansatz sieht die Verwendung von Wolframkarbid-Würfeln mit einer speziellen, schräg zulaufenden Geometrie um die druckübertragenden Stempelflächen vor. In der Kombination mit einer kleineren Probenanordnung lassen sich so in Experimenten die Maximaldrücke bis auf mindestens 30 GPa steigern.

Der zweite Beitrag beschreibt die Erzeugung von Druck- und Temperaturbedingungen für Verformungsexperimente (19 GPa und 1800 K), die für den unteren Teil der Übergangszone (in ca. 600 km Tiefe) im Erdmantel charakteristisch sind. Bei dieser Weiterentwicklung steht die Sechs-Stempel-Presse mit individuell steuerbaren Druckstempeln des Bayerischen Geoinstituts im Vordergrund. Diese Apparatur stellt einen wesentlichen Fortschritt gegenüber früheren Deformationswerkzeugen mit weitaus niedrigeren Druckbereichen dar. Die neue Technik ermöglicht somit die rheologische Erforschung der tiefen Bereiche der Übergangszone im Erdmantel.

Hochdruck-/Hochtemperaturexperimente mit Neutronenstreuung liefern uns wichtige Informationen über das Verhalten leichter Elemente (z. B. H und C) und ihrer Nachbarelemente (z. B. Mg, Al und Si) in Kristallstrukturen, da diese Elemente für Neutronen einen deutlich unterschiedlicheren Streuungsquerschnitt aufweisen als für Röntgenstrahlen. Der dritte Beitrag dieses Kapitels beschreibt Planungen für ein effizientes Detektorsystem, das an der Neutronenquelle des FRM II in Garching mit einer Hochdruckpresse für Radiographie und Strahlbeugung (**S**ix **A**nvil **P**ress for **Hi**gh Pressure **R**adiography and Diffraction – SAPHiR) kombiniert wird. Zusätzlich werden großvolumige Probenan-ordnungen mit weiten Stempelabständen für Multianvil-Pressen entwickelt. Beide Entwicklungen sind für die Anwendung von Neutronen in den Hochdruck-Experimenten sehr wichtig, da sowohl der Neutronenfluss des Primärstrahls als auch die Neutronen/Probe-Wechselwirkungen nur relativ schwach sind.

Silikatperowskite in Form von Einkristallen mit Edelsteinqualität werden für Untersuchungen elastischer Eigenschaften des unteren Erdmantels eingesetzt. Diese Kristalle werden unter hohem Druck in einer Diamantstempelzelle kombinierten Röntgenbeugungs- und Brillouinspektroskopie-Messungen ausgesetzt. Die Synthese derartig reiner Kristalle stellt eine große Herausforderung dar; derzeitige Fortschritte sind im vierten Beitrag beschrieben.
Nickel ist ein wichtiges Element des Erdinneren, insbesondere als Bestandteil des metallischen Erdkerns. Der abschließende Artikel dieses Kapitels stellt Bestimmungen der magnetischen und elastischen Eigenschaften von Nickel bei Drücken bis 260 GPa mit Hilfe der nuklearen Vorwärtsstreuung von Röntgenstrahlung an einem Synchrotron vor.

3. Research Projects

3.1 Earth and Planetary Structure and Dynamics

The early evolution of terrestrial planetary bodies was marked by accretion from embryos and planetesimals that led to their final size and by differentiation that led to their typical internal structure with a metallic core surrounded by a silicate mantle. These processes are at the center of the ERC project ACCRETE at the Bayerisches Geoinstitut and are hence well represented in the current annual report, including the first three contributions in this section. They are all concerned with accretion itself through collision modeling in N-body simulations or the consequences for planetary structure and composition.

With a half-life of 9 Ma the Hafnium-Tungsten (Hf-W) chronometer is very sensitive to processes in the early solar system, and can be used to investigate communalities and differences in the origin between the terrestrial planets for which we have rock samples (Mars and Earth). Based on N-body simulations the first contribution argues that a high embryo mass is required at the beginning of accretion to explain the current Hf-W ratio for Mars and the Earth. In such simulations, Mars is best represented as a stranded embryo that has not experienced a late stage impact history. The Moon forming giant impact on Earth, by contrast, is required in the simulations to have occurred relatively late in the formation history, *i.e.*, ~ 100 Ma into the formation of the solar system.

Impacts onto embryos or planetesimals will lead to partial melting, and in extreme cases to magma oceans on the planetary body. The extent and timing of melting obviously depends on the size and frequency of impacts. It has often been assumed that magma has solidified in between impacts, a hypothesis that is questionable at least for large impacts. In the second contribution this is looked at in detail for an Earth-forming N-body simulation. The authors find that in the early accretion history – as long as the impactors are relatively small – this assumption is satisfied. At a later stage solidification hinges on the radiation of heat from the planet. In the presence of a shielding atmosphere that may, for example, originate from evaporation of the magma itself, there is insufficient time for complete solidification, leading to very different impact dynamics.

Also based on N-body simulations that produce an Earth-like planet in terms of mass and final heliocentric distance the third contribution considers chemical scenarios for the composition of the original embryos and planetesimals that can lead to a primitive mantle composition. In fitting primitive mantle composition it has become apparent that the original bodies require a varying oxidation state, with a reduced composition near the Sun, *i.e.*, < 1 astronomical units (AU), and fully oxidised composition beyond 4 AU, with partial oxidation in between. If compositions at >9 AU are assumed to be CI chondritic, then the water budget of the Earth can also be accounted for by accretion.

The final two contributions of the section, by contrast, deal with the state of the modern Earth, considering the state of the Earth's mantle and the thermal evolution of subduction zones. In the first contribution a thermo-elastic model for mantle minerals is presented that can be used to interpret the physical state of the mantle in terms of temperature and different compositional models. More importantly yet, such a model provides a basis for including thermodynamics and elasticity in geodynamic and seismological studies of the Earth's mantle.

Subduction zones are the major source for buoyancy and material transport in mantle convection as they cycle differentiated material from the surface back into the solid Earth. While many aspects of subduction on the thermal state of the Earth's mantle have been considered, the heat produced or consumed due to metamorphic reactions has not been adequately addressed in previous simulations. In the final contribution of the section the effect of metamorphic reactions in terms of phase transformations and devolatilisation is considered based on phase relations and self-consistently computed thermodynamic properties and then integrated into the heat budget of the slab. In this study it was found that temperature variations due to realistic slab properties and solid-fluid reactions do not exceed 70 °C, but different sections of the differentiated slab (sediments, basalt and serpentinised harzburgite) experience distinct thermal evolution, possibly leading to a decoupling of the different layers.

a. *Numerical studies of terrestrial planet formation (S.A. Jacobson and D.C. Rubie; A. Morbidelli/Nice, D.P. O'Brien/Tucson, S.N. Raymond/Bordeau and K.J. Walsh/Boulder)*

The formation of terrestrial planets can be modeled by N-body simulations that include the gravitational evolution of a disk of planetesimals and embryos. Many of the details of such a disk are unknown, but the bimodal mass distribution between planetesimals and embryos is a product of oligarchic growth. We experimented with varying the initial mass of each embryo and the initial ratio of the total mass between the embryo and planetesimal populations. Isotopic ratios of different planets, here with a focus on the Hf-W system, can be used to see whether a planetary formation hypothesis is plausible.

We discovered that large embryo masses are necessary to explain the rapid growth of Mars as constrained by the Hf-W radiogenic system. The systems with the highest initial embryo mass (0.08 Earth masses) are the ones most consistent with the constraints from isotopic data. This is a strong argument for the hypothesis that Mars is a stranded embryo, *i.e.*, most of its growth occurred during the runaway phase of terrestrial planet formation and it did not participate in the giant impact phase that, *e.g.*, led to the formation of the Earth-Moon system.

For Earth-like systems we discovered that the ratio of the total mass in the two populations controls the timing of the last giant (Moon forming) impact: As the initial ratio of total embryo mass to total planetesimal mass increases, the average Moon forming impact time is delayed, so we can match different interpretations of the terrestrial Hf-W data. Dynamics alone cannot determine which interpretation is correct, however we see that the time of the last giant impact is correlated in each set of initial conditions with the mass of the late veneer. We can use this correlation to determine an age for the Moon formation event independent of all radiogenic systems by estimating the mass of the late veneer from the highly siderophile element abundances in the Earth's mantle (Fig. 3.1-1). This estimate gives a late accreted mass of 0.5 % the mass of the Earth. From this estimate, we determine a dynamical formation for the Moon at 95 My, and rule out an early Moon formation (< 40 My). Such an estimate is consistent with other interpretations and other isotopic systems. In order for the Moon forming impact to occur so late in the formation history of the terrestrial planets there must be more mass in the embryo population initially than in the planetesimal population by more than a factor of four. The Moon forming impacts found in the N-body simulations are consistent with newly theorized scenarios using more sophisticated soft-particle hydrocode simulations.

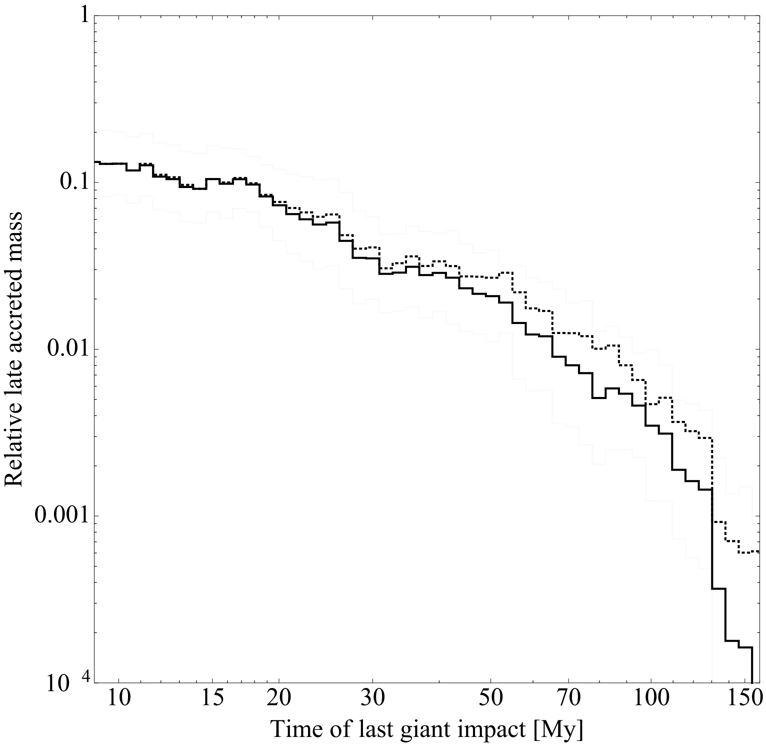

Fig. 3.1-1: The Late veneer mass as a function of the time of the last giant (Moon forming) impact. The solid staircase is a running geometric mean of the Grand Tack simulations and the shaded region covers the 1-sigma geometric uncertainty. The dotted staircase is the running mean for all Earth-like planets created in these simulations. The dashed line is the estimate of the late veneer mass from the highly siderophile element record and the gray region is the associated 1-sigma uncertainty.

b. *Melting due to impacts on growing proto-planets (J. de Vries and D.C. Rubie; F. Nimmo/Santa Cruz and H.J. Melosh/West Lafayette)*

As presented in the previous contribution the terrestrial planets in our solar system were formed by a series of collisions between smaller bodies – a process that is modelled numerically using N-body accretion simulations. Planetary embryos grow by accreting smaller bodies from their so called ‘feeding zone’ and collide with one another when they enter their mutual feeding zones. The energy involved in each collision causes large-scale melting, which allows metal-silicate segregation to occur, resulting in an episode of core formation. To develop a model of the compositional evolution of our rocky planets based on a collisional history predicted by N-body accretion models, estimates of the amount of melting and the pressure- and temperature-conditions at the base of the magma ocean are required. To determine the amount of melting for each of the several hundred to thousands of collisions, as calculated from an N-body model, a reliable and efficient shock/melting model is needed.

Full three-dimensional models are computationally too time-consuming, whereas two-dimensional models cannot be used for non-vertical impacts due to their assumed symmetry in the third dimension. Therefore, a parameterised model is used, which describes the amount and depth of melting based on the energy needed to melt a dunite mantle (and in cases of deep melting an iron core) and the energy available from the impact. The available energy depends on the impact angle and velocity as well as on the impactor size and the material properties of both the impactor and the target.

Once the depth of melting is known, the pressure and liquidus temperature at that depth can be determined, and our aim is to use such conditions to model core formation and siderophile element partitioning. Ideally, these results should be independent of the specific N-body model used for the collision history. However, since the amount of melting depends on the size of the impactor and the target is assumed to solidify between impacts, many small impactors will result in shallower melting depths than a small amount of larger impactors for the same time period (Fig. 3.1-2). The initial size distribution of the bodies in the N-body models therefore influences the results. In an attempt to solve this issue, the assumption of solidification between impacts is investigated.

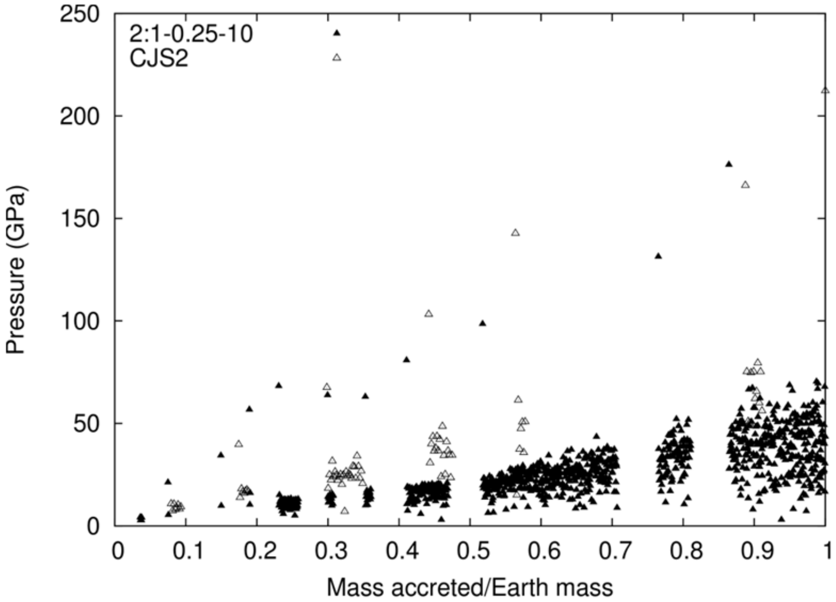

Fig. 3.1-2: The pressure at the melting depth as a function of the mass of the growing planet for all collisions that finally create an Earth-like planet. Two different N-body accretion models are used, a model with a large number of relatively small bodies (2:1-0.25-10A, open triangles) and a model with a smaller number of large bodies (CJS2, filled triangles).

To do this, a model is developed to estimate the cooling time of a global magma ocean. This model balances the heat flux through the planet's surface with the latent heat released during crystallisation and the heat released through secular cooling. The heat flux is approximated by a constant value. However, this value is strongly dependent on the amount of atmosphere present. It is likely that large impacts remove most of the atmosphere of the target, thereby increasing the surface heat flux. However, degassing of a magma ocean creates a new, possibly very dense atmosphere, decreasing the heat flux through the surface by as much as 3 orders of magnitude. Calculations have been done for both end members.

In general, at the start of accretion the impacts are close together. Most of these impacts are small and will cause only small amounts of melting. However, some of these collisions occur between two similar-sized bodies resulting in a deep magma ocean that cannot crystallise before the next impact. Figure 3.1-3 shows results for a model with relatively large bodies. With the assumption of no insulating atmosphere, all but one of the magma oceans crystallise before the next impact. With a dense atmosphere present, a more significant number of magma oceans would still be molten when the next impact occurs.

Future work will look into this in more detail and study the differences between impacts on a magma ocean compared with a solid surface.

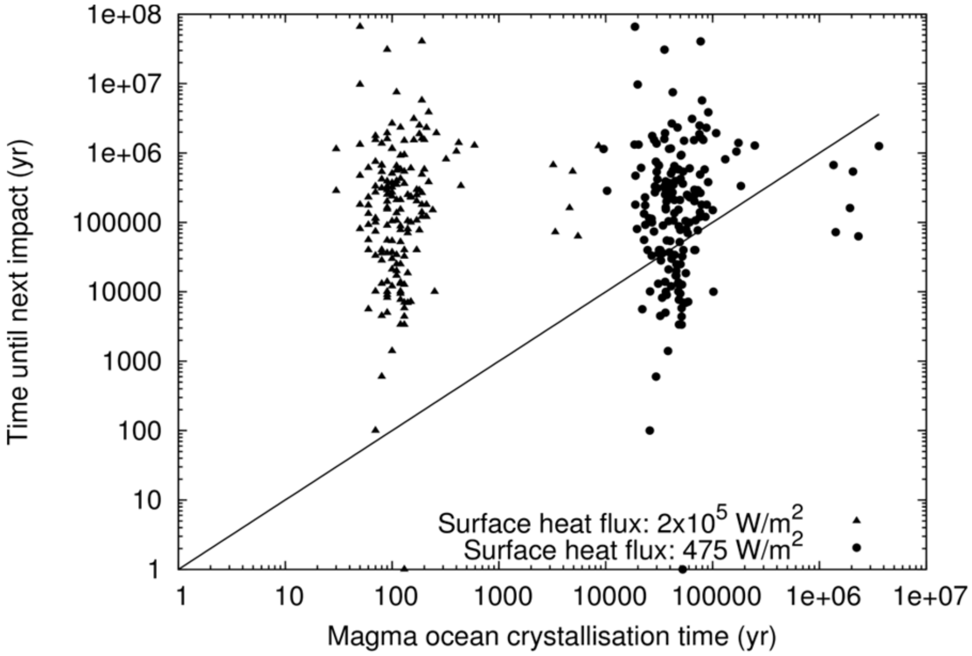

Fig. 3.1-3: Crystallisation time versus time until the next impact for the CJS2 model. All points above the line represent magma oceans that crystallise before the next impact. In the case where there is no atmosphere present (flux = 200,000 W/m^2, triangles) only one impact happens on a molten surface. When a dense atmosphere is taken into account (flux = 475 W/m^2, circles), a large number of impacts would happen on a molten surface.

c. *Early differentiation of the terrestrial planets and implications for the compositions of embryos and planetesimals in the early solar system (D.C. Rubie, S.A. Jacobson and D.J. Frost; A. Morbidelli/Nice, D.P. O'Brien/Tucson, H. Palme/Frankfurt and E. Young/Los Angeles)*

The accretion of the terrestrial planets of our Solar System, Mars, Earth, Venus and Mercury, occurred on a timescale of 10-100 My through numerous high-energy collisions with planetesimals and embryos (Moon- to Mars-size bodies respectively) as discussed in contribution 3.1.a. In order to provide new tests of the validity of such simulations, we are combining the N-body accretion results with models of planetary core-mantle differentiation. Each collision is considered to create a deep magma ocean and results in an episode of core formation by facilitating metal-silicate segregation as discussed in the previous contribution of this annual report. Based on assigned bulk compositions of accreting material, a model for the pressure-temperature conditions of metal-silicate equilibration and experimental data on element partitioning at high pressure, the compositions of equilibrated metal and silicate are determined for each core-formation event. In this way, the evolution of mantle and core compositions for each planet can be tracked throughout its accretion history – and mantle model compositions resulting from a given accretion simulation can then be compared with the actual compositions.

We consider simulations that produce an Earth-like planet in terms of mass and final heliocentric distance just as in the preceding contribution. Least squares regressions are then performed in order to adjust 2-4 fitting parameters such that the model mantle composition calculated for the Earth-like planet is identical or close to that of the Earth. We currently use primitive mantle concentrations of SiO_2, FeO, Ni, Co, V, Ta, Nb, and Cr as fitting constraints. The parameters that are refined in least squares regressions include the pressure at which metal and silicate equilibrate: this is considered to to be a fixed fraction of the planet's core-mantle boundary pressure at the time of impact and therefore increases as the planet grows. The other fitting parameters are those that are used to define the compositions of the original embryos and planetesimals as a function of their heliocentric distances of origin. The main compositional variable is oxygen content which is defined by specifying the proportions of Fe that are present as metal and as FeO in silicate. Compositions can thus be varied from highly reduced (99.9 % Fe as metal) to fully oxidised (no metal). The oxygen content of reduced compositions can be further decreased by specifying that a fraction of the available Si is initially dissolved in the metal.

The compositions of primitive bodies as a function of their original heliocentric distance are critical in the model for obtaining good fits to the mantle composition of the Earth. We assume that compositions (oxygen contents) vary systematically with heliocentric distance rather than randomly and we have investigate a broad range of possible composition-distance models. For example, a model in which oxygen content is constant with heliocentric distance gives an unacceptably poor fit to the Earth's mantle composition. The only models that provide good fits involve bodies that originate close to the Sun (*e.g.*, < 1 AU) having highly reduced compositions, those originating further out (*e.g.*, between 1 and ~ 4 AU) being partially oxidised and those originating beyond ~ 4 AU being fully oxidised. In addition, when planetesimals originating from beyond ~ 9 AU have a CI composition, which includes 20 wt.% water, realistic Earth mantle H_2O concentrations are obtained. An example of a successful composition-distance model is shown in Fig. 3.1-4. However, this model, which involves a gradient in oxidation state, is not unique and equally good results are obtained with a model that involves a step in oxidation state.

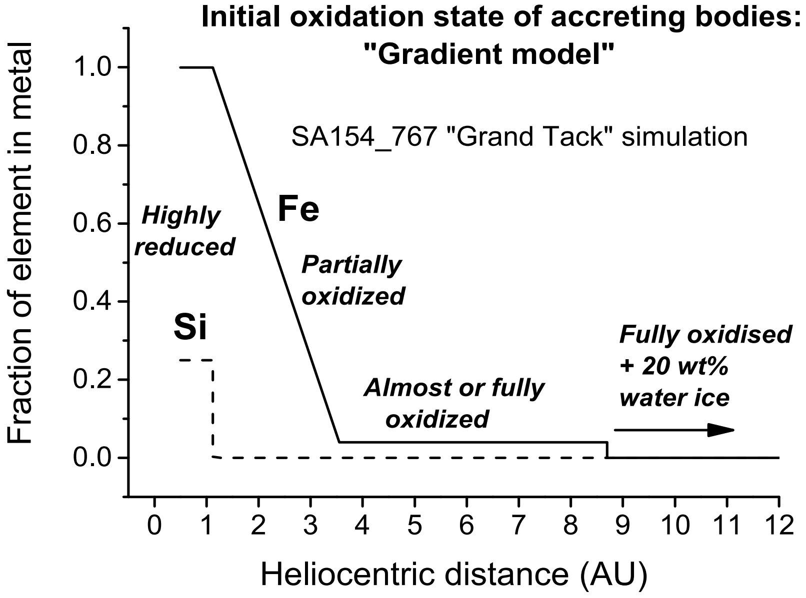

Fig. 3.1-4: Fitted composition-distance model for N-body simulation SA154_767. Compositions of embryos and planetesimals that form at < 1 AU are highly reduced with 99.9 % of Fe as metal and < 20 % of total Si initially dissolved in the metal. Between 1 AU and ~ 4 AU there is a compositional gradient with the proportion of Fe present as metal decreasing with increasing distance. Beyond ~ 4 AU compositions are almost or completely oxidised with little or no metal present.

Oxygen fugacities of a solar gas are orders of magnitude more reducing than the intrinsic oxygen fugacities at which the terrestrial planets and meteorite parent bodies formed but are consistent with the region of highly-reduced compositions at < 1 AU shown in Fig. 3.1-4. Thus extensive oxidation must have occurred in the early solar sytem with oxidation of Fe to form an FeO component in silicates being the major consequence (c.f. Fig. 3.1-4). The most likely oxidant was water. The oxidation gradient shown in Fig. 3.1-4 can be explained as follows: Due to the net inflow of material in the solar nebula, ice-covered dust moves inwards from beyond the snow line. Inside the snow line, water ice sublimes, thus adding H_2O to the vapour phase. As temperatures continue to rise and material continues to move inwards, H_2O-rich vapour reacts with Fe-bearing dust which results in oxidation. Inward still, vapour is H_2O-poor because the products of sublimed water ice have not mixed all the way to the innermost solar system. Here Fe remains free of oxidation and highly-reduced compositions are preserved.

d. *Elasticity of mantle minerals in a thermodynamic model (T. Chust and G. Steinle-Neumann; H.-P. Bunge/Munich)*

Over the past years we have developed an extensible software framework for mineralogical thermodynamics and geophysical applications. Using a database of thermodynamic model parameters for different minerals, a stable phase assemblage can be determined through Gibbs energy minimisation at any given pressure, temperature and bulk composition. The same framework of thermodynamic functions used to solve the optimisation problem is also available to compute various material properties like density and elastic moduli. This information can in turn be used in geodynamic or seismological models.

Densities and elastic moduli of phases with $MgSiO_3$ bulk composition at ambient temperature are presented in Fig. 3.1-5. The assemblage properties are discontinuous at phase changes from olivine+quartz to orthopyroxene (around 0.8 GPa), from orthopyroxene to high-pressure clinopyroxene (4.4 GPa), from high-pressure clinopyroxene to wadsleyite+stishovite and ringwoodite+stishovite (11.5 GPa), and from ringwoodite+stishovite to periclase+stishovite (22 GPa). In addition to the properties for the stable phase assemblage the figure shows those for Mg-Majorite between 10 GPa and 25 GPa, where this phase could be expected to occur naturally at higher temperature.

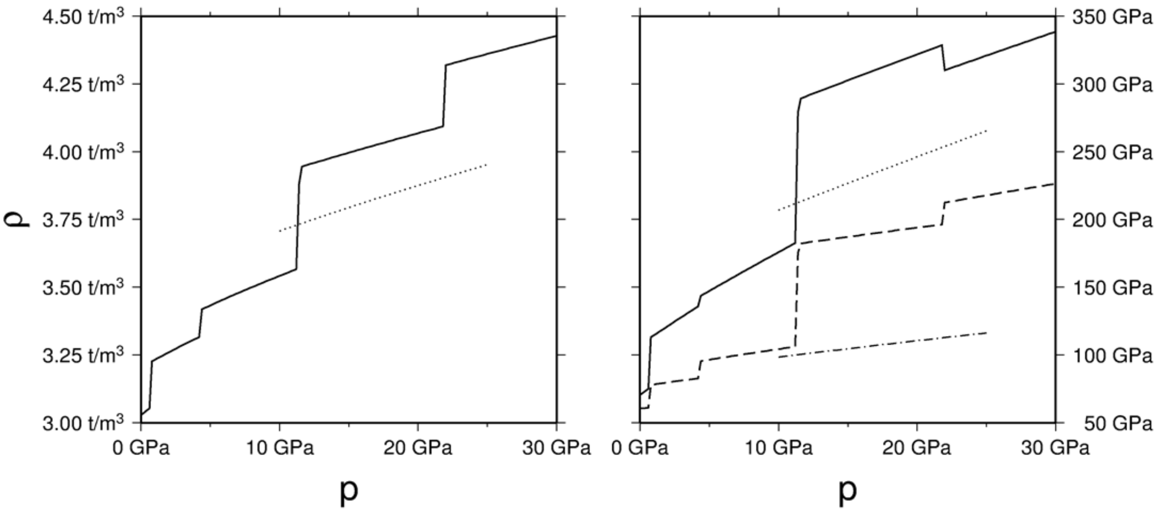

Fig. 3.1-5: Density, bulk and shear modulus of phases with $MgSiO_3$ bulk composition at 300 K. On the left panel, the density of the stable phase assemblage is shown with a solid line. On the right panel, the bulk and shear modulus of the stable phase assemblage is shown in solid and dashed lines, respectively. The stable phases are, in order of increasing pressure: olivine+quartz, enstatite, high-pressure clinoenstatite, wadsleyite+stishovite, ringwoodite+stishovite, and periclase+stishovite. While not stable at ambient temperature, the density and elastic moduli of $MgSiO_3$ majorite garnet are included for comparison due to its importance in the transition zone (dotted and desh-dotted lines).

Figure 3.1-6 shows densities and elastic moduli of phases with pyrolitic bulk composition along an adiabat with a footing temperature of 1650 K, computed consistently with the optimisation of the phase composition. The properties for the stable phase assemblage are plotted together with values from the preliminary reference Earth model for comparison. The assemblage properties undergo marked changes with the phase transitions from olivine to wadsleyite (~ 14.5 GPa), from wadslyeite and ringwoodite to akimotoite (between 20.5 and 21.5 GPa), from akimotoite and garnet to perovskite (between 21 GPa and 29 GPa), and from the perovskite to the post-perovskite phase (~ 125 GPa). The transformations to and from pyroxenes and their polymorphs are more gradual under the pyrolite bulk composition constraints in contrast to the sharp discontinuities seen in Fig. 3.1-5, but mostly the same phases are present in the stable phase assemblages. The prominent drop of the bulk modulus in the $MgSiO_3$ composition at 22 GPa at room temperature (Fig. 3.1-5), does not appear in the pyrolite composition for two reasons: (a) Perovskite is stable at lower mantle conditions above ~ 21 GPa; (b) other phases are lowering the average bulk modulus at pressures below 22 GPa: most important here is an increasing amount of Majorite in the stable assemblage at pressures between 10 GPa and 21 GPa, with a lower bulk modulus than wadsleyite.

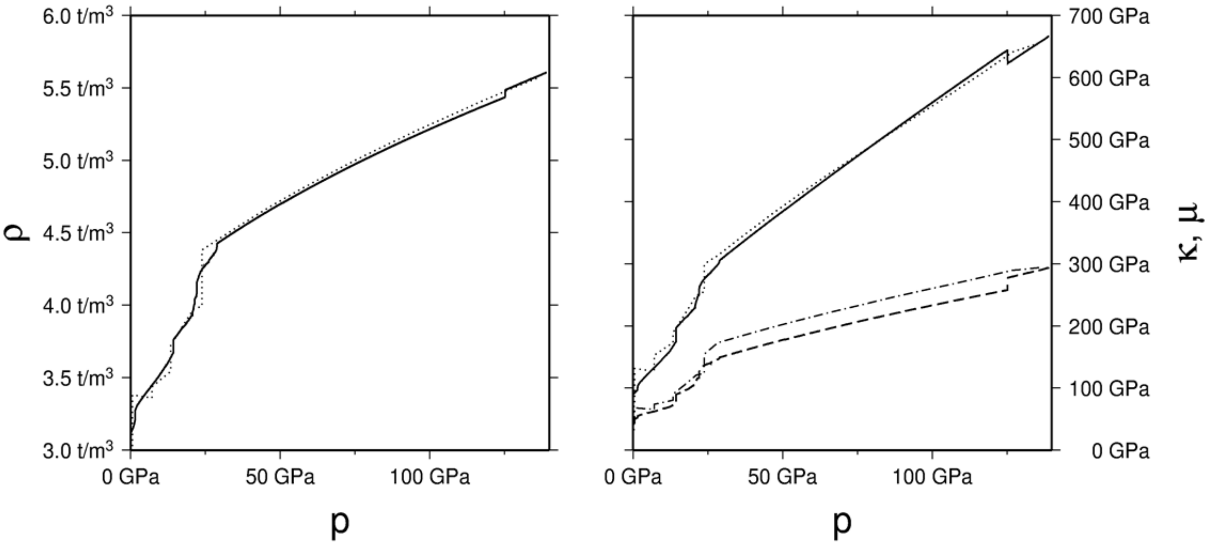

Fig. 3.1-6: Density, bulk and shear modulus of stable phases with bulk composition $(MgO)_{1.2878}(FeO)_{0.1594}(CaO)_{0.0759}(Al_2O_3)_{0.0573}(Na_2O)_{0.0028}(SiO_2)$ along an adiabat starting at zero pressure and 1650 K. In the left panel, the density of the stable phase assemblage is shown in a solid line, the density profile from PREM in a dotted line. In the right panel, the bulk and shear moduli of the stable phase assemblage are shown in solid and dashed lines, respectively. Values from PREM are included with dotted and dash-dotted lines, respectively.

While the slopes of the curves in Fig. 3.1-6 between the simulated values and the seismological reference model show a good match, the positions of phase transitions are shifted to slightly lower pressures in the simulation results and the absolute values for the shear modulus are not a perfect match. Both the shear modulus and the position of phase transitions are very sensitive to temperature; for perovskite μ increases by ~ 50 MPa/K with falling temperature (around ~ 50 GPa, ~ 1500 K) suggesting that the adiabat is "too hot". A lower footing temperature for the adiabat would generally lower the transition pressures and sharpen the transition between different phase assemblages and hence bring the discontinuities in better agreement with seismological observations. By lowering the footing temperature by 200-300 K also the overall agreement in density and elastic properties between the thermodynamic model and the seismological observations would significantly be improved.

e. *Effects of metamorphic reactions on the thermal evolution of subduction zones (Z. Chemia/ Copenhagen, D. Dolejš/Prague; G. Steinle-Neumann)*

The thermal evolution of subducting lithosphere is of primary importance for understanding physical properties, phase transformations, fluid migration and melting regimes at convergent plate boundaries. Various factors influencing the thermal structure of a subduction zone have been considered, including age, geometry and rate of subducting lithosphere, shear stress across the subduction interface, rheology, radioactive heating, and variable thermal conductivity. At the same time substantial heat production or consumption can occur due to metamorphic reactions which have often been neglected in numerical calculations. The extent to which metamorphic reactions, *i.e.*, phase transformations, net transfer and devolatilisation reactions, can affect the thermal structure of a subducting slab is insufficiently understood even though it has been noticed in the late seventies. Previous attempts to include heat of reactions in numerical calculations have led to incomplete or contradictory results. These approaches were based on adjusting heat capacity for rock undergoing reactions in an *ad-hoc* fashion. Here we include metamorphic reactions in the heat budget of the slab, derived from phase equilibria and self-consistent thermodynamic properties.

In order to gain detailed insight into the slab behaviour we construct a three-component model, which consists of oceanic sediments, basaltic crust, and depleted harzburgite mantle (which we presented in a previous annual report). For these three lithologies we compute stable phase assemblages as a function of pressure and temperature, their fluid compositions and thermodynamic properties. Free fluid phases occur in the reactions and can either be retained in pore spaces or expelled from the slab, creating two different scenarios: a fluid-bearing or fluid-free slab. In order to separate contributions from variable physical properties (heat capacity *vs*. density variation) and metamorphic reactions we compute a non-reactive slab as well in which we keep the phase assemblage at the onset of subduction fixed.

Deviations in the thermal evolution of the different slab components from reference subduction paths can be directly computed from the heat budget and are shown in Fig. 3.1-7. As a reference we have chosen subduction paths from the literature for the Nicaraguan subduction zone using isoviscous (left column) and olivine rheology (right column), leading to colder and hotter subduction paths, respectively. We investigate temperature profiles at the surface of the slab for the sediments (upper row), at 1 km depth into the slab for the sediment-basalt interface (middle) and at 7 km for the basalt-harzburgite interface (lower row).

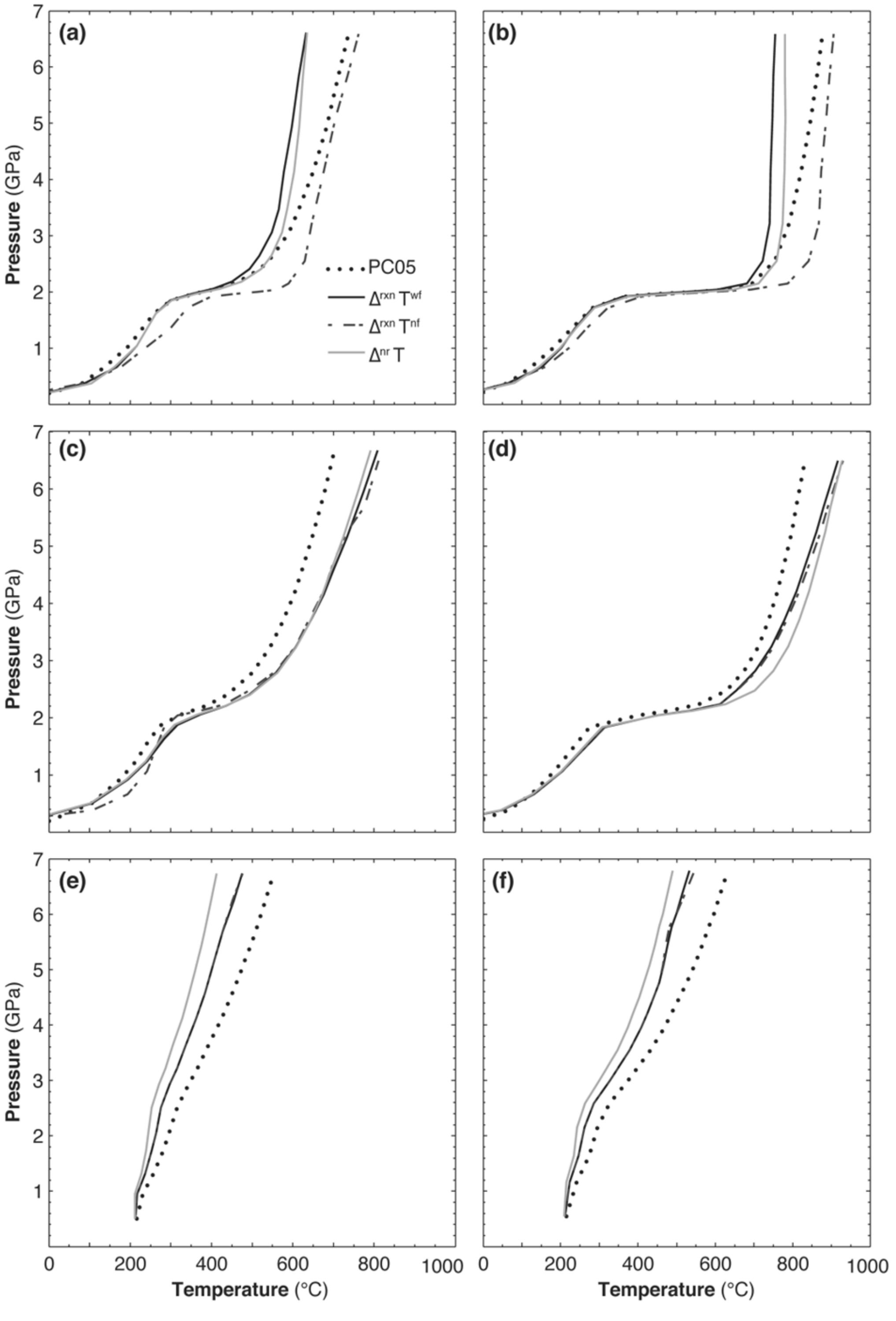

Fig. 3.1-7: Geotherms of the slab calculated at the surface of each lithological layer: (**a-b**) at slab surface, (**c-b**) at the sediment-oceanic crust interface, (**e-f**) at the oceanic crust-mantle interface. Dotted line represents P-T paths adopted from the literature (PC05) for isoviscous mantle wedge rheology (**a**, **c** and **e**) and temperature-stress dependent olivine rheology (**b**, **d** and **f**). Corrections are applied to the initial P-T paths based on the following models: (i) variable thermodynamic parameters (grey lines); (ii) metamorphic reactions with the free fluid phase retained in the rock (solid lines); (iii) metamorphic reactions with instantaneous fluid release (dashed lines).

For the sediments variable thermodynamic parameters lead to colder geotherms relative to the reference, reaching differences in the range of 100 °C at 7 GPa. The situation for harzburgite is similar, while in the basalt layer variable thermodynamic parameters lead to hotter subduction paths.

When fluid is retained in the sediments, metamorphic reactions add little heat to the slab, but as fluid in the sediments is formed at relatively low pressure-temperature conditions, the expulsion of free fluid phases leads to significantly higher temperatures, similar to the reference geotherms: due to higher heat capacities of the fluid phases compared to the solid rock fluid-bearing rocks experience slower heating. The extent to which a free fluid phase is retained in the rock is determined by its deformation behaviour. For wet quartzite, used as a proxy here, the deformation behaviour changes from brittle to viscous in the range of 250-300 °C, corresponding to a pressure of 1-1.5 GPa on the reference geotherm. With a porosity of 0.5-1 % in the lower part of the upper crust some volatiles will be released into the mantle wedge even in the brittle regime; combined with complete fluid release in the viscous deformation regime at pressures exceeding 1 GPa (40 km depth) the fluid-free scenario appears more appropriate for subducting sediments.

For the basalt, metamorphic reactions also do not contribute significantly to the heat budget during subduction, changing the temperatures only by ~ 20 °C relative to the non-reactive rock. As no substantial devolatilisation occurs in the basalt up to ~ 500 °C, the fluid-retaining and fluid-free subduction paths only diverge at this temperature or ~ 2 GPa, with a noticeable shift only in the hotter subduction paths of the olivine rheology. In the harzburgite, metamorphic reactions heat the slab by as much as 50 °C relative to the non-reactive rock, but as for basalt there is little difference between the fluid-bearing and fluid-free case because metamorphic reactions do not liberate any water up to 500 °C, a temperature that is not exceeded up to 7 GPa at the crust-mantle interface.

Our modeling is the first attempt to address the thermal state of multilayer subducting slab in a self-consistent manner with thermodynamic data and phase equilibrium constraints. The results indicate that realistic slab properties and solid-fluid reaction do not cause temperature variations greater than 70 °C for isoviscous mantle wedge rheology but strong thermal decoupling and distinct melting behaviour in individual lithologies is expected to occur in models with variable olivine rheology.

3.2 Geochemistry

Geochemical exchanges during the accretion of the Earth were likely part of a dynamic process where metallic iron in impacting material segregated and sank rapidly through the silicate mantle. Due to the size of separating metal and the speed of the sinking process, significant portions of the metal may have remained out of equilibrium with the surrounding mantle at the raised pressures and temperatures experienced on the way to the core. The first study in this section seeks to address this issue by determining the rate of chemical diffusion of silicon, a likely light element in the core, within iron metal. By quantifying the time required for diffusive equilibration, constraints can be placed on the dynamics of core formation.

Determining how segregating metal might have reacted with the deep lower mantle forms the focus of the following two studies. Here there are great technical challenges because experiments at these pressures must be performed in the laser heated diamond anvil cell where the recovery and analysis of the micron scale samples is very difficult and requires innovative techniques. A major result is that large proportions of the light elements silicon and oxygen are found to enter iron metal at conditions equivalent to a deep magma ocean extending into the lower mantle.

The following four studies are designed to allow the conditions of core formation to be constrained from an assessment of the relative depletions of siderophile (metal loving) elements from the Earth's silicate mantle. The first of these examines whether the composition of the silicate melt influences metal silicate partitioning. This is mainly important for determining whether variations in melt composition, which can occur during experiments, may affect partitioning results. The next 3 studies examine the effects of sulphur dissolved in liquid iron metal on metal silicate partitioning of siderophile, highly siderophile and volatile siderophile elements respectively. The results on all three groups of elements are similar in that sulphur brings metal silicate partition coefficients closer to those required to explain the concentrations of these elements in the present day Earth's mantle. A final study on core formation examines the partitioning and the stable isotope fractionation of nitrogen between metal and silicate. In addition to the most abundant nitrogen isotope, with a mass of 14, there is a less abundant heavier stable isotope with a mass of 15. Experiments in this study show that nitrogen is moderately siderophile but that the lighter isotope partitions more strongly into liquid metal. This can potentially help to explain the enrichment of the heavier isotope in the outer portions of the Earth.

The next three contributions in this section deal with the effect of ferric iron on melting relations and mineral stabilities in the Earth's mantle. The study by Sorbadère *et al.* focuses on the so-called "$Fe^{3+}/\Sigma Fe$ paradox" in MORB magmas, which refers to their surprisingly constant $Fe^{3+}/\Sigma Fe$-ratios despite significant variations in the degree of partial melting. A potential explanation for this phenomenon is that mineral/melt partition coefficients of Fe^{3+}

increased with increasing degree of partial melting, a hypothesis which is being experimentally tested. Myhill *et al.* examine the effect of iron oxidation state on the solidus temperature of a synthetic peridotite analogue. While the peridotite solidus is known to be depressed at low pressure as more iron enters the higher oxidation state, to date, no systematic data were available at high (> 4 GPa) pressure. The first results indicate that there is also a strong effect on the solidus at deep upper mantle conditions. The following study also deals with the effect of iron oxidation state on mineral phase relationships in the upper and lower mantle. By incorporating experimental data on Fe^{3+}-bearing high-pressure mineral phases into existing thermodynamic models it will become possible to accurately predict phase relations and calculate Fe^{3+} activities even under lower mantle conditions.

Hydrous phase relations in the upper mantle are the topic of the next two studies. In the first, a new method involving the addition of water in the form of solid $H_2Pt(OH)_6$ is used to explore the previously inaccessible H_2O-rich part in the MgO-SiO_2-H_2O system. The second seeks to determine the phase relations of hydrated oceanic crust as hydrous minerals break down during subduction. The results suggest that the stability field of potassium-rich micas varies strongly as a function of the water content of the subducting crust.

In an examination of the storage and recycling of halogens in the Earth's mantle, Roberge *et al.* have determined the solubility of fluorine in olivine, wadsleyite and ringwoodite at transition zone conditions. It was found that the former two minerals can incorporate up to ~ 0.1 wt.% F, which means that the transition zone alone could store more fluorine than what is commonly assumed to occur in the entire silicate-rich part of the Earth. The following study by Beyer and Frost focuses on the refinement of a garnet-clinopyroxene geobarometer, *i.e.*, an equation for determining the pressure of equilibration of rocks from the chemical analysis of the mineral assemblage. This geobarometer is particularly valuable because it is applicable to eclogite xenoliths found in kimberlites and thus allows insights into the formation of cratonic lithosphere and diamonds. The next contribution by Liu *et al.* deals with the behaviour of copper during mantle melting and the subsequent fractional crystallization of the primary magmas. Partitioning experiments performed at 0.75-3.5 GPa and 850-1300 °C with melts ranging from komatiitic to haplogranitic composition reveal that Cu becomes increasingly compatible in silicate and oxide minerals with increasing degree of fractional crystallization, but not to the point that it would become depleted in the residual silicate melt.

The last two contributions relate to the process of magma mixing in upper crustal magma chambers. By conducting crystallization experiments on hydrous alkaline basalts and trapping exsolved fluid in the form of synthetic fluid inclusions, Gutiérrez and Audétat determined which major and trace elements tend to be transported from underplating basalts into overlying, more evolved magmas within zoned magma chambers. In the following study on natural quartz phenocrysts from the Bandelier Tuff, New Mexico, Audétat finds that the occurrence of Ti-rich quartz rims on Ti-poor quartz cores results dominantly from changes in temperature and TiO_2 activity following an event of magma mixing, rather than from changes in pressure.

a. *High P-T experiments and first principles calculations of Si and Cr diffusion in liquid iron: kinetic implications for the chemical evolution of planetesimal cores (E.S. Posner, D.C. Rubie, D.J. Frost and G. Steinle-Neumann; R. Caracas/Lyon)*

The density of the Earth's outer core is ~ 10-15 % too low to be composed of pure Fe-Ni alloy and is therefore considered to contain significant concentrations of one or more light elements. Silicon is a likely candidate as it is depleted in the Earth's mantle relative to chondrites and has been shown to become increasingly siderophile at elevated temperatures and under reducing conditions. Metal-silicate partitioning studies reveal that considerable amounts of Cr, which is also chemically depleted in the Earth's mantle, was likely sequestered into metallic core-forming melts. Both Si and Cr have been shown experimentally to undergo isotopic fractionation during metal-silicate differentiation, which has been used to explain the depletion of light Si and Cr isotopes in the Earth's mantle and provides further support that these elements were, in fact, partitioned into the core during core formation.

According to current models of the Earth's core-mantle differentiation, substantial amounts of Si and Cr should have partitioned into the metallic Fe-Ni cores of early accreted bodies. In contrast to these predictions, however, the Si and Cr contents of iron meteorites, which are derived from the metallic cores of early-formed planetesimals, are surprisingly low (*e.g.*, < 1 ppm). Recent studies of magnetized achrondrites reveal that planetesimal parent bodies likely possessed liquid metallic cores that underwent convection during their formation. Such convection would result in the chemical mixing and transport of chemical components in liquid iron, such as Si and Cr, to the body's core-mantle boundary (CMB). Ongoing chemical interaction at the CMB of larger bodies, such as the Earth, has been used to model and interpret anomalous seismic observations from the laterally heterogeneous buoyant layer atop the Earth's liquid outer core; however, the concentration and spatial distribution of alloying element(s) in the CMB remain unknown.

The solubility of Si and Cr in liquid iron has been shown experimentally to increase with temperature, such that the alloy component of a planetesimal core should decrease during cooling. We propose that molten planetesimal cores originally contained high concentrations of Si and Cr but that these elements became increasingly lithophile during cooling and were extracted from the core by reaction at the base of the silicate mantle at a rate controlled by their diffusion through boundary layers. We are testing this hypothesis and modelling the rate of chemical evolution of planetesimal cores using diffusion kinetic data of Si and Cr in liquid iron, as determined both experimentally and using molecular dynamics simulations.

Chemical diffusion of Si and Cr in liquid iron has been investigated experimentally under *P-T* conditions of 3-11 GPa and 1859-2223 K using a multianvil press. Samples are diffusion-couples consisting of 1.2 mm diameter highly-polished cylindrical disks of (1) 99.97 % Fe and (2) Fe-alloy sintered from a mixture of 91 wt.% Fe, 8 wt.% Si and 1 wt.% Cr powders. Each diffusion couple is contained in an MgO capsule that is inserted into a high-pressure multianvil assembly. Due to rapid diffusion in the small liquid samples, a series of zero-time non-isothermal experiments are conducted at each pressure at variable heating rates (*dT/dt*) and final quench temperatures (T_f). Recovered capsules are cut and polished parallel to the axis of the cylindrical sample and profiles are measured by 10 μm-step line scans using a JEOL JXA-8200 electron microprobe. Data analysis and model fits of Si and Cr profiles at 7 GPa are shown in Fig. 3.2-1 and 3.2-2. An optimized interface location is obtained using a

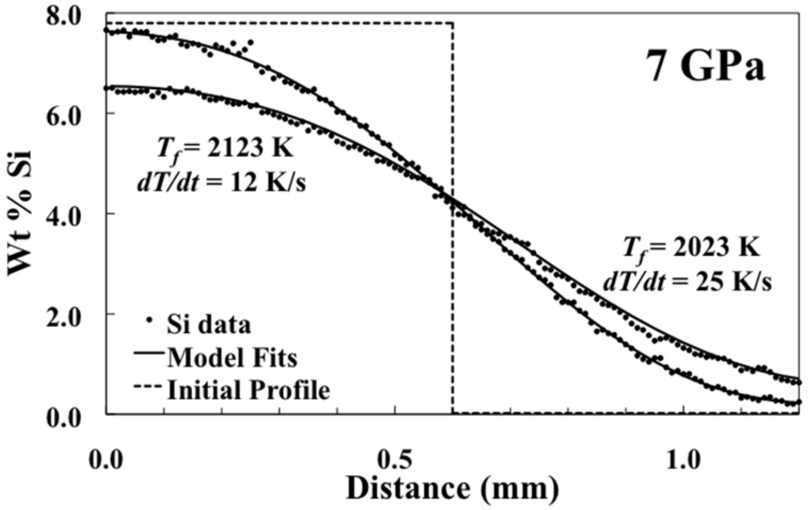

Fig. 3.2-1: Si diffusion in liquid Fe at 7 GPa. Plots show initial concentration profiles (dashed line), quenched Si data (circles), and model fits to zero-time profiles (solid line). The values of T_f and *dT/dt* represent heating rate above 1473 K and quench temperature, respectively.

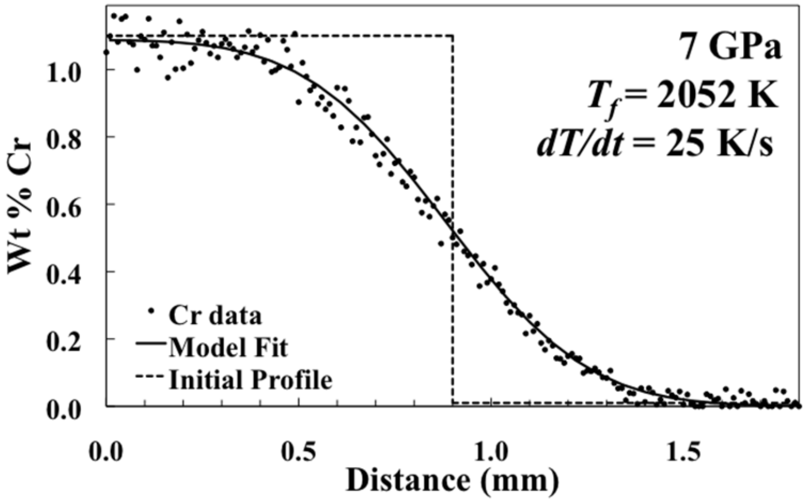

Fig. 3.2-2: Cr diffusion in liquid Fe at 7 GPa. Plots show initial concentration profiles (dashed line), quenched Cr data (circles), and model fits to zero-time profiles (solid line). The values of T_f and *dT/dt* represent heating rate above 1473 K and quench temperature, respectively.

least squares fit combined with a finite difference simulation of the profiles. The next step is to fit all profiles simultaneously in order to refine the Arrhenius parameters (activation energy, activation volume, etc.) and to expand the dataset to a broader range of *P-T* conditions.

To extend our dataset to *P-T* conditions of the Earth's core-mantle boundary, we have begun first principles molecular dynamics (FP-MD) calculations based on density-functional theory (DFT). The exchange and correlation potential is represented by the generalized gradient approximation (GGA-PBE) with valence electrons represented by plane waves with a cutoff energy of 550 eV in the projector augmented wave (PAW) method implemented in VASP code. We employ iron supercells containing 108 atoms, overheat them to 5000 K to induce melting, compress the liquid along several lower isotherms and then allow for changes in chemistry (Si, Cr, O, Ni, S). Diffusion coefficients will be computed from the trajectories of the atoms in the simulation cell via the Einstein relation.

b. *Tungsten and molybdenum partitioning between silicate and iron melts in the laser heated diamond anvil cell (S. Petitgirard, D.C. Rubie and V. Laurenz; A.J. Campbell and R.A. Fischer/Chicago, L. Hennet/Orleans, D. Harries and F. Langenhorst/Jena)*

A key to understanding the process of core formation is to measure how a wide range of elements partition between metallic iron, that segregated to form the core, and silicate liquid (the magma ocean from which the metal segregated) at various conditions of pressure (*P*), temperature (*T*) and oxygen fugacity (fO_2). Currently, most siderophile element partitioning studies have been performed at pressures below 25 GPa in large volume multianvil presses, and extrapolation to much higher pressures is often required, *e.g.*, to 80 GPa, when modelling core formation. In order to improve core formation models, it is therefore important to obtain partitioning data experimentally to much higher *P* and *T*.

The aim of this study is to measure the partitioning of W and Mo, two moderately siderophile elements (MSE), between silicate liquid, of primitive mantle composition, and Fe-Ni melts from samples synthesized in laser-heated diamond anvil cells (LH-DAC) and multianvil presses over the entire range of magma ocean pressure-temperature conditions, *i.e.*, 5-80 GPa and 2000-4000 K.

In order to obtain a complete and reliable data set, we are using state of the art techniques to: i) cutting thin slices from our micron-scale recovered samples using a focused ion beam (FIB) and ii) mapping and quantifying element concentrations in our FIB foils at the nano-scale using highly sensitive probes with high spatial resolution. An example of an FIB foil is shown in Fig. 3.2-3 and shows the two coexisting liquids on the scale of 10 microns.

After recovering the samples they were characterized using a nano-XRF at the Deutsches Elektronen-Synchrotron (DESY, Hamburg, Germany). An example of an XRF map from the sample shown in Fig. 3.2-3 is given in Fig. 3.2-4. From the XRF maps, the region of interest

(ROI) can be identified, for example, by defining the distribution of one element such as iron. The ROIs that correspond to the iron melt and the silicate melt can thus be analyzed separately. Further measurements and investigations are in progress and will be complemented using transmission electron microscopy and nano-SIMS analysis.

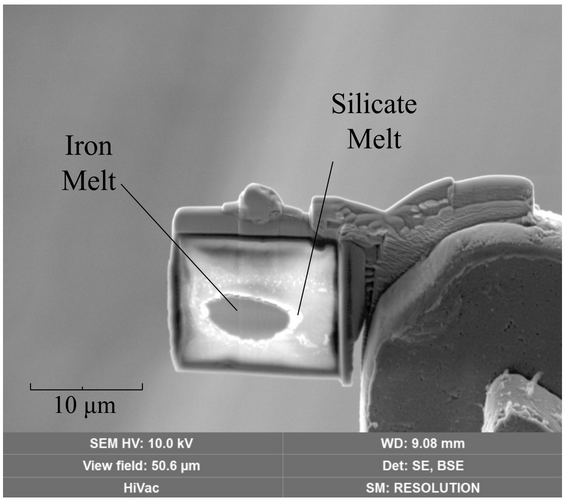

Fig. 3.2-3: Backscattered electron image of a typical FIB lamella cut from a sample synthesized at 72 GPa and 4000 K in the laser heated DAC. The grey part in the center of the lamella is the metallic alloy liquid and the bright part surrounding it is the silicate melt which is approximately 1-2 microns thick.

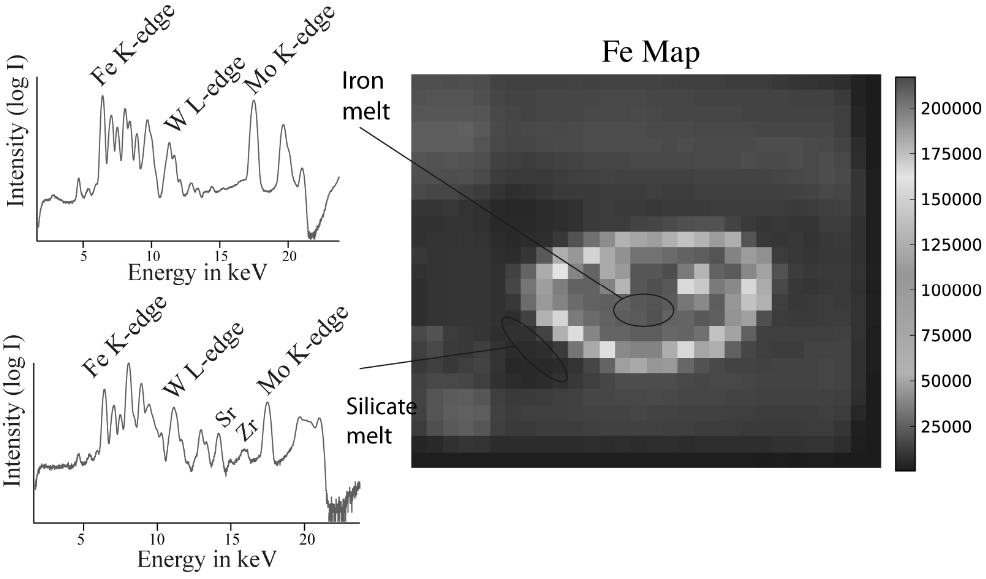

Fig. 3.2-4: Right side, iron K-edge X-ray fluorescence map of the sample described in Fig. 3.2-3. Regions of interest can be identified, and several pixels, corresponding to data points, can be analyzed to give the silicate melt and the iron melt compositions. On the left side are two spectra from these two ROIs indicating less Mo in the silicate melts and the presence of trace elements such as Zr and Sr that are strictly incompatible with the iron melt. The pixel size is 0.5×0.5 micrometers and the intensity is in counts per 10s.

c. *Metal-silicate partitioning of Co, Ni, V, Cr, Si, and O up to 100 GPa and 5500 K (R.A. Fischer and A.J. Campbell/Chicago; N. Miyajima, D.J. Frost and D.C. Rubie; D. Harries, F. Langenhorst and K. Pollok/Jena)*

During core formation, metal and silicate of accreted bodies equilibrated with the proto-Earth in a series of partitioning reactions, characterized by average (or time-integrated) partition coefficients that can be calculated assuming a bulk Earth that is chondritic in nonvolatile elements. Comparisons to experimentally-measured partition coefficients allow constraints on the time-integrated conditions of core-mantle equilibration, providing valuable input into more complex chemical models of Earth's evolution. Partitioning has been studied extensively in the multianvil press, but very few studies extend to pressures above ~ 25 GPa. In this study, we measure the metal-silicate partitioning of Co, Ni, V, Cr, Si, and O at higher pressures and temperatures.

Iron-rich alloys doped with trace elements were synthesized using a piston-cylinder apparatus at BGI, and $(Mg,Fe)_2SiO_4$ ringwoodite was synthesized from natural olivine using a multianvil press at BGI. Thin foils of the alloys were loaded in a diamond anvil cell between layers of ringwoodite. Samples were laser-heated at the University of Chicago to melt the metal and silicate. After decompression, samples were cut parallel to the compression axis into sections ~ 100 nm thick with a focused ion beam (FIB) at Friedrich-Schiller-Universität Jena. Chemical analyses of all elements except oxygen in the coexisting metal, silicate, and oxide were performed using energy dispersive X-ray spectroscopy (EDXS) in a transmission electron microscope (TEM) at BGI. An example of a TEM image of one of our FIB sections is shown in Fig. 3.2-5. Later, samples were further thinned by FIB to ~ 60 nm and analyzed by electron energy loss spectroscopy (EELS) in the TEM to determine the Fe/O ratio of the metal. Analysis was performed on a suite of six experiments from pressures of 25, 31, 43, 57, 58, and 100 GPa and temperatures above the silicate liquidus, up to 5500 K.

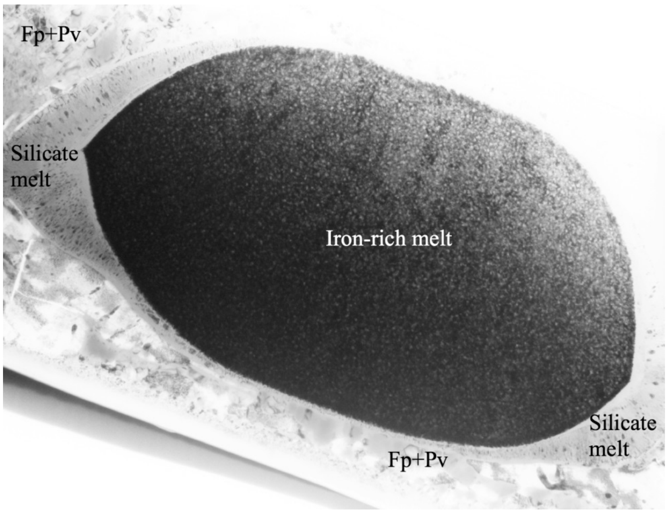

Fig. 3.2-5: A TEM image of an FIB section of a metal-silicate partitioning sample from a laser-heated diamond anvil cell experiment, quenched from 100 GPa and 5500 K. Iron-rich melt contains Si,O-rich inclusions formed upon quenching, in addition to ferropericlase and perovskite (Fp+Pv). The central iron melt is ~ 13 micrometers in diameter.

Our results are generally consistent with other recent findings, although our $\log(K_D)$ values for cobalt are ~ 0.1-0.2 log units lower. Some of our experiments contain carbon in the metal, which is seen to have a significant effect on the partitioning of V and Cr. Our results help to resolve discrepancies in the literature data of these elements by demonstrating the effects of C on element partitioning. Figure 3.2-6 illustrates the partitioning of silicon compared to results of previous studies, as a function of inverse temperature. The metal in the experiment from 100 GPa and 5500 K contains 9 wt.% silicon and an estimated 11 wt.% oxygen (Fig. 3.2-5), which is a significantly higher percentage of light elements than the Earth's outer core is thought to contain.

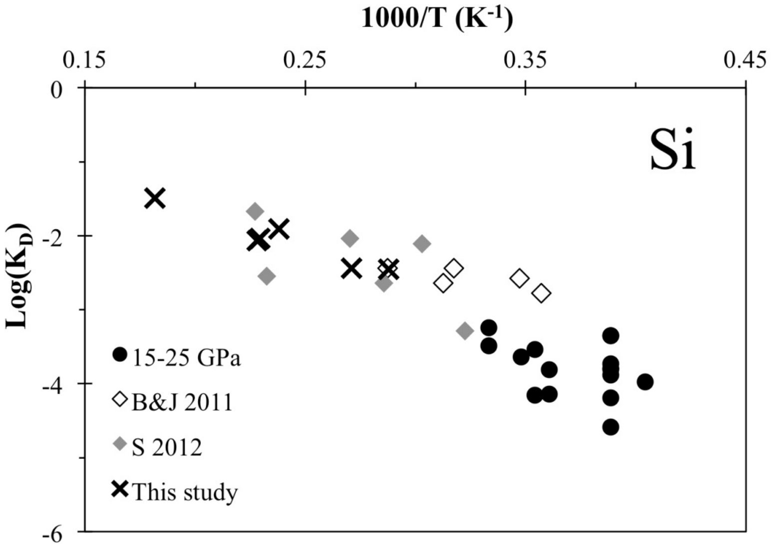

Fig. 3.2-6: The exchange coefficient K_D (iron-normalized) for silicon as a function of 1000/T compared with previously reported values from the literature. All data are corrected to a peridotite melt composition. S 2012: J. Siebert, J. Badro, D. Antonangeli, F.J. Ryerson, Earth Planet. Sci. Lett. 321-322, 189, 2012. B&J 2011: M.A. Bouhifd, A.P. Jephcoat, Earth Planet. Sci. Lett. 307, 341, 2011. 15-25 GPa: references from S 2012.

d. *The influence of polymerization on silicate-metal partitioning of Co, W and Ni (A.C. Seclaman and R. Caracas/Lyon; D.J. Frost)*

Element partitioning between silicate and metallic melts can be influenced by a range of factors, such as pressure, temperature, oxygen fugacity, composition and melt structure. Here we investigate the latter and focus on the influence of the degree of polymerization on the partitioning of Co, W and Ni at 3GPa, 8GPa and 1850-1950 °C. Pressure is known to decrease the metal-silicate partition coefficient of Ni and Co, making them more lithophile (silicate loving) at high pressure. Previous experiments, however, have also observed well defined changes in the slope of the metal-silicate partition coefficient for these elements as a function of pressure, which may result from changes in melt structure. On the other hand lower pressure experiments are often performed with mafic silicate melt compositions, whereas at higher pressures ultramafic compositions are often employed. Such changes in composition could potentially lead to variations in melt polymerization, which could influence the partition coefficient. Experiments were performed in an attempt to clarify this issue.

In order to approximate in a quantitative manner the degree of polymerization in our silicate melts we used a polymerization factor, being the ratio between the number of non-bridging oxygen atoms and the tetrahedrally coordinated cations (NBO/T). Silicate compositions were fabricated from high purity oxides and carbonates. Concentrations of SiO_2 and MgO were varied between different starting mixtures to obtain different desired NBO/T values: from highly depolymerized (NBO/T=3.64) to highly polymerized (NBO/T = 1.22). The Mg/(Mg+Fe) ratio varied between 0.6 and 0.8. 1 wt.% of NiO, CoO and WO_3 were added to the silicate materials. After mixing in an agate mortar the silicate compositions were pressed into pellets and reduced in a gas mixing oven at an fO_2 of -11 log bar units. 50 % of pure Fe powder was mixed with the silicate sample to produce the final starting mixture.

Experiments were performed in a multianvil apparatus, using an 18/11 assembly and employing a section of two-hole alumina thermocouple tubing as a capsule. Metal silicate experiments at high pressure are generally performed in MgO capsules, however the reaction of MgO with the silicate material during the experiment results in a tendency for high values of NBO/T. Heating was performed using a $LaCrO_3$ furnace and the temperature was measured by thermocouple or, when this failed, by controlling the power output of the heating system. Samples were quenched after a reaction time of 5 to 10 minutes.

Fe metal segregated from the silicate above the silicate liquidus (Fig. 3.2-7). Alumina contamination of the silicate melt from the capsule was detected using an SEM-EDS system. Due to the increased Al_2O_3 content, the final NBO/T values were lower than initially predicted, but different degrees of polymerization were still achieved. As the next step high resolution, microprobe and LA-ICPMS analyses will be performed in order to calculate the partition coefficients.

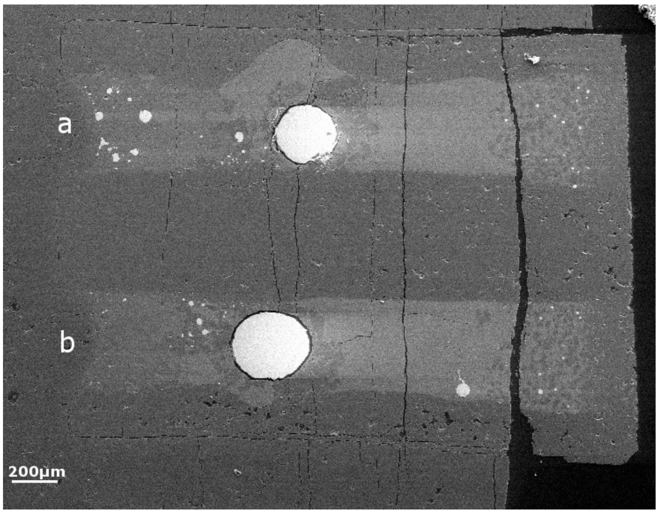

Fig. 3.2-7: A SEM-BSE image of two highly polymerized samples in a double alumina capsule, where spheres of bright metallic melt can be seen to have segregated in both samples a) and b).

e. *Does a S-rich melt influence the partitioning behaviour of Ni and Co during core formation? (V. Laurenz, J. Premier, D.C. Rubie and D.J. Frost)*

Towards the later stages of Earth's accretion, material was delivered that was rich in volatiles such as sulphur and water. During this stage, a small volume of FeS-rich melt likely formed and segregated to the Earth's core, stripping highly siderophile elements from the mantle, which would otherwise appear overabundant. This late-stage removal of the so-called "Hadean matte" would have influenced, to some extent, the abundance of all chalcophile elements in the mantle. The principal question addressed here is how and to what extent the presence of S changes the partitioning behaviour of chalcophile elements such as Co and Ni.

In order to test this, we have studied the partitioning behaviour of Co and Ni in S-bearing systems. A synthetic peridotite composition was equilibrated with metal or sulphide along the Fe-FeS join, doped with 5 wt.% Ni and 1 wt.% Co. A layer of metal or sulphide was sandwiched between peridotite powder and encapsulated in single crystal MgO capsules. All experiments were carried out at 2200 °C and 6 GPa in a multianvil apparatus. Typical run products consist of a metal or sulphide sphere coexisting with quenched silicate melt. Also, ferropericlase crystallised on the interface between the silicate and the MgO capsule. Major element compositions of metal or sulphide, silicate and ferropericlase were determined by electron microprobe, whereas concentrations of Ni and Co in the silicate were analysed by LA-ICP-MS. From the composition of the metal (or sulphide) and the silicate, exchange coefficients (K_D) for Ni and Co were calculated from:

$$K_D = \frac{X_M^{metal} / X_{MO_{n/2}}^{silicate}}{(X_{Fe}^{metal} / X_{FeO}^{silicate})^{n/2}}$$

where X is the mole fraction of element M in metal or $MO_{n/2}$ in the silicate and n denotes the valence state of element M in the silicate melt. At conditions prevailing during core formation Ni and Co are thought to be present in the divalent state (*i.e.*, Ni^{2+} and Co^{2+}). Sulphide-silicate exchange coefficients were calculated accordingly.

Overall, it can be observed that both Ni and Co become less siderophile with increasing S-concentration along the Fe-FeS binary, *i.e.*, exchange coefficients of Ni and Co decrease with increasing S. However, Ni is affected more strongly than Co. Their K_D's converge towards S-rich compositions (Fig. 3.2-8), implying that the late stage removal of a "Hadean matte" to the core may help to explain the similar abundances of Ni and Co in the Earth's mantle, in addition to the effects of pressure and temperature which have been previously reported in the literature.

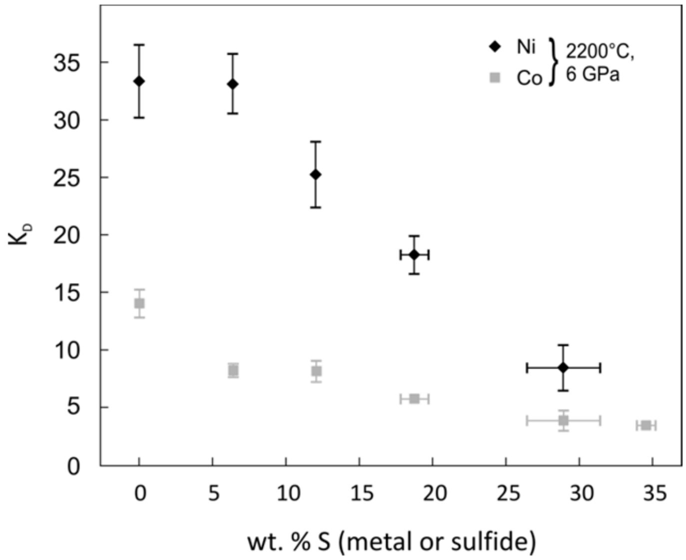

Fig. 3.2-8: Exchange coefficients of Ni and Co are plotted versus concentration of S in the metal or sulphide, respectively. Exchange coefficients of both Ni and Co decrease with increasing S-content.

f. *The dependence of siderophile element partitioning on pressure, temperature, fO_2 and Si- and S-contents (A.K. Vogel, D.C. Rubie, D.J. Frost and A. Audétat; H. Palme/Frankfurt)*

The Earth accreted through numerous collisions with planetesimals and embryos, with the energy released being likely sufficient to cause one or more deep global magma oceans to form over the course of accretion. The Earth's metallic core formed by the segregation of liquid metal from liquid silicate and was probably completed within the first 100 million years of solar system history. Metal-silicate segregation involved the extraction of siderophile (metal-loving) elements into the Earth's core. Experimental determinations of the liquid metal/liquid silicate partitioning behaviour of both refractory and volatile elements provide important insights into the processes and conditions of core formation, because partitioning is generally dependent on pressure, temperature, oxygen fugacity and composition.

We have performed high-pressure/high-temperature experiments in the multianvil apparatus, covering a pressure and temperature range of 11-24 GPa and 2200-2800 K respectively. Partitioning behaviour has been determined for the elements Ni, Co, W, Mo, Sn, Sb, Ge, Cu, Pb, As, P, Ag and Au, which were added to an Fe-rich metal layer that was sandwiched between silicate layers with a peridotitic composition. In addition Si was added in various proportions to the metal to control oxygen fugacity and S was also added in some instances to examine its influence on partitioning. Oxygen fugacities varied from -2 to -5 logarithmic units relative to the iron-wüstite buffer. Samples were analysed using the electron probe and laser ablation inductively coupled plasma mass spectrometry. The partitioning of an element M is expressed in the form of a partition coefficient (concentration of M in the metal over its concentration in the silicate) – or as an exchange coefficient that includes Fe and FeO concentrations and is consequently independent of oxygen fugacity.

Sn and Pb are relatively volatile elements with similar condensation temperatures and are depleted to the same extent in the Earth's mantle, which requires similar partition and exchange coefficients. Yet experimentally determined exchange coefficients for these elements differ by approximately one order of magnitude when the metallic liquid is pure Fe. Our experiments indicate, however, that increasing the metal S content leads to a decrease in the exchange coefficient for Sn, whereas Pb is hardly affected (Fig. 3.2-9). If core forming metal contained approximately 10 wt.% S, then the similar depletions of Sn and Pb in the Earth's mantle could be explained. Similarly, the influence of S can also account for the relative abundances of Ge, As and Ag in the Earth's mantle. Relative to Ge and As, Ag is slightly more depleted in the mantle, but the experiments show that in the absence of S it is by far the least siderophile of the three elements. As shown in Fig. 3.2-10, however, the partition coefficients for all elements become similar when approximately 10 wt.% S is present in the metal phase. This provides strong evidence that volatile element fractionation during core formation occurred in the presence of S bearing metallic liquids, which supports a later addition of volatile material during accretion, which was consequently more S-rich.

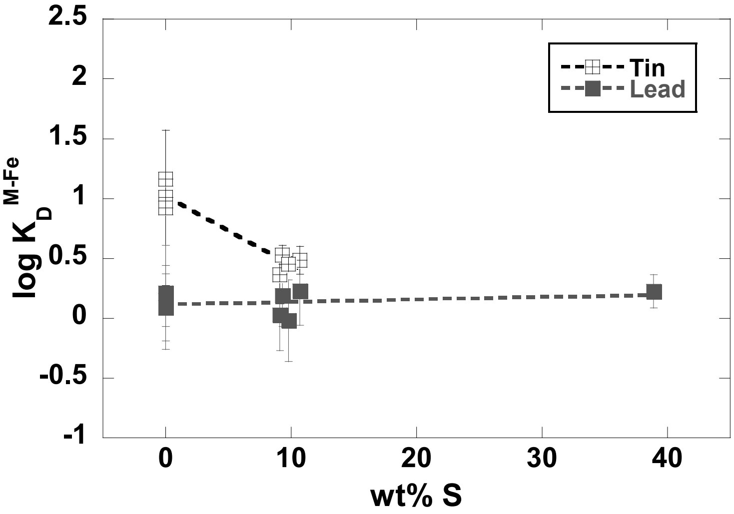

Fig. 3.2-9: Logarithmic exchange coefficients plotted against S content of the metal for the elements Sn and Pb at 11 GPa and 2573 K. At around 10 wt.% S the exchange coefficients for both elements converge, which explains the similar depletions of Sn and Pb in the Earth's mantle.

We, furthermore, found that the non ideal interaction of Si with the elements of interest acts to minimize the effect of fO_2 on siderophile behaviour. We conclude that reducing conditions in the early stages of core formation, as proposed by various models, do not necessarily result in complete depletion of siderophile elements from the mantle, depending on the extent of the non ideal interaction of Si in the metal phase. In addition, a significant influence of pressure and temperature on the exchange coefficients for the elements studied has not been observed, which enables us to draw conclusions about core formation processes even though the experiments were performed at relatively narrow range of conditions.

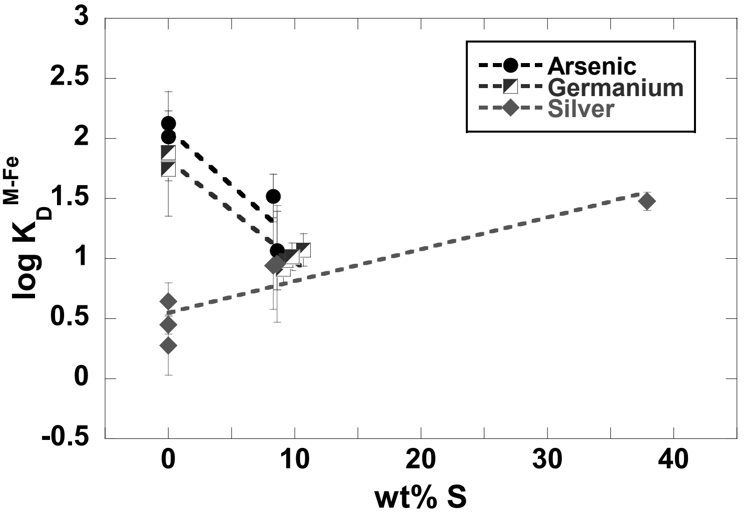

Fig. 3.2-10: Exchange coefficients for the elements As, Ge and Ag plotted against S content of the metal from experiments at 11 GPa and 2573 K. Increasing S contents can explain the relative abundances of these elements in the Earth's mantle, since - contrary to S-free systems - the more depleted element Ag becomes more siderophile than Ge and As with increasing S contents and *vice versa*.

g. *The influence of sulphur on the partitioning behaviour of HSEs during segregation of the Earth's core (V. Laurenz, D.C. Rubie and D.J. Frost)*

The highly siderophile elements (HSEs - Os, Ir, Ru, Rh, Pt, Pd, Re, Au) are unique geochemical tracers of Earth's accretion and differentiation history. Due to their defining property of extremely high metal-silicate partition coefficients ($D_{\mathrm{HSE}} > 10^4$), the HSEs were effectively scavenged from the Earth's mantle during core formation, leaving the mantle strongly depleted in HSEs. Additionally, it is known from high-pressure, high-temperature experimental work that the HSEs show large differences in D_{HSE}, which would lead to fractionated HSEs patterns in the mantle. After core formation was complete, a "late-veneer" of highly oxidized, chondritic material then delivered a small amount of HSEs back to the mantle, establishing the near-chondritic proportions estimated for the primitive upper mantle. However, most experimental work on HSE partitioning has been carried out in S-free systems. As S is known to strongly influence the partitioning behaviour of chalcophile trace elements, it may also have played a significant role for the behaviour of the HSEs. Since it is likely that S was only added to Earth during the later stages of accretion, its effect would become important especially during the late stages of accretion and core formation.

In order to investigate the effect of S on the behaviour of the HSEs during core formation, we have studied the metal-silicate and sulphide-silicate partitioning of Pt, Pd, Ru and Ir under high-pressure/high-temperature conditions. The starting silicate was a primitive mantle composition, which was synthesized from oxides and carbonates. In order to reduce all Fe^{3+} to

Fe^{2+} and to prevent the formation of HSE-nanonuggets in the silicate, the peridotite powder was reduced in a 1-atm gas mixing furnace at 1200 °C and an oxygen fugacity of ΔFMQ-2. This peridotite composition was equilibrated with a range of compositions along the Fe-FeS binary (5 wt.% S - 35 wt.%. S), and doped with two of the HSEs at a time (10 wt.% each). All experiments were performed in a multianvil apparatus at 2200 °C and 11 GPa using single crystal MgO capsules. Quenched silicate and metal or sulphide were analysed by electron microprobe for their major element concentrations, while trace element abundances were determined using LA-ICP-MS.

Overall, it can be observed that all HSEs become less siderophile with increasing S-concentration in the metal or sulphide. However, the least siderophile HSEs show only a small effect, while the more siderophile HSEs are strongly influenced. The exchange coefficient (K_D) for Pd decreases only by half an order of magnitude from a S-free metal to a sulphide composition. In contrast, the effect is much more pronounced for Ir, where the K_D decreases by around three orders of magnitude. As a result the K_D of Pt, Pd, Ru and Ir converge with increasing S concentrations in the metal or sulphide phase (Fig. 3.2-11). These results have important implications for our understanding of Earth's accretion and core formation history. To a large extent, Earth was accreted from S-free material and partitioning of siderophile elements between core-forming metal and silicate mantle can be modelled

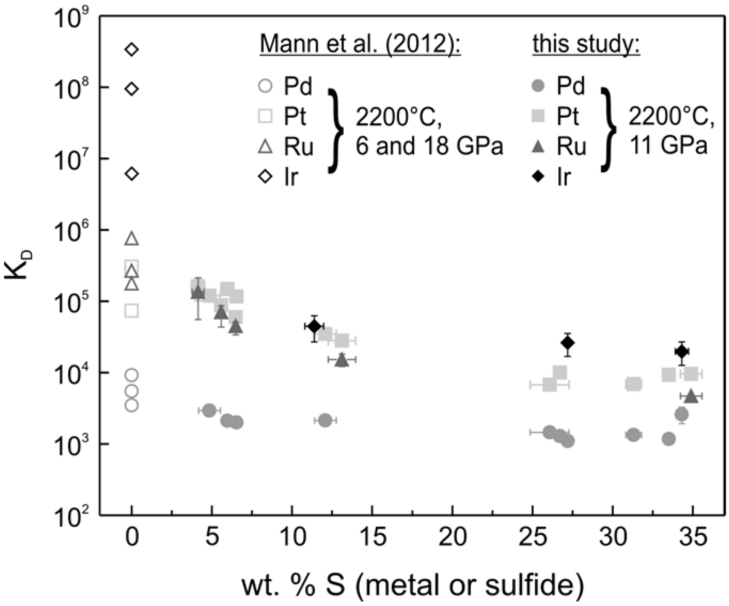

Fig. 3.2-11: Exchange coefficients (K_D) of the HSEs are plotted versus S-concentration in the metal or sulphide, respectively. While in S-free compositions the K_D of the HSEs differ by several orders of magnitude (Mann U., Frost D. J., Rubie D. C., Becker H. and Audétat A. (2012) GCA 85, 593-316), the exchange coefficients converge with increasing S concentrations. A S-rich melt segregating to the core would result in almost unfractionated HSE patterns in the Earth's mantle, in contrast to the S-free case.

using experimentally determined high-temperature, high-pressure partition coefficients in S-free systems. The silicate portion becomes strongly depleted in HSEs during this phase, producing highly depleted but fractionated HSEs patterns in the Earth's mantle. However, during the late stages of accretion the metal segregating to the core becomes progressively more S-rich, which changes the partitioning behaviour of the HSEs dramatically. The results of this study show, that the HSEs can be extracted to the core by a S-rich melt with only small inter-element fractionation, producing the near-chondritic ratios of the HSEs in the Earth mantle. Subsequently, a "late veneer" of chondritic material delivered HSEs to the mantle after core formation ceased. The results of this study underline the importance of taking into account the effect of S on the partitioning behaviour of trace elements when modelling accretion and core formation.

h. *Nitrogen partitioning and isotopic fractionation between liquid Fe-Ni alloy and silicate melts (Y. Li; B. Marty/Nancy; S. Shcheka and H. Keppler)*

Nitrogen is a volatile element that may constrain the evolution and interaction of Earth's different reservoirs. The nitrogen distribution and its isotopic composition in Earth's different reservoirs, *i.e.*, atmosphere, crust, mantle, and core, are primarily controlled by factors such as the chemical composition of the initial Earth-forming materials, the accretion model of the Earth, and the behaviour of nitrogen during and after the Earth's accretion. The present atmosphere contains ~ 4 x 10^{21} g nitrogen. However, the nitrogen abundance in the total Earth remains unknown, and the estimated nitrogen abundance from 2 to 40 ppm in the silicate Earth is quite model-dependent. The chondrite-normalized nitrogen abundance in both the depleted upper mantle and the atmosphere is indeed much more depleted than for other volatiles such as argon, water, and carbon. Therefore, it is likely that most of the nitrogen initially contained in the Earth-forming materials may have been retained in Earth's very deep interior, either the deeper mantle or the core. However, to date, the capacity of Earth's core to segregate nitrogen from the silicate Earth and its effect on the nitrogen isotope distribution in the Earth has not been systematically investigated.

Earth's various reservoirs have different nitrogen isotopic compositions. The Earth's upper mantle, relative to the atmosphere, is depleted in the ^{15}N isotope, with δ^{15}N values around -5 ‰; whereas the combined atmosphere and crust have an average δ^{15}N value of about +2 ‰. The mean δ^{15}N of oceanic mantle plumes is +3.0±2.1 ‰ for 28 samples and 4±2.1 ‰ for 18 samples with ^{40}Ar/^{36}Ar > 1000, which are consistent with the δ^{15}N values of +3.3±1.8 ‰ for 17 samples of continental mantle plumes. Recent studies have reported very negative δ^{15}N values (-39.4 ‰) in upper mantle-, transition zone-, and lower mantle-derived diamonds, which are interpreted as a preserved signature of the primitive mantle. An isotopic fractionation of Si, Fe, and C between core and mantle has been suggested. Therefore, it would be important to test whether there may also be nitrogen isotopic fractionation between liquid Fe-Ni alloy and silicate melt at high temperatures and pressures, in order to better understand the Earth's nitrogen evolution and the possible effect of core-formation on the nitrogen isotopic composition of the bulk silicate Earth.

We have designed experiments to systematically investigate both the partitioning of nitrogen and the nitrogen isotopic fractionation between liquid alloy and silicate melts. A series of experiments have been performed at 1600-1800 °C and 2-7 GPa using piston cylinder and multianvil apparatus for nitrogen partitioning and isotopic fractionation between liquid Fe and silicate melt with a composition similar to that of MORB. Graphite-lined platinum capsules were used to enclose the starting material, and NH_4NO_3 was used as a nitrogen source. In all the experiments, nitrogen was undersaturated, so that no free fluid phase was present. Some run products (Fig. 3.2-12) have been analyzed by CO_2-laser static gas source mass spectrometry. For one sample at 2.5 GPa and 1700 °C, preliminary analytical results show that the nitrogen partition coefficient between liquid Fe and silicate melt is 17±1; the partition coefficient was calculated using the nitrogen weight in the quenched Fe metal (10295±376 ppm) divided by the nitrogen weight in the quenched silicate glass (611±22 ppm). The nitrogen isotopic fractionation between liquid Fe and silicate melt is $\delta^{15}N = -4.1 \pm 2.8‰$. The high nitrogen partition coefficient between liquid Fe and silicate melt demonstrates that during core-formation a significant amount of nitrogen in the magma ocean may have been segregated into the core, and the core could be an important nitrogen reservoir. The isotopic fractionation between the liquid Fe and the silicate melt may imply that core-formation did have an important effect on the nitrogen isotopic composition of the silicate Earth, resulting in ^{15}N enrichment in the silicate Earth.

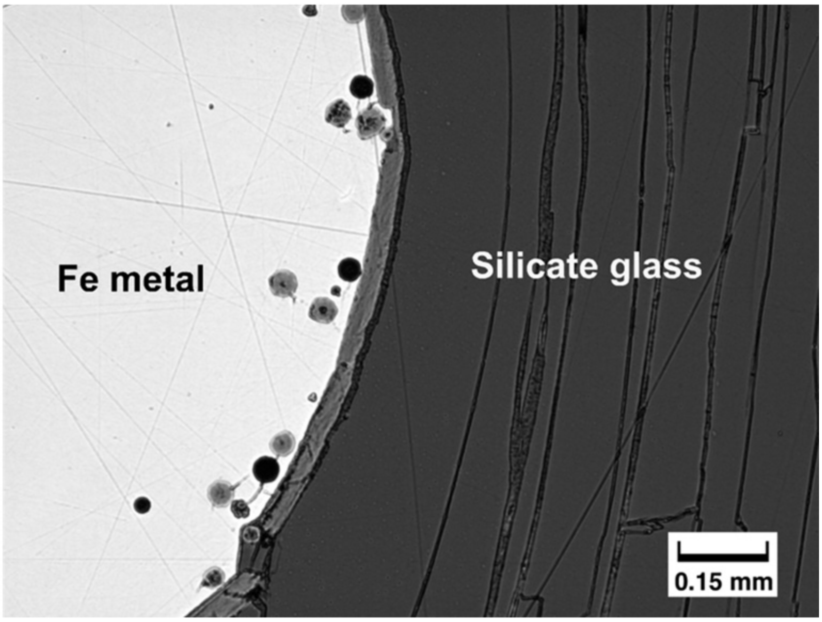

Fig. 3.2-12: Products of one run conducted at 1600 °C / 2 GPa in the piston cylinder apparatus. The composition of silicate is chosen to be similar to that of MORB.

i. *Determining the behaviour of ferric iron during MORB petrogenesis (F. Sorbadère, D.J. Frost and C.A. McCammon)*

The oxidation state of iron in MORB glasses is proposed to be directly related to the oxygen fugacity (fO_2) of the upper mantle from which it derives. Recently measured $Fe^{3+}/\Sigma Fe$ ratios in MORB show a very narrow range, from 0.15 to 0.18, with a global average of 0.16±0.01, which corresponds to a fO_2 close to the fayalite-magnetite-quartz (FMQ) buffer. For comparison, oceanic island basalts which derive from lower degrees of melting than MORB display higher $Fe^{3+}/\Sigma Fe$ ratio, *i.e.*, about 0.29. This is consistent with Fe^{3+} behaving incompatibly during partial melting (*i.e.*, $D_{Fe^{3+}}^{\mathrm{min}/melt}$ ranging from 0.1 to 0.2). Hence, $Fe^{3+}/\Sigma Fe$ ratios in MORB are expected to display a certain degree of variation as well, depending on degrees of partial melting and fractional crystallisation, similar to the behaviour of other incompatible elements. However, Fe_2O_3 contents of primitive MORB do not vary with melt-fraction related parameters such as the $Na_2O(8)$ (*i.e.*, the Na_2O content at 8 wt.% MgO), suggesting a relatively constant oxygen fugacity (fO_2) operating over various degrees of melting (Fig. 3.2-13). Studies of other redox sensitive elements, such as V and Cr, which have variable valence states and partition coefficients as a function of fO_2 also seem to imply that mantle melting occurs over a relatively small range of fO_2. Although correlations between $Fe^{3+}/\Sigma Fe$ ratios and indices of low-pressure fractional crystallization have been recognized in global MORB, they are not systematic. The absence of clear correlations between the $Fe^{3+}/\Sigma Fe$ ratio of MORB and the degrees of partial melting and/or fractional crystallization implies that this ratio is controlled or even buffered by some additional process.

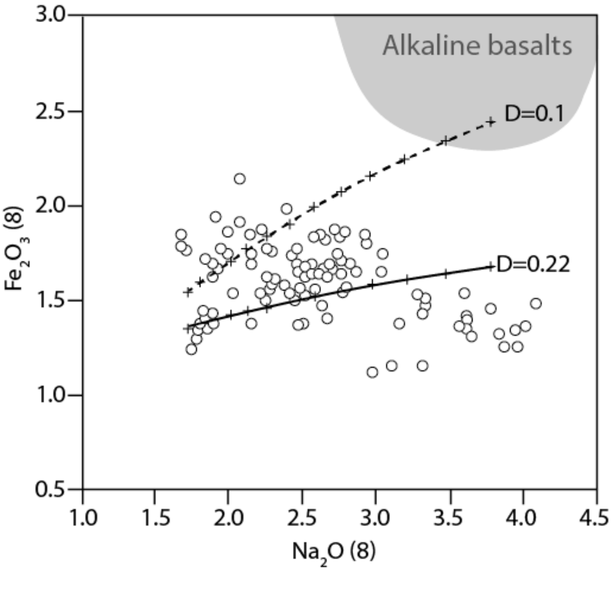

Fig. 3.2-13: Plot of Fe_2O_3 (8) as a function of Na_2O (8) for MORB (open circles) modified from Cottrell and Kelley (2011; EPSL 305, 270-282). Oxide concentrations were corrected for fractionation to 8 wt.% MgO. Curves show the theoretical evolution of melts derived from a MORB-mantle source assuming between 8 and 20 % of partial melting and Fe_2O_3 mineral/melt partition coefficients of 0.1 and 0.22. Alkaline basalts from oceanic islands are also reported for comparison (grey field) (GEOROC data-base).

One possibility to account for this $Fe^{3+}/\Sigma Fe$ paradox might be a change in the Fe^{3+} partition coefficient between mineral and melt as a function of the degree of peridotite melting (Fig. 3.2-13). The decrease in the Fe^{3+} content of the melt expected for increasing melt extraction would have to be off-set by a process that would make Fe^{3+} more incompatible at higher degrees of melting. To determine the effect of temperature and fO_2 on the Fe^{3+} partition coefficient between spinel and liquid during the partial melting of a MORB-mantle source, we have performed partial melting experiments of the peridotite MPY-90 at 1.5 GPa, between 1320 and 1430 °C (*i.e.*, 2 and 20 % of melting respectively), over a range of fO_2 varying from FMQ-2 to FMQ+2. Changes in fO_2 were obtained using different capsule materials (*i.e.*, graphite, rhenium, platinum), and were measured using an Ir-Fe alloy redox sensor.

A first stage of partial melting experiments was performed using a technique which allows the extraction of small degree melts into micro-fractures formed in the graphite capsule during the experiment (Fig. 3.2-14a). The melt compositions were then re-synthesized to perform a second stage of experiments consisting of a melt layer surrounding by a peridotite layer, in a sandwich configuration (Fig. 3.2-14b). This technique allows the generation of large pools of melt that can be easily analyzed by Mössbauer spectroscopy. The $Fe^{3+}/\Sigma Fe$ ratios of spinel and other minerals will be measured by electron energy loss spectroscopy using a transmission electron microscope.

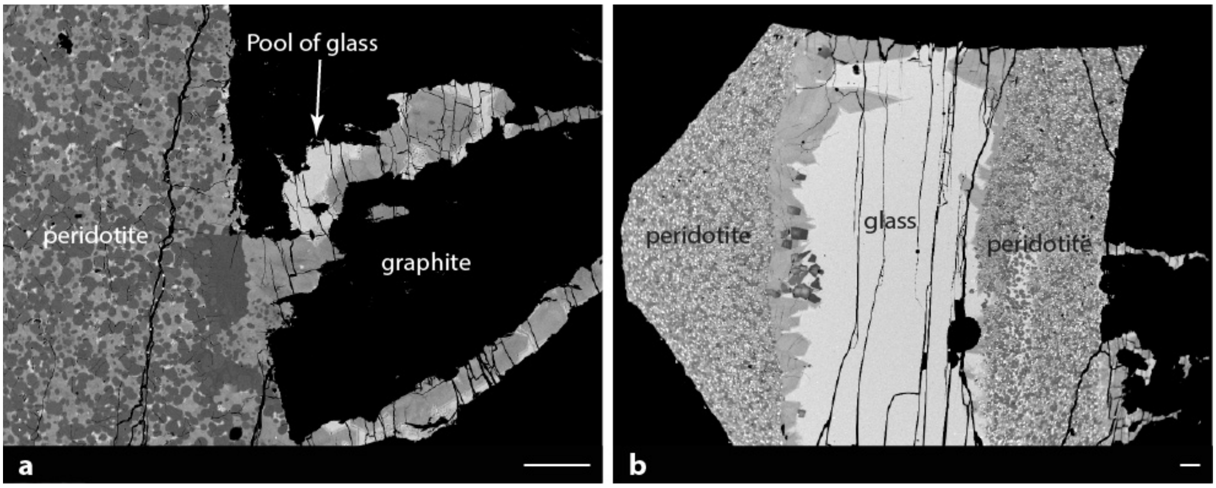

Fig. 3.2-14: Backscattered electron images showing **(a)** micro-dikes into the graphite capsule (technique developed by Laporte *et al.* (2004; CMP 146, 463-484), and **(b)** peridotite and its derived glass in a sandwich configuration. Both scale bars = 100 µm.

j. *The effect of ferric iron on melting relations in the upper mantle (R. Myhill, L. Ziberna and D.J. Frost)*

The mantle is usually considered to be a fairly reducing environment, with only a relatively small amount of bulk Fe_2O_3 ($Fe^{3+}/\Sigma Fe < 0.03$), residing in spinel or garnet. Nevertheless, high ferric iron concentrations may reside in some regions of the mantle. Subduction zones transport significant quantities of oxidised materials into the mantle, and disproportionation of ferrous iron during perovskite formation in the lower mantle may cause net mantle oxidation if the iron can segregate into the core. The idea that highly oxidised mantle materials exist is supported by the discovery of inclusions of magnetite and other Fe^{3+}-rich phases trapped within diamonds.

At low pressure, the oxidation state of iron has a profound effect on the melting relations in simplified mantle compositions. However, the effects at elevated pressures have not been systematically investigated. Experiments in the FeO-Fe_2O_3 system indicate that relatively small amounts of ferric iron could stabilise melt at low temperatures. We have further investigated this possibility by examining the effect of ferric iron in the Fe-Mg-Si-O (FMSO) and Ca-Fe-Mg-Al-Si-O (CFMASO) systems.

Multianvil experiments have been conducted at 6 GPa between 1300 and 1600 °C, using completely oxidised starting materials. Spark-eroded multi-chamber Pt capsules are used to maintain highly oxidising conditions. Some of the ferric iron is reduced until the Pt-PtO_2 buffer is reached. Fe loss to the capsule as estimated by EPMA is minor under such oxidising conditions on the timescales of the experiments. Experimental results are compared with those run in Re capsules (ReO_2 formation buffers the oxygen fugacity to much lower values than PtO_2).

An SEM image of run products from an experiment performed at 1500 °C is shown in Fig. 3.2-15. Starting materials were synthetic enstatite and hematite, mixed in varying proportions. Quenched melt is visible as fine-grained groundmass containing hematite. EPMA analysis reveals that the hematite contains several percent Mg and Si, and the melt contains similar atomic proportions of Fe, Mg and Si. Our experiments suggest that the eutectic in the oxidised FMSO system lies at ~ 1300 °C.

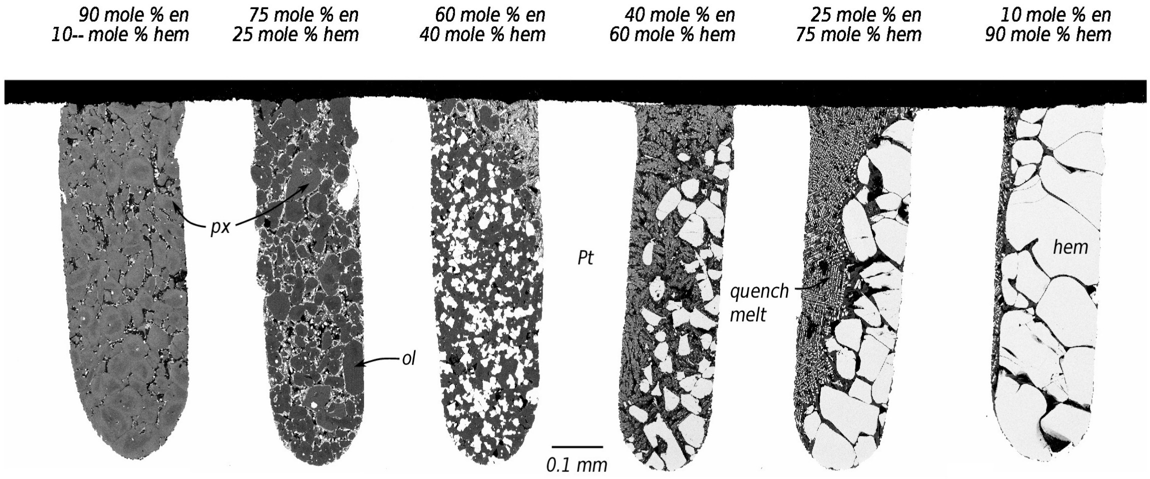

Fig. 3.2-15: SEM-BSE analysis of experiments spanning the enstatite-hematite join at 1500 °C and 6 GPa. Phase abbreviations are as follows: *ol* = olivine; *px* = pyroxene (enstatite-rich); *hem* = hematite; *Pt* = platinum.

k. *The thermodynamics of iron redox reactions at high pressures and temperatures (R. Myhill, D.J. Frost, D.O. Ojwang' and T. Boffa Ballaran)*

Thermodynamic models of mantle minerals have been extremely valuable for experimentalists, seismologists and geodynamicists studying the deep Earth. They have been used to predict the evolution of mineral assemblages and the location of seismic discontinuities. They also provide data which can be used to model mantle advection and convection.

The addition of mineral end-members which can undergo redox reactions and their activity-composition relationships in solid solutions would greatly increase our ability to model the evolving chemistry of the mantle. In particular, the addition of end-members containing ferric iron would enable self-consistent analysis of processes such as the reduction of carbonates during diamond formation or the experimentally-observed disproportionation of iron in the presence of garnet or perovskite.

In this study, we build on the self-consistent thermodynamic dataset of Holland and Powell (*J. Met. Geol.* 29.3, p333, 2011) using experimental data to add ferric-iron bearing end-members. Further data is used to construct activity-composition relationships for known solid-solutions including spinel, garnet, pyroxene and perovskite. New end-members include the recently discovered Fe_4O_5 and a magnesium-bearing counterpart $MgFe_3O_5$.

Our new datasets can be used to calculate the oxygen fugacity at high pressure and temperature of equilibria that are potentially useful for buffering the oxygen fugacity in experiments. For example, in Fig. 3.2-16 we show the stable phases of iron and its oxides at 1200 °C as a function of pressure and oxygen fugacity. We also show the evolving oxygen fugacity of the buffering equilibrium fayalite-magnetite-quartz (FMQ) as the various phases

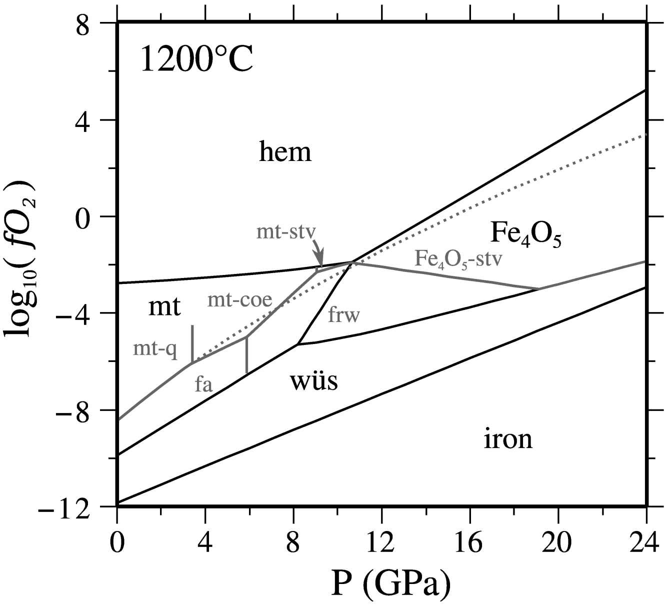

Fig. 3.2-16: Iron and iron oxide stabilities at 1200 °C as a function of pressure and oxygen fugacity. Phase boundaries are drawn in black. High-pressure analogues of the fayalite+O_2 → magnetite + quartz (FMQ) buffer are also shown (grey solid lines), along with the metastable extension of the FMQ buffer (dotted line). Mineral abbreviations are as follows:- hem: hematite; mt: magnetite, wüs: wüstite solid solution $Fe_{1-y}O$, q: quartz, coe: coesite, stv: stishovite, fa: fayalite, frw: ferroringwoodite.

transform to new polymorphs with increasing pressure. At pressures above 6 GPa a new mixed-valance iron oxide becomes stable with the stoichiomety Fe_4O_5. After Fe_4O_5 becomes stable its stability field expands with respect to magnetite, which consequently becomes unstable above 10 GPa. The FMQ buffer evolves into a buffering assemblage involving Fe-end-member ringwoodite, stishovite and Fe_4O_5 which buffers oxygen fugacities at values that decrease with pressure above 10 GPa. With the addition of magnesium end members to the system the stability of an Fe_4O_5 phase in the mantle can also be assessed. These calculations show that Fe_4O_5 could form in the transition zone at oxygen fugacities near the metastable FMQ buffer.

l. *High-pressure melting in H_2O-rich systems (R. Myhill and D.J. Frost)*

The formation of melts and fluids in the deep mantle (> 200 km) is an important issue for interpreting areas of low shear wave velocity, understanding the origin of exotic lavas such as kimberlites and producing models for the loss of volatiles from subducting slabs. The subduction of oceanic lithosphere creates a route for hydrogen to enter the mantle. Fluids are progressively lost from the subducting slab as it heats up but mineral-bound hydrogen can be carried deeper into the interior within a range of hydrous and nominally anhydrous minerals. Beneath arcs, these water-rich fluids cause metasomatism and induce large degrees of melting in the overlying mantle wedge. Fluids released at greater depths likely continue to influence the slab and overlying mantle, affecting rheology and causing metasomatism.

Determining the composition of H_2O-rich liquids released at high pressures and temperatures has traditionally been a problem for experimental petrologists. Melt compositions do not quench to a glass and so cannot be directly analysed. The liquidus H_2O content can be determined for simple congruent melting compositions by performing experiments with different bulk H_2O contents and finding the compositions that brackets the liquidus. This is possible if H_2O can be accurately added to the starting materials, which is more easily achieved if it can be added as a stoichiometric solid phase such as $Mg(OH)_2$. However, the range of H_2O contents that can be added with $Mg(OH)_2$ is limited.

We have conducted multianvil experiments in the MgO-SiO_2-H_2O system at 13 GPa, using solid platinic acid ($H_2Pt(OH)_6$) as a novel H_2O source. Using solid starting materials allows us to use spark-eroded multi-chamber capsules, so that several compositions can be run at the same conditions and the liquidus can be bracketed in one experiment. Short experimental run durations and $Pt_{90}Rh_{10}$ and Au capsules are used to prevent H_2O loss. Compositions have been chosen to span a large fraction of the normally inaccessible brucite-quartz-water ternary (Fig. 3.2-17a). Although the H_2O -rich melt formed from these compositions cannot be quenched, its presence is inferred from large dendritic crystals of hydrous phases and minor overgrowths on phases which existed in solid form at high temperature. To provide an example, we present SEM-BSE images of four out of twelve chambers from a single experiment (Fig. 3.2-17b). Sample compositions covered part of the brucite-water join. It is known that brucite melts incongruently at high pressure, but the melt composition has not been constrained. In our experiments, periclase which was originally dissolved into the melt is seen as bright overgrowths on preexisting equant periclase crystals. The remainder of the melt crystallised into a mixture of brucite and H_2O. The MgO-H_2O liquidus at 13 GPa and 1400 °C is found at approximately 62 mol.% H_2O. These measurements allow internally consistent thermodynamic models to be developed that that are based on a mechanistic understanding of how H_2O dissolves in melts at high pressure.

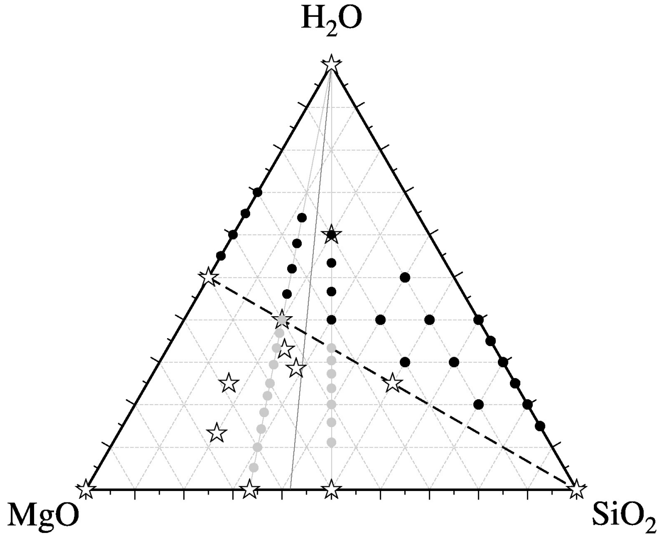

Fig. 3.2-17a: The MSH molar ternary, illustrating the starting compositions for this project (black), those analysed previously (grey) and known high-pressure solid phases (white stars). Normally, solid starting compositions would be restricted to compositions lower in H_2O than the brucite + quartz binary (black dashed line).

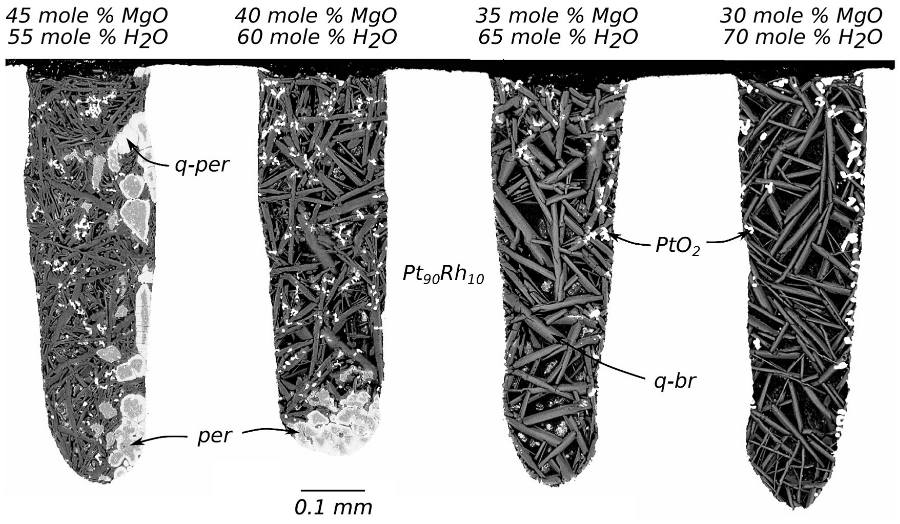

Fig. 3.2-17b: Experimental run products from 13 GPa and 1400 °C along the brucite-H_2O binary. The two magnesium oxide phases are periclase (non-quench and quenched; per and q-per) and brucite (q-br). The liquidus is crossed between 60 and 65 mol.% H_2O.

m. *The fate and behaviour of volatiles during subduction of oceanic crustal material towards the deep mantle (A. Rosenthal and D.J. Frost)*

Knowledge of the abundance and distribution of volatiles (*i.e.*, C-O-H) in the Earth's deep interior remains controversial but is very important in terms of understanding the evolution of surface volatile reservoirs. Estimates for the Bulk Silicate Earth (BSE) H_2O-budget range from 200-2000 ppm H_2O, which is from ¼ to ~ 5.5 times the mass of the world's oceans. The chief means of replenishment of the Earth's interior with volatiles over much of geological time is subduction (*i.e.*, the transport of crustal material into the Earth's deep interior by large-scale tectonic processes), but constraints on this process in the deeper mantle are poor because no natural samples are returned to the surface from the deeper regions of subduction zones. Thus, the only way to determine the volatile content of subducted material is to simulate high-pressure and -temperature conditions equivalent to conditions of the Earth's interior by using high-pressure experimental facilities.

In this study the maximum storage capacity, substitution mechanism and behaviour of H_2O in hydrous and nominally anhydrous minerals (NAMs) is being studied with relevance to the processes occurring during subduction of hydrated oceanic crustal material into the deep upper mantle. A particular interest is to determine the H_2O content of NAMs within sections of subducting oceanic crust at the conditions where nominally hydrous phases (such as phengite) are breaking down to release H_2O that would then leave the slab. The H_2O trapped in NAMs at these conditions is likely subducted into the deep mantle. A novel approach is being employed involving two experimental stages. Firstly conditions are identified where hydrous minerals, such as phengite, break down in a hydrous eclogitic assemblage. The compositions of all mineral phases are determined at the point of dehydration. Then in a second stage of the experiments pre-synthesised mono-mineralic layers of NAM are sandwiched between the eclogitic assemblages and run for several days to allow the mineral phases to equilibrate with the fluid. Due to the size of the mono-mineralic layers they can be easily analysed to determine their H_2O contents. This is an original approach as earlier studies concentrated on the direct measurement of H_2O in single-mineral phases only, *i.e.*, not in equilibrium with bulk mineral assemblages. The proposed method allows thus analysis of small % H_2O in eclogitic NAMs at different pressures and temperatures in tiny experimental run products by using mono-mineralic mineral layers.

Here we present preliminary results from the first stage of the experiments where phase relations are determined for a subducted crustal composition (oceanic basalt composition GA1) containing varying amounts of H_2O (up to 7 wt.%) at varying temperatures (sub-solidus to near solidus) and pressures (6-10 GPa; *i.e.*, from ~ 200 to ~ 330 km depth). Experiments yield well-crystallised assemblages of garnet ± clinopyroxene ± coesite/stishovite ± rutile ± phengite ± vapour. The stability of phengite can be accurately determined under varying conditions of pressure, temperature, buffering mineral paragenesis and bulk H_2O concentration. In addition, K_2O in phengite and clinopyroxene decreases with increasing bulk H_2O content at subsolidus conditions for a given pressure and temperature (Fig. 3.2-18).

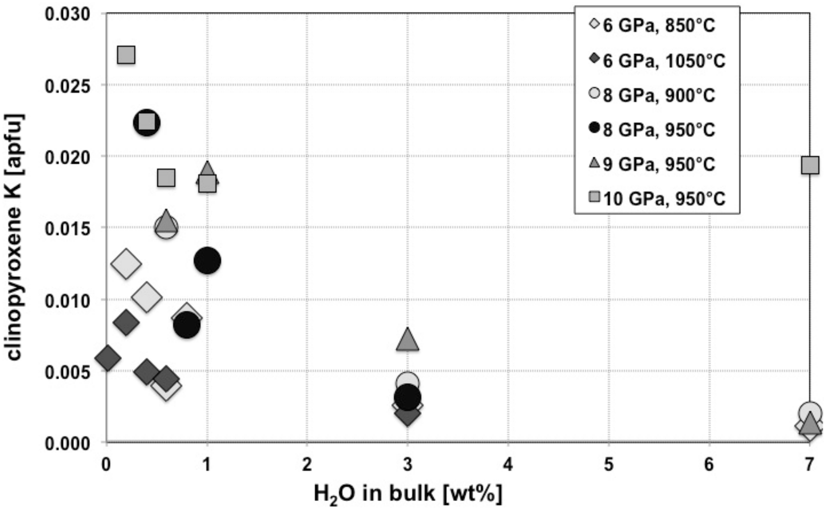

Fig. 3.2-18: Compositional variations in clinopyroxene as a function of pressure, temperature and bulk H_2O content. *K* [apfu] in clinopyroxene decreases with increasing bulk H_2O content at subsolidus conditions at given *P* and *T*.

Mineral phase compositions measured by electron microprobe analyses (EMPA) are now being used to prepare subsequent layered experiments. This will allow the direct measurement of H_2O in eclogitic NAMs using Fourier-transform infrared (FTIR) spectroscopy, secondary ion probe techniques (SIMS) or elastic recoil detection analysis (ERDA). The results will be used to place constraints on the fluxes of H_2O recycled into the mantle at subduction zones, a critical step in the distribution of the Earth's overall volatile budget.

n. *Fluorine solubility in wadsleyite and ringwoodite (M. Roberge, H. Bureau and G. Fiquet/Paris; D.J. Frost; N. Bolfan-Casanova/Clermont-Ferrand; C. Raepsaet, S. Surble and H. Khodja/Saclay)*

Relatively little is known above the cycling and storage of volatile elements in the Earth (H, C, Cl, F, …), despite the fact that these elements are of primary importance for understanding the emergence of life on our planet, and also the dynamics and the differentiation of the Earth into various reservoirs (core, lower mantle, upper mantle, crust, and atmosphere).

In this study we have focused on fluorine, the most abundant halogen element. Whereas heavier halogen elements, Cl, Br and I, are depleted in the bulk silicate Earth (BSE; *i.e.*, Earth without the core) relative to carbonaceous chondrites, F is enriched, suggesting that this element may be stored at depth in mantle minerals. For a long time, the main fluorine carriers in the upper mantle were thought to be hydrous and minor accessory minerals such as apatite, micas and amphibole. Recently, F solubility has been intensively studied in nominally anhydrous mantle minerals (olivine, garnet, pyroxene), where a few tens of ppm F were found. However, nothing is known about the possibility to incorporate F at higher depth, in the mineral assemblages of the transition zone (from 410 to 660 km, TZ) or lower mantle.

In this study, we aim at determining whether the TZ may be a potential storage zone for fluorine. Indeed, wadsleyite (Wd) and ringwoodite (Rw; $(Mg,Fe)_2SiO_4$) can incorporate high amounts of water (up to 3.3 wt.% H_2O). Since the ionic radius of OH^- and F^- are similar it is likely that F substitutes for OH in these mineral lattices, as has been demonstrated for other mineral phases (*e.g.*, amphibole).

We have experimentally investigated the solubility of F in olivine (Ol), Wd and Rw at the TZ conditions. Experiments have been performed in multianvil presses at BGI and at LMV Clermont Ferrand. Experiments were performed at the conditions of the TZ from 14 to 22 GPa; from 1100 to 1450 °C and for several hours. Powders were prepared in order to obtain bulk compositions of Fo_{90} together with a slight excess of SiO_2 (Mg/Si atomic ration of 1.75), they were mixed with NaF in excess (5 wt.% F). Syntheses were carried out under both anhydrous and hydrous conditions (2 wt.% water, added as $Mg(OH)_2$), in order to determine the effect of water on the fluorine solubility values. The obtained Ol, Wd and Rw crystals were found to be larger than 10-20 µm allowing F and H_2O quantification through micro-analysis techniques. We have used several ion beam techniques of the nuclear microprobe of LEEL, CEA Saclay to map element concentrations within areas of crystals. We used PIGE (Particle Induced Gamma Ray Emission, proton micro-beam of ~ 3×3 µm^2) for F; and ERDA (Elastic Recoil Detection Analysis, ^{4}He micro-beam of ~ 4×16 µm^2) for H.

Results show that fluorine contents are ranging from 323±32 to 1235±124 ppm F, when water contents are ranging from 428±65 to 1404±197 ppm H_2O in the hydrous samples. Fluorine contents slightly decreases with the increasing temperature (Fig. 3.2-19). No clear relationship has been observed between water and F concentrations, except the fact that the highest fluorine concentrations are found in anhydrous Wd and Rw (1045±105 and 1235±124 ppm F,

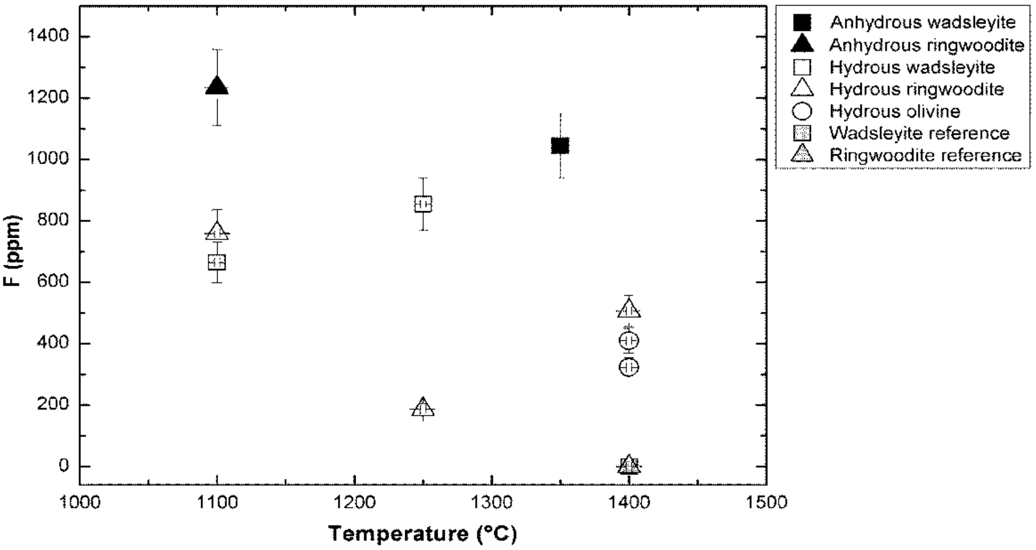

Fig. 3.2-19: Fluorine content in ppm versus temperature of the experiment for anhydrous and hydrous wadsleyite, ringwoodite and olivine.

respectively), while in hydrous samples the highest F contents are 855±86 ppm F for Wd, 760±76 ppm F for Rw and 410±41 ppm F for Ol. Fluorine and water contents are higher in Wd and Rw than in Ol.

In view of these results, and assuming saturation of the transition zone with respect to fluorine, the F content of the BSE would be 43 ppm F, which is about twice the value of 25 ppm assumed for the BSE. Our results show that significant amounts of F could be stored in the transition zone, where it may have been recycled through the subduction of slabs together with water.

o. *Experimental calibration of a garnet-clinopyroxene geobarometer for mantle eclogites (C. Beyer and D.J. Frost)*

Geobarometry measurements are essential for understanding the tectonic processes responsible for the formation and migration of rocks within the Earth and can provide vital information on the depth of magmatic and metasomatic processes evident in mantle xenoliths. Eclogite rocks are formed from mafic protoliths within high-grade metamorphic belts and ultra-high-pressure terrains where their presence indicates pressures of at least 1 GPa. Eclogites are also found as mantle xenoliths, however, in kimberlites erupted within the cratonic lithosphere. Eclogitic rocks account for only a small percentage of mantle xenoliths from such localities, but their significance outweighs their abundance for several reasons. Eclogitic xenoliths are of great economic interest due to their higher yield of diamonds relative to peridotitic xenoliths. Due to their proposed origin as mafic oceanic crustal rocks they would seem to trace subduction processes related to the evolution of the cratonic lithosphere. However, it has also been proposed that at least some eclogite xenoliths are magmatic rocks formed as deep seated cumulates. Due to their potentially central role in the formation and evolution of the cratonic lithosphere it is very important to be able to reconstruct the P/T conditions at which eclogitic xenoliths equilibrated.

The substitution of Al in clinopyroxene on the tetrahedral position is highly pressure-dependent and suitable to calculate the pressure of eclogitic rocks. There are several promising approaches using the Ca-Tschermak compound in clinopyroxene as a geobarometer in the literature. In this study we have examined the equilibrium:

$$\underset{\text{Grossular}}{2/3\ Ca_3Al_2Si_3O_{12}} + \underset{\text{Pyrope}}{1/3\ Mg_3Al_2Si_3O_{12}} = \underset{\text{Diopside}}{CaMgSi_2O_6} + \underset{\text{Ca-Tschermak}}{CaAlAlSiO_6} \qquad (1)$$

We expand the model by taking into account the sodium-bearing jadeite compound using thermodynamic interaction terms and perform calibration experiments using a natural bulk composition. The derived geobarometer should be applicable to most eclogitic rocks and we tested the geobarometer with the results of many other experimental studies covering a wide range of compositions and experimental conditions. Our barometer agrees well with the majority of experiments.

High-pressure experiments were performed between 4 and 7 GPa in a 1000 ton Kawai-type multianvil apparatus and in a 500 tons press equipped with a Walker-type module. Experiments at lower pressure (3 GPa) were conducted using an end-loaded piston cylinder apparatus. Experimental charges yielded homogeneous, euhedral to subhedral garnet and clinopyroxene crystals along with quenched silicate melt.

Figure 3.2-20 shows a P-T diagram for a number of eclogitic mantle xenoliths and diamond inclusions derived using the geobarometer developed in this study. The resulting pressures are in good agreement with estimated geotherms for cratonic lithosphere and the occurrence of diamonds in the deepest xenoliths. Therefore, we provide a unique tool for getting reliable pressure estimates for eclogitic mantle xenoliths and inclusions in diamonds.

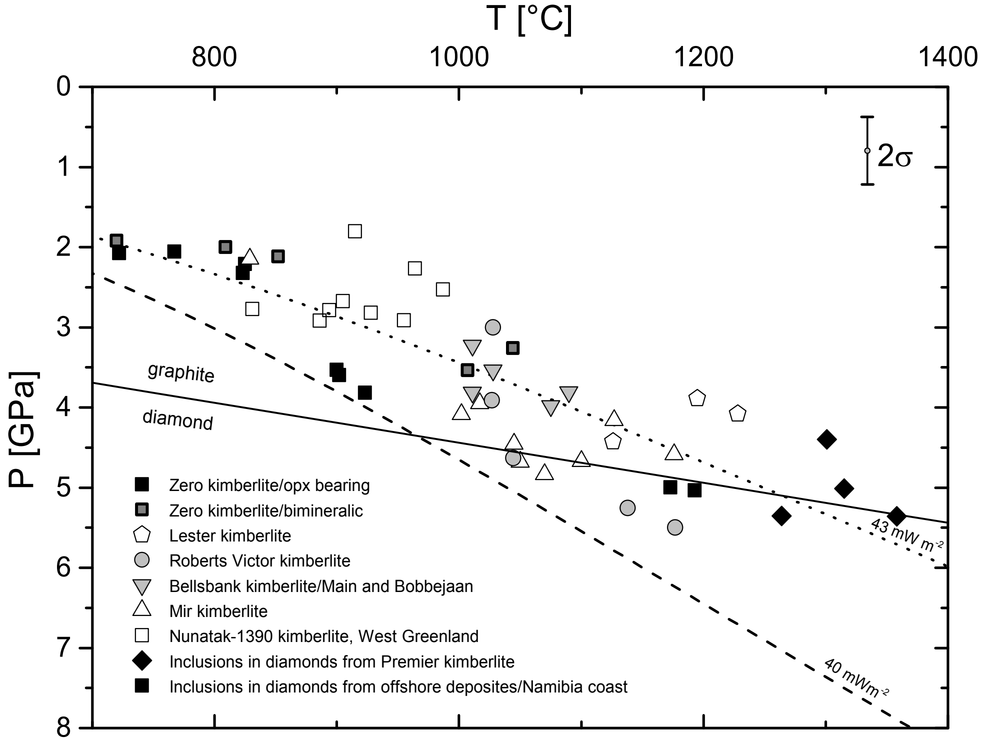

Fig. 3.2-20: P-T calculations of natural eclogite samples from various kimberlites. The graphite-diamond transition and typical cratonic geotherms calculated for a surface heat flow of 40 and 43 mWm^{-2} are shown for orientation. The temperature for each sample is calculated using the Ellis and Green (1979) geothermometer.

p. *Solubility and partitioning of copper between silicate minerals, oxides, pyrrhotite and mafic to felsic silicate melts (X. Liu and X. Xiong/Guangzhou; A. Audétat, H. Keppler and Y. Li)*

The solubility and partition coefficients of Cu between solid phases and silicate melts ($D_{Cu}^{mineral/melt}$) constrain the distribution and evolution of Cu during partial melting and magmatic differentiation. Many published $D_{\mathrm{Cu}}^{\mathrm{mineral/melt}}$ values, in particular those for silicate minerals and oxides, are problematic and may not be suitable to predict the behaviour of Cu in magmatic processes, due to a variety of problems in the determination of partition coefficients, such as low concentration of Cu in the silicate minerals and/or partitioning disequilibrium due to Cu loss to the noble-metal capsules during high-P and high-T experiments. To avoid these problems and to obtain more precise $D_{\mathrm{Cu}}^{\mathrm{mineral/melt}}$ values, we used $Pt_{95}Cu_5$ and $Au_{95}Cu_5$ alloy capsules as Cu source to determine the solubility and partitioning of Cu between silicate minerals, oxides, pyrrhotite and silicate melts at various conditions of melt composition, pressure, temperature and oxygen fugacity (fO_2). Here, we report new data on Cu solubility in various silicate melt compositions and on Cu partitioning in dacitic bulk compositions between silicate minerals, oxides and melts.

The experiments were conducted in piston cylinder presses using various starting melt compositions including komatiite, basalt, $Di_{70}An_{30}$, dacite and haplogranite at 0.75-3.5 GPa, 850-1300 °C and fO_2 varying from IW to HM buffers. Within these experimental conditions, pressure seems to have no effect on the solubility of Cu, while temperature, fO_2, and melt composition/structure have obvious effects. Apparent Cu solubility (Cu concentration in the melt at a fixed Cu activity << 1.0) increases nearly linearly with increasing temperature (from 850-1250 °C) and fO_2 (from IW to HM buffer). These results are consistent with data of previous studies. Figure 3.2-21 shows that Cu solubility in the melt decreases from komatiitic to $Di_{70}An_{30}$, basaltic, dacitic and granitic compositions, suggesting that the degree of melt polymerization (Xnf/X; *i.e.*, – the ratio of the molar fraction of network – forming cations to all cations) has an important effect on Cu solubility. The scatter of data at fixed Xnf/X values

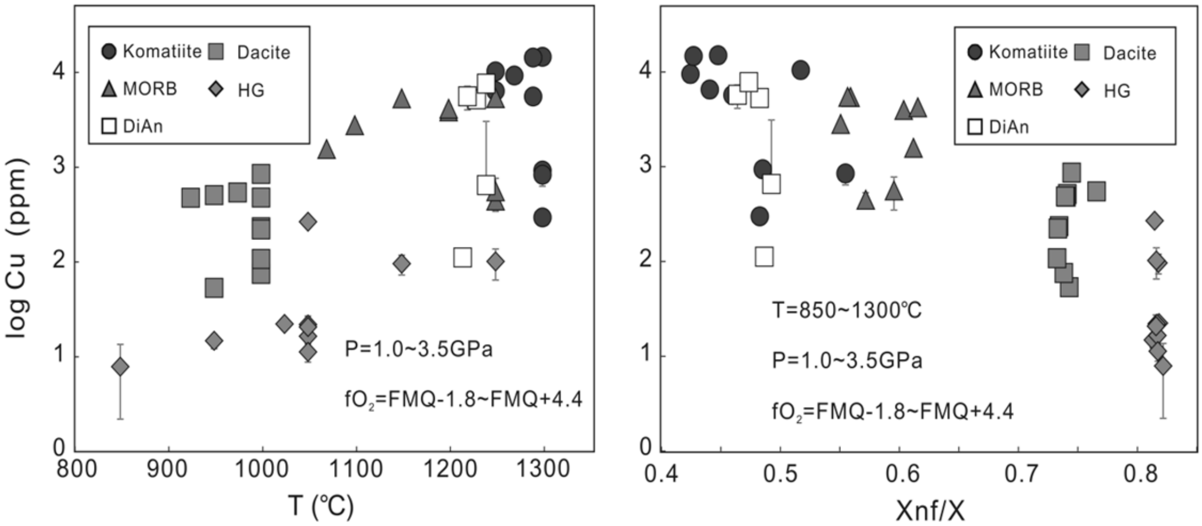

Fig. 3.2-21: Variation of Cu solubility in silicate melts with temperature (left) and the degree of melt polymerization (Xnf/X; right). The symbols represent different starting materials used in the experiments.

(right panel of Figure 3.2-21) is due to variations in temperature and fO_2 conditions. The decrease of Cu solubility with the increasing degree of melt polymerization (Xnf/X) may be explained by the amount of non-bridging oxygen atoms. As melt polymerization increases, the amount of non-bridging oxygen atoms available to bond with Cu decreases, and consequently, the solubility of Cu in the melt decreases. This also suggests that Cu in silicate melts acts a network modifier rather than a network former.

Copper partitioning between silicate minerals, oxides and melts with dacitic composition was systematically investigated at 1.0-2.5 GPa, 950-1000 °C and fO_2 ranging from the graphite buffer to the HM buffer. Measured mineral – melt partitioning values ($D_{Cu}^{mineral/melt}$) are 0.17-0.45 for cpx (9 pairs), 0.03-0.06 for garnet (7 pairs), 0.08-0.12 for amphibole (3 pairs), 1.67 for spinel (1 pairs), 0.12-0.25 for opx (2 pairs), 0.26 for olivine (1 pair), 0.12 for plagioclase (1 pair) and 561 for pyrrhotite (1 pair). Compared to $D_{Cu}^{mineral/melt}$ values obtained from komatiitic and MORB compositions at 1.0 - 3.5 GPa, 1200-1300 °C and fO_2 ranging from graphite buffer to HM buffer (0.04-0.14 for olivine, 0.04-0.09 for opx, 0.02-0.23 for cpx, 0.19-0.77 for spinel, 0.03-0.05 for garnet and 0.02 for plagioclase; Liu *et al.* 2014, GCA 125:1-22), those obtained from the dacitic composition are generally higher. For any given melt composition $D_{Cu}^{mineral/melt}$ values decrease with increasing temperature. These results suggest that the partition coefficients are governed by the solubility of Cu in the silicate melt. As discussed above, Cu solubility in the silicate melt increases with increasing temperature and decreasing degree of melt polymerization, hence $D_{Cu}^{mineral/melt}$ values in hot, little-polymerized, mafic magmas can be expected to be lower than in cool, polymerized, dacitic magmas if the change in Cu-solubility in the coexisting minerals is comparatively small. During the evolution of magmas from mafic to felsic compositions Cu should thus become increasingly compatible in the crystallizing minerals. However, in sulfide-free magmas the $D_{Cu}^{mineral/melt}$ values will always remain low enough to lead to enrichment of Cu in the residual melt.

q. *Element partitioning between mafic magma and exsolved fluids at near-solidus conditions (X. Gutiérrez and A. Audétat)*

Upper-crustal magma chambers are commonly replenished by mafic magmas ascending from depth, resulting in magma underplating. Fluids released during the quenching of these hot, mafic magmas against overlying, cool, felsic magma are thought to transport sulphur and other volatiles into the upper parts of the magma chamber. Some of the metals present in porphyry-type ore deposits are believed to originate via the same mechanism from mafic magmas. However, there are no experimental data available to test this hypothesis. The aim of this study was to explore whether such data can be obtained by means of experiments involving synthetic fluid inclusions.

In a first step, natural, mafic alkaline rock powder was hydrated with S- and Cl-bearing fluid in a piston-cylinder experiment at 1200 °C and 10 kbar to produce a homogeneous, nearly crystal-free glass. This glass was then loaded together with an uncracked quartz piece into a new Au capsule and equilibrated in a cold-seal pressure at 850 °C and 2 kbar for one day; afterwards the fluid-inclusion formation in the quartz piece was initiated by *in situ* cracking. The capsule was then held at 850 °C and 2 kbar for another 6 days to allow the cracks within the quartz piece to heal and thereby trap fluid in the form of synthetic fluid inclusions. The hydrated starting glass and the fluid inclusions recovered from the second experiment were analyzed by laser-ablation ICP-MS for major and trace elements. For the fluid inclusions prior characterization by micro-thermometry was necessary to be able to convert the relative element concentrations determined by LA-ICP-MS into absolute values.

During equilibration at 850 °C and 2 kbar the hydrous glass transformed into ≥ 95 % crystals plus a few weight percent fluid. The retrieved quartz piece contains numerous fluid inclusions up to 50 µm in size (Fig. 3.2-22). Microthermometric investigation revealed that the trapped fluid has a very low salinity of only ~ 0.4 wt.% $NaCl_{equiv.}$ This result was unexpected because the starting glass contained ~ 2000 ppm Cl and ~ 5 wt.% H_2O. A plot of element concentrations measured in the starting glass against those measured in the fluid inclusions (Fig. 3.2-23a) suggests that S and B have the highest affinity to the fluid phase, followed by alkalies and Pb, then transition elements, and finally Al and Mg. It needs to be noted that this plot allows only relative (*i.e.*, not absolute) partition coefficients to be determined, as the composition of the starting glass was measured before the experiment, whereas the fluid was analyzed after the experiment, hence without knowing the exact amount of fluid present after the experiment it is not possible to do mass balance calculations.

To check whether equilibrium was attained between fluid and solid residue, we performed an additional experiment in which the natural rock powder was directly equilibrated with fluid without the intermittent step of melting and hydration. Again, fluid inclusion formation

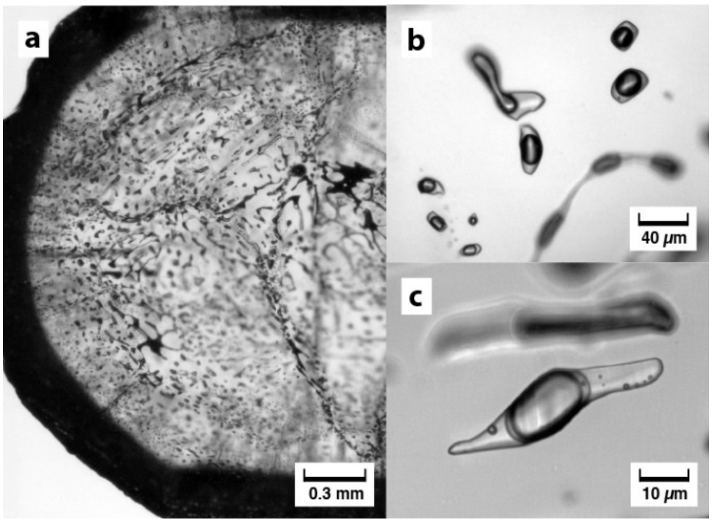

Fig. 3.2-22: Photomicrographs of synthetic fluid inclusions in quartz. (a, b) view at room temperature; (c) view of an inclusion at -10 °C. The meniscus around the central vapour bubble is composed of liquid CO_2, and the rounded grains within the aqueous solution are elemental sulphur.

was initiated after 1 day and the capsule held at 850 °C and 2 kbar for 6 more days. Fluid inclusions analyzed from this run (XG19) have the same composition (within analytical uncertainty) as those analyzed from the crystallization experiment described above (XG10), suggesting that equilibrium was indeed attained (Fig. 3.2-23b).

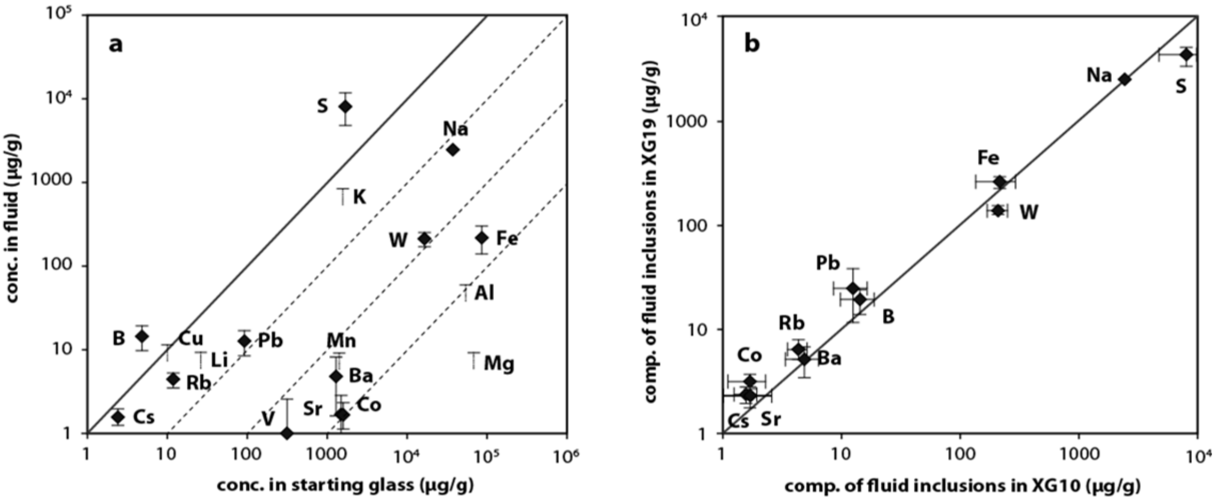

Fig. 3.2-23: (**a**) Element concentrations measured in hydrated mafic starting glass versus element concentrations measured in fluid inclusions trapped after crystallization of this glass at 850 °C and 2 kbar. Elements that could be analyzed only in the starting glass but not in the fluid inclusions are shown by half error bars starting at the detection limit of the fluid inclusion analyses. (**b**) Composition of fluid inclusions in the experiment with hydrated glass (XG10) versus fluid inclusions compositions in an experiment starting directly with crushed rock powder (XG19). The good match between the two results suggests that equilibrium between fluid and solids was attained.

r. *Origin of Ti-rich rims in magmatic quartz phenocrysts from the Bandelier Tuff, southwestern USA (A. Audétat)*

The titanium content of quartz phenocrysts is a function of temperature, pressure and the activity of TiO_2 (a_{TiO2}) in the magma. During cooling of a magma at constant pressure and a_{TiO2}, the Ti content of crystallizing quartz continuously decreases. However, quartz crystals from silicic volcanic tuffs commonly show abrupt increases in Ti concentrations from core to rim, as revealed by trace element analysis and cathodoluminescence (CL) images. The origin of these Ti-rich rims has been a matter of debate in recent years, with some researchers attributing them to changes in temperature, and others attributing them to changes in pressure, both assuming constant a_{TiO2}.

This study on two quartz phenocrysts from the Upper Bandelier Tuff (New Mexico, USA) aims at resolving these issues by combining melt inclusion analyses with CL imaging and trace element analysis of adjacent quartz. Through analysis of major and trace elements in the melt inclusions both a_{TiO2} and temperature (the latter via zircon saturation thermometry) can be reconstructed, which are then used in conjunction with Ti-in-quartz (TitaniQ) thermobarometry on the surrounding quartz to estimate pressure. In this way, all parameters affecting Ti solubility in quartz can be reconstructed at the scale of individual growth zones within quartz phenocrysts. CL images of polished quartz grains were produced using a scanning electron microscope equipped with an ellipsoidal mirror. Compositions of unexposed melt inclusions and the surrounding host quartz were determined by laser-ablation ICP-MS (Fig. 3.2-24). Activity of TiO_2 in the silicate melt was calculated based on the solubility model of Kularatne and Audétat (2014; *GCA* 125:196-209); zircon saturation temperatures are based on the model of Watson and Harrison (1983; *EPSL* 64:295-304); and pressures were calculated based on the TitaniQ model of Huang and Audétat (2012; GCA 84:75-89). The presence of small (< 10 µm), euhedral zircon inclusions in both low-Ti quartz cores and high-Ti rims proves that the silicate melt was saturated in zircon at all times.

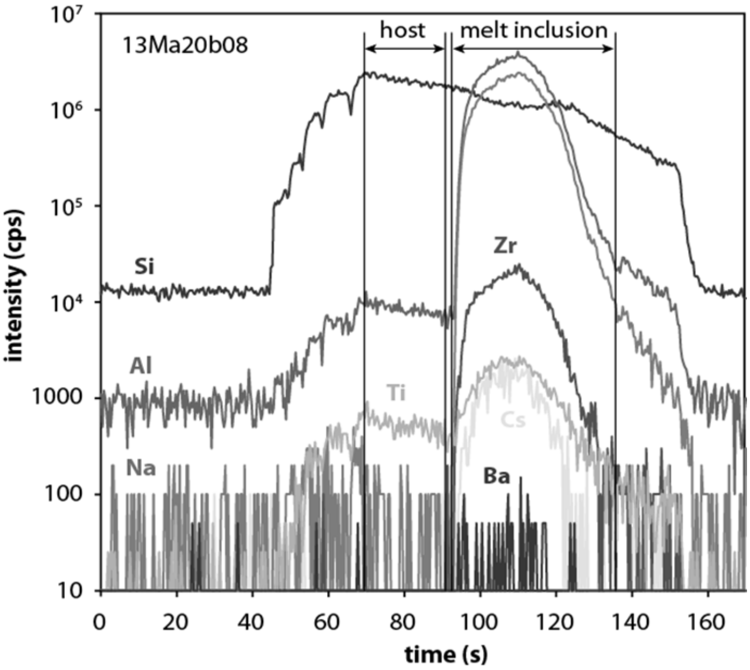

Fig. 3.2-24: Laser-ablation ICP-MS signal of melt inclusion #4 drilled out of sample Bandelier A-E. The indicated integration intervals were used to calculate the composition of host quartz and melt inclusion, respectively.

The results summarized in Fig. 3.2-25a suggest that the low-Ti core of sample Bandelier A-E from the Bandelier Tuff crystallized at ~ 820 °C and 2.4 kbar pressure, whereas the high-Ti rim crystallized at ~ 880 °C, 1.5-2.4 kbar pressure and slightly higher a_{TiO2}. Zircon saturation temperatures are in agreement with pre-eruption magma temperatures estimated from Fe-Ti-oxides (~ 840 °C), and pressures agree with independent pressure estimates of 2.0±0.5 kbar based on volatile contents of melt inclusions, stratigraphic reconstruction and seismic evidence. Based on the TitaniQ model of Huang and Audétat (2012) it can be calculated that in this specific sample the rim-ward increase in Ti concentration is due to a combination of increased temperature (49 % contribution), lower pressure (31 %) and higher a_{TiO2} (20 %). In sample Bandelier B-I (Fig. 3.2-25b) the rim-ward increase in Ti is predominantly due to an increase in a_{TiO2} (58 % contribution) and to smaller degrees due to changes in pressure (29 %) and temperature (12 %). The results suggest that in both examples the Ti-rich rims formed as a result of heating and concomitant melt modification, as happens during a magma chamber replenishing event. This interpretation is further supported by the rim-ward increase of compatible elements (*e.g.*, Ba) and simultaneous decrease in incompatible elements (*e.g.*, Cs), which suggests that cool, evolved, residual melts mixed with fresh, hotter, less evolved melts.

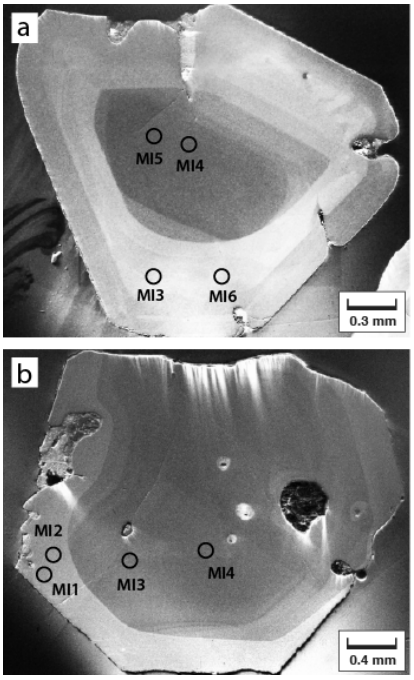

sample Bandelier A-E		from melt inclusion analysis Al/ (Na+K)	TiO2 (wt%)	*a*TiO2 K&A	Cs (µg/g)	Ba (µg/g)	Zr (µg/g)	T_{zirc} (°C)	from qtz analysis Ti_{qtz} (µg/g)	$P_{TitaniQ}$ (kbar)
core	MI4	1.05	0.061	0.18	6.0	0.9	218	821	34	2.4
	MI5	1.04	0.060	0.17	6.3	2.4	228	824	33	2.4
rim	MI3	1.07	0.121	0.22	3.4	16.3	373	875	63	2.1
	MI6	1.10	0.118	0.20	3.1	16.2	382	883	74	1.5

sample Bandelier B-I		from melt inclusion analysis Al/ (Na+K)	TiO2 (wt%)	*a*TiO2 K&A	Cs (µg/g)	Ba (µg/g)	Zr (µg/g)	T_{zirc} (°C)	from qtz analysis Ti_{qtz} (µg/g)	$P_{TitaniQ}$ (kbar)
core	MI3	1.10	0.053	0.15	6.6	0.7	248	839	32	2.0
	MI4	1.00	0.057	0.20	6.9	0.9	228	819	35	2.1
rim	MI1	1.12	0.103	0.29	3.7	19	254	843	73	1.5
	MI2	1.20	0.117	0.33	2.6	40	255	851	76	1.5

Fig. 3.2-25: Cathodoluminescence images of two polished quartz grains from the Upper Bandelier Tuff, with the locations of analyzed melt inclusions (MI) indicated by circles. Results obtained from LA-ICP-MS analysis of these melt inclusions and their surrounding host quartz are shown on the right. Al/(Na+K) refers to the aluminium saturation index, T_{zirc} to the zircon saturation temperature, and Ti_{qtz} to the Ti concentration in quartz.

3.3 Mineralogy, Crystal Chemistry and Phase Transitions

Studies of the crystal structure of minerals and their evolution with pressure and temperature are fundamental to our understanding of the Earth's interior and the knowledge of how processes that occur deep within the Earth can influence those that take place at the surface. Seemingly small changes in the crystal structure of materials, for example, the degree of tilting of polyhedral structural units, can profoundly influence physical properties such as elasticity and stability relative to other structures. Single crystal measurements of $CaIrO_3$ perovskite have demonstrated that compression takes place primarily by distortion of B-site octahedra instead of simple tilting, which may account for the higher stiffness of $CaIrO_3$ perovskite compared to other *Pbnm* Ca-oxide perovskites. The degree of octahedral tilting in *Pbnm* perovskites can be easily calculated from cell parameters derived from powder X-ray diffraction data if octahedra remain undistorted; however single crystal measurements of $(Mg,Fe)(Si,Al)O_3$ perovskite have shown that powder data underestimate tilting angles and that a change in iron valence state could influence elastic properties. Another important parameter is the spin state of iron atoms, and *in situ* measurements of $(Mg,Fe)(Si,Al)O_3$ perovskite at pressure and temperature conditions of the lower mantle have established that Fe^{2+} transforms to the intermediate-spin state, while Fe^{3+} remains in the high-spin state.

The addition of volatile elements to the crystal structure of mantle phases can significantly influence their elastic and rheological properties. High-pressure experiments conducted on $(Mg,Fe)(Si,Al)O_3$ perovskite have shown changes in the solubility of water as a function of pressure and temperature, while similar experiments conducted on ceramic perovskites demonstrated a high solubility of Ar coupled to the formation of oxygen vacancies. These latter results show unambiguous evidence that neutral noble gases can easily occupy vacancies of appropriate size in crystal structures, and confirm silicate perovskite to be an important host of argon in the lower mantle. Oxygen vacancies have also been identified in the $CaTiO_3$-$CaFeO_{2.5}$ system using a novel method involving the transmission electron microscope that demonstrates the preference of Fe^{3+} for the octahedral site. The position of hydrogen in crystal structures can be determined using neutron diffraction, and measurements on superhydrous phase B, a potentially important phase in the lower part of the transition zone associated with cold slabs, show positions within large channels that are responsible for the high water capacity of the structure and would likely lead to fast water diffusion through the structure.

Single crystals provide detailed information on structures and symmetry that cannot always be obtained from experiments on polycrystalline material. Single crystals of $NaNiF_3$ perovskite that were partially transformed to the post-perovskite structure show strong topotactic relations indicative of a martensite-like transformation mechanism that could provide an explanation for the observed seismic anisotropy at the bottom of the lower mantle. Garnet is an important phase in the upper mantle and transition zone that can be described as a complex solid solution of many endmembers, where single crystal studies of these pure phases as well as their solid solutions can be used to link garnet crystal chemistry to physical and chemical properties. Single crystals of $Fe_3Fe_2Si_3O_{12}$ "skiagite" were used to study the iron oxidation state in garnet as a function of pressure, while single crystals of $Ca_3Al_2Si_3O_{12}$ grossular, $Ca_3Cr_2Si_3O_{12}$ uvarovite, and their solid solutions have been synthesised in order to measure their thermoelastic parameters. These can be used to construct models to determine the internal pressures of garnet inclusions in natural diamond.

Phase transformations in simple oxides show a rich complexity. SiO_2, for example, has more than 30 known stable or metastable phases, a number of which are abundant in nature. Mechanisms of structural transitions to high-pressure polymorphs are not well understood, which motivated a single crystal study on one of the bridging phases in the SiO_2 transformation series that shows a large stability range of cristobalite X-I for which single crystal refinements are still ongoing. Iron oxides also undergo many high-pressure phase transformations, but additionally with changes in iron valence and phase stoichiometry. Results of high-pressure experiments on the recently discovered phase Fe_4O_5 combined with thermodynamic calculation of phase boundaries show that Fe_4O_5 is stable over a wide range of pressures and temperatures, emphasising its importance when assessing the thermodynamics, oxygen fugacity and phase relations of iron-containing phases in the Earth's mantle. Using single crystal X-ray diffraction, a new polymorph of Fe_2O_3 was discovered with the double perovskite structure that transforms further at higher pressure and temperature to a phase isostructural with post-perovskite and resolves previous controversies regarding behaviour in the 40-60 GPa range. Studies at ambient conditions of natural samples of hydrothermally altered vein minerals show distinct generations of Fe_2O_3 that are well crystallised with nanoscale dimensions, which provide insight into the stability of phases that could be used for the storage of radioactive waste.

Questions regarding the fate of carbon and the nature of the deep carbon cycle have motivated studies of the crystal chemistry and phase transitions involving carbonates at mantle pressures and temperatures. Innovative measurements in a diamond anvil cell have enabled the melting temperature of $MgCO_3$ to be determined up to 84 GPa, while post mortem analysis reveals that decarbonation took place in at least one of the experiments. Single crystal measurements of iron-bearing carbonates establish the transition pressure of the high-spin to low-spin transition and its shift to higher pressure with increasing temperature. Laser heating produced a transformation to one or more new C-rich phases that were shown by both XANES and synchrotron Mössbauer source spectroscopies to contain a significant portion of Fe^{3+}. New methodology using the transmission electron microscope that involves scanning transmission electron imaging and precession electron diffraction techniques provides possibilities to study these and many other transformations and crystallographic relationships at a sub-nanometer scale.

a. *High-pressure structural evolution of $CaIrO_3$ perovskite (K.S. Kularatne, A. Kurnosov and T. Boffa Ballaran; R.G. Trønnes/Oslo)*

$CaIrO_3$ perovskite (*Pbnm*) and post-perovskite (*Cmcm*) phases are compounds isostructural with $MgSiO_3$ perovskite. $CaIrO_3$ post-perovskite, which is the stable phase at ambient conditions, transforms at 1-3 GPa and temperatures > 1350 °C to the $CaIrO_3$ perovskite structure, providing an ideal low-pressure and low-temperature analogue for the $MgSiO_3$ perovskite to post-perovskite phase transformation which occurs at the extreme conditions of 125 GPa and 2500 K. However, in order to assess whether the $CaIrO_3$ compounds can be used as analogues to investigate the phase transition from perovskite to post-perovskite in the $MgSiO_3$ system, prior knowledge of their atomic structures and their response to changes in pressure and temperature is essential.

We have therefore studied the structural behaviour of orthorhombic (*Pbnm*) $CaIrO_3$ perovskite up to 9.59 GPa by means of single-crystal high-pressure diffraction. Intensity measurements of two single-crystals of $CaIrO_3$ perovskite $49\times89\times15$ μm^3 and $63\times35\times10$ μm^3 in size were performed on an Xcalibur diffractometer using a diamond anvil cell with neon (Ne) as pressure transmitting medium and a ruby chip as pressure calibrant. Crystal structure refinements of $CaIrO_3$ perovskite were performed using the SHELXL97 program. $CaIrO_3$ perovskite is highly distorted with respect to the cubic aristotype (see BGI Annual Report 2012). However, contrary to the behaviour of other Ca-oxide perovskites, for example $CaSnO_3$ and $CaTiO_3$, the octahedral tilts and in particular the out-of-phase tilt do not increase with increasing pressure (Fig. 3.3-1). Instead, compression of the $CaIrO_3$ structure occurs via distortion of the octahedral sites. Since distortion of stiff octahedra requires much more energy that simple tilting of rigid octahedra, our results may explain why $CaIrO_3$ perovskite is much stiffer than the other orthorhombic (*Pbnm*) Ca-oxide perovskites whose compression takes place by tilting of the octahedra with only minor octahedral distortion.

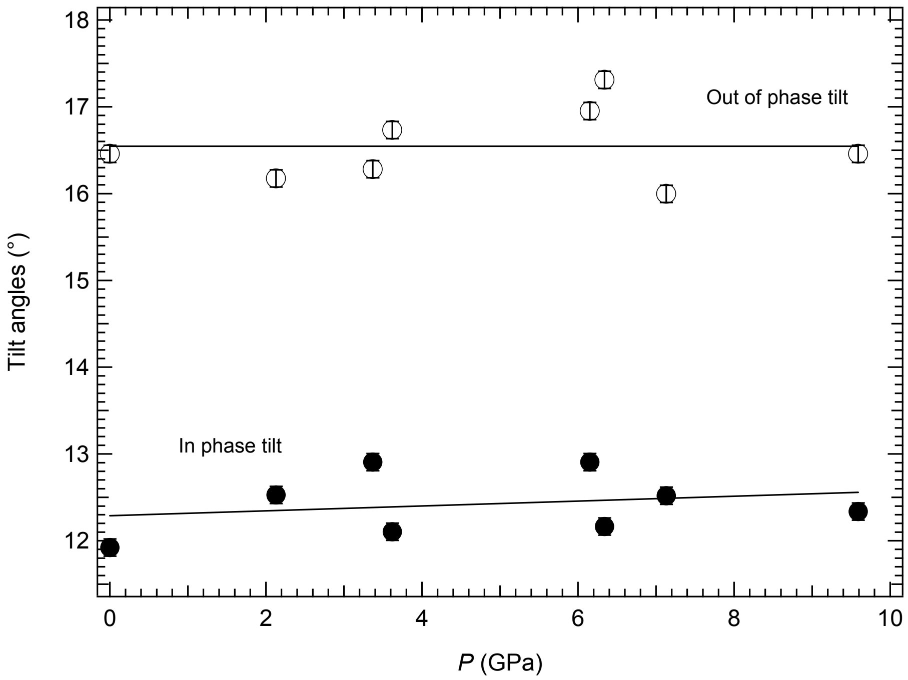

Fig. 3.3-1: Variation with pressure of the tilt angles of $CaIrO_3$ perovskite. Note especially that the out-of-phase tilt appears to be independent of pressure.

b. *Effect of cation substitution on octahedral tilting in $(Mg,Fe)(Si,Al)O_3$ perovskite (C.A. McCammon, R. Sinmyo, E. Bykova, I. Kupenko, V. Potapkin and L.S. Dubrovinsky)*

The crystal structure of $(Mg,Fe)(Si,Al)O_3$ perovskite, the phase widely believed to dominate the Earth's lower mantle, is an orthorhombic *Pbnm* modification of the cubic perovskite structure. The orthorhombic distortion arises from rotation and tilting of the SiO_6 octahedra, where the degree of octahedral tilting can be expressed in terms of different rotations of the pseudo-cubic unit cell, for example as a combination of tilting about two orthogonal directions (angles θ and φ), or a single tilt about the diagonal of the pseudo-cubic unit cell (angle Φ) (Fig. 3.3-2). The simplest method of estimating tilt angles between octahedra in *Pbnm* perovskites is from the unit cell parameters. Provided the octahedra remain regular, the single tilt angle Φ is given by $\Phi = \cos^{-1} (\sqrt{2}\, a^2/bc)$. Literature studies based on powder diffraction data have reported that Fe substitution in $MgSiO_3$ perovskite reduces the tilt angle, while the addition of Al increases it. These results are based on the assumption of non-distorted octahedra, however, which may not be correct. More accurate determinations of octahedral tilting are provided by single-crystal refinements, and in view of the importance of octahedral tilting to the stability and elastic properties of the perovskite phase, we undertook a single-crystal X-ray diffraction study of $(Mg,Fe)(Si,Al)O_3$ perovskite.

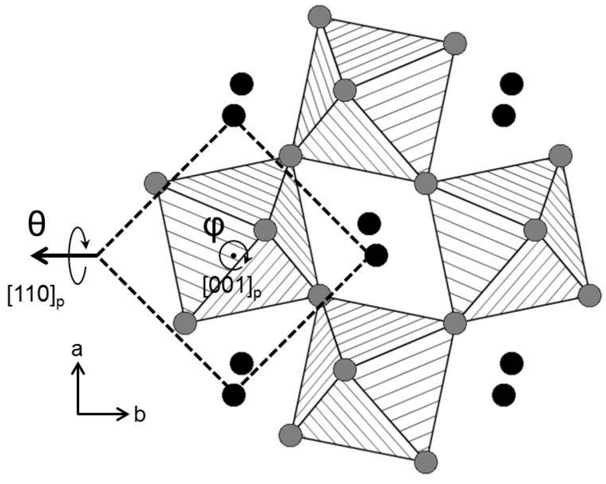

Fig. 3.3-2: Schematic illustration of octahedral tilting in *Pbnm* $MgSiO_3$ perovskite (Z = 4). Viewed down the orthorhombic c axis, the pseudo-cubic unit cell (Z = 1) (shown as dashed lines) can be tilted about the pseudo-cubic $[110]_p$ direction (angle θ) and the pseudo-cubic $[001]_p$ direction (angle φ), or described as a single tilt about the pseudo-cubic $[111]_p$ direction (angle Φ). For simplicity, only the θ and φ angles are shown.

The sample was synthesised from mixed oxides using a Kawai-type multianvil press at 26 GPa and 2073 K for 50 minutes. Electron microprobe analysis and Mössbauer spectroscopy showed the composition of the sample to be $Mg_{0.946(17)}Fe^{2+}_{0.045(4)}Fe^{3+}_{0.011(1)}Si_{0.997(16)}O_3$. Selected single crystals were examined using an Oxford Diffraction Xcalibur diffractometer

(Mo-Kα radiation, λ = 0.71073 Å) with a CCD detector. A total of 1115 reflections were collected covering the range 5.18° < 2θ < 31.26°. Symmetry equivalent reflections were merged (R_{int} = 0.068), resulting in 189 reflections with $I > 2\sigma$ that were used for the full matrix least-squares refinement of the structure.

The octahedral tilt angle calculated from our data using the cell parameter method is consistent with previous refinement data from the literature as well as the linear trends shown by the extensive literature dataset for polycrystalline $(Mg,Fe)(Si,Al)O_3$ perovskite (Fig. 3.3-3a). The cell parameter method shows an opposing effect of Fe and Al to respectively decrease and increase the tilt angle, where the effect of Al substitution in the absence of Fe increases the tilt angle even more compared to the case when Fe is also present. Tilt angles calculated from unit cell parameters are not always accurate, however, since octahedra are assumed to remain regular, and tilt angles are typically underestimated if octahedra become slightly distorted. More realistic tilt angles can be calculated directly from the atomic coordinates, which for *Pbnm* perovskites are given as follows:

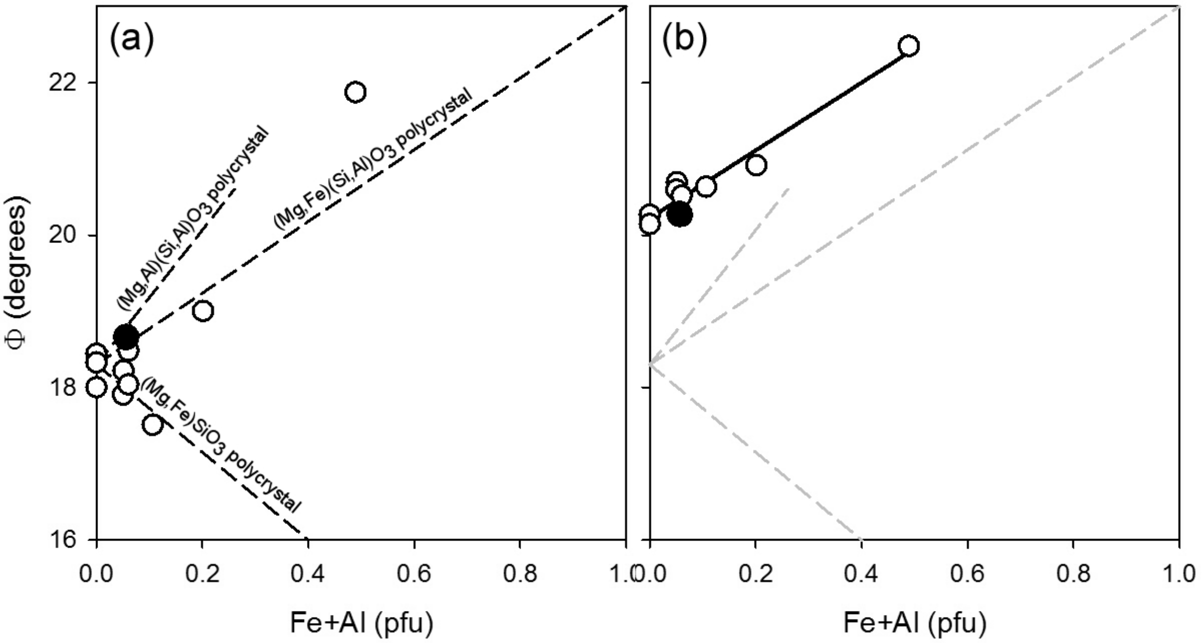

Fig. 3.3-3: Variation of tilting angle Φ for $(Mg,Fe)(Si,Al)O_3$ perovskite with cation composition (Fe+Al) in cations per formula unit (pfu) calculated from single-crystal refinements based on (**a**) unit cell parameters, and (**b**) atomic coordinates. The solid circle is derived from our data, open circles are calculated from data in the literature, and the dashed lines indicate the linear trends derived from polycrystalline data (shaded grey in part **b**).

$\tan\theta = 4\,(u_{O1}^2 + v_{O1}^2)^{1/2}/c$; $\tan\varphi = 4\,(u_{O2}^2 + v_{O2}^2)^{1/2}/(a^2 + b^2)^{1/2}$; $\cos\Phi = \cos\theta\cos\varphi$

where

$u_{O1} = a\, x_{O1}$; $v_{O1} = b\,(0.5 - y_{O1})$; $u_{O2} = a\,(0.25 - x_{O2})$; $v_{O2} = b\,(y_{O2} - 0.25)$

and x_{On} and y_{On} are the fractional atomic coordinates of the nth oxygen atom. The more accurate tilt angles calculated from the atomic coordinates show clearly that the variation of tilt angle with composition is essentially the same for a given amount of Fe or Al substitution, independent of composition, which implies that individual octahedra must be more distorted with trivalent cation substitutions (Al or Fe^{3+}) compared to divalent cation substitutions (Fe^{2+}) into the dodecahedral site, even when octahedra are only occupied by Si. Such effects can influence the relative compressibility of octahedra, which in turn can affect the bulk compressibility. Oxidation of Fe^{2+} to Fe^{3+} in $(Mg,Fe)(Si,Al)O_3$, for example, would be predicted to change octahedral distortion without necessarily changing the octahedral tilting angle, but could affect elastic properties.

c. *Electronic spin state of Fe,Al-containing $MgSiO_3$ perovskite at lower mantle conditions (I. Kupenko, C.A. McCammon, R. Sinmyo and C. Prescher; A.I. Chumakov, A. Kantor and R. Rüffer/Grenoble; L.S. Dubrovinsky)*

Iron-, aluminium-containing magnesium silicate perovskite (FeAlPv) is believed to be the main component of the Earth's lower mantle. The electronic spin state of iron in different valence states in FeAlPv may affect thermal and electrical conductivities, thermodynamic and other properties of the Earth's interior. Numerous high-pressure studies of iron in FeAlPv have been performed and many of the studies gave conflicting results. Despite the many investigations, a systematic study of FeAlPv with mantle composition at mantle conditions is still lacking. Moreover most predictions of FeAlPv behaviour at lower mantle conditions have been inferred from studies on samples quenched from high temperature or from *ab initio* calculations.

Mössbauer spectroscopy is one of the best methods to study the valence and spin state of iron at high pressure. However, conventional energy-resolved Mössbauer spectroscopy utilises radioactive sources with low brilliance. Therefore high-pressure Mössbauer studies require collection times that are too long to be effectively applied for laser-heated diamond anvil cells (DACs). The time domain analogue of traditional Mössbauer spectroscopy is realised via time-resolved Nuclear Forward Scattering (NFS) of synchrotron radiation. In contrast to radioactive sources the synchrotron beam has high brilliance and can be focused to a 10 µm horizontal and 5 µm vertical spot. The method allows rapid and high quality measurements in DACs at high pressures and, if coupled with laser heating, also at high temperatures.

We have investigated silicate perovskite with composition $Mg_{0.83}Fe_{0.21}Al_{0.06}Si_{0.91}O_3$ relevant for the lower mantle at pressures up to 81 GPa and temperatures up to 2000 K using conventional MS and synchrotron NFS combined with double-sided laser heating in a DAC. Room temperature Mössbauer and NFS spectra at low pressure are dominated by high-spin

Fe^{2+}, with minor amounts of Fe^{3+} and a component assigned to a metastable position of high-spin Fe^{2+} in the A-site predicted by computational studies (Fig. 3.3-4). NFS data show a sharp transition (< 20 GPa width) from high-spin Fe^{2+} to a new component with extremely high quadrupole splitting, similar to previous studies. Mössbauer data show the same transition, but over a broader pressure range likely due to the higher pressure gradient. The new Fe^{2+} component is assigned to intermediate-spin Fe^{2+}, consistent with previous X-ray emission spectroscopy studies. NFS data at high temperatures and high pressures comparable to those in the lower mantle are consistent with the presence of Fe^{2+} only in the intermediate-spin state and Fe^{3+} only in the high-spin state. Our results are therefore consistent with the occurrence of spin crossover only in Fe^{2+} in Fe-, Al-containing perovskite within the lower mantle.

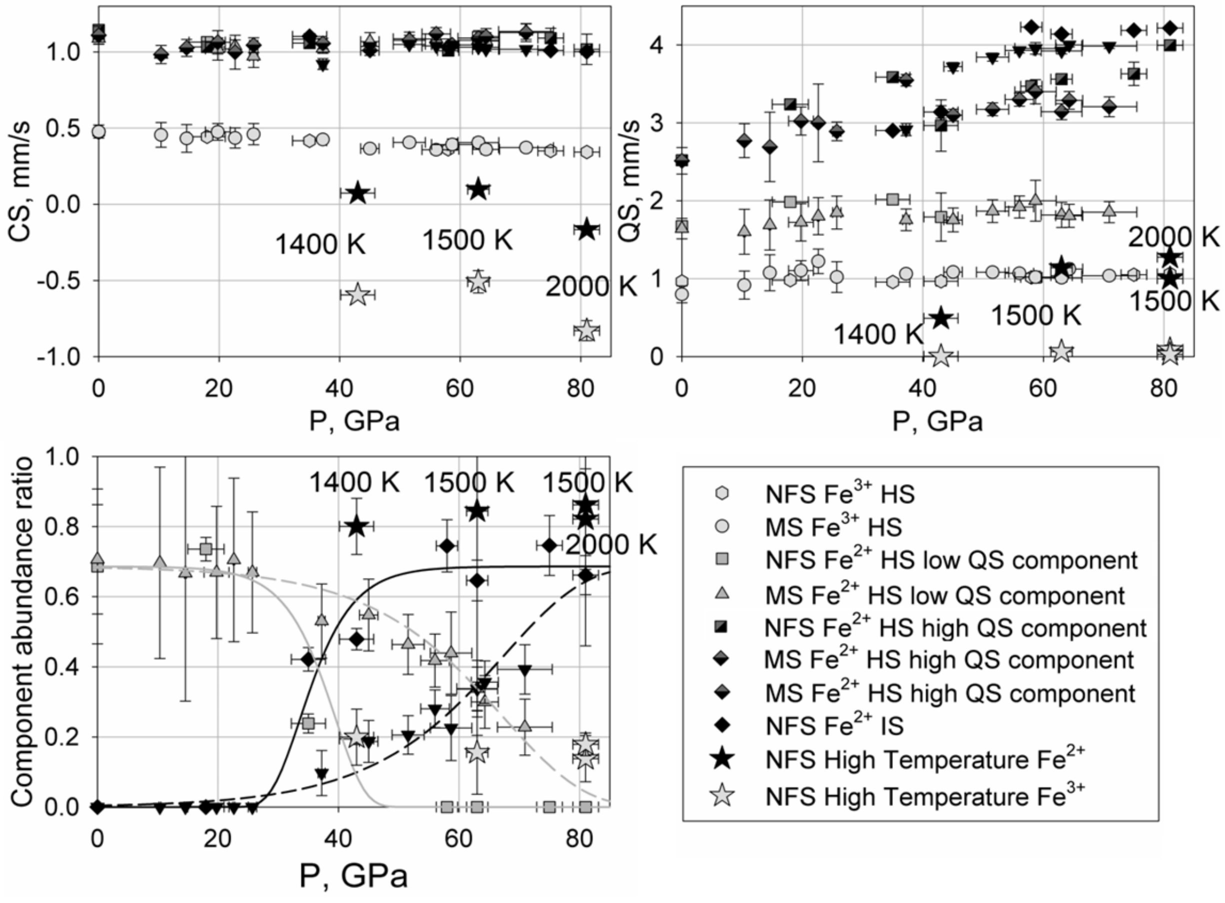

Fig. 3.3-4: Effect of pressure on the hyperfine parameters of $Mg_{0.83}Fe_{0.21}Al_{0.06}Si_{0.91}O_3$ perovskite as measured by Mössbauer spectroscopy (MS) and Nuclear Forward Scattering (NFS): (**a**) Centre shift (CS); (**b**) Quadrupole splitting (QS); (**c**) Relative abundance. Grey and black curves indicate the trends of the relative abundance for the Fe^{2+} high-spin (HS) low QS and Fe^{2+} intermediate-spin (IS) components, respectively, while the dashed and solid curves indicate the trends for the MS and NFS data, respectively. For clarity the relative abundance of the Fe^{3+} and HS high QS Fe^{2+} components are not shown, which remain relatively constant at all pressures at values of 20 % and 10 %, respectively.

d. *Water solubility in (Mg,Fe)(Si,Al)O_3 perovskite (J. Chen/Miami; M.G. Pamato; Y. Lin/ Stanford; T. Katsura, T. Kawazoe and L. Ziberna)*

Water can significantly influence the elastic and rheological properties of mantle minerals. The solubility of water in the dominant lower mantle phase, (Mg,Fe)(Si,Al)O_3 perovskite, is still the subject of intense debate, however. In addition to water solubility, the mechanism of water incorporation and the nature and abundance of defects are also important parameters that can influence elastic and rheological properties. To obtain important information on these parameters, we have undertaken a study of water solubility in iron-free and iron-bearing aluminous magnesium silicate perovskite, with particular focus on the influence of pressure, temperature and composition. Experiments were conducted on several compositions of (Mg,Fe)(Si,Al)O_3 perovskite by loading starting materials of either oxide mixtures or pre-made glass into platinum capsules that were subsequently welded, where thin gold liners were used for Fe-containing samples and a piece of oxidised iron was added to buffer oxygen fugacity. Water-saturated conditions were produced either from brucite used in the place of MgO, or the addition of distilled water. Experiments were conducted using the 1000 ton Kawai-type multianvil press at BGI with 7/3 cell assembly, and pressures and temperatures were estimated using previous calibrations for the same cell. Most run products contained multiple phases with grain sizes sufficient to allow analysis of individual phases (Fig. 3.3-5).

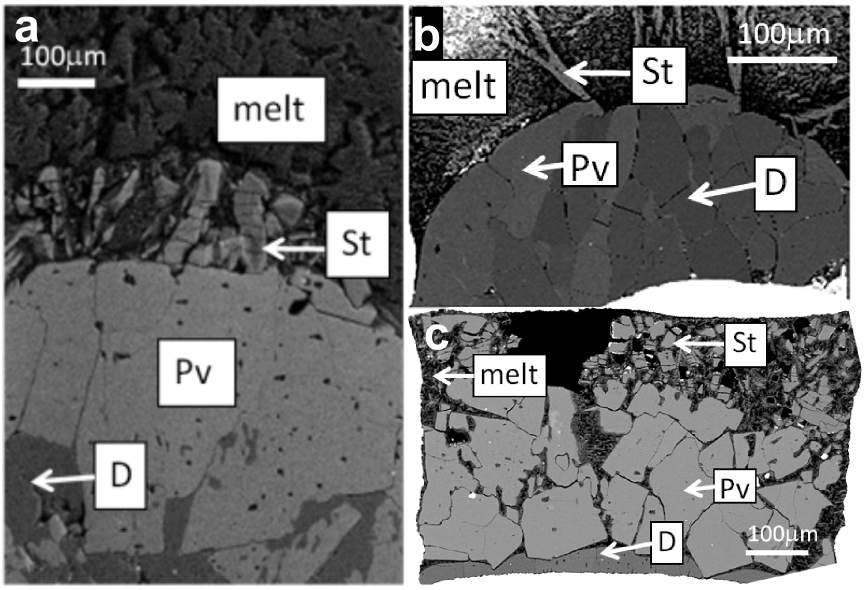

Fig. 3.3-5: Back-scattered electron images of recovered samples synthesised from oxide mixtures (Mg# = 100) with 5 wt.% Al_2O_3 + brucite run at the following conditions: (**a**) 26 GPa and 1900 °C; (**b**) 26 GPa and 2100 °C; (c) 27 GPa and 1900 °C. Pv: (Mg,Al)(Si,Al)O_3 perovskite; D: Phase D; St: stishovite.

Chemical compositions were determined using the electron microprobe and water content was measured using secondary ion mass ion spectrometry. Preliminary results indicate a decrease in the solubility of water in the perovskite phase as a function of increasing temperature, and an increase in water solubility with increasing pressure. Further investigation of these samples is underway using X-ray diffraction, FTIR and Raman spectroscopy to study the structure and bonding response to the incorporation of water in these aluminous perovskites.

e. *High noble gas solubilities in Ga-doped $CdGeO_3$ perovskites (S. Shcheka and H. Keppler)*

Recently, experiments at Bayerisches Geoinstitut showed that at high pressure, noble gases readily dissolve in $MgSiO_3$ perovskite. Neutral noble gas atoms probably occupy oxygen vacancies, which result from the substitution of Si by Al in tetrahedral coordination ($2Si^{4+} = 2Al^{3+} + V_O$) or are related to low silica activity ($V_{Si} = 2V_O$). However, the metastability of $MgSiO_3$-perovskite at ambient conditions makes it difficult to fully investigate the substitution mechanism of noble gases in this phase. Moreover, the abundance of oxygen vacancies in silicate perovskite is low compared to that in a number of ceramic perovskites with general formula $A^{2+}B^{4+}O_3$. Doping of these perovskites with trivalent cations produces solid solutions $A^{2+}(B_{1-x}M_x)O_{3-0.5x}$ that may provide a good model for understanding the behaviour of noble gases in silicate perovskite.

In order to study noble gas solubility in ceramic perovskites, $CdGeO_3$ and $CaPbO_3$ compositions were chosen as starting materials. They show the same structural transitions as observed in the $MgSiO_3$ system, but at lower pressures. $CdGeO_3$ perovskite was synthesised in a 1200t multianvil press by annealing a stoichiometric mixture of GeO_2 and CdO together with 5 wt.% of Ga_2O_3 and Ar, Kr or Xe at 12.5 GPa and 1000 °C for 1 hour (Fig. 3.3-6a). Gallium was used as a trivalent doping agent to enhance the formation of oxygen vacancies. Only the samples with numerous empty cavities indicating saturation of the samples with noble gas were analysed. $CaPbO_3$ perovskite is stable above 5 GPa. However, we failed to synthesise La-doped $CaPbO_3$ directly from oxides.

The chemical composition of run products including their Ar content was measured by electron microprobe. The synthesised $CdGeO_3$ perovskites with average formula $Cd_{1.065}(Ge_{0.937}Ga_{0.041})_{0.978}O_3$ demonstrate that Ga^{3+} readily substitutes for Ge^{4+} on the octahedral site, resulting in the formation of oxygen vacancies. It is also supported by the observation that the total number of cations per formula unit is above two when recalculated to three oxygen atoms. Analyses of Ar show that more than 1000 ppm of Ar is homogeneously dissolved in $CdGeO_3$. X-ray element distribution mapping shows that high Ar content corresponds to the perovskite phase only (Fig. 3.3-6b). No Xe (detection limit 300-400 ppm by weight) was found in $CdGeO_3$ by electron microprobe.

Our data show unambiguous evidence that neutral noble gases can easily occupy vacancies of appropriate size in crystal structures, which may not only happen at lower pressure conditions. The observations in the ceramic model system also fully confirm that silicate perovskite is an important host of argon in the lower mantle, while the phase does not easily incorporate xenon.

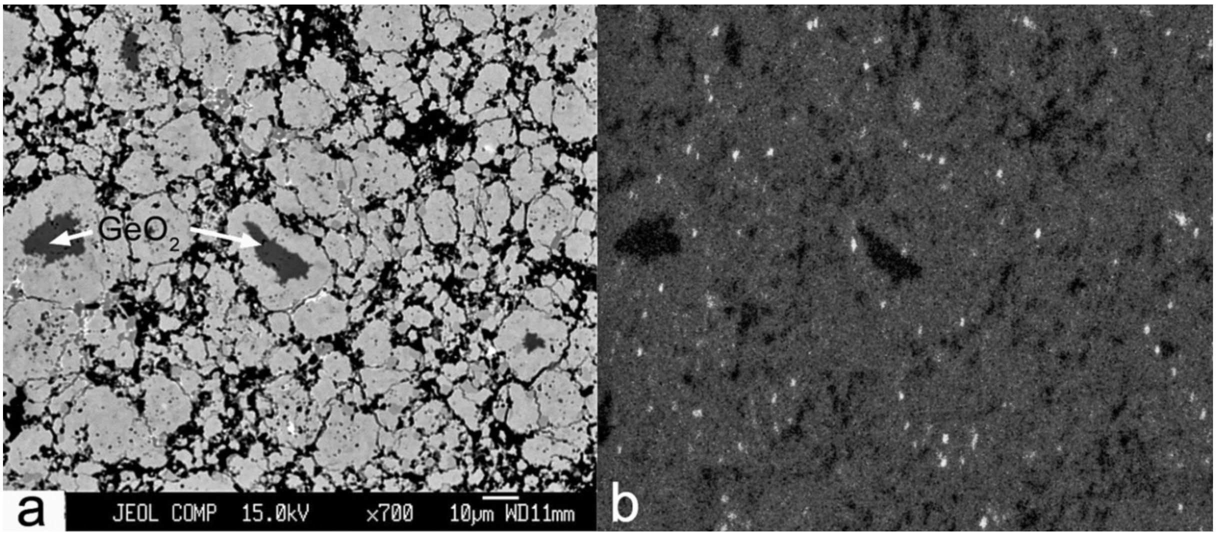

Fig. 3.3-6: $CdGeO_3$ perovskite synthesised at 12.5 GPa and 1000 °C. (**a**) BSE image; (**b**) X-ray distribution map of Ar in the same area. Bright spots represent Ar-filled inclusions located close to the surface.

f. *Electron channelling spectroscopy of Fe^{3+} bearing orthorhombic perovskites in transmission electron microscopy (N. Miyajima and X. Gutiérrez)*

Electron channelling spectroscopy is a powerful technique to determine the site occupancy of elements in complex mineral solid solutions (*e.g.*, garnet, spinel and perovskite). We can localise an inelastic scattering along specific atom planes or columns by setting excitation error (s) around a Bragg condition. This phenomenon is known as an electron channelling effect. The effect has been used in ALCHEMI (Atom Location by CHanneling Enhanced Microanalysis) for energy dispersive X-ray spectroscopy (EDXS) and electron energy loss spectroscopy (EELS) in a transmission electron microscope (TEM). However, the latter is more difficult to perform even qualitatively, because the signal-to-noise ratio is usually very low under the planner channelling conditions due to the off-axis measurement by EELS-aperture under the two-beam excitation condition. We report preliminary results of atomic site-specific analyses of Fe^{3+}-bearing orthorhombic perovskite in the $CaTiO_3$-$CaFeO_{2.5}$ system under electron channelling conditions in the EDXS.

The specimen of Fe^{3+}-bearing orthorhombic perovskite was synthesised from a starting chemical composition of $Ca(Ti_{0.8},Fe_{0.2})O_{2.9}$ using an oxygen-fugacity controlled furnace at 1320 °C with oxygen fugacity one log unit above the iron-wüstite buffer. The quenched sample was studied by EDXS in a TEM. The sample contains two distinct phases having different iron contents as follows: Fe-poor: $Ca_{1.08}(Ti_{0.84}Fe^{3+}_{0.16})_{\Sigma 1.00}O_3$ and Fe-rich: $Ca_{1.05}(Ti_{0.82}Fe^{3+}_{0.21})_{\Sigma 1.03}O_3$.

The ALCHEMI-EDXS method for the latter Fe-rich perovskite with Fe^{3+} = 0.20 per formula unit indicates a preferential distribution of ferric iron into the octahedral sites (Fig. 3.3-7). The increase of intensity of the Fe-K line corresponds to that of the Ti-K line, indicating coexistence of both cations on the site. The phase displays defect contrasts in the TEM image and diffuse scattering in the electron diffraction pattern and cannot be indexed with a $GdFeO_3$-type *Pbnm* unit cell of $CaTiO_3$ orthorhombic perovskite (Fig. 3.3-8), although the Fe-poor phase displays a homogeneous contrast and can be indexed with the *Pbnm* unit cell. Therefore, the further identification of the type of defects in the Fe-rich phase can be important for a basic understanding of the relations between the crystal chemistry (*e.g.*, oxygen vacancies) and physical properties (*e.g.*, compressibility under high pressure) in Fe^{3+}-bearing perovskite as an analogue of $MgSiO_3$ perovskite in Earth's lower mantle.

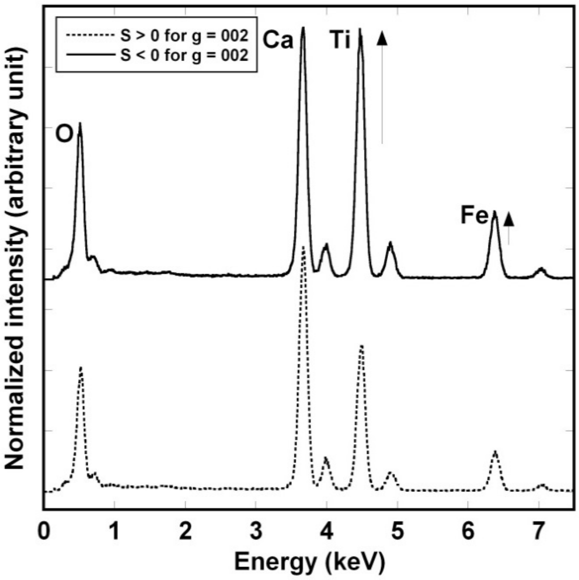

Fig. 3.3-7: Comparison of energy-dispersive X-ray spectra for Fe^{3+}-bearing $CaTiO_3$ perovskite that was oriented parallel to a systematic diffraction direction (*d*-spacing = 0.78 nm, see inset of Fig. 3.3-8), taken under two different orientation conditions. Lower: dodecahedral sites preferentially selected with s > 0 against ***g*** = 002 (orthorhombic setting). Upper: Octahedral sites selected with $s < 0$. Relative intensity of peaks of Fe-Kα line increases under the $s < 0$ condition, which indicates a preference of ferric iron for the octahedral site.

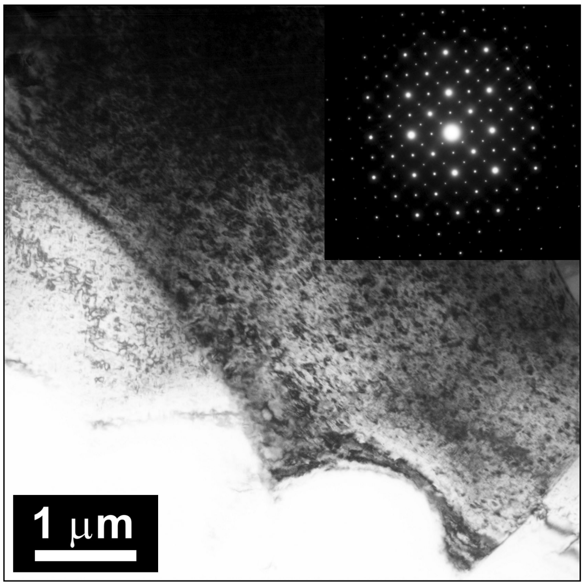

Fig. 3.3-8: Typical bright field TEM image of the Fe-rich perovskite phase, displaying a dusty contrast. The inset shows the corresponding selected area electron diffraction pattern with diffuse scattering along systematic diffraction directions (d-spacing = 0.78 nm).

g. *The determination of hydrogen positions in superhydrous phase B (D.M. Trots, A. Kurnosov and D.J. Frost; T. Hansen/Grenoble)*

Water exists in the Earth's mantle in a number of different forms. It may exist as a free fluid phase; it may be dissolved in silicate melts or incorporated into nominally anhydrous minerals, such as the polymorphs of Mg_2SiO_4 (forsterite, wadsleyite and ringwoodite). It may also be incorporated into nominally hydrous high-pressure silicate phases, such as dense hydrous magnesium silicate (DHMS) phases, which have to date mainly been characterised in the MgO-SiO_2-H_2O ternary system. The DHMS phases, referred to as A, B, D, E, and superhydrous phase B (SHyB), might be stable at the pressure and temperature conditions compatible with cold portions of subducting slabs and they may form a network of phases with overlapping stability fields that transport water into the lower mantle. Although the existence of DHMS in nature is still under debate, SHyB might be stable within ultramafic compositions coexisting with ringwoodite at conditions compatible with subducting slabs in the lower part of the transition zone. The formation of hydrous minerals such as SHyB may influence the mechanical and rheological properties of slabs, and the ultimate dehydration might potentially be related to the processes causing deep-focus earthquakes. Any attempt to understand the stability or transport properties of such hydrous phases, however, would benefit from an understanding of the crystal structure, including the mechanism of hydrogen substitution.

However, the available information from the literature concerning the predominant locations of hydrogen atoms in the structure of the SHyB is inconsistent. In order to shed light on the fine details of water incorporation in the structure of SHyB, we have undertaken neutron diffraction which is the most rigorous and direct method for determination of deuterium site occupancies in crystalline phases because neutron scattering cross sections are not a function of atomic mass as for X-ray diffraction and are relatively large for deuterium.

Sufficient volumes of high-pressure silicates were synthesised for neutron diffraction studies using the 5000 tonne large volume multianvil press at Bayerisches Geoinstitut. The neutron powder diffraction measurements were performed at the high-flux powder diffractometer installed at the neutron reactor at the *Institut Laue-Langevin* in Grenoble, France.

The structure of SHyB can be considered as an ordered alternation of two structural motifs along the *a*-axis: the first motif is composed of double octahedral-tetrahedral OT layers consisting of the edge-shared MgO_6 octahedra and vertex-linked SiO_4 tetrahedra, whereas the second motif is built up of octahedral O layers containing edge-shared MgO_6 and SiO_6 octahedra (Fig. 3.3-9). These layers interchange as …–O–OT–OT–O–OT–OT–O–… sequence. Large channels occur in the structure along the *b*-axis inside the OT layers formed between the edge-shared octahedra and the vertex-linked tetrahedra.

The structural model based on *Pnn*2 symmetry was used for SHyB, which was supported by spectroscopic results in the literature. Application of Fourier synthesis with subsequent analyses of difference nuclear density maps and Rietveld fits reveal two distinct positions for deuterium at 4c (0.194, 0.052, 0.596) and at 4c (0.186, 0.119, 0.388), as shown in Fig. 3.3-10 by white arrows. This means that deuterium resides within large channels which are formed between edge-shared octahedra and vertex-linked tetrahedra along the *b*-axis of the SHyB structure (D1 and D2 in Fig. 3.3-9). These channels are responsible for the high water capacity of the structure and would very likely lead to fast water diffusion through the SHyB structure.

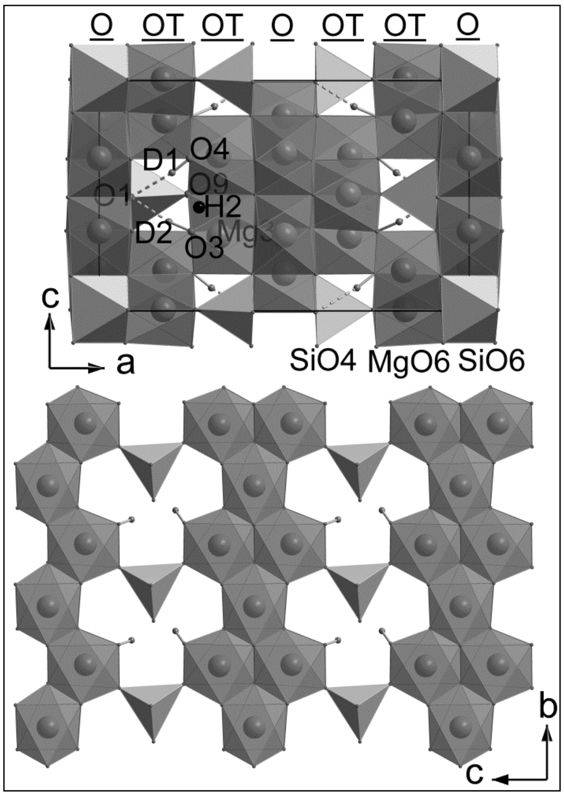

Fig. 3.3-9: Polyhedral representation of the SHyB crystal structure along the *b*-axis and stacking within OT layers with hydrogens along the *a*-axis. The H2 position was spectroscopically assigned from the polarisation direction of the band near 3347 cm^{-1} in single-crystal infrared spectra by using a number of assumptions.

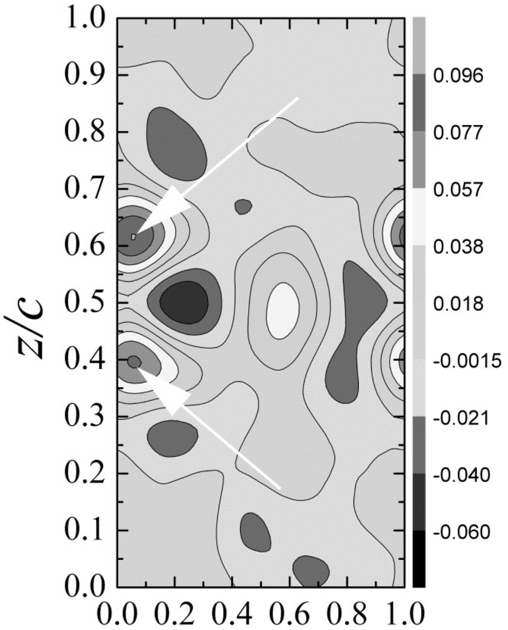

Fig. 3.3-10: Difference nuclear density at a level of $x \approx 0.19$ in *Y-Z* cross-section at 300 K as an example, two pronounced maxima around $y \approx 0.05$, $z \approx 0.6$ and $y \approx 0.05$, $z \approx 0.4$ are clear; the difference nuclear density is measured in fm/Å^3 units.

h. *Topotactic relations between perovskite and post-perovskite in the fluoride analogue system NaNiF$_3$ (D.P. Dobson/London; N. Miyajima; F. Nestola and M. Alvaro/Padova; N. Casati/Villigen; C. Liebske/Zürich; I.G. Wood/London and A.M. Walker/Bristol)*

The post-perovskite (PPv) phase of MgSiO$_3$ has been invoked to explain many of the 'anomalous' features of the D" region of the Earth's mantle just above the core-mantle boundary. In particular, the layer-like structure of PPv gives it strong elastic anisotropy and means that it should deform preferentially on relatively few slip systems allowing crystallographic preferred orientation to develop under strain in the lowermost mantle. Several attempts have been made to interpret the observed seismic anisotropy of D" in terms of simple models of mantle flow under an assumed slip system in PPv; local studies find that the slip plane which best produces seismic anisotropy which is closest to the seismic observations is the (001) plane, consistent with recent experiments in MgSiO$_3$ PPv. However, this slip system cannot explain the observed seismic anisotropy in global studies and in particular the reversal of the vertical transverse isotropy (VTI) texture from horizontal shear-wave polarisations faster in cold regions to vertical polarisations faster in hot regions cannot be explained by a simple flow model and slip on the (001) plane.

We have been investigating the transformation mechanism between perovskite (Pv) and PPv using the analogue system NaNiF$_3$. In this system the transition between Pv and PPv occurs at ~ 16 GPa and PPv is metastably recoverable to ambient conditions allowing its properties to be investigated by a wide range of techniques. Single crystals of NaNiF$_3$ Pv which have been partially transformed to PPv show strong topotactic relations indicative of a martensite-like transformation mechanism (Fig. 3.3-11). If this mechanism also occurs in MgSiO$_3$ and if it is the same for the (retrograde) transformation from PPv to Pv this inherited texture readily explains the observed seismic anisotropy in D" with cold regions comprising PPv deforming by slip on the (001) and hot regions comprising Pv with an inherited texture. We have now grown single crystals of PPv and partially transformed them back to Pv (Fig. 3.3-12) to investigate the mechanism of the retrograde transformation.

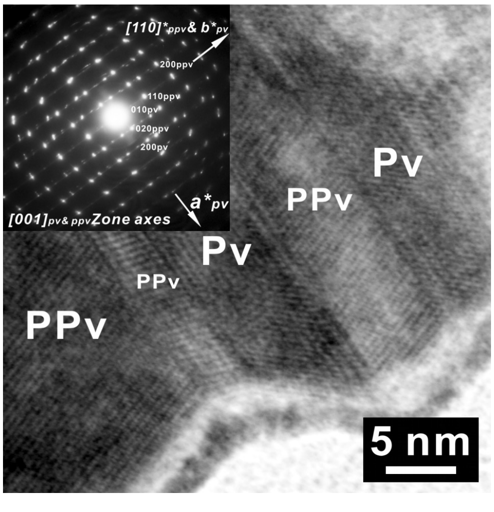

Fig. 3.3-11: High-resolution TEM image of perovskite (Pv) and post-perovskite (PPv) domains in NaNiF$_3$. The inset is a selected area electron diffraction pattern from the interface. The electron diffraction pattern indicates the topotaxy relationships between the two structures.

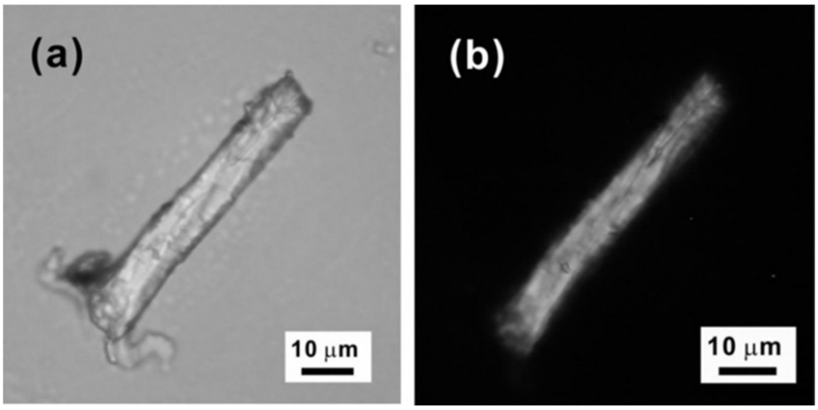

Fig. 3.3-12: Transmitted light optical micrographs of the $NaNiF_3$ PPv single crystal under (a) plane polarised light and (b) crossed polarisers.

i. *Synthesis of single crystals of "skiagite" ($Fe_3Fe_2Si_3O_{12}$) and a high-pressure XANES investigation (L. Ismailova and L.S. Dubrovinsky; N.A. Dubrovinskaia/Bayreuth; A. Bobrov/ Moscow; I. Kantor/Grenoble; V. Cerantola)*

Garnet is one of the dominant phases in mantle mineral assemblages and it is often found as inclusions in natural diamonds. Because of the compositional complexity of natural garnets, the relationships between the composition of mantle garnets and PT-conditions of their formation are still semi-empirical. In this connection, of special importance are investigations of high-pressure components of garnets, namely majorite, knorringite and "skiagite". The latter component is the most poorly studied, so our study is focussed on collecting experimental, thermodynamic, spectroscopic, and structural data for this phase. The results of this study may be applied to the problem of the formation of ultra-deep diamonds, which often contain garnet inclusions with high "skiagite" content. The presence of both di- and trivalent iron in its composition allows us to consider "skiagite" as an important indicator of the oxidation state of iron in the Earth's mantle.

The iron end-member of "skiagite" garnet was synthesised using the 1200-tonne Sumitomo multianvil hydraulic press. A mixture of Fe_2O_3, FeO and SiO_2 was loaded into a Pt capsule isolated from $LaCrO_3$ heaters with MgO tubes and enclosed in a doped magnesium oxide (MgO + 5wt.% Cr_2O_3) octahedron. The experiment was performed at 9.5 GPa using a 18/11 assembly with a heating time of roughly 10 minutes. X-ray single crystal diffraction was performed at the European Synchrotron Radiation Facility (ESRF) in Grenoble, France at beamline ID09a, which confirmed the purity of the sample and showed the presence of single crystals.

Fe K-edge X-ray absorption near-edge structure (XANES) spectra were recorded at beamline ID24 at ESRF for single crystals of "skiagite" garnet at pressures up to 61 GPa at room temperature in a diamond anvil cell. The XANES spectra are shown in Fig. 3.3-13, where differences that occur at the absorption edge with increasing pressure might be due to reduction of Fe^{3+} to Fe^{2+}.

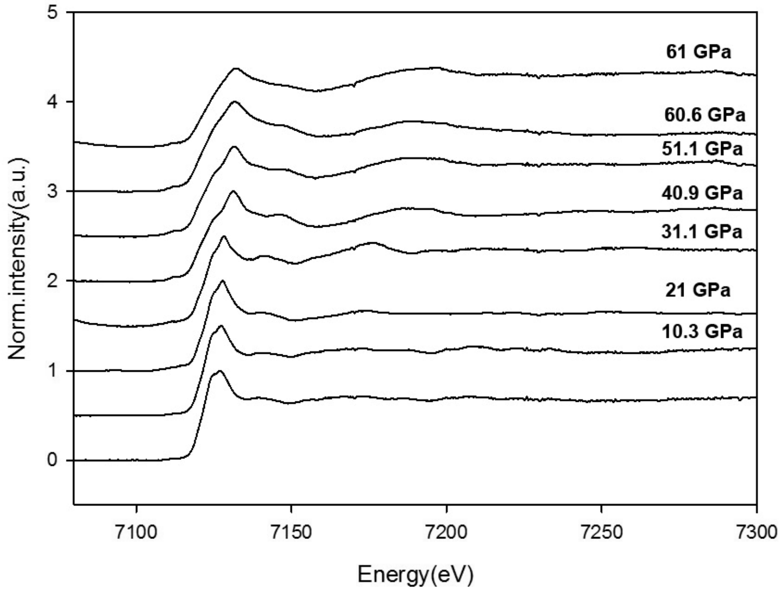

Fig. 3.3-13: Normalised Fe K-edge XANES spectra of single crystal of "*skiagite*" collected at the indicated pressure and room temperature.

j. *Synthesis of large gem-quality crystals of grossular ($Ca_3Al_2Si_3O_{12}$), uvarovite ($Ca_3Cr_2Si_3O_{12}$) and their solid solutions (S. Milani and F. Nestola/Padova; M.G. Pamato, L. Ziberna and T. Boffa Ballaran)*

Some of the diamonds formed in the sub-cratonic lithospheric mantle contain mineral, fluid and melt inclusions which have been trapped during diamond formation. These inclusions provide a direct window to parts of the Earth's upper mantle which are otherwise inaccessible to direct observation. Study of these inclusions in diamonds, therefore, is important for better constraining the chemical and physical conditions which determine the processes of the diamond formation. Garnets are one of the most abundant mineral inclusions found in diamonds, and they have a complex chemical composition being mainly solid solutions of pyrope ($Mg_3Al_2Si_3O_{12}$), almandine ($Fe_3Al_2Si_3O_{12}$), grossular ($Ca_3Al_2Si_3O_{12}$), and uvarovite ($Ca_3Cr_2Si_3O_{12}$).

The pressure and temperature at which the diamond-inclusion pairs grew have been calculated by applying classical geothermobarometric methods based on the chemical exchange between minerals. However, these geothermobarometers can be applied only when the appropriate set of mineral assemblages is present in the same inclusion. Recently, a method based on the pressure exerted by the diamond on the mineral inclusions and on the stresses in the surrounding diamond has been applied to obtain the pressure of the diamond source for olivine inclusions. The method can be applied to any single mineral inclusion; however, it requires accurate knowledge of the thermoelastic parameters (bulk modulus, thermal expansion, shear modulus, temperature derivative of the bulk modulus) for both diamond and inclusion. The aim of this study is to provide precise and accurate bulk moduli for garnets with complex composition, since in the literature only data for the endmembers can be found.

The first step of this project requires synthesis of grossular-uvarovite garnet single crystals which are those that appear least frequently in the literature. The use of single crystals is particularly important because it provides better constraints on the bulk modulus derivatives for such compositions. Preliminary syntheses of grossular, uvarovite, Gr_{50}-Uv_{50}, and Gr_{25}-Uv_{75} were performed in multianvil experiments. In order to optimise the environmental conditions for crystal growth (at least 70 µm in length), several experiments were carried out. Water was used as a flux. It was mostly introduced using $Al(OH)_3$ powder, but in some experiments where this was not possible, molecular water was used. We successfully obtained single crystals in our first experiments, and sample characterisation as well as further high-pressure syntheses is underway.

k. *High-pressure behaviour of cristobalite under quasi-hydrostatic conditions (A. Cernok, E. Bykova and L.S. Dubrovinsky)*

Silica exhibits a rich polymorphism with more than 30 known stable or metastable phases, most of which occur at ambient to moderate pressures (< 9 GPa). Some of these phases, such as quartz, cristobalite or coesite, consist of frameworks of SiO_4 tetrahedra and are abundant in nature. Cristobalite crystallises in its cubic form, known as β-cristobalite, above 1470 °C and at atmospheric pressure. The tetragonal α-phase is a metastable polymorph of SiO_2 which appears upon cooling of cubic β-cristobalite to ambient temperature and it can be found in natural acidic volcanic rocks.

It is generally accepted that tetragonal α-cristobalite transforms to monoclinic cristobalite II at ~ 1.5 GPa and the structure of this transition and the higher-pressure polymorph is well studied, most recently reported in the literature in a study using single crystal X-ray diffraction. Above ~ 10 GPa cristobalite II is found to transforms to cristobalite X-I. Apart from the recent determination of the unit cell parameters, the structure of the cristobalite X-I still remains unknown. Further compression of cristobalite X-I above pressures exceeding ~ 35 GPa leads to formation of cristobalite X-II, and this polymorph was reported to have the structure of α-PbO_2, which is considered to be the structure of the silica under lower mantle conditions (SiO_2 polymorph with the mineral name *seifertite*). Motivated by these recent studies, our aim is to understand how the structure of this "bridging phase", cristobalite X-I, evolves under pressure and how it transforms to the α-PbO_2 phase.

We performed high-pressure DAC experiments using *Böhler-Almax* diamond anvil cells with 250 µm diamond culet size and neon as the pressure-transmitting medium. The cristobalite single crystal was ~ 20-30 µm long and ~ 15 µm thick, and it was placed along with a ruby chip inside a pressure chamber of 125 µm diameter and ~ 40 µm thickness drilled in a pre-indented Re gasket. X-ray diffraction of the starting material revealed a tetragonal unit cell of α-cristobalite, in good agreement with literature data (a = 4.970(4) Å, c = 6.909(12) Å, V = 171.0(8) Å^3). *In situ* Raman spectra were collected up to 62 GPa in steps of 3-5 GPa (Fig. 3.3-

14a). There have been only two other high-pressure Raman spectroscopy studies on cristobalite reported in the literature. One was performed up to 22 GPa in quasi-hydrostatic conditions and focused on cristobalite I-II transition, while the other was carried out up to 61 GPa in non-hydrostatic conditions. The spectra we obtained are in good agreement with the quasi-hydrostatic conditions experiment in their studied pressure range as well as with the non-hydrostatic conditions experiment up to approximately 20 GPa. Above this pressure we observe a subtle change in our spectra, which could indicate the formation of a stishovite-like phase (Si in octahedral position) above 20 GPa as suggested previously in the literature. Such changes may be obscured in the non-hydrostatic experiment reported in the literature where they are suppressed by changes near 35 GPa, attributed to the formation of cristobalite X-II, which was found to be quenchable in these previous experiments. We observe that phase X-I persists in the entire investigated pressure range and that it is not quenchable – upon decompression it transforms to a phase that has a Raman spectrum that is similar to that of the starting α-cristobalite (Fig. 3.3-14b).

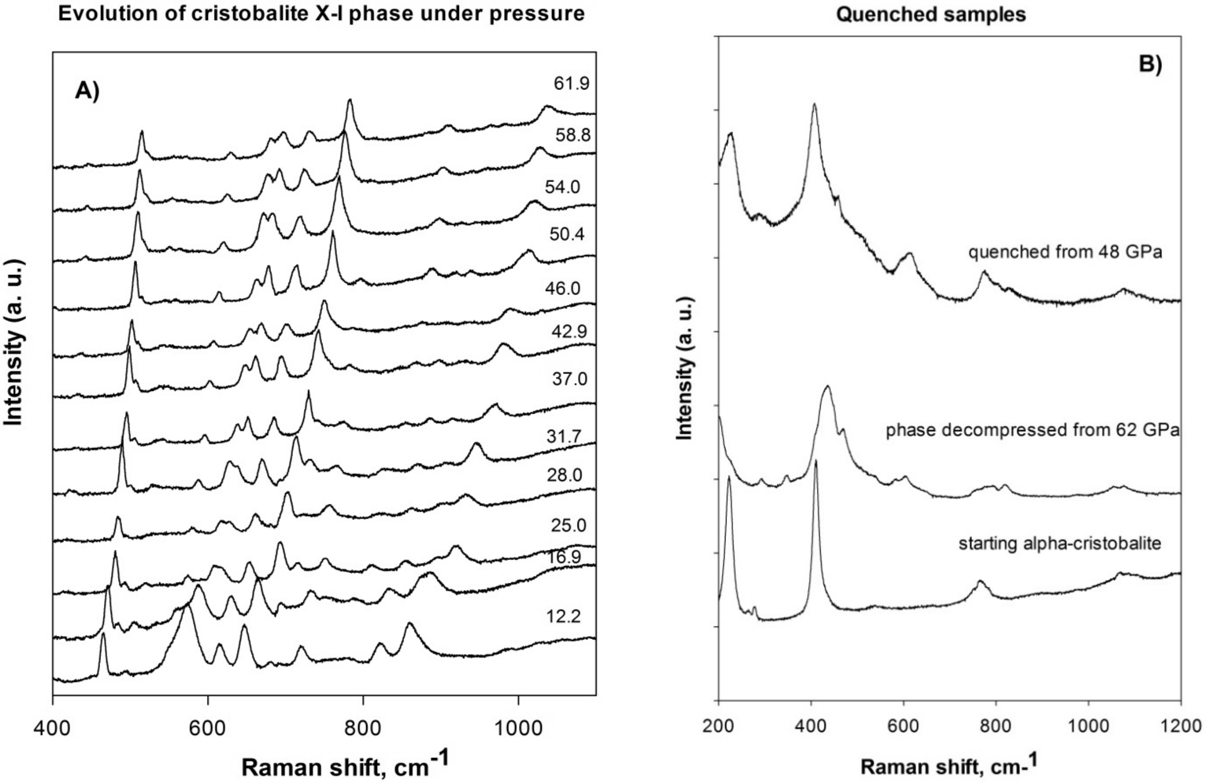

Fig. 3.3-14: (**a**) Raman spectra collected up to ~ 61 GPa during compression, showing evolution of the cristobalite X-I phase. (**b**) Raman spectra of the samples quenched from the indicated pressures compared to the spectrum of the original α-cristobalite.

We collected high-pressure single crystal data at beamline ID09A at ESRF, Grenoble, up to 10 GPa, and at Extreme Conditions Beamline P02.2 at Petra III, Hamburg, to near 70 GPa. We confirmed the phase transition to cristobalite II and above 10 GPa to phase X-I. Indexing of the diffraction patterns from phase X-I collected at 17 GPa yields a primitive monoclinic unit cell with $a = 6.5899(9)$ Å, $b = 4.0493(6)$ Å, $c = 6.841(8)$ Å, $\beta = 98.15(3)°$ and most likely with space group $P2_1/c$ or $P2_1/n$, which is similar to the cell parameters reported previously in the literature. The analysis of single-crystal X-ray diffraction data from experiments at higher pressures is currently underway.

l. *The stability field and microstructures in high-pressure iron oxide, Fe_4O_5 (D.O. Ojwang', R. Myhill, L. Ziberna, N. Miyajima, D.J. Frost and T. Boffa Ballaran)*

The discovery of Fe_4O_5, a mixed-valence iron oxide phase that can be synthesised at high pressure and temperature, suggests that the current iron-oxygen phase diagram is more complicated than originally proposed and requires revision. In order to understand phase relations in the Fe-O system, it is imperative to understand the behaviour of natural iron-bearing minerals such as Fe_3O_4, Fe_2O_3, FeO and Fe_4O_5 at high pressures and temperatures. The aim of this study is to constrain the stability field of Fe_4O_5 at the P-T conditions corresponding to those of the Earth's upper mantle.

Experiments have been performed in the pressure range between 5 and 22 GPa and temperatures between 1000 and 1400 °C using the multianvil apparatus employing both Re and Mo capsules to vary the oxygen fugacity conditions. Phase identification and characterisation of the recovered run products were performed using X-ray powder diffraction and scanning electron microscopy with electron backscatter diffraction. Transmission electron microscopy (TEM) was used to elucidate the microstructure and twinning of Fe_4O_5.

We calculated the stability of the Fe_4O_5 phase from thermodynamic data for comparison with our experimental results. Thermodynamic data for wüstite (wüs), magnetite (mt), hematite (hem), and Re and ReO_2 were taken from the literature. For Fe_4O_5, the thermal equation of state was determined from literature data, while the heat capacity was approximated as the molar sum of the values for magnetite and wüstite. The standard enthalpy and entropy of formation were then fit to the experimentally-determined position of the reaction 2mt = Fe_4O_5 + hem reported in the literature. The resulting position of the Fe_4O_5 = wüs + mt reaction is in excellent agreement with the experimental data (Fig. 3.3-15).

A peculiar feature of the recovered samples is the presence of magnetite, particularly for syntheses runs at conditions where only Fe_4O_5 should be present. A TEM study of several Fe_4O_5 crystals revealed that Fe_3O_4 and Fe_4O_5 are intergrowth lamellae that share certain crystallographic orientations according to a topotactic relationship (Fig. 3.3-16), suggesting that Fe_4O_5 undergoes a retrograde reaction to magnetite during quenching, decompression or sample preparation. The results from this study emphasise the importance of taking Fe_4O_5-type phases into account when assessing the thermodynamics, oxygen fugacity and phase relations in the Earth's mantle.

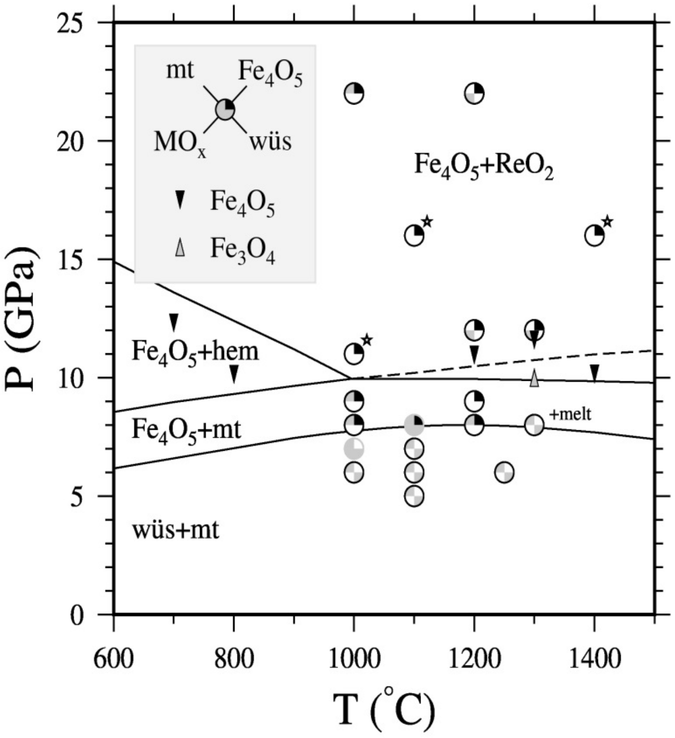

Fig. 3.3-15: Experimental data and calculated phase assemblages for a starting composition slightly more oxidised than Fe_4O_5 in equilibrium with a rhenium capsule. Abbreviations: wüs = wüstite $Fe_{1-y}O$; mt = magnetite; hem = hematite; MO_x = metal oxide (where M is the capsule material). Symbols outlined in black are experiments conducted with rhenium capsules; those outlined in grey are experiments conducted with molybdenum capsules (more reducing), which accounts for the presence of wüstite above 6 GPa. The tips of the arrows show the pressure-corrected data for the reaction 2mt = Fe_4O_5 + hem, with the fitted reaction drawn as a mixed solid and dotted line.

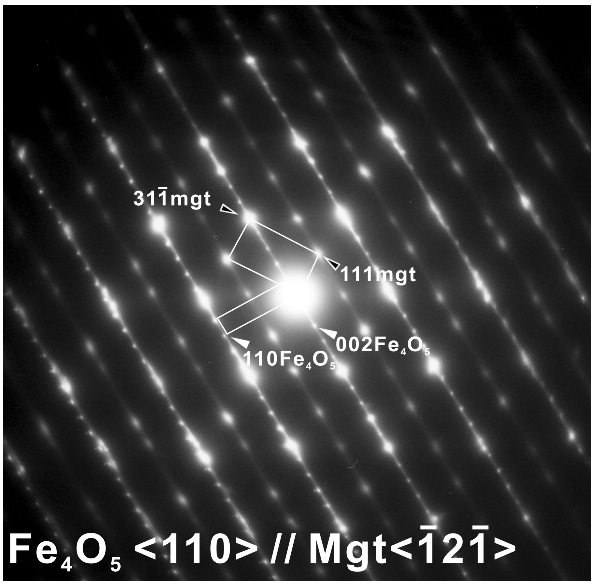

Fig. 3.3-16: Selected area electron diffraction pattern taken across a twin lamellae intergrowth of Fe_3O_4 magnetite in a crystal of Fe_4O_5, obtained along the <110> and <-12-1> zone axes of Fe_4O_5 and Fe_3O_4 domains, respectively. A topotactic relationship between Fe_3O_4 and Fe_4O_5 is clearly visible.

m. *Novel high-pressure monoclinic Fe_2O_3 polymorph (E. Bykova; M. Bykov and N.A. Dubrovinskaia/Bayreuth; L.S. Dubrovinsky; V.B. Prakapenka/Argonne, Z. Konôpková and H.-P. Liermann/Hamburg)*

The high-pressure behaviour of iron sesquioxide, Fe_2O_3, has long been a subject of research due to its importance for understanding the Earth's interior. Moreover the compound is interesting from a physics viewpoint since it undergoes diverse transformations at pressures from 40 to 60 GPa: structural transformation to an orthorhombic phase with large volume discontinuity (~ 10 %); drop in resistivity; spin crossover of Fe^{3+}; and disappearance of the ordered magnetic state. The ability of the enigmatic crystal structure of the "orthorhombic phase" to shed light on the physics of the observed pressure-induced phenomena has been controversial for a long time. Perovskite and Rh_2O_3-II structural types have been proposed as candidates for the high-pressure structure, and both were based on Mössbauer data supplemented with powder X-ray diffraction (XRD).

A reconstructive phase transition was reported to occur during laser heating of Fe_2O_3 compressed at or above 70 GPa. The powder diffraction pattern was indexed with the $CaIrO_3$ type structure; however no crystallographic data were available so far. It is noteworthy that the $CaIrO_3$ structural type is the high-pressure modification of $(Mg,Al)(Si,Fe)O_3$ perovskite, known as a post-perovskite, while the transition perovskite to post-perovskite is responsible for an abrupt increase in density of the D" layer, which is the deepest part of the mantle.

The uncertainty in the crystal structure of Fe_2O_3 in the 40-60 GPa pressure region and the absence of crystallographic data for the post-perovskite Fe_2O_3 phase motivated a series of high-pressure and high-temperature XRD experiments on single crystals, since powder XRD data have limitations, both in accurate unit cell determination and in structure solution and refinement. High-quality single crystals of Fe_2O_3 were placed inside diamond anvil cells, compressed to 71 GPa, heated with a laser, and then decompressed, while single crystal XRD was measured concurrently.

We report discovery of a novel high-pressure polymorph of Fe_2O_3 by means of *in situ* high-pressure single crystal XRD. The transition occurs under compression of hematite to ~ 54 GPa, resulting in about 10 % volume reduction. The phase crystallises in the monoclinic space group $P2_1/n$ with $a = 4.588(3)$, $b = 4.945(2)$, $c = 6.679(7)$ Å and $\beta = 91.31(9)°$. The crystal structure of monoclinic Fe_2O_3 (m-Fe_2O_3) can be described as the so-called double perovskite (or cryolite-type) structure with the general formula $A_2B'B''O_6$. Figure 3.3-17 illustrates the relation between the m-Fe_2O_3 and orthorhombic $GdFeO_3$-type (space group *Pbnm*) perovskite structures. Both consist of a 3-dimensional network of tilted corner-shared BO_6 octahedra (B site in orthorhombic perovskite and crystallographically non-equivalent B' and B'' sites in monoclinic double perovskite) with additional A-atoms located inside bicapped trigonal prismatic voids (A-site). In monoclinic cryolite-type double perovskites B' and B'' atoms have distinctly different atomic radii, either due to an occupation with different atomic species (eg., Ca_2FeMoO_6, Ca_2MnWO_6) or with cations of alternating charges (eg., $Ba_2Bi^{3+}Bi^{5+}O_6$). In the case of Fe_2O_3 all metal sites are occupied by Fe but interatomic distances differ: Fe3-O (A site) distances are considerably larger than Fe1-O and especially Fe2-O (B' and B'' sites) distances, which might be due to change in the electronic (low-spin, LS, and high-spin, HS) state of the iron atoms. Spin crossover (HS to LS transition) of Fe^{3+} in one of structural sites associated with the shift in interatomic distances might be responsible for the monoclinic distortion in the structure of Fe_2O_3. The drastic volume reduction at approximately 54 GPa also supports this assumption.

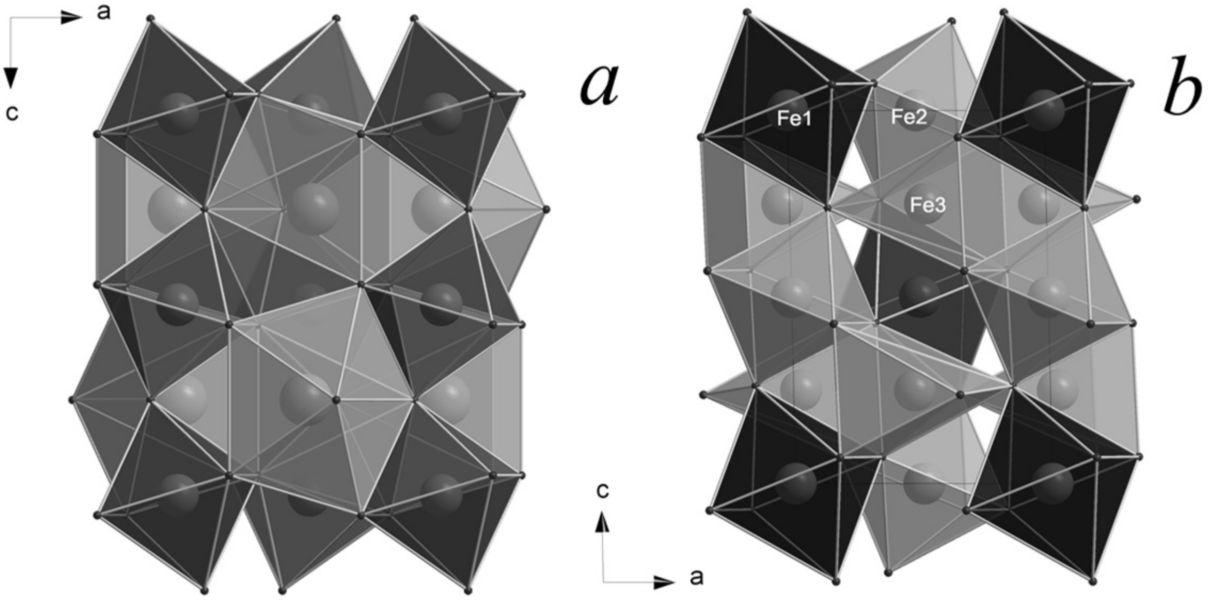

Fig. 3.3-17: Relation between (**a**) orthorhombic $GdFeO_3$-type perovskite and (**b**) double perovskite cryolite-type structures. The perovskite structure contains a 3-dimensional network of corner-shared FeO_6 octahedra (*B*-position) and additional Fe atoms located in bicapped trigonal prismatic voids (*A*-position). In the double perovskite structure the *B*-position is occupied by two alternating atomic species (Fe1 and Fe2 designated as darker and lighter octahedral, respectively).

We observed no phase transition to the orthorhombic Rh_2O_3-II structure upon compression at ambient temperature up to at least 71 GPa. Laser heating to ~ 2100±100 K at pressures above 70 GPa promotes a transition to the *Cmcm* $CaIrO_3$-type phase. Our decompression experiments show that the *Cmcm* phase transforms back to the hematite structure between ~ 25 and 15 GPa.

n. *Nanoscale hematite inclusions in late magmatic xenotime-(Y) from the Variscan hydrothermal vein system in Jáchymov/Czech Republic (J. Plášil/Prague and R. Škoda/Brno; N. Miyajima)*

An interesting occurrence of xenotime-(Y) was documented from hydrothermal veins in Jáchymov (Czech Republic). Based on the paragenetic relationships among the vein minerals, it was concluded that xenotime-(Y) belongs to the oldest minerals within the vein and its origin is probably related to late magmatic or very early hydrothermal activity. The "younger" mineral association comprises both hypogene and supergene minerals of U, Cu, Bi, V and As. Our research is focused on understanding the alteration of U-minerals with regard to the long-term storage of nuclear fuel and the stability of phases which can be used for storing radionuclides in their structures. The current study offers a good example of a "durable" mineral, xenotime-(Y), exposed for a long time to a cyclic hydrothermal system.

According to the powder X-ray diffraction, xenotime-(Y) exhibits crystal sizes ranging from 50 to 150 nm. Electron microprobe analysis (EMPA) shows that the examined xenotime-(Y) had lost the primary U from the structure (only 0.69 wt.% UO_2), probably early in its history. The corresponding CHIME (Chemical Th-U-total Pb Isochron Method) ages, ranging from 270 to 25 MA (with reasonably high errors on the ages) gave a general idea about the cyclic hydrothermal activity (and cyclic U and Pb-loss) which led to the "healing up" of the xenotime structure through geologic time. A peculiar property of the examined xenotime-(Y) is its reddish colour. EPMA shows homogeneous Fe_2O_3 contents (up to 4.30 wt.%). The entire gangue is strongly hematitised, and hematite occurs in several apparently distinct generations. Thus, the presence of hematite inclusions inside aggregates of xenotime-(Y) was expected. Transmission electron microscope (TEM) and high resolution TEM (HRTEM) investigations were undertaken using a TEM operating at 200 kV in order to investigate the nature of the hematite inclusions. According to the TEM observations, hematite forms nano-sized domains and aggregates in xenotime-(Y) (Fig. 3.3-18a). HRTEM investigations on the xenotime documented a well-crystallised form (Fig. 3.3-18b). The origin and the fate of hematite inside xenotime-(Y) continue to be the subject of ongoing research.

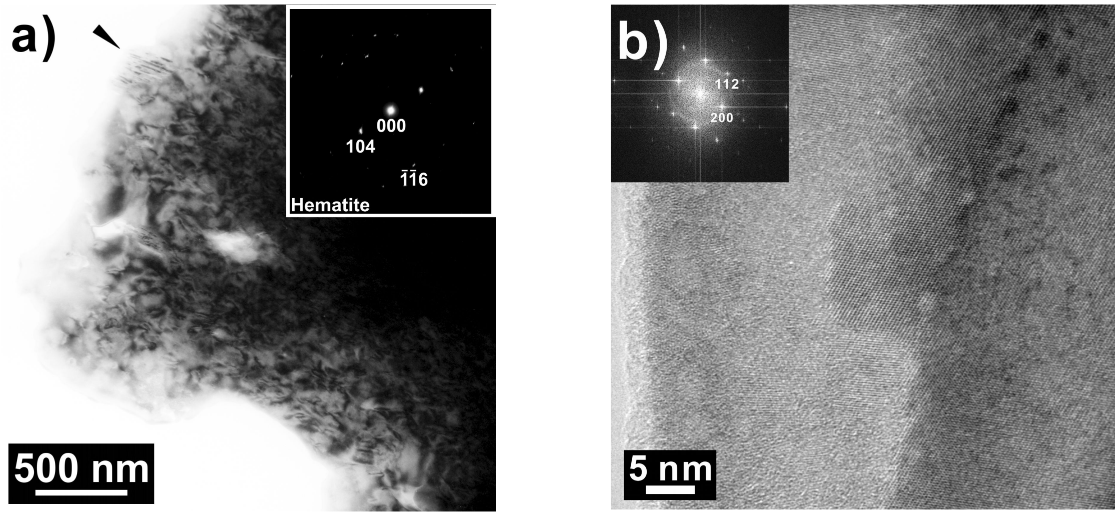

Fig. 3.3-18: (**a**) Bright field TEM micrographs of xenotime-(Y) with hematite nano-aggregates (marked by arrow) identified by selected area electron diffraction (SAED). (**b**) HRTEM image of xenotime-(Y). Insets are the corresponding SAED pattern in (**a**) and the Fourier transform pattern of the image in (**b**).

o. *Chemical stability of magnesite at high pressures and temperatures (N.A. Solopova and L.S. Dubrovinsky; N.A. Dubrovinskaia/Bayreuth; Yu.A. Litvin and A.V. Spivak/ Chernogolovka)*

Studies of inclusions in ultra-deep diamonds suggest that magnesite, $MgCO_3$, can be a major stable carbonate in the lower mantle and play an important role in the deep carbon cycle. A new phase of magnesite, $MgCO_3$-II, was reported at pressures above 120 GPa and high temperatures. However, information about the melting curve of magnesite at high pressures is limited.

We have studied the high-pressure high-temperature behaviour of magnesite, the stability of the melt and its decomposition in static compression experiments between 12 and 84 GPa and temperatures up to 3500 K using the diamond anvil cell (DAC) technique with laser heating. In our experiments samples consisted of a magnesite powder (99.99 % purity) that occupied the entire pressure chamber. Several black spheres of boron-doped diamond (BDD) of about 15-20 µm in diameter were placed into the central part of the sample (Fig. 3.3-19) and used as heat absorbers upon laser heating and as sensors for monitoring the melting process (see below). Samples were first pressurised to the desired pressure at ambient temperature and then heated using a double-sided portable laser heating system. The spectroradiometric technique was used for temperature measurements. The optical response of the system was calibrated using the melting of platinum and tungsten. Pressure in the cell was determined from the shift of the position of the diamond Raman band in spectra taken from the centre of the diamond anvil. After laser heating the samples were analysed *in situ* at high pressures using Raman spectroscopy. The LabRam system (Horiba Scientific Inc.) with a He-Ne-laser (excitation wavelength 632.8 nm, spectral resolution 2 cm^{-1}) and Dilor XY Raman spectrometer with an Ar^{+} ion laser (514.5 nm, Coherent Innova 300, spectral resolution 1 cm^{-1}) were used.

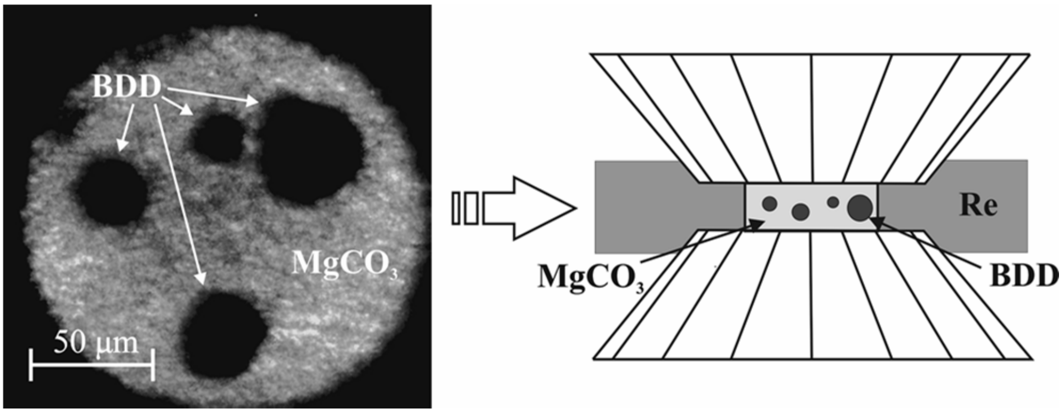

Fig. 3.3-19: Optical micrograph (left) and schematic diagram (right) of the pressure chamber of a DAC containing magnesite powder and four spheres of boron-doped diamond (BDD). The image was taken at a pressure of 38 GPa.

We developed a special method for detection of the melting event during the heating of magnesite as follows. BDD spheres surrounded by solid magnesite are fixed in the pressure chamber so that they do not move. Upon laser irradiation they absorb heat which is transferred to the surrounding magnesite. BDD has a high melting point and sustains very high temperatures, so that at a certain point magnesite starts melting. In the forming liquid the sphere becomes mobile and moves out of the laser beam (the size of the laser spot and the BDD sphere are comparable). This results in an abrupt drop of temperature. In order to avoid significant temperature gradients within the absorber that can lead to mechanical breakage, the BDD spheres were heated from both sides while still maintaining a temperature gradient. One side of the sphere was kept roughly 300 K colder than the other side in order to generate thermal stress in the heated area to facilitate movement of the sphere when the surrounding magnesite melted. We report melting temperatures (T_m) at a given pressure as those measured from the colder side to avoid overestimating T_m.

Figure 3.3-20 shows two cycles of laser heating of a BDD sphere (light absorber). After the first cycle the position of the laser spot was adjusted and the same sphere was heated again. A sudden decrease of temperature was observed in both cycles (points 1 and 2 in Fig. 3.3-20), and the highest temperature points (2200±150) K) correspond to melting of magnesite at 38±1 GPa (pressure was measured at ambient temperature after heating). Inspection of the temperature-quenched sample using Raman spectroscopy showed that magnesite did not change upon high-temperature treatment (Fig. 3.3-21, line 1), thus confirming that the process that we observed was melting. The same procedure was applied in a series of experiments at pressures between 12 GPa and 84 GPa and temperatures up to about 2750 K.

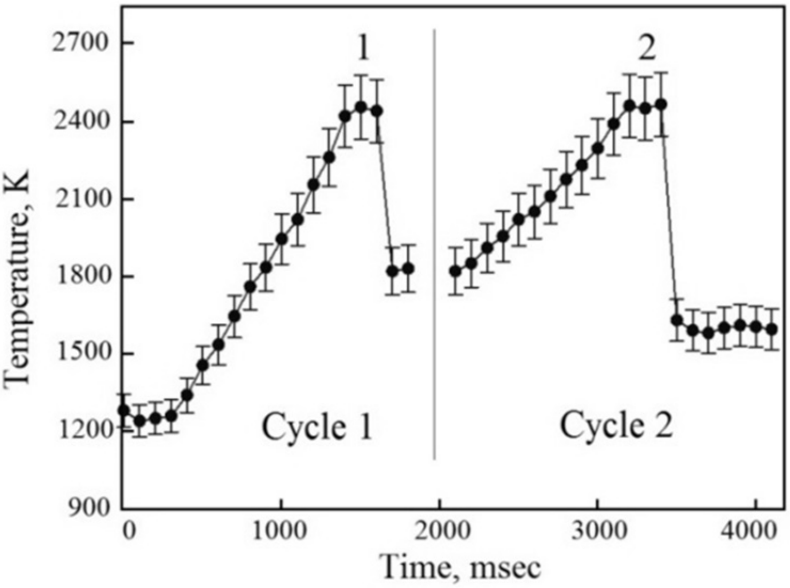

Fig. 3.3-20: Temperature-time paths during two different laser heating cycles of magnesite at 38 GPa.

In Raman spectra of the material quenched after heating above 2800±100 K at 38±1 GPa, we observed characteristic features of MgO fluorescence (Fig. 3.3-21, line 2). Magnesium oxide occurs as a result of carbonate decomposition by the reaction $MgCO_3 = MgO + CO_2$. It may happen that CO_2 decomposes into a carbon phase and oxygen, but the high fluorescence of MgO prevents the detection of possible carbon phases.

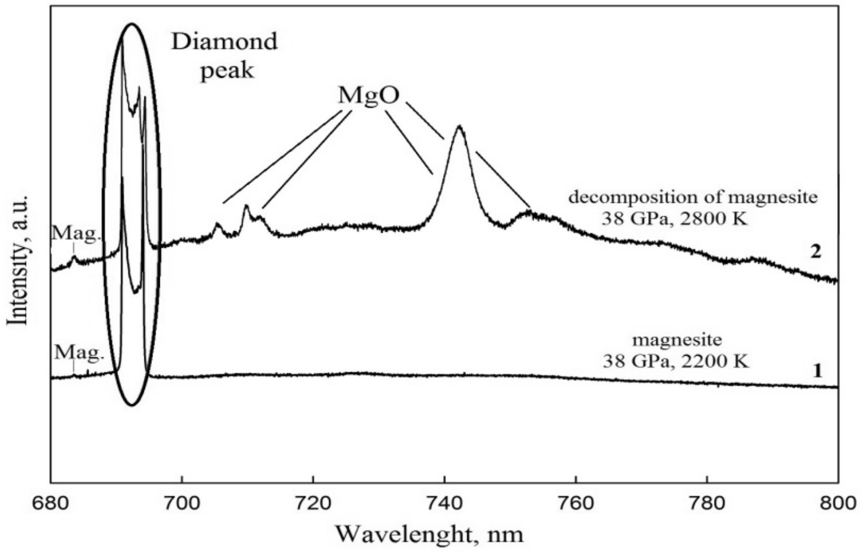

Fig. 3.3-21: Raman spectra of magnesite at 38 GPa treated at different temperatures.

p. *Fe-bearing carbonates in the Earth's lower mantle (V. Cerantola, L.S. Dubrovinsky and C.A. McCammon)*

In the past decades studies of the destiny of carbon (C) inside the deep Earth have raised many questions: Which phases are potential hosts for carbon down to the Earth's deep mantle? How is C exchanged between different phases? How do pressure, temperature and oxygen fugacity influence the stability of C-bearing phases? Carbon is transported to the Earth's interior by means of subduction primarily in the form of carbonates. The main carbonate end-members are calcite ($CaCO_3$), magnesite ($MgCO_3$) and siderite ($FeCO_3$). These three components and their binary and ternary solid solutions have been widely studied at $P < 3.5$ GPa and $T < 1100$ °C (corresponding to the shallow upper mantle). Only after seismological studies showed the presence of stagnant subducted slabs in the lower mantle and carbonates were discovered in diamonds originating from depths below the transition zone has attention been focused on the fate of carbonates at ultrahigh pressures and temperatures. The two endmembers, calcite and magnesite, have been intensively investigated, the latter being stable at pressures and temperatures up to the core-mantle boundary (CMB) without decomposition. However, only limited information is available for siderite and $MgCO_3$-$FeCO_3$ solid solutions. The presence of iron could be an important factor in the stabilisation of these phases due to spin crossover involving its *3d* electrons, which reduces the unit cell volume and thereby enhances stability. Fe-bearing carbonates could potentially be fundamental C-host phases down to the CMB; however further studies are required to answer this question.

We performed experiments using synthetic $FeCO_3$ and $Mg_{0.74}Fe_{0.26}CO_3$ single crystals at pressure and temperature conditions up to 65 GPa and 2500 K, respectively. High pressure (HP) and high temperature (HT) were achieved by means of diamond anvil cells (DACs) combined with double-sided laser heating or an external resistive heating system. Neon and KCl were employed as pressure media, where the latter was used only in HPHT experiments to better insulate the samples from the anvils during laser heating.

High-pressure experimental runs at ambient temperature on $FeCO_3$ and $Mg_{0.74}Fe_{0.26}CO_3$ using Synchrotron Mössbauer Source (SMS) spectroscopy at ESRF and in house Raman spectroscopy at BGI confirmed that iron spin crossover takes place in single crystals between 41-45 and 45-48 GPa for SMS and Raman observations, respectively (Fig. 3.3-22). The quadrupole doublet of Fe^{2+} (octahedral coordination) in the Mössbauer spectra becomes a singlet after the spin transition. HPHT Raman experiments indicate that spin crossover shifts to higher pressures at $T > 650$ K. Moreover, HPHT SMS data show a transformation of $Mg_{0.74}Fe_{0.26}CO_3$ at 58 GPa and 2100 K to a new phase that is quenchable and contains at least 20 % of Fe^{3+} in the structure (Fig. 3.3-23). X-Ray Absorption Near Edge Structure (XANES) spectra confirm the transformation of $FeCO_3$ and $Mg_{0.74}Fe_{0.26}CO_3$ to one or more new C-rich phases at $P > 35$ GPa and $T \sim 2000$ K. Single crystal X-Ray diffraction patterns collected on the same samples after temperature quench support these observations. In summary we have demonstrated that the transition pressure of iron spin crossover in Fe-bearing carbonates is composition dependent, and it is strongly influenced by HT which stabilises the high spin state at higher P. New C-rich phases were also obtained at HPHT as observed by XANES and SMS spectroscopy, where the latter data show an abundance of Fe^{3+} in the crystal structure. Further studies are required to better constrain the stability of carbonates in the lower mantle.

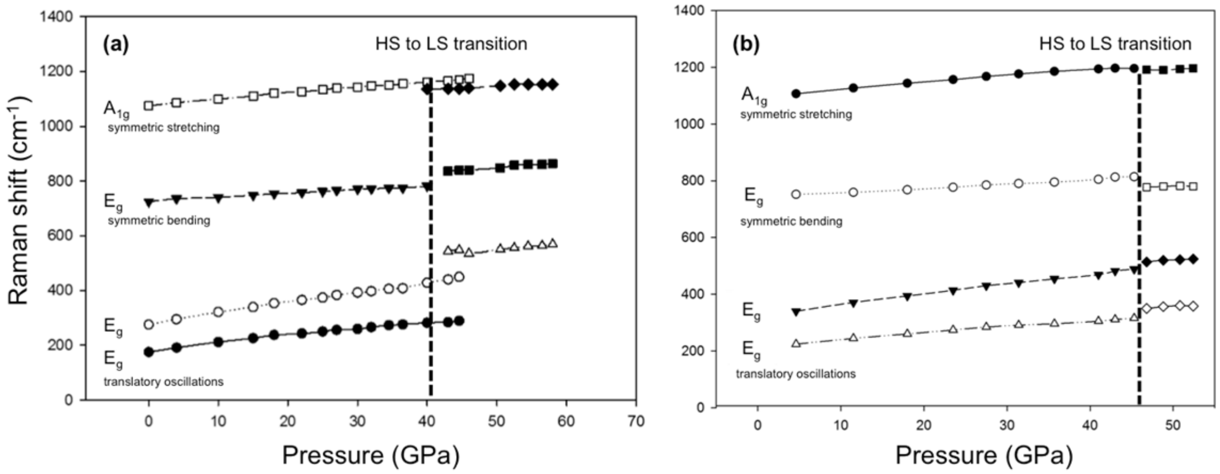

Fig. 3.3-22: (**a**) $FeCO_3$ and (**b**) $Mg_{0.74}Fe_{0.26}CO_3$ Raman active modes plotted versus pressure. The spin crossover point is recognised as a change in the Raman shift to lower frequency. The dashed lines specify the pressures at which the transition takes place.

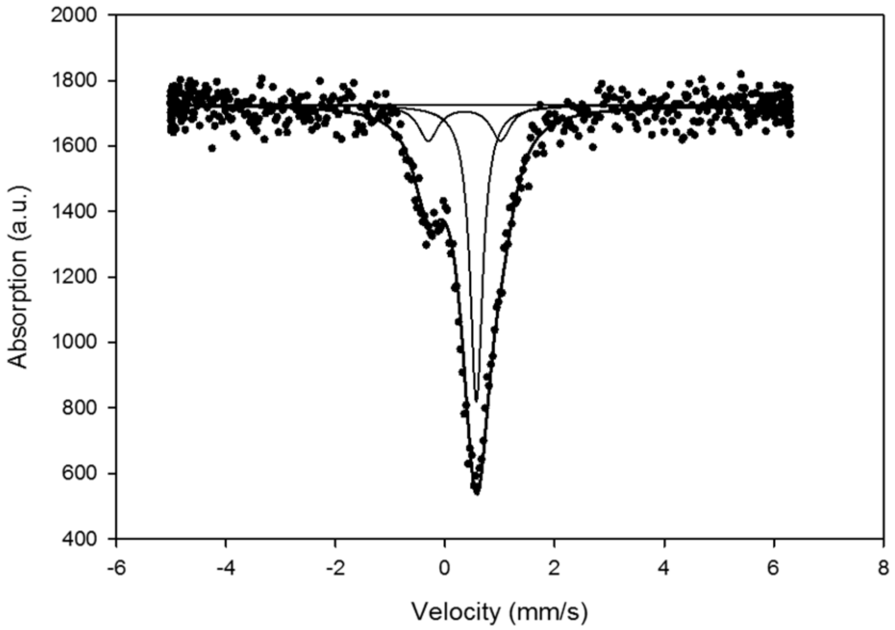

Fig. 3.3-23: $Mg_{0.74}Fe_{0.26}CO_3$ SMS spectrum (solid circles) collected after heating at 2500 K and 58 GPa. The spectrum is fit with a singlet corresponding to low-spin Fe^{2+} and a doublet corresponding to Fe^{3+}.

q. *New electron imaging and diffraction techniques for rock-forming minerals: HR-STEM imaging and precession electron diffraction (N. Miyajima; G. Janssen-Harms/Eindhoven)*

Current developments in scanning transmission electron microscopes (STEMs) allow us to observe the interior of minerals and their interfaces at high resolution down to the sub-nanometer scale. Observation of target materials is the first step and the observed microstructures can inspire new developments in mineral science. We present an overview of scanning transmission electron imaging and precession electron diffraction techniques for rock-forming minerals using the FEG scanning transmission electron microscope (FEI Titan G2 80-200 S/TEM) newly installed in BGI that is operated at 80-200 kV.

The advanced STEM system offers four different images acquired on Bright Field (BF), Dark Field (DF), Annual Bright Field (ABF) and High Angle Annual Dark Field (HAADF) detectors that are situated at different scattering angles on the ray path. Examples of high resolution STEM imaging of misfit dislocations between clinopyroxene and clinoamphibole that clearly indicate the existence of a third phase in the interface are shown in Fig. 3.3-24. The BF image, mainly consisting of coherently scattered electrons at low angle (~ 10 mrad), displays a phase contrast image compatible with conventional high resolution TEM (HRTEM) images. On the other hand, the contrast in the STEM-HAADF image, incoherently scattered electrons at high angle (> 50 mrad), is proportional to the Z-numbers of atoms in the minerals. Spatial resolution can be achieved approximately to 0.16 nm. The scanning electron beam, focused to the sub-nanometer scale, is useful for energy-dispersive X-ray spectroscopy

(EDXS) and electron energy loss spectroscopy (EELS), and provides an ideal chemical probe for both spectroscopies.

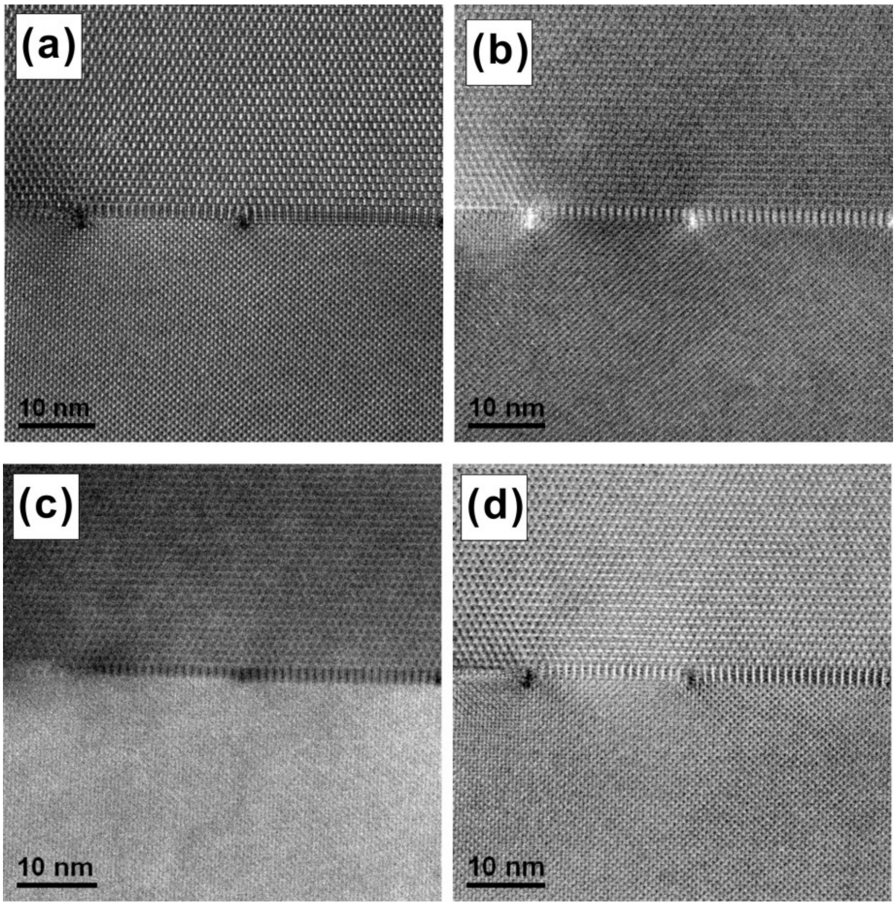

Fig. 3.3-24: High resolution STEM images of misfit dislocations (black dots in image (**a**) between amphibole lamellae (upper) and clinopyroxene (lower), indicating the existence of a third phase in the interface: (**a**) bright field, (**b**) dark field, (**c**) high angle annual dark field, (**d**) annual bright field.

The new STEM is also equipped with a precession electron diffraction (PED) system. PED acquisition can provide more kinematical diffraction intensities than a diffraction pattern recorded on a zone axis with a static beam. In the PED mode, the incident beam is never directed exactly along the target zone axis, so dynamical diffraction effects are reduced. The diffraction technique combined with the post-column energy filter (EFTEM/EELS) system gives an energy-filtered electron diffraction pattern obtained only by elastically scatted electrons. Examples of energy-filtered selected area diffraction patterns of the same clinopyroxene are shown in Fig. 3.3-25. The PED pattern covers a larger range of reciprocal space. Combined with corrections for dynamical interaction, information on site occupancies in minerals can be refined by obtaining kinematical diffraction intensities on the CCD detector.

We are now exploring the integration of both techniques with more conventional TEM data (BF, DF and HRTEM images) to investigate the mechanism of mineral reactions and transformations at the nanometre scale.

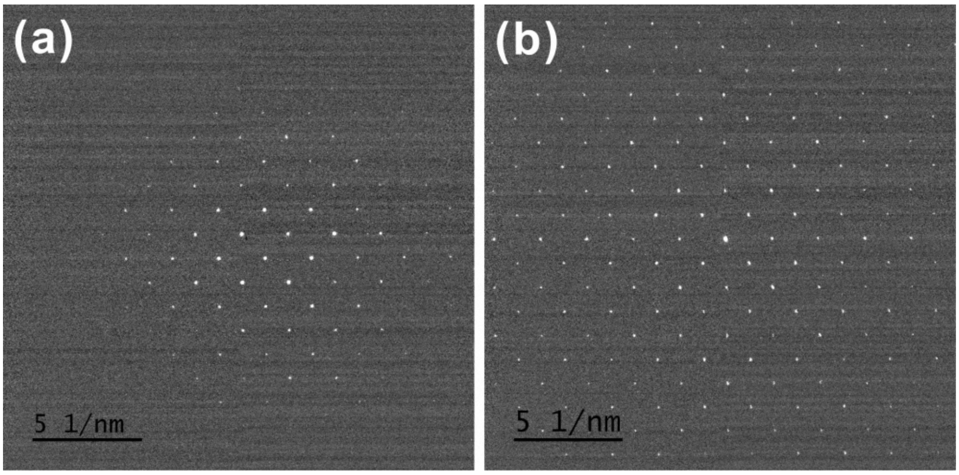

Fig. 3.3-25: Energy-filtered selected area diffraction patterns of the [001] zone axis of clinopyroxene (**a**) without and (**b**) with a precession movement (1 degree).

3.4 Physical Properties of Minerals

The relationship between structure and physical properties of materials is at the center of interest of a variety of scientific disciplines. Accurate data on the physical properties of minerals, in particular, are important because they provide the only way to interpret geophysical and seismological observations. In fact, as the information of the magnitude and location of radial and lateral changes in acoustic wave velocities, electrical conductivity and magnetization within the Earth becomes more and more detailed, knowledge of the elastic, thermal and magnetic behaviour of the possible minerals present in the deep Earth is necessary for explaining these observations in terms of temperature, chemical heterogeneity, mass and heat flow, phase transformations, etc.

Laboratory measurements of compressional and shear wave velocities of mantle minerals play a fundamental role in constraining the seismic models of the Earth's interior. In this context, the use of Brillouin spectroscopy on single-crystals has become the technique of choice at BGI since it allows the determination not only of the full elastic tensor of low-symmetry materials, but also their anisotropic behaviour. In the first three contributions of this section longitudinal and shear wave velocities are reported for single-crystals of majoritic garnets, NAL (aluminium-rich phase) and pure and Fe-bearing $MgSiO_3$ perovskites. These results show how such experiments, although more challenging and time consuming than those performed with powdered samples, give better constraints on the effect of temperature and chemical substitution on the elastic behaviour of minerals.

Electrical conductivity measurements provide an alternative approach for constraining the chemistry and structure of the Earth's interior. The fourth and fifth contributions of this section describe two complementary techniques for studying electrical properties of minerals. A multianvil apparatus has been used to perform electrical conductivity experiments on previously deformed assemblages. These data will be used in conductivity models for explaining the anomalous conductivity contrast in different regions across the asthenosphere. A laser heated diamond anvil cell has been used, instead, for studying the electrical conductivity of an Al,Fe-bearing $MgSiO_3$ perovskite at the pressures and temperatures of the lower mantle.

Minerals are not only important because they are the materials which form the solid Earth and as such determine the dynamic processes occurring in the Earth's interior, but they also can be used as templates for oxide-type materials that are of interest in materials research, as in the case of quartz (SiO_2) which is the most studied form of silica and hibonite ($CaAl_{12}O_{19}$) which is extensively used in the concrete industry. In the second before last contribution of this section the elastic behaviour of quartz at high pressure has been reinvestigated by means of single-crystal Brillouin spectroscopy in order to resolve the controversy among the different studies present in the literature. In the last contribution the oxidation state of Ti substituting in the mineral hibonite has been determined using energy electron loss spectroscopy and UV/Vis absorption spectroscopy.

a. *Single crystal elasticity of majoritic garnet at high pressure and temperature (M.G. Pamato, A. Kurnosov, T. Boffa Ballaran, D.J. Frost, L. Ziberna, M. Giannini and D.M. Trots; S.N. Tkachev, K.K. Zhuravlev and V.B. Prakapenka/Chicago)*

Seismological studies are fundamental for understanding the chemistry and structure of the Earth's interior, providing a method for tracing the chemical anomalies caused by the subduction of oceanic lithosphere. Garnets belonging to the majorite-pyrope system, ($MgSiO_3$ – $Mg_3Al_2Si_3O_{12}$) are stable in subducting slabs throughout the entire transition zone, and as such can influence their physical-chemical properties and their buoyancy. The aim of this study is to determine the elastic properties and density of majoritic garnet at high pressures and temperatures in order to better constrain the seismic models.

We have measured *P-V-T* data and compressional and shear sound velocities, *V*p and *V*s, of two single crystals of majoritic garnet ($Mg_{3.24}Al_{1.53}Si_{3.23}O_{12}$) by means of Brillouin spectroscopy and X ray diffraction. Single-crystals of majoritic garnet were synthesized in a multianvil apparatus at 17 GPa and 1900 °C. The crystals were double side polished up to 10-18 µm in thickness and loaded in piston cylinder diamond anvil cells together with Ne as pressure transmitting medium. A single crystal of Sm:YAG, whose fluorescence has been calibrated against an absolute pressure determination, was used as pressure calibrant. In addition, to better constrain the temperature inside the pressure chamber without relying uniquely on the thermocouple, we have combined the fluorescence shifts of Sm:YAG, which is independent of temperature, with the fluorescence shift of ruby chips which are strongly temperature dependent. The measurements of sound velocities and density were performed at the BMD-13 (GSECARS) at the Advance Photon Source/Chicago. The samples were measured first upon compression up to approximately 21 GPa at room temperature and then heated to 540 K. During heating the pressure increased to 30 GPa, therefore Brillouin spectra and density were measured along an isothermal run (at 540 K) upon decompression.

The variation with pressure of the shear and compressional wave velocities at room temperature and at high temperature (540 K) are reported in Fig. 3.4-1. Preliminary analysis of our recent data show that the shear and compressional wave velocities of our samples are about 2 % larger than those obtained by means of Brillouin spectroscopy for an iron bearing majoritic garnet. To address whether a small amount of Fe substituting into the garnet structure may have such a strong effect on the elastic properties of majoritic garnets, we aim to perform high-pressure Brillouin measurements in combination with X-ray diffraction on iron bearing majoritic garnets. The crystals will be loaded in a diamond anvil cell together with neon. This will provide quasi-hydrostatic conditions also at pressures higher than 14 GPa which is the hydrostatic limit of methanol:ethanol:water mixtures employed in the study previously reported in the literature.

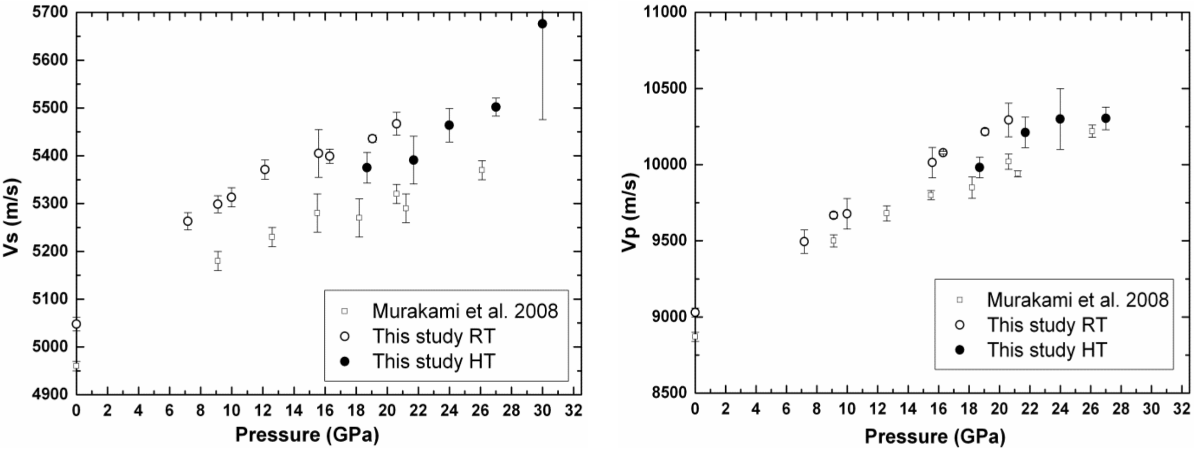

Fig. 3.4-1: Variation of shear (Vs, left) and compressional (Vp, right) wave velocities of $Mg_{3.24}Al_{1.53}Si_{3.23}O_{12}$ as a function of pressure. Open circles: this study, room temperature measurements; filled circles: this study, 540 K; open squares: room temperature data on Fe-bearing majoritic garnet (Murakami M., *et al.* Earth Planet. Sci. Lett. 274, 339-345, 2008).

b. *High-pressure single crystal elasticity of NAL phase (M.G. Pamato, A. Kurnosov, T. Boffa Ballaran, D.M. Trots and D.J. Frost)*

At lower mantle conditions, between 600 and 1300 km, subducting mid-ocean ridge basalt (MORB) can contain more than 20 % of an aluminium-rich phase, which is referred to as NAL (short for new Al-rich) phase. (see Pamato et. al, Yearbook 2012). Evidence for the existence of the NAL phase has been observed in sublithospheric diamonds, where composite multiphase inclusions have been found with similar bulk compositions to NAL. Given that a significant proportion of the lower mantle may be comprised of subducted crust, the NAL phase may be an important contributor to the bulk elastic properties of the lower mantle.

To date several studies have been conducted on the structure, stability and compression of NAL phase both in complex and simplified systems. However, there are still no data on the single crystal elasticity of NAL phase determined experimentally. Besides theoretical calculations, elasticity measurements have been performed only in one study on a polycrystalline sample. These experiments simply provide aggregate properties and, therefore do not give any information on the anisotropy of the sound velocities nor can they constrain the complete elastic tensor of low symmetry materials.

Here we report for the first time an experimental determination of the full elastic tensor of large single-crystals of $Na_{1.07}Mg_{1.58}Al_{4.91}Si_{1.26}O_{12}$ NAL phase (synthesized in a multianvil apparatus at 2260 °C and 20 GPa), by means of Brillouin scattering spectroscopy at room and high pressure up to 20 GPa. Two high quality single crystals of NAL were selected for Brillouin scattering measurements and were polished into parallel plates with a thickness of approximately 15 µm. The crystals were then loaded into two piston cylinder diamond anvil cells for X-ray and Brillouin measurements. Simultaneous acquisition of the density and sound velocities of the NAL crystals was performed at the Bayerisches Geoinstitut (see Kurnosov *et al.*, Yearbook 2010). The elastic constants C_{ij} were extracted by simultaneously fitting 6 dispersion curves (3 solutions for each crystal) to the experimentally measured acoustic velocities $V_{P,S1,S2} = f(C_{ij})$. Aggregate velocities as well as elastic moduli were calculated from the C_{ij}'s using the Voigt-Reuss-Hill averaging scheme and reported as function of pressure in Fig. 3.4-2 and Fig. 3.4-3 respectively.

The experimental values are close to those obtained from theoretical calculations. However, our shear velocities and shear moduli values are larger than those reported in the literature for a polycrystalline NAL phase. This discrepancy is likely due to the highly anisotropic behaviour of the NAL phase which we can clearly observe in our single-crystal study. At pressures corresponding to ~ 1000 km (~ 40 GPa), NAL is expected to transform to the calcium ferrite type aluminium phase (CF). Our next aim is to experimentally determine the elasticity of NAL up to 40 GPa to see whether such discontinuity is likely to be seismically detectable.

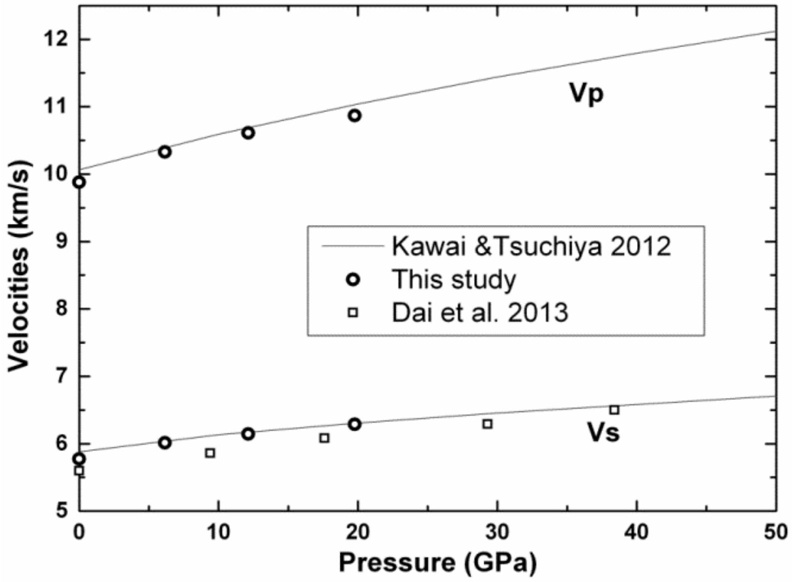

Fig. 3.4-2: Variation of shear (Vs) and compressional (Vp) wave velocities of $Na_{1.07}Mg_{1.58}Al_{4.91}Si_{1.26}O_{12}$ NAL as a function of pressure. Open circles: this study; open squares: experimental results from Dai L. *et al.* (Phys. Chem. Miner. 40, 195-201, 2013). Theoretical calculation results are reported as solid curves (Kawai K. and Tsuchiya T., Am. Mineral. 97, 305-314, 2012).

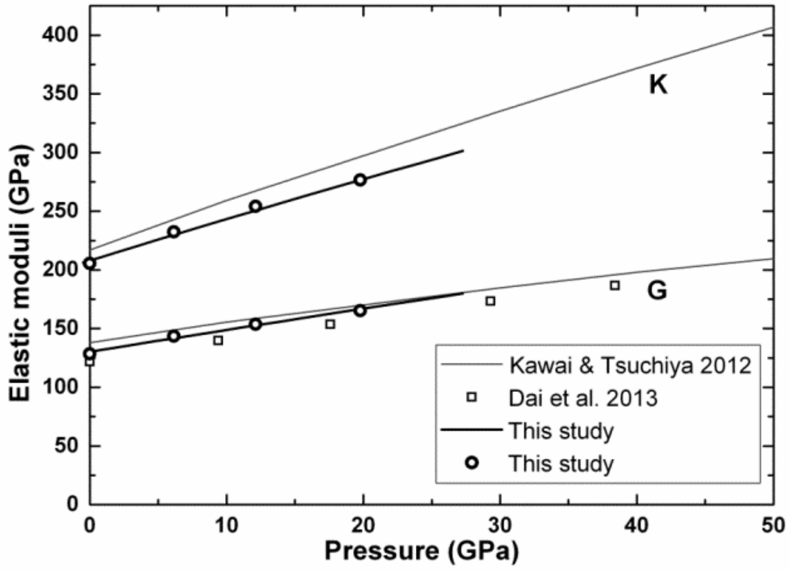

Fig. 3.4-3: Pressure-dependencies of the bulk and shear moduli for the NAL phase investigated in this study are shown as open circles. The dark solid lines are Birch-Murnaghan equation of state fits through the experimental data of this study. The light solid curves are bulk moduli calculated by Kawai K. and Tsuchiya T. (Am. Mineral. 97, 305-314, 2012). Open squares are measurements from Dai L. *et al.* (Phys. Chem. Miner. 40, 195-201, 2013).

c. *Single crystal elasticity and effect of Fe^{2+} on elastic properties of $MgSiO_3$ perovskite (A. Kurnosov, T. Boffa Ballaran, D.M. Trots and D.J. Frost)*

Knowledge of the elastic properties of candidate lower mantle minerals at the conditions of the deep Earth is a crucial issue for interpreting seismological observations and for explaining observed seismic velocity anomalies. Perovskite structured $MgSiO_3$ is widely accepted to be the dominant phase in the Earth's lower mantle, where it coexists with ferropericlase. Chemical substitutions in $MgSiO_3$ perovskite, hence, may be one of the reasons for seismic velocity anomalies observed in the lower mantle.

Here we report compressional and shear sound velocities of $MgSiO_3$ perovskite in comparison with $(Mg,Fe)SiO_3$ perovskite containing 4 mol.% of the $Fe^{2+}SiO_3$ component. Two differently oriented single-crystals of magnesium silicate perovskite containing 4 mol.% of the $Fe^{2+}SiO_3$ component [$(Mg,Fe)SiO_3$] and two single crystals of end-member $MgSiO_3$ perovskite have been studied by means of simultaneous Brillouin spectroscopy and X-ray diffraction *in situ* in diamond anvil cells. Helium was used as pressure transmitting medium and experiments were performed so far in the pressure range from ambient to 16 GPa. The data at each pressure were fitted for the two crystals with identical composition simultaneously in order to reduce correlations among the C_{ij} constants. Using the data from two crystals with different non-specific orientations we were able to obtain all 9 independent C_{ij} elastic constants for orthorhombic symmetry at different pressures.

As pressure scale is a major issue in the investigation of physical properties of mantle minerals we used the simultaneous measurements of density and sound velocities to accurately determine the absolute pressure for all our data. This provides a self-consistent data set to be compared with seismic data for the lower mantle.

The C_{ij} constants obtained at each pressure have been used to calculate the adiabatic bulk modulus (Ks) and shear modulus (G) using the Reuss-Voigt-Hill approximation. Shear and compressional sound velocities (Vs and Vp) were calculated for both samples from Ks, G and the experimentally measured densities (Fig. 3.4-4). The shear wave velocities obtained in this study differ from those obtained from powder data reported in the literature, possible due to the anisotropy of perovskite.

Iron substitution into the perovskite structure has a negligible effect on Vp in agreement with our previous compressibility study (see Boffa Ballaran *et al.* Yearbook 2011), whereas it gives rise to lower shear wave velocities with respect to pure $MgSiO_3$ perovskite (Fig. 3.4-4).

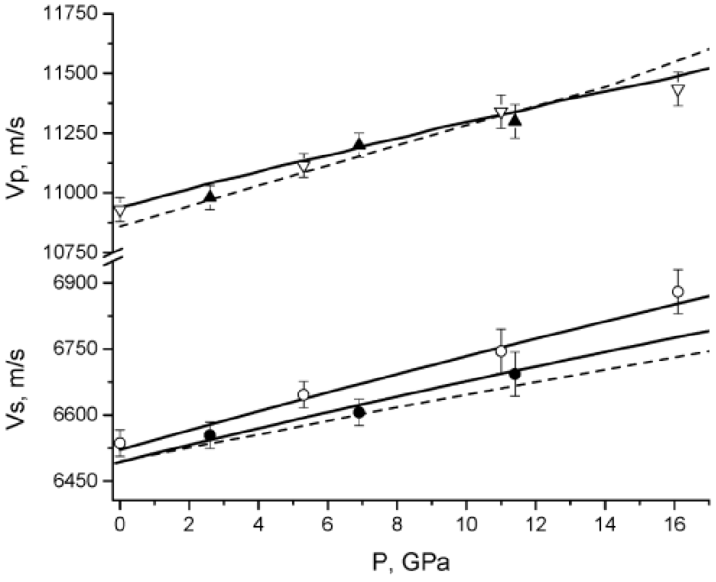

Fig. 3.4-4: Variation of shear (Vs) and compressional (Vp) wave velocities of $MgSiO_3$ and $(Mg,Fe)SiO_3$ as a function of absolute pressure. Open symbols: $MgSiO_3$ perovskite; solid symbols: $(Mg,Fe)SiO_3$ perovskite; solid curves: 3rd order Birch-Murnaghan equation of state fits; dashed curves: data of Murakami *et al.* (EPSL, 256, 47-54, 2007) on polycrystalline perovskite (Vp in this case was not determined experimentally).

d. *Investigation of the electrical properties of deformed mantle materials (A. Pommier/Tempe, D. Kohlstedt/Minneapolis, K. Leinenweber/Tempe and J. Tyburczy/Tempe; T. Katsura)*

The motion of rigid plates that comprise the Earth's lithosphere relative to the underlying convecting mantle is thought to promote the formation of sheared rock zones beneath the lithosphere. Deformation of these rocks has been suggested to explain geophysical anomalies detected in the asthenosphere. Seismically, these anomalies are often correlated to the presence of a seismic low velocity zone (LVZ) characterized by reduced P- and S-wave velocities. Electrically, magneto telluric (MT) surveys have observed anomalous conductivity contrasts in different regions across the asthenosphere. Interpretation of these geophysical features involves the presence of partial melts due to pressure-release melting of upper mantle rocks, sub-solidus variation in the mineral content over that depth interval, and/or presence of nominally anhydrous minerals with high water contents. All of these likely sources of LVZ may result in rheological weakening and require investigation in the laboratory.

The aim of our project is to perform electrical experiments on previously deformed assemblages (under compression and torsion) that are relevant candidates to explain the physical and chemical heterogeneities in the upper mantle. Conductivity models derived from the experimental results will be used as part of the interpretation of magneto telluric data. Reasonable mantle assemblages under asthenospheric conditions include hydrous olivine, olivine-basalt and olivine-carbonate melt.

At Bayerisches Geoinstitut (BGI), preliminary electrical conductivity/impedance spectroscopy measurements were performed on previously deformed (under compression) hydrous olivine at 200-700 °C and 2 GPa in a multianvil apparatus. Measurements were performed in two perpendicular directions, in order to investigate electrical anisotropy (Fig. 3.4-5). Real and imaginary components of the impedance were measured in response to an AC signal in the 10^6Hz - 10^{-2}Hz frequency range using an impedance gain/phase analyzer (Solartron 1260, Schlumberger Co.), with voltage amplitude of 0-1V. The results obtained at BGI are in excellent agreement with those collected at Arizona State University/Tempe using

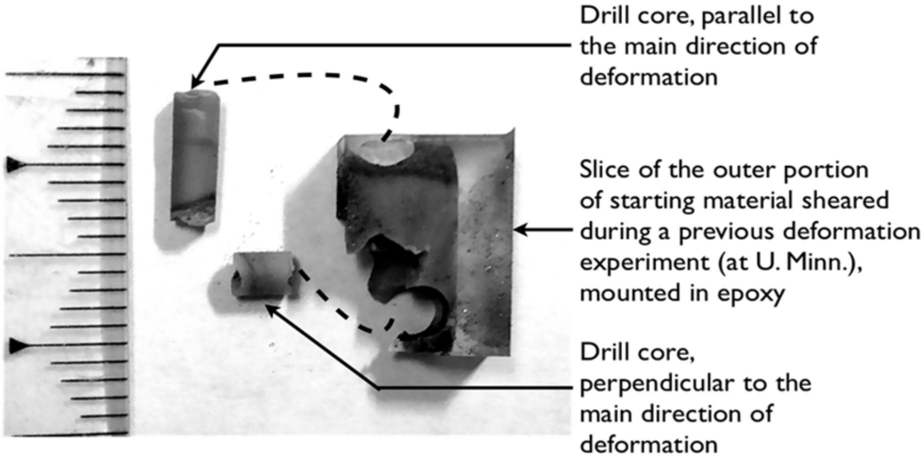

Fig. 3.4-5: Preparation of the starting material used for electrical conductivity experiments. The starting material is previously deformed in a Paterson apparatus (Univ. Minn.). The outer part of the column (corresponding to the part with the highest deformation) is extracted (dashed lines) in order to perform core drilling in different directions. These drill cores are then cut into slices for electrical measurements in the multianvil apparatus.

a different electrical conductivity cell, demonstrating the reproducibility of the electrical measurements and good inter-laboratory agreement in the measurements.

e. *Electrical conductivity of Al, Fe-bearing perovskite under lower mantle conditions (R. Sinmyo and G. Pesce; E. Greenberg/Tel-Aviv; C.A. McCammon and L.S. Dubrovinsky)*

Laboratory measurements of the electrical conductivity of minerals provide important constraints on the chemistry and structure of the Earth's interior. We have measured the electrical conductivity of Al, Fe-bearing perovskite (Pv), the most abundant lower mantle phase, using a laser-heated diamond anvil cell (LHDAC). The sample with composition $Mg_{0.83}Fe_{0.21}Al_{0.06}Si_{0.91}O_3$ ($Fe^{3+}/\Sigma Fe$ ratio ~ 0.4) was synthesized at 26 GPa and 2073 K using a multianvil press. Sample resistance was measured *in situ* at high pressure and high temperature up to 82 GPa and 2000 K. The cell assemblage is shown in Fig. 3.4-6. Results show a continuous increase in electrical conductivity with increasing pressure, in contrast to previous studies of $(Mg,Fe)SiO_3$ perovskite and a pyrolite assemblage where a decrease in conductivity was observed at higher pressure. Our results suggest that (1) the incorporation of aluminium in Pv has a strong effect on its electrical conductivity and its evolution with pressure; (2) spin crossover of Fe^{3+} does not occur or its effect on the conductivity is small in Al, Fe-bearing Pv, and (3) the contribution of ferropericlase to the electrical conductivity of pyrolite may be significant. The electrical conductivity profile of the Earth's lower mantle derived from geomagnetic data can be better explained by a pyrolitic bulk chemical composition rather than a non-pyrolitic model such as one based solely on perovskite (Fig. 3.4-7).

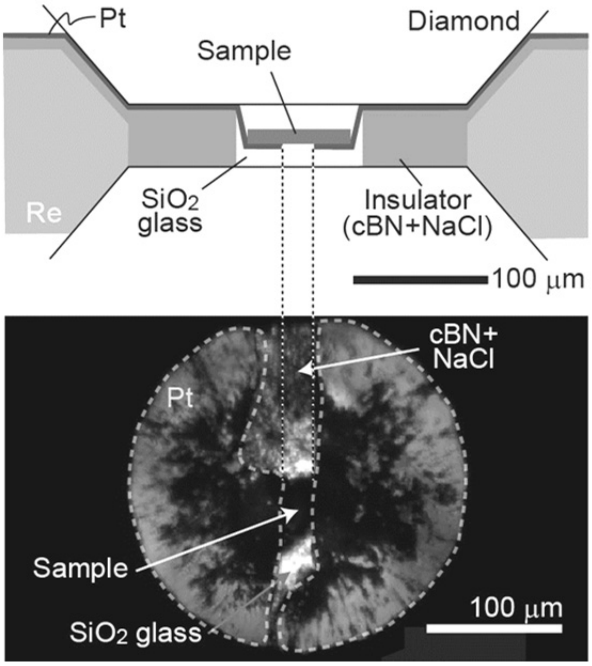

Fig. 3.4-6: Schematic cross section of the diamond anvil cell after compression and optical image of the sample while compressed at 69 GPa.

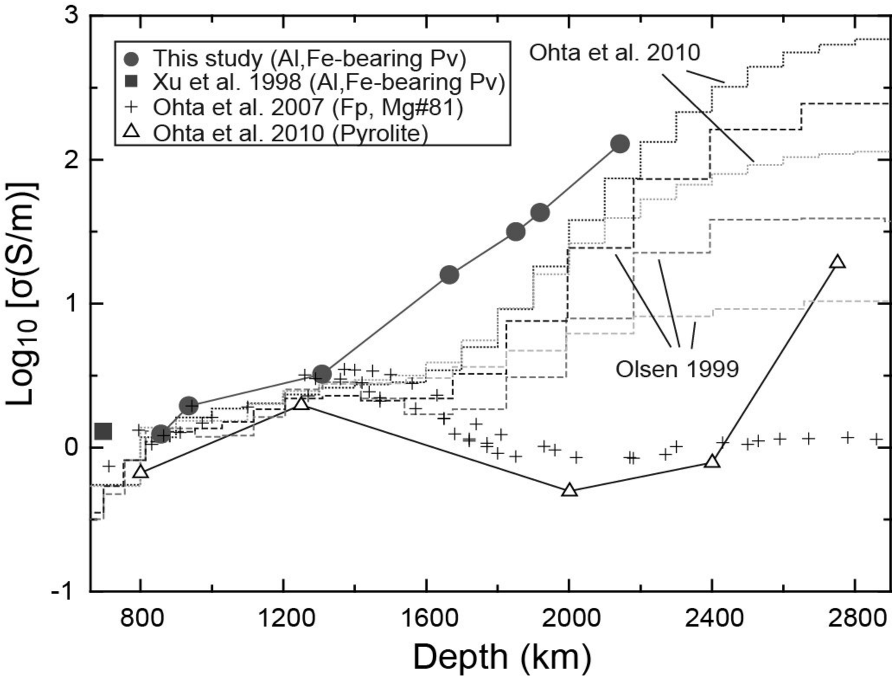

Fig. 3.4-7: Electrical conductivity profile of lower mantle phases along an adiabatic geotherm. Filled circles: Al, Fe-bearing Pv, this study; open triangles: pyrolite material reported in a previous study; crosses: $(Mg_{0.81}Fe_{0.19})O$ Fp from a previous study. Dashed and dotted lines show geomagnetic observations. The geotherm was taken from the literature.

f. *Elastic behaviour of α-quartz at high pressure (D.M. Trots, A. Kurnosov, T. Boffa Ballaran and D.J. Frost)*

For a long time, quartz has attracted the attention of scientists in diverse fields due to its geological and technological importance. However, there are still controversies among the results describing its high-pressure elastic properties measured with different techniques. In particular, quartz elasticity predicted by means of density functional theory (DFT) strongly differs from that determined experimentally by means of Brillouin spectroscopy. Since the elastic parameters extracted from the pressure dependency of the unit-cell parameters of α-quartz (see Trots *et al.*, Yearbook 2010) are in good agreement with those obtained from the DFT calculations, we have decided to measure Brillouin spectra of single crystals of quartz at high pressure in order to elucidate the possible origin of such differences.

Double-side polished single crystals of quartz with dimensions of 60×60×18 μm^3 were loaded into a 4-screw piston cylinder BGI-diamond anvil cells (DAC) suitable for diffraction and spectroscopic measurements using He as pressure transmitting medium. Brillouin measurements have been performed so far at ambient pressure and 11.2 GPa. Sound velocities collected at 11.2 GPa as well as the resulting fit to the Christoffel equations for the trigonal space group $P3_221$ are presented in Fig. 3.4-8.

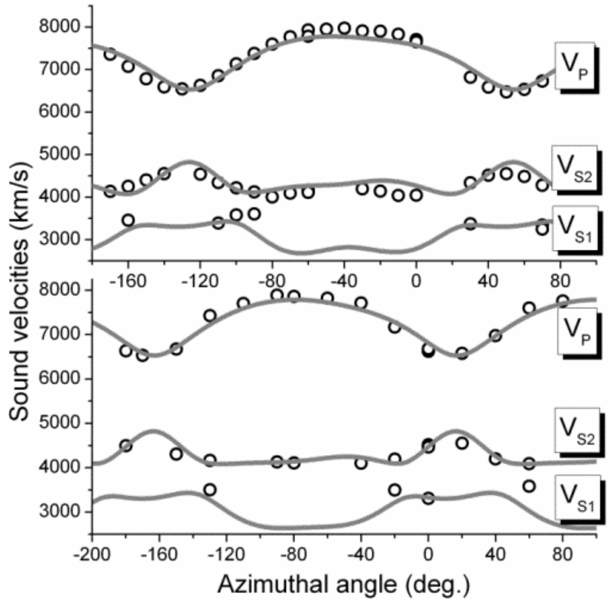

Fig. 3.4-8: Sound velocities of two single-crystal plates of α-quartz at 11.2 GPa reported as a function of crystallographic orientation (open circles). Solid curves through the symbols are the fits obtained by fitting the data for both crystals simultaneously resulting in the following elastic constants: $C_{11} = 138$, $C_{12} = 67$, $C_{13} = 85$, $C_{33} = 153$, $C_{44} = 75$, $C_{14} = -4$ GPa.

The unit-cell parameters collected as a function of pressure have been fitted using a linearized 3rd-order Birch-Murnaghan equation of state to obtain the linear compressibilities of *a* and *c* axes up to 20 GPa (solid curves in Fig. 3.4-9). Independent values of the linear bulk moduli have been obtained from the elastic constant of quartz predicted by means of DFT calculation and obtained from previous Brillouin measurements (Fig. 3.4-9). Our dynamic Brillouin scattering data are clearly different from those already reported in the literature and are in excellent agreement with both static diffraction experiments and DFT calculations. These results suggest that redetermination of the complete C_{ij} tensor for quartz at pressures up to 20 GPa is necessary to better constrain the causes of the instability which drives its amorphisation above such pressure.

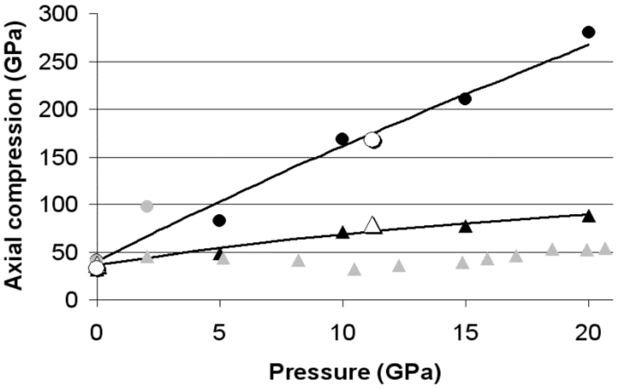

Fig. 3.4-9: Pressure dependency of the axial compression for α-quartz. Triangles: *a* axis; circles: *c* axis. Solid curves represent the linear compression calculated from the 3rd order Birch-Murnaghan equation of state parameters obtained fitting our unit-cell vs *P* diffraction data. Empty symbols: Brillouin scattering measurements obtained in this study; Black symbols: DFT calculation; grey symbols: previous Brillouin scattering measurements. Note that previous experimental data for compression along the *c*-axis are shown only up to approximately 2.5 GPa, because they have unphysical negative values at higher pressures.

g. *Ti^{3+} in hibonite, oxygen fugacity vs. crystal chemistry (M. Giannini and T. Boffa Ballaran; F. Langenhorst/Jena)*

Hibonite, ideal formula $CaAl_{12}O_{19}$, is found commonly in Calcium-Aluminium-rich inclusions (CAIs) in meteoritic carbonaceous chondrites. Hibonite is one of the very first phases to appear in the condensation sequence of a hot gas of Solar composition and ^{26}Mg isotopic measurements indicate that hibonite represents one of the most pristine materials of our Solar system. Titanium can replace Al in the structure of hibonite and it has been proposed that its oxidation state can be linked to the oxygen fugacity (fO_2) of the Solar nebula during CAIs formation. However, such hibonites also contain a significant amount of Mg which may arise from a possible coupled substitution of Ti^{4+} + Mg^{2+} for 2 Al^{3+}, independent from oxygen fugacity. In order to better understand the influence of Mg substitution on the oxidation state of Ti at any oxygen fugacity, we have synthesised Ti- and Ti-Mg- bearing hibonites at different fO_2 using a citrate-based sol-gel method. These samples were characterised by means of energy electron loss spectroscopy (EELS) and UV/Vis absorption spectroscopy.

EEL spectra of synthetic samples prepared from batches of the same starting material equilibrated at different fO_2, reveal subtle changes mainly in the peak width of the Ti $L_{2,3}$ edge correlated with oxygen fugacity. It appears, therefore, that the presence of Ti^{3+} into the hibonite structure is associated with peak broadening of the EEL spectra. Since an accurate fitting of these complex spectra is challenging, we have quantified the peak broadening using the autocorrelation method and calibrated it vs. the Ti^{3+} concentration of a reference hibonite sample containing only Ti. This allowed us to evaluate the spectral width of Ti-Mg-bearing hibonites in terms of Ti^{3+} concentrations. The results on synthetic samples indicate that the variation of Ti^{3+} with fO_2 (Fig. 3.4-10) clearly depends on the Ti : Mg ratio. Oxygen fugacity has clearly a minor effect on samples whose chemical composition present a Ti : Mg ratio close to 1: 1 (gel2 and gel6 in Fig 3-4.10) which appear to favour a coupled substitution according to $2Al^{2+} = Ti^{4+} + Mg^{2+}$. Gel4, instead, having more atoms of Ti than Mg show a larger variation of Ti^{3+} content with oxygen fugacity.

Since collecting EEL spectra of hibonite is time consuming as well as very challenging, due to the small amount of Ti present, we have used the Ti^{3+} content determined from the EEL spectra to determine the molar extinction coefficient of Ti^{3+} in hibonite. To this end we have collected UV/Vis spectra for several crystals of the samples previously study with EEL spectroscopy. The hibonite crystals were appropriately aligned with the *c* axis // to *E* before measuring the UV/Vis spectra.

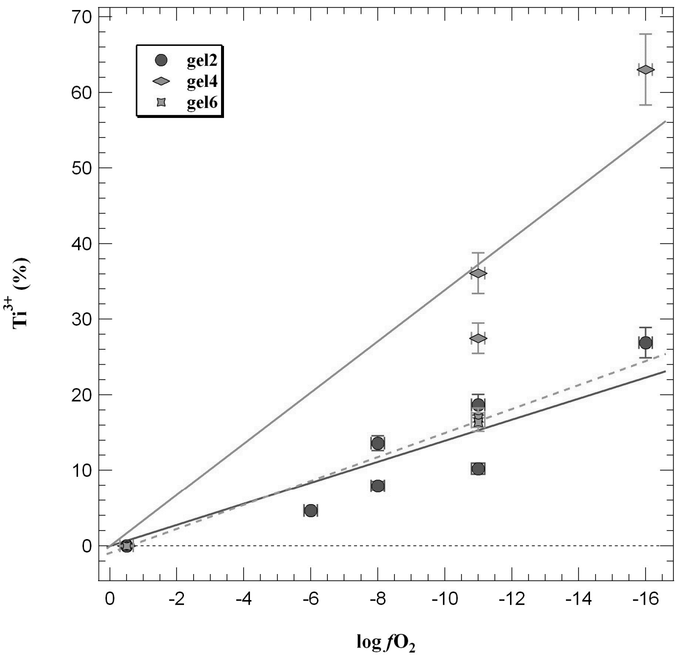

Fig. 3-4.10: Variation with oxygen fugacity of the Ti^{3+} / Ti total content of the synthetic hibonite samples calculated from broadening of EEL spectra.

3.5 Fluids, Melts and their Interaction with Minerals

The textures of igneous rocks record information on the processes that occurred during the evolution and solidification of magmas. In principle, these textures should provide tight constraints on the timescales of magmatic processes, just as the compositions of coexisting phases constrain pressure and temperature. However, all available models suffer from the fact that they are not directly calibrated against experimental data, since the direct observation of the crystallization of magmas proved to be difficult or impossible. The contribution at the beginning of this section reports the first direct observation of olivine crystallizing from a basaltic melt, including the full sequence of nucleation, crystal growth and texture development. The observations show that crystal size distribution (CSD) theory, which is often used to extract kinetic data from textures of igneous rocks, is fundamentally flawed. Nucleation and crystal growth do not occur simultaneously, as assumed by CSD theory, and crystal growth rates are not constant. Rather, crystal growth rate increase with crystal size, which largely determines the observed CSD patterns. This effect of proportionate growth has previously been observed in model systems at low temperature, but the data shown here is the first evidence that proportionate growth also occurs during the solidification of natural magmas.

The behaviour of sulfur in silicate melts is strongly linked to the environmental impact of volcanic eruptions and to the processes that lead to the formation of hydrothermal ore deposits. Under oxidizing conditions, a large part of the sulfur may be locked up in anhydrite $CaSO_4$, which limits the amount of sulfur that may be released in a gas phase. The stability and solubility of anhydrite, however, has so far only been poorly studied. New data presented in the second contribution of this chapter provide a new calibration of anhydrite solubility over a wide range of melt compositions. The following contribution looks at the solubility of zircon in silicic melts, which may be used as a geothermometer. A new experimental setup is used to supplement existing data on zircon solubility.

Melting deep in Earth's mantle usually requires the presence of volatiles, such as H_2O and CO_2, as the volatile-free solidus of the mantle peridotite is located at temperatures that are considerably higher than a normal geotherm. Very few studies, however, have looked at possible interactions between H_2O and CO_2 in silicate melts at high pressure. Data on the partitioning of water between a basaltic melt and forsterite at 13 GPa and 1500 to 1700 °C presented in a contribution in this chapter suggest that adding CO_2 causes H_2O to partition more strongly into the silicate melt. This would imply that interaction with CO_2 enhances the melting point depression caused by water in the mantle and this effect could be important for stabilizing silicate melts in the deeper parts of the upper mantle. Carbonate melts may also occur in parts of the mantle, and they may be particularly important as agents responsible for the crystallization of diamond. The last contribution in this chapter provides new data on melting equilibria in multicomponent carbonate systems at 12 to 23 GPa.

a. In situ *observation of crystal growth in basalt melt and the development of crystal size distribution in igneous rocks (H. Ni and H. Keppler; F. Schiavi/Clermont-Ferrand, Y. Chen/Hefei; M. Masotta; Z. Li/Ann Arbor)*

The textures of igneous rocks record information on their thermal history. Crystal size distribution (CSD) theory is a commonly used tool to derive kinetic information from observed textures. However, CSD theory makes several assumptions that have never been experimentally tested: (1) Crystal growth rates are constant and to not depend on crystal size; (2) nucleation of crystals and the growth of crystals occur simultaneously; and (3) nucleation rates increase exponentially with undercooling. Here we provide direct evidence from *in situ* observations that some of the underlying assumptions of CSD theory are fundamentally flawed.

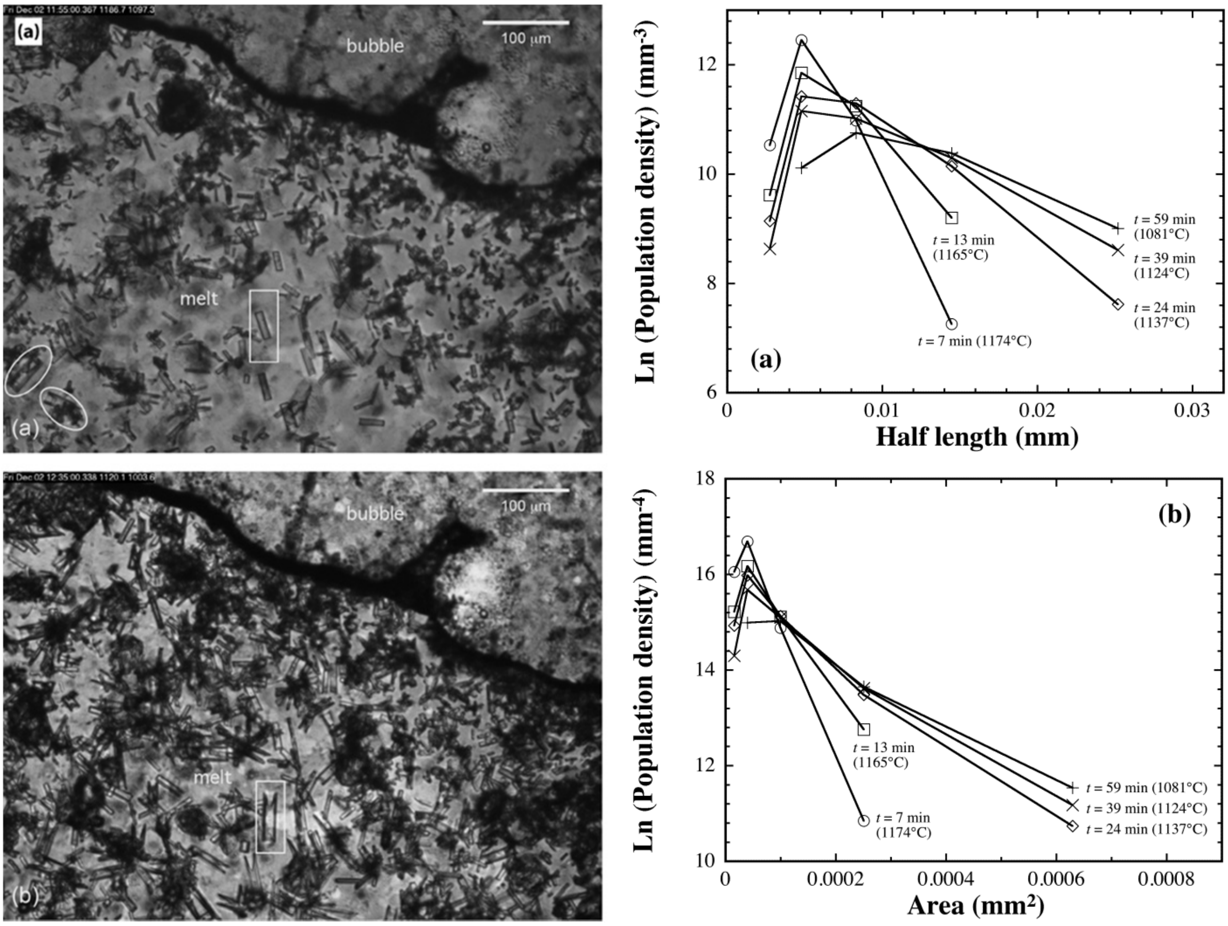

Fig. 3.5-1: (**a**) Photomicrographs of olivine crystals in basaltic melt cooling at 100 °C/hour in basalt. Top: T ~ 1142 °C, most olivine crystals showed a tabular habit with some exceptions (two examples are shown inside an ellipse); Bottom: T ~ 1062 °C, numerous hopper crystals formed (one example is shown inside a rectangle). (**b**) Counterclockwise rotation of two-dimensional crystal size distributions (CSDs) during cooling of basalt, according to (top) half-length along [100]; and (bottom) crystal area. Five logarithmic size bins are applied.

The moissanite cell is an extremely powerful tool for studying the crystallization of magmas, because it allows capturing crystal growth *in situ* (using a microscope connected to a digital camera), with much better control of sample geometry and temperature than commonly used heating stages. We used this experimental technique to investigate the crystallization of a high-K basaltic melt upon cooling from 1240 °C at different cooling rates. Olivine and/or clinopyroxene nucleated before plagioclase. Importantly, nucleation was only observed in a narrow temperature and time interval below the liquidus. During cooling at 100 °C/hour, the morphology of olivine and clinopyroxene transited from tabular to hopper habit (Fig. 3.5-1a), with crystal growth rates ranging from 2×10^{-9} m/s to 7×10^{-9} m/s for olivine and from 6×10^{-9} m/s to 17×10^{-9} m/s for clinopyroxene. Multiple melt inclusions were trapped in closed hopper olivine crystals, the formation of which does not appear to require complex cooling-reheating as previously suggested. By first approximation, crystal grow rate was found to be proportional to crystal size, in contrast to the uniform growth rate assumed in CSD theory. Two-dimensional length- and area-based crystal size distributions (CSDs) show counter clockwise rotation around axes of 8 µm and 100 μm^2, which is attributed to the proportionate crystal growth (Fig. 3.5-1b). CSDs also indicate the dissolution of small crystals (Ostwald ripening). Both observations are inconsistent with conventional CSD theory, which would predict a parallel shift of CSD curves with time.

The experimental data show that conventional analyses of crystal size distributions of igneous rocks may be in error – the slope of the CSD cannot be interpreted in terms of a uniform growth rate and the intercept with the vertical axis does not correspond to a nucleation density.

b. *Anhydrite solubility in hydrous silicate melts (M. Masotta and H. Keppler)*

During volcanic eruptions, large quantities of sulfur are commonly released in the form of sulfur dioxide (SO_2) or rarely hydrogen sulfide (H_2S). The injection of sulphur compounds into the stratosphere and the subsequent formation of sulphate aerosols is the main cause for the global cooling of surface temperatures often observed after explosive volcanic eruptions. The quantity of sulfur released during these eruptions is primarily controlled by the initial sulphur content in the melt and by the fluid/melt partition coefficient of sulphur. However, a large fraction of the sulfur in a magma reservoir may be locked up in sulfur-bearing minerals, particularly pyrrhotite (FeS) and anhydrite ($CaSO_4$). This will greatly affect the amount of sulfur that may be released on the short timescales of an explosive volcanic eruption. Anhydrite is one of the most common minerals in differentiated, sulfur-rich magmas, but the factors controlling its stability are not fully understood.

In order to investigate anhydrite stability, we have performed phase equilibria experiments in rapid-quench and TZM autoclaves, using four synthetic magma compositions (andesite, dacite, rhyodacite and rhyolite), for a range of conditions typical for magma chambers in subduction zone settings (P = 200 MPa, T = 800 - 950 °C and fO_2 ranging from NNO + 0.5 to HM). Oxygen fugacity is the main parameter controlling the stability of anhydrite in the melts investigated. At log fO_2 = NNO + 0.5 only sulfides are present, whereas at log fO_2 > NNO + 0.5, anhydrite is present in all the experiments performed at $T < T_{\text{liquidus}}$ (Fig. 3.5-2a). Anhydrite solubility increases with temperature and with melt composition in the sequence rhyolite, rhyodacite < dacite < andesite (Fig. 3.5-2b). Published sulfur solubility models tested against our experimental data fail to predict the concentration of sulfur in anhydrite-saturated melts, with sometimes very large errors (Fig. 3.5-2c).

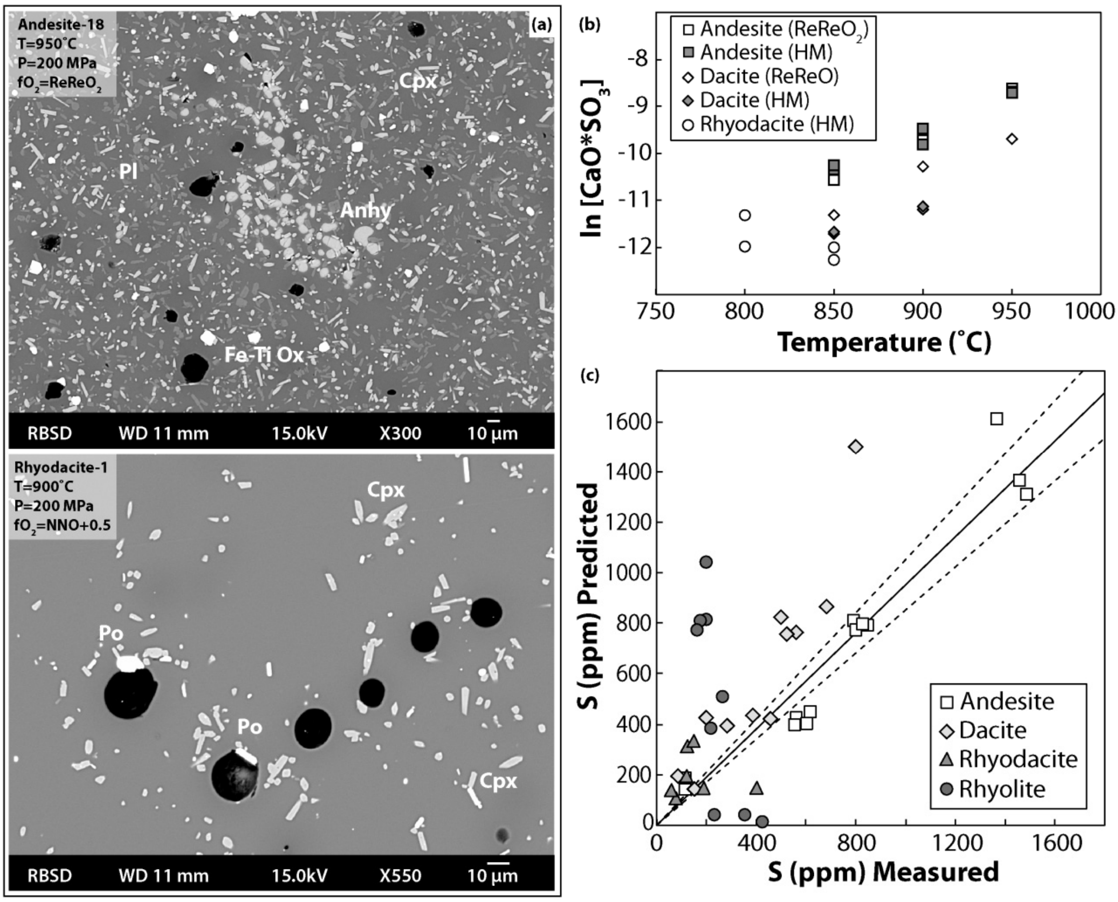

Fig. 3.5-2: (**a**) SEM pictures of two experiments performed at different oxidation state with andesite (top) and rhyodacite (bottom). At the more oxidizing conditions, anhydrite is stable, whereas at more reducing conditions a Fe-sulfide phase is present. Abbreviations: Pl: plagioclase; Cpx: clinopyroxene; Anhy: anhydrite; Fe-Ti Ox: Fe-Ti oxide; Po: pyrrothite. (**b**) Logarithm of anhydrite solubility product ([CaO][SO_3]) in silicate melts at different temperature. (**c**) Test of the SCAS model of anhydrite solubility after Baker and Moretti (RiMG vol. 73, 2011) against our experimental data.

Our data will allow the recalibration of anhydrite solubility models as a function of melt composition, temperature and oxygen fugacity. These models will allow much better predictions of the sulphur yield of volcanic eruptions.

c. *Zircon solubility in silicic peralkaline melts (H. Mohseni and A. Audétat)*

Zircon is a common accessory mineral in intermediate and silicic rocks. In fact, nearly all rhyolites and granites seem to have crystallized at zircon-saturated conditions. The Zr content of rhyolite melts can thus be used to constrain crystallization temperatures via zircon saturation thermometry. This thermometer has been experimentally calibrated on subaluminous and peraluminous melt compositions and thus should be applied only to such compositions, as limited experimental data from peralkaline melt compositions indicate far higher zircon solubilites. The purpose of this study was to develop a zircon saturation thermometer specifically for peralkaline rhyolites.

We investigated zircon saturation in hydrous haplogranite melts with molar Al_2O_3/(Na_2O+K_2O) (=ANK)-ratios ranging from 0.8 to 1.2. In a first step, anhydrous glasses with large ZrO_2 concentration gradients over several millimeters length were produced by melting stacks of powder layers containing between 10 µg/g and 2 wt.% Zr for 8 hrs at 1600 °C in an 1 atm furnace. Pieces of these glasses were then sealed together with H_2O into gold capsules and equilibrated 7-28 days at 750 - 900 °C and 2 kbar in cold-seal pressure vessels. Three more runs were conducted at 1100 °C and 1.4 kbar for 6 days in TZM vessels.

The experiments showed that nucleation of zircon crystals is very sluggish, preventing zircon crystallization in all but the most Zr-oversaturated parts of the glasses. In those areas in which crystallization took place, it was found that the first precipitating mineral phase was baddeleyite rather than zircon, and that this baddeleyite only slowly reacted with the surrounding melt to zircon. To aid the nucleation process we thus equilibrated the starting glasses in contact with single crystals of zircon, ZrO_2 or TiO_2. The latter substrate greatly enhanced the nucleation and led to growth of zircon crystals also within less oversaturated glass portions (Fig. 3.5-3). Laser-ablation ICP-MS traverses were then measured along concentration profiles parallel to the rutile crystal, and zircon solubilities were determined by assuming that the first appearance of zircon marks the transition from zircon-saturation to zircon-oversaturation.

The results of this study are generally in good agreement with those of previous studies, except for our metaluminous and peralkaline data at 1100 °C (Fig. 3.5-4). A potential explanation for this discrepancy is that our data were affected by uptake of up to 2 wt.% TiO_2 in the vicinity of the rutile single crystal, which may have interfered with zircon solubility and ultimately led to lower saturation values. For the fitting we thus used only our 800 and 900 °C data points plus two peraluminous runs at 1100 °C and combined these data with those of previous investigations. This yielded the following equation for zircon solubility in peralkaline silicic melts as a function of temperature (in Kelvin) and molar Al_2O_3/(Na_2O+K_2O):

$$\log ZrO_2\,(\text{wt.\%}) = 1.0676 / [1 - 5162 * \exp(- 7.11 * ANK)] * 10^4/T + \exp[- 36.114 + 36.847 / ANK + 45.865 * \ln(ANK)]$$

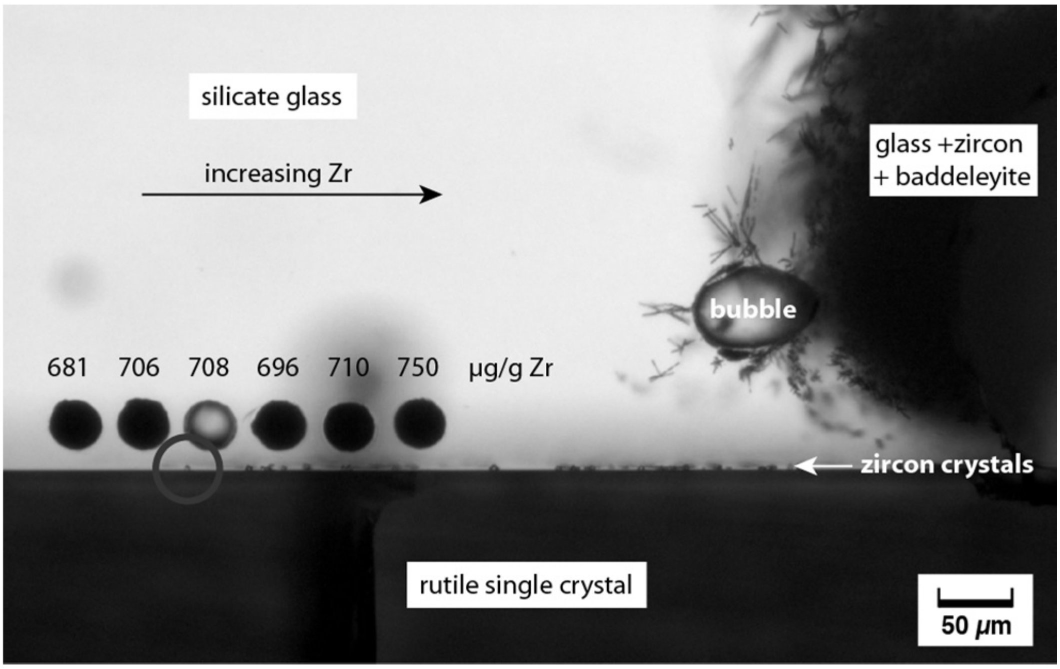

Fig. 3.5-3: Transmitted-light photomicrograph of the run product of experiment *HMA18* (ANK=1.0; 5.19 wt.% H_2O, 900 °C / 2 kbar, 10 days). The image shows clear, crystal-free glass in the Zr-poor parts in the upper left, zircon+baddeleyite crystals in the Zr-rich parts in the upper right, and small zircon crystals that grew at the contact to the rutile single crystal. Also visible are six LA-ICP-MS pits; measured Zr concentrations are indicated above. The circled zircon crystal marks the transition between zircon-undersaturated to zircon-oversaturated glass portions, *i.e.*, in this run zircon saturation appears to have been reached at ~ 700-710 µg/g Zr.

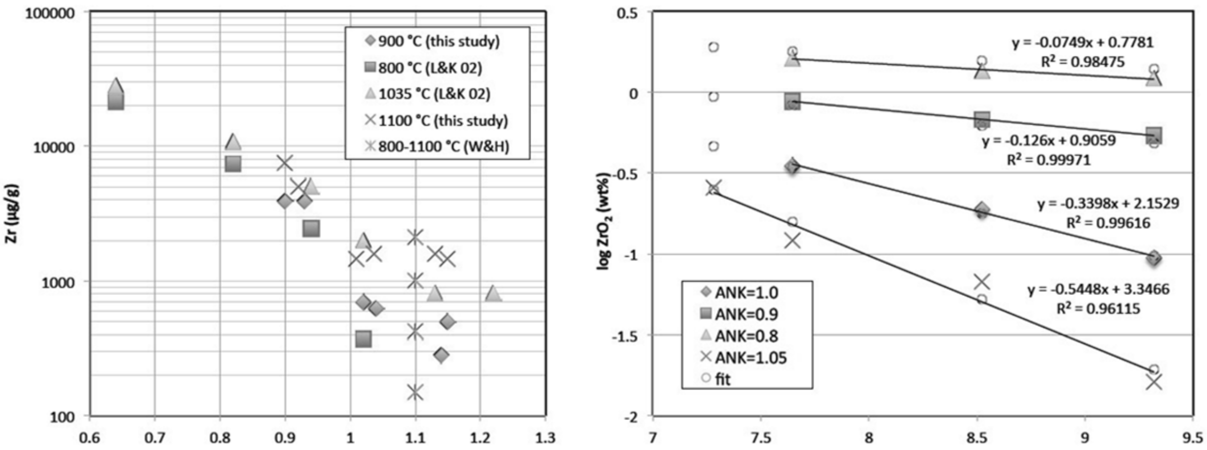

Fig. 3.5-4: Left: Zircon solubilities determined in this study compared to data of Linnen and Keppler (2002; GCA 18: 3293-3301) and Watson and Harrison (1983; EPSL 64: 295-304). Right: Arrhenius plot of log ZrO_2 (wt.%) versus $10^4/ T$ (K) for four ANK values (0.8, 0.9, 1.0 and1.05). ZrO_2 solubilities predicted by the regression equation given in the text are shown as small, open circles.

d. *The effect of CO_2 on the distribution of H_2O in the upper mantle and the production of volatile-bearing melts (D. Novella and D.J. Frost; E.H. Hauri/Washington DC; H. Bureau and C. Raepsaet/Paris)*

Constraints on the possible formation of hydrous melts in the deep mantle can be obtained by assessing the distribution of H_2O between peridotite minerals and plausible low-degree melt compositions. A rigorous description of volatile-induced melting processes in the mantle, however, should also consider the influence of CO_2, the second most abundant volatile in the upper mantle. The presence of dissolved CO_2 may lower the H_2O activity in melts, while having a similar influence on depressing the mantle solidus. The concentration of H_2O in minerals coexisting with such melts should decrease, but the influence on the mineral/melt H_2O partition coefficient may be minimal, depending largely on the degree to which CO_2 influences the melt H_2O activity.

We have investigated the effect of CO_2 on the forsterite-melt distribution of H_2O at depths corresponding to the bottom of the upper mantle (~ 400 km). High-pressure and high-temperature experiments were performed by means of a multianvil apparatus at 13 GPa and temperatures between 1500 and 1700 °C. The experiments were conducted in the simplified systems $MgO-SiO_2-H_2O$ (MSH) and $MgO-SiO_2-H_2O-CO_2$ (MSCH) using starting materials with $H_2O/(H_2O+CO_2)$ weight ratios of 0.69 and 0.80 and a molar Mg/Si ratio of ~ 2 (≥ 1.93). The H_2O content of forsterite crystals produced in the experiments was determined by means of NanoSIMS and elastic recoil detection analyses (ERDA). The melt liquidus volatile content was bracketed by employing a series of compositions with varying bulk volatile contents at the same pressure and temperature and identifying the bulk composition where forsterite disappears from the assemblage.

In the MSH system, forsterite H_2O contents are observed to decrease with increasing temperature, from ~ 4300 ppm wt. H_2O at 1500 °C to ~ 1300 ppm wt. H_2O at 170 °C, which results from a decrease in H_2O activity as more silicate enters the melt. For the MSCH system, the concentration of H_2O in forsterite also drops as the CO_2 content of the melt increases. At 1500 °C, a plausible mantle temperature at ~ 400 km, forsterite contains ~ 2150 and ~ 1040 ppm wt. H_2O for melt $CO_2/(H_2O+CO_2)$ ratios of 0.80 and 0.69, respectively. Using the measured forsterite H_2O contents, the bracketed liquidus total volatile contents and the known bulk $CO_2/(H_2O+CO_2)$ ratios, forsterite-melt H_2O partition coefficients ($D^{f/m}_{water}$) were determined for the MSH and MSCH systems. Uncertainties in total melt volatile contents increase below 1700 °C as the compositions melt incongruently, however, uncertainties for all partition coefficients at a given temperature should be similar and in the same direction. The calculations assume fluid undersaturated conditions. Values of $D^{f/m}_{water}$ in the MSH and MSCH systems are displayed in Fig. 3.5-5. The forsterite/melt partition coefficient of water is lowered by the presence of CO_2 with the effect diminishing with increasing temperature. Differences are observed among values of $D^{f/m}_{water}$ determined in H_2O and H_2O+CO_2 systems at 1700 °C that are within the calculated errors. At 1600 and 1500 °C, however, $D^{f/m}_{water}$ drops by over 50 % as the weight fraction of CO_2 increases to only ~ 0.3.

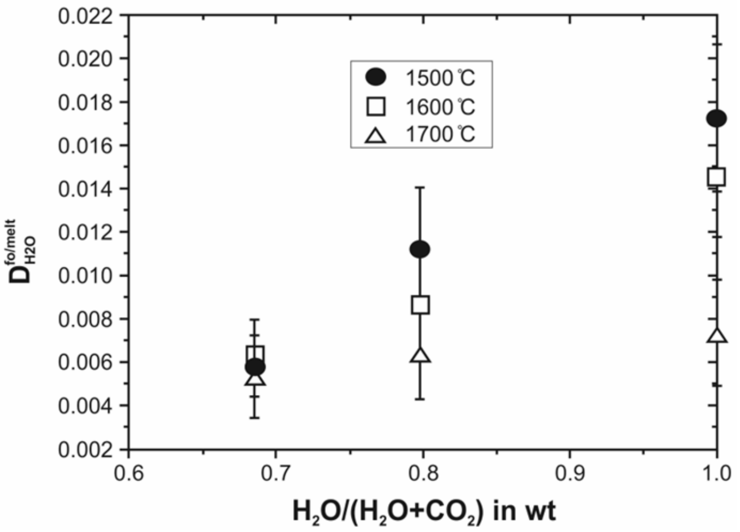

Fig. 3.5-5: The forsterite/melt partition coefficient of water as a function of the weight $H_2O/(H_2O+CO_2)$ ratio at 13 GPa and 1500, 1600 and 1700 °C.

As $D^{f/m}_{water}$ appears to decrease in the presence of CO_2 in hydrous melts, the amount of water necessary in the mantle to cause peridotite melting below the volatile-free solidus should be reduced. The melt fraction produced for a given bulk mantle water content will also be raised significantly. As this effect must result from a lowering of the activity of H_2O in the melt, it should affect all minerals coexisting with the melt, although the magnitude of the effect may vary due to differing mineral H_2O substitution mechanisms. CO_2 should, therefore, enhance the production of hydrous melts at the base of the upper mantle, where seismological studies have proposed that melts may be present.

e. *Melting relationships in the multicomponent carbonate system $MgCO_3$ - $FeCO_3$ -$CaCO_3$ - Na_2CO_3 at 12 to 23 GPa (A.V. Spivak, E.S. Zakharchenko and Y.A. Litvin/Chernogolovka; N.A. Solopova and L.S. Dubrovinsky)*

Carbonatites often occur as low-degree partial melts in the mantle and they may be important agents involved in the formation of ultra-deep diamonds. Therefore, the melting phase relations in a multicomponent carbonate system were studied at 12 - 23 GPa and 800 to 1650 °C using multianvil press. The starting mixture for the experiments consisted of 26 wt.% $FeCO_3$, 26 wt.% $MgCO_3$, 25 wt.% $CaCO_3$ and 23 wt.% Na_2CO_3. The experimentally determined phase relations in this system are shown in Fig. 3.5-6.

Partial melting occurs between the solidus curve and the liquidus. A Mg-Fe carbonate solid solution is the liquidus phase. At lower temperatures, the phase assemblages Mg,Fe)CO_3 + $(Ca,Na_2,Fe)CO_3$ + liquid and $(Mg,Fe)CO_3$ + $(Ca,Na_2,Fe)CO_3$ + $Na_2(Ca,Fe)(CO_3)_2$ + liquid are observed. The subsolidus phase assemblage is $(Mg,Fe)CO_3$ + $(Ca,Na_2,Fe)CO_3$ +

$Na_2(Ca,Fe)(CO_3)_2$. Above the liquidus, only one single liquid carbonate phase appears to exist. Just above the solidus, carbonatite melt coexists with several carbonate solid solutions. The melting temperatures determined here are significantly below those of an average mantle geotherm. The data therefore confirm that carbonatites are stable under transition zone and lower mantle conditions.

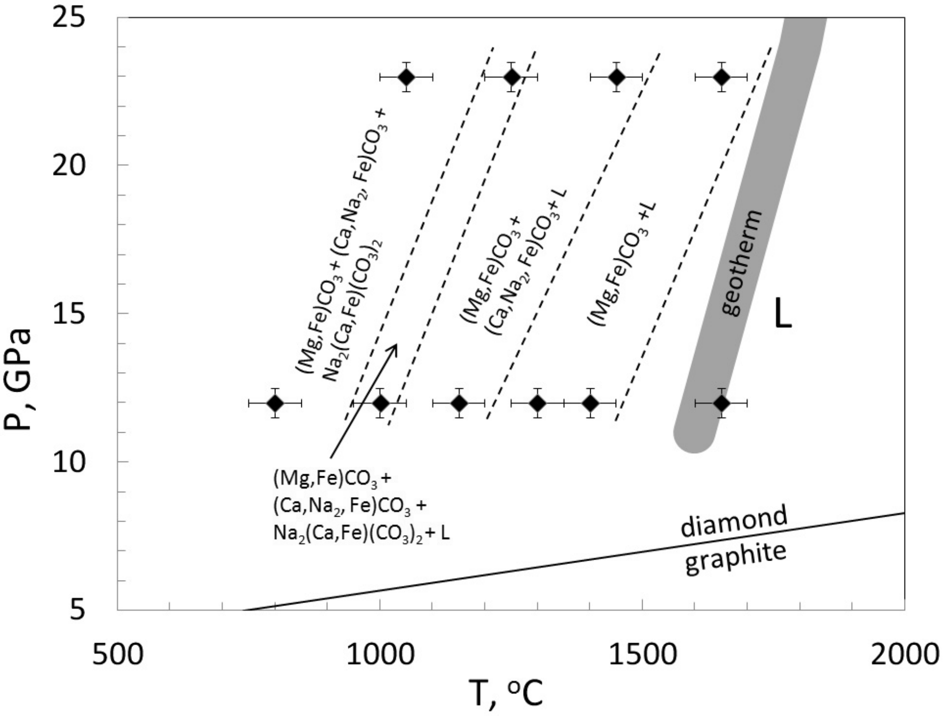

Fig. 3.5-6: Melting phase relationships in the system $MgCO_3$–$FeCO_3$–$CaCO_3$–Na_2CO_3.

3.6 Rheology

Knowledge of rheological properties of Earth-forming minerals is indispensable for understanding the dynamics and evolution of the Earth. Therefore, significant efforts have been made to understand rheology of minerals and rocks under high-pressure and high-temperature conditions corresponding to the Earth's interior. Experimentally such investigations are particularly difficult since it is not only necessary to establish stable P-T conditions and sample environments, but also to maintain deviatoric stresses and strains (shape changes) over relatively long time periods. Natural strain rates in the mantle are on the order of 10^{-12} /s or lower, whereas those in laboratory experiments are practically 10^{-7} /s or higher. Accordingly, experimental results need to be extrapolated over 5-6 orders of magnitude. However, deformation processes are driven by various kinds defects (point defect, dislocation, sub-grain boundary and grain boundary), and the behaviour of these defects can be quantified experimentally without the need to copy natural time scales. Lastly there is a very large number of intrinsic and extrinsic factors influencing rheological behaviour, all of which need to be kept constant or controlled in a deformation experiment.

In order to overcome these difficulties, the Geoinstitut has developed two kinds of strategies to understand rheology of minerals and rocks. The first strategy is to perform direct deformation experiments with advanced technologies. The Geoinstitut recently introduced the 6-axis multianvil press, a powerful tool to conduct deformation experiments over a wide P-T range. The first contribution of this chapter focuses on the lattice preferred orientation (LPO) of lawsonite to examine whether the nature of the low velocity layer in subduction zones can be explained by the LPO of lawsonite. The results of this study have declined this explanation. The second contribution aims to understand the interaction of melt and solid under shear conditions reporting an increase in the amount of orthopyroxene with increasing shear strain rate. This may indicate that the amount of pyroxene is related to reactive surface area. The third project attempts to clarify the effect of the transition from spinel-peridotite to garnet-peridotite on the mechanical properties and vice versa. Preliminary results show that higher amounts of garnet are produced under concurrent deformation, *i.e.*, a higher reaction rate under deviatoric stresses. In addition to these in-house experiments, wadsleyite deformation in its stability field was studied, for which the rotational Drickamer apparatus in combination with *in situ* X-ray observation was employed at a synchrotron radiation facility, NSL-II. The preliminary results indicate relatively low activation energy and a very high activation volume for this mineral of the mantle transition zone.

The second strategy is to understand the very basic processes of mineral creep such as point defect or dislocation mobility in different minerals. In the fifth project, grain-boundary Si self-diffusion coefficients were measured because it is considered to be the rate-limiting process for Coble diffusion creep. This study shows that the pressure, temperature and water content dependence of Coble creep in olivine are all small, and predict that the mechanism transition from diffusion to dislocation creep occurs with increasing depth in the upper mantle. The last two contributions report results of dislocation recovery experiments. They give the mobility of different types of dislocations in olivine, which is an essential process in dislocation creep and the resulting LPOs. It was found that the dislocation mobilities for the [100](010) and [001](010) systems are indistinguishable at the investigated P,T conditions, although the [100](010) system is most frequently observed in naturally deformed olivine.

a. *Crystallographic preferred orientation of lawsonite experimentally deformed at high pressure and temperature: implications for low velocity layers in subduction zones (R. Iizuka/Matsuyama, V. Soustelle, N. Walte and D.J. Frost)*

The upper part of subducting slabs likely consists of hydrated mafic rocks. Seismically observed low-velocity layers (LVLs) at depths of 100-250 km in the upper part of subducted slabs should therefore have their origin in the physical properties of the hydrated mafic rocks. Lawsonite ($CaAl_2(Si_2O_7)(OH)_2$ H_2O) is a hydrous mineral in mafic rocks and its stability field probably reaches down to depths greater than 150 km, *i.e.*, deeper than the serpentine stability field. Because of its high elastic anisotropy, a suitable crystallographic preferred orientation (CPO) of lawsonite may cause low seismic-wave velocities in subducted slabs. Lawsonite CPO was previously investigated in natural samples. The P-T conditions in such a study were, however, much lower than the above conditions (< 2.5 GPa corresponding to ~ 80 km depth, < 400 °C). The present study aims to investigate the development of CPO of lawsonite under different P-T conditions and compare the obtained CPOs with those of the previous studies in order to examine whether the lawsonite CPO can account for the LVLs or not.

The starting material was a powder of natural lawsonite with a grain size of less than 30 µm, and was acid-treated to remove contamination by calcite. This powder was loaded into a Pt capsule and deformed by pure shear using the 6-axis multianvil apparatus at pressures of 2.5 and 5 GPa and at temperatures of 400 and 500-700 °C, respectively. The strain rate ranged from 10^{-5} to 10^{-6} s^{-1} with a finite strain of *ca.* 0.3. Samples deformed at 5 GPa and 500-700°C gave coarse-grained (20-50 µm) porphyroclasts surrounded by a fine-grained matrix of ~ 2 µm in grain size. The fine-grained matrix showed only weak or almost no CPO. Therefore the fine-grained part does not cause seismic anisotropy. The absence of CPO in the fine grained-part may be due to the dominance of diffusion creep and/or cataclastic flow rather than dislocation creep. In contrast to the fine-grained part, the porphyroclasts form a CPO with a maximum concentration of the [010] axis in the shortening direction and [100]-axis girdles in the extension directions (Fig. 3-6.1 (a) and (b)). The dominant slip system suggested by these observations is [100](010). The obtained CPOs are essentially the same between experiments at 500 and 700 °C. On the other hand, a sample deformed at 2.5 GPa and 400 °C shows no characteristic texture and CPO (Fig. 3.6-1 (c)).

The present results disagree to those of previous studies conducted at similar P-T conditions. The very weak CPOs observed at 5 GPa, 500 and 700 °C may result from lower finite strain and higher strain rates in our experiments.

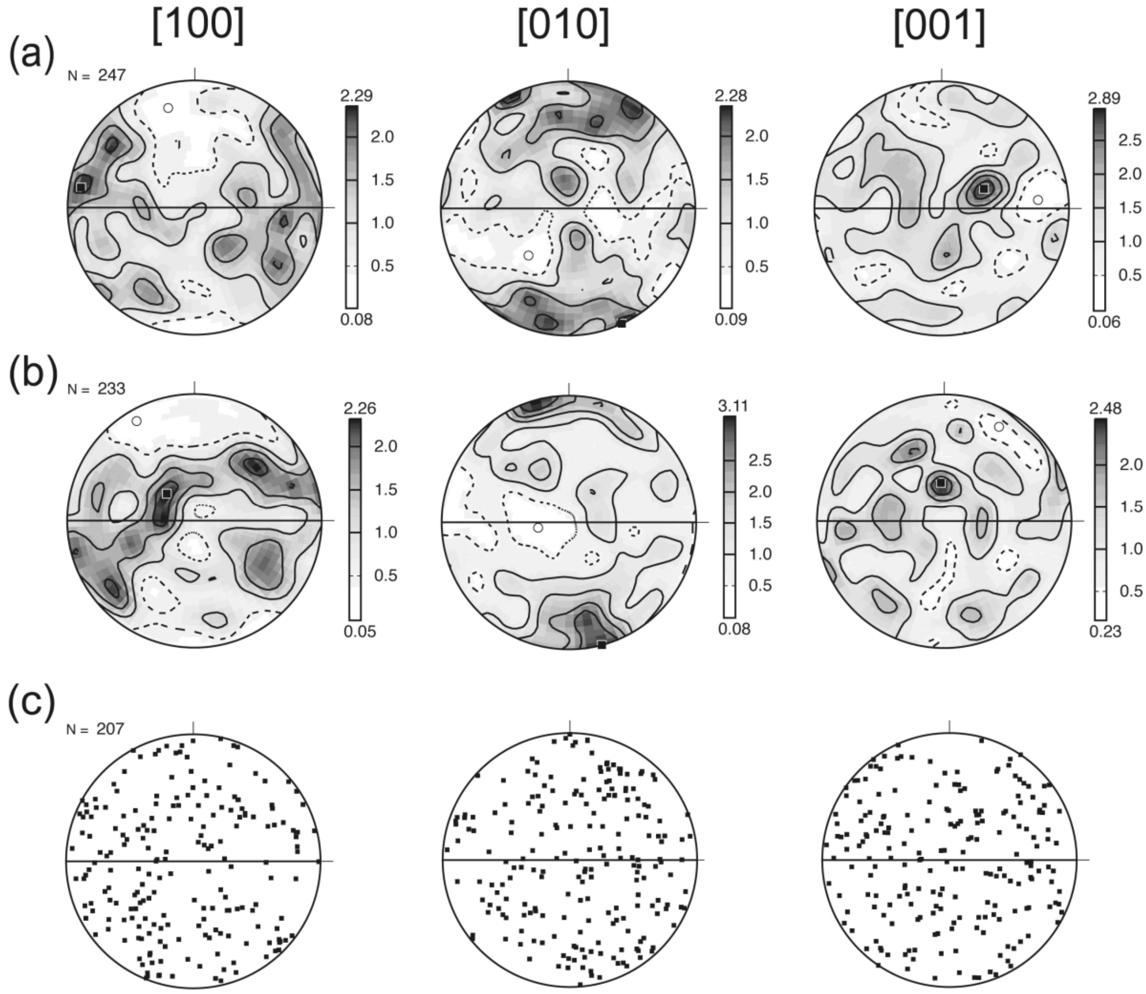

Fig. 3.6-1: Distributions of three crystallographic axes of lawsonite porphyroclasts deformed at (a) 1.7×10^{-5} s^{-1}, 5 GPa and 700 °C, (b) 1.9×10^{-5} s^{-1}, 5 GPa and 500 °C, and (c) 1.2×10^{-5} s^{-1}, 2.5 GPa and 400 °C. The shortening and extension axes are N-S and E-W, respectively.

b. *Melt migration and melt-rock reactions in the deforming Earth's upper mantle: Experiments at high pressure and temperature (V. Soustelle and N.P. Walte; M.A.G.M. Manthilake/Clermont-Ferrand; D.J. Frost)*

We investigated the importance of melt-rock reactions for the interpretation of melt migration in deforming mantle rocks. Previous experimental and theoretical studies investigating the extraction of partial melt assumed chemical equilibrium between melt and solid matrix. However, these studies showed that segregation and migration of melt have different orientations from those inferred from natural samples showing melt-rock interaction. This discrepancy made interpretation, modelling and geophysical analysis of melt extraction difficult. In order to reconcile the discrepancy, we conducted deformation experiments in a melt-rock system.

A series of simple-shear deformation experiments were conducted using the 6-axis multianvil apparatus at 2 GPa and 1150 ºC. The sample was an aggregate of San Carlos olivine mixed with 10 % of Si-rich hydrous basaltic melt. The samples were sheared by hard alumina pistons with 45º cutting with a strain rate from 1×10^{-5} to 7×10^{-4} s^{-1}. The finite strain ranged from 0.3 to 2. The reaction between the melt and olivine produced orthopyroxene with minor amounts of clinopyroxene.

Important results from these experiments are the correlation of the amounts of crystallized pyroxene with the shear strain rate (Fig. 3.6-2a) and no correlation with time (Fig. 3.6-2b). The following processes may account for these observations: (1) shear heating, *i.e.*, mechanical dissipation; (2) strain energy increase; (3) local pressure drop; (4) surface energy variation, *i.e.*, increase of the reactive surface area. In processes (1) and (2), the energy increase may be too low to account for the variation in pyroxene crystallization. The process (3) would lead to chemical heterogeneity, but this is not clearly observed in our experiment.

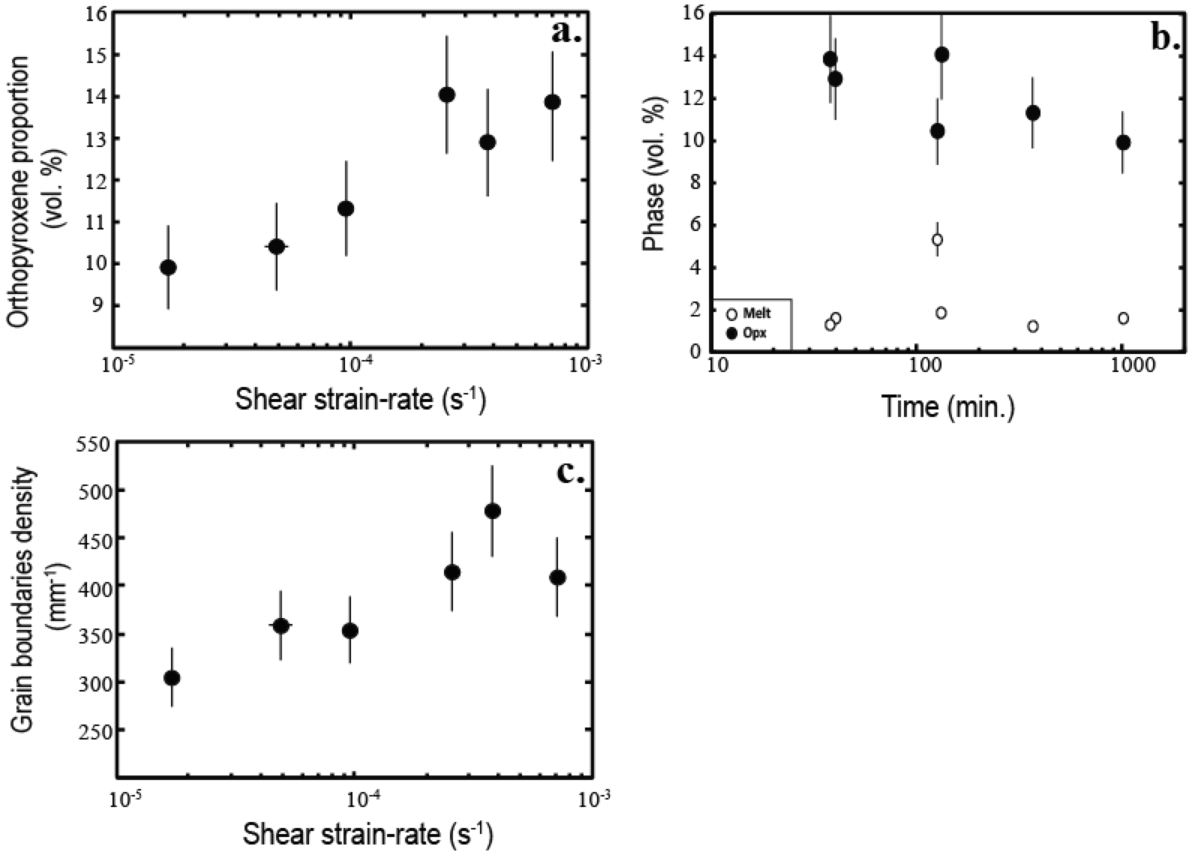

Fig. 3.6-2: Proportion of orthopyroxene as a function of shear strain rate (a) and time (b). Proportion calculated by binary images processed from energy-dispersive X-ray spectroscopy maps by using ImageJ software. (c) Grain boundary density as a function of shear strain rate, calculated using MTEX software on electron back-scattered diffraction data.

For these reasons, process (4) should be responsible. It may be supported by the observation that the grain-boundary density increases with increasing strain rate, which increases reaction surfaces between melt and olivine (Fig. 3.6-2c).

The olivine grains show the A-type crystallographic preferred orientation (CPO), in which the [100] axes form a girdle with one or two maxima in the shear plane. The maximum concentration of the [001] axes becomes closer to the shear direction with increasing strain. This pattern could be explained by a change of the dominant olivine slip direction from [100] to [001] with increasing strain rate, a partitioning of the deformation between the melt-rich band and olivine matrix, or a large contribution of diffusion creep.

Orthopyroxene displays stronger CPO than olivine with the maximum concentration of the [001] axes close to the shear direction, and a maximum concentration of the [100] and [010] axes close to the normal to the shear plane. This CPO pattern may result from the deformation of the orthopyroxene under relatively high water and Al contents.

c. *Deformation fabrics at the transition from spinel to garnet lherzolite in the CMAS system (F. Heidelbach)*

Natural rocks display abundant evidence to show that deviatoric stresses change mineralogy. Nevertheless, the influence of concurrent plastic deformation on phase transitions has received relatively little attention. In this project, we are investigating the reaction from clinopyroxene + orthopyroxene + spinel to garnet + olivine in the CMAS system under shear conditions. Starting materials were produced from glasses of the appropriate composition in piston cylinder experiments at 1 GPa and 1000 °C for up to 10 days in order to increase grain size. In addition, up to 10 wt.% of water was added to the starting glass powder for the same purpose. The resulting samples show grain sizes of about 5-15 μm for all phases. Samples were then deformed in the 6-axis multianvil press in the garnet stability field at 950/1170 °C and 2 GPa to pure shear up to 30 % at strain rates of $2.5\text{-}5\times10^{-6}$ sec^{-1}.

Samples showed extremely homogeneous strain distribution and no strong development of CPO, indicating that deformation likely occurred by diffusion-assisted grain boundary sliding (Fig. 3.6-3). Preliminary results show that the production of garnet is significantly higher in the deformed sample (about a factor of 5) than in the statically annealed reference sample indicating that deviatoric stresses enhance the reaction rate. Newly formed garnet grains at the phase boundaries have a grain size up to 10 μm and form larger (> 100 μm) domains of equal orientation both in the statically and dynamically reacted samples. In the deformed samples, however, the orientation domains show continuous orientation dispersion, indicating that orientation changes continuously with progressive deformation similar to porphyroblastic growth. Further experiments to quantify the enhancement of reaction rate with strain (rate) are under way.

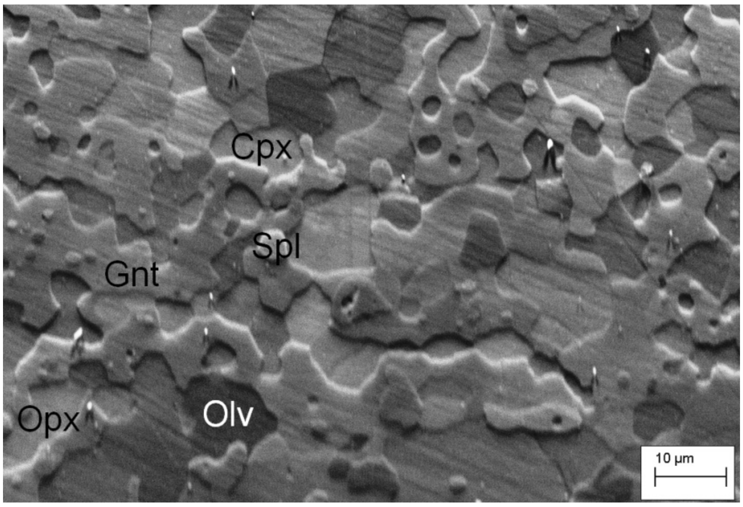

Fig. 3.6.-3: SEM orientation contrast image of experimental run product after deformation in pure shear to 30 % strain at 2 GPa and 1170 °C (garnet stability field); compression direction vertical, extension direction horizontal.

d. *High pressure (~ 19 GPa) and temperature (~ 2000-2200 K) deformation experiments on polycrystalline wadsleyite in the rotational Drickamer apparatus (R.J.M. Farla, G. Amulele/New Haven, J. Girard/New Haven, N. Miyajima and S. Karato/New Haven)*

Rheological properties of transition zone minerals such as wadsleyite are critical in the understanding of dynamics of this region. Controlled laboratory deformation experiments on transition zone minerals under high pressure and temperature conditions provide the most direct information on the processes operating in the Earth (such as convection and subduction). However, quantitative deformation experiments under these conditions are difficult, and only limited data are available.

In this study, we used a rotational Drickamer apparatus (RDA) to deform nearly-dry, fine-grained wadsleyite polycrystals under high pressure and temperature conditions at NSLS at Brookhaven National Laboratory. We deformed at 3 stepped strain rate increments of 6×10^{-6}, 2×10^{-5}, and 6×10^{-5} s^{-1} by controlling the rotation rate of the top tungsten carbide anvil. During deformation, X-ray diffraction patterns of wadsleyite were continuously taken by 7 multi-element detectors oriented between 0° and 180° azimuth and one at 270° azimuth to provide the lattice d-spacing. The stresses were calculated from the difference in lattice spacing among the (141), (240) and (040) planes (Fig. 3.6-4A). The strain was determined from the orientation of a Mo strain marker visible in X-ray radiograph images.

As Fig. 3.6-4 shows, the 'steady-state' stresses at each strain rate vary with temperature conditions and slip plane. The strain rate step tests provide information on the exponential stress dependence $\sigma_{\mathrm{ave}}^{n}$, with $n \approx 3.5$ for the lower temperature experiments (B071), suggesting dislocation creep was active. The higher-temperature experiments reveal lower stress exponents of $n = 2.5$ to 1.6, suggesting a change in deformation mechanism possibly associated with grain size reduction via recrystallization and partial phase transformation to ringwoodite. A tentative flow law for dislocation creep of wadsleyite gives an activation energy of $E_a \approx 230$ kJ mol^{-1} and activation volume of $V^* \approx 32\times10^{-6}$ m^3 mol^{-1}.

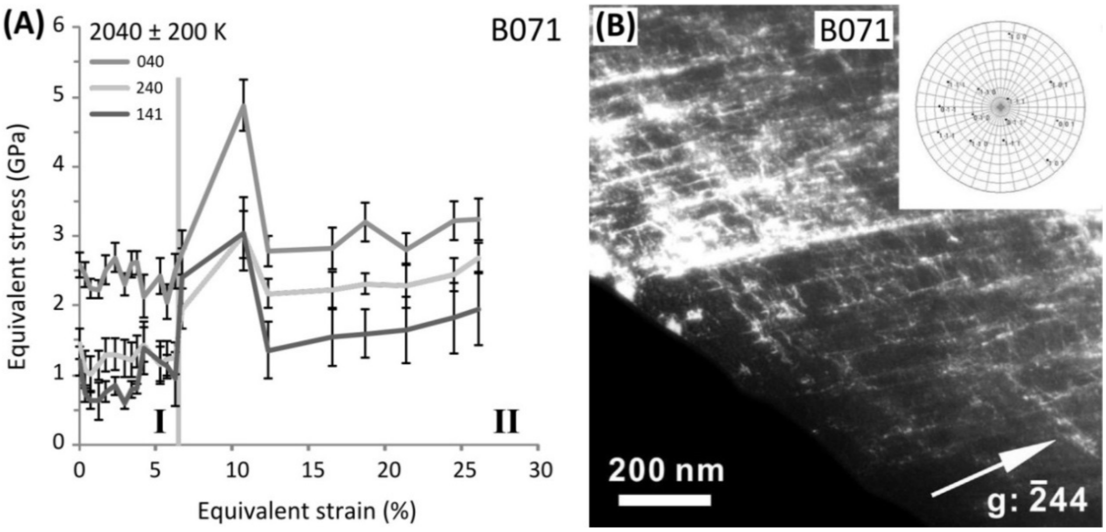

Fig. 3.6-4: (A): equivalent stress versus equivalent strain data for each wadsleyite plane belonging to sample B071. The change in rotation/strain rate is indicated by the vertical grey line separating regimes I from II, to represent strain rates of 6×10^{-6}, $2\times10^{-5}\times s^{-1}$, respectively. (B): the dislocation microstructure for this sample in a TEM image. Despite the high dislocation density in most grains, some individual dislocation lines can be observed here with <111> Burgers vectors.

To verify whether dislocation creep operated during deformation, we conducted TEM analysis on several samples. Figure 3.6-4B shows that the dislocation density is extremely high, reflecting the high differential stresses on the sample experienced during deformation. The dominant slip system appears to be ½<111>{101}. Other activated slip systems may include [100](001) slip.

e. *Deformation mechanism in the upper mantle inferred from silicon lattice and grain-boundary diffusion coefficients (H. Fei, S. Koizumi/Tokyo, N. Sakamoto/Sapporo, M. Hashiguchi/Sapporo, H. Yurimoto/Sapporo, D. Yamazaki/Misasa and T. Katsura)*

The dynamic flow in the Earth's upper mantle is controlled by creep of minerals. Dislocation creep results in non-Newtonian rheology and potentially seismic anisotropy, whereas diffusion creep results in Newtonian rheology and no seismic anisotropy. The determination of the dominant deformation mechanism is thus essential to understand mantle dynamics. Previous studies based on olivine deformation experiments suggest that dislocation creep dominates in shallow upper mantle, while diffusion creep dominates in deeper regions with a transition depth of 200-250 km. However, we note that those experiments used polycrystalline samples over-saturated in water. In such an experimental setup, significant amounts of free fluid should have existed on the grain boundaries and enhanced the sliding between grains. The upper mantle should be under-saturated with water, and therefore the enhancement of sliding between grains by free water should not occur. Therefore, previous studies may have misinterpreted the deformation mechanism in the upper mantle.

The dislocation creep and Nabarro-Herring diffusion creep in olivine are controlled by silicon lattice diffusion, whereas the Coble diffusion creep is controlled by grain-boundary diffusion. Here we measured silicon grain-boundary diffusion coefficient ($D_{\mathrm{Si}}^{\mathrm{gb}}$) in a fine grained iron-free forsterite aggregate samples as a function of pressure (P), temperature (T), and water content on the grain boundaries ($\delta C_{\mathrm{H2O}}^{\mathrm{gb}}$. δ is the grain boundary width). Comparing $D_{\mathrm{Si}}^{\mathrm{gb}}$ with our previously determined silicon lattice diffusion coefficient ($D_{\mathrm{Si}}^{\mathrm{lat}}$) data we find that the activation volume for $\delta D_{\mathrm{Si}}^{\mathrm{gb}}$ (~ 1.8 cm^3/mol) is nearly the same as that for $D_{\mathrm{Si}}^{\mathrm{lat}}$ (~ 1.7 cm^3/mol): pressure has little effect on the deformation mechanism in the upper mantle (Fig. 3.6-5a); the activation energy for $\delta D_{\mathrm{Si}}^{\mathrm{gb}}$ (~ 240-250 kJ/mol) is much lower than that for $D_{\mathrm{Si}}^{\mathrm{lat}}$ (~ 410-420 kJ/mol): Coble creep should dominate at low temperature conditions, whereas Nabarro-Herring creep and dislocation creep dominates at high temperature (Fig. 3.6-5b). The water content exponent for $\delta D_{\mathrm{Si}}^{\mathrm{gb}}$ ($r^{\mathrm{gb}} \approx 0.22$) is even smaller than that for $D_{\mathrm{Si}}^{\mathrm{lat}}$ ($r^{\mathrm{gb}} \approx 1/3$): the effects of water on olivine creeps are thus all small (Fig. 3.6-5c).

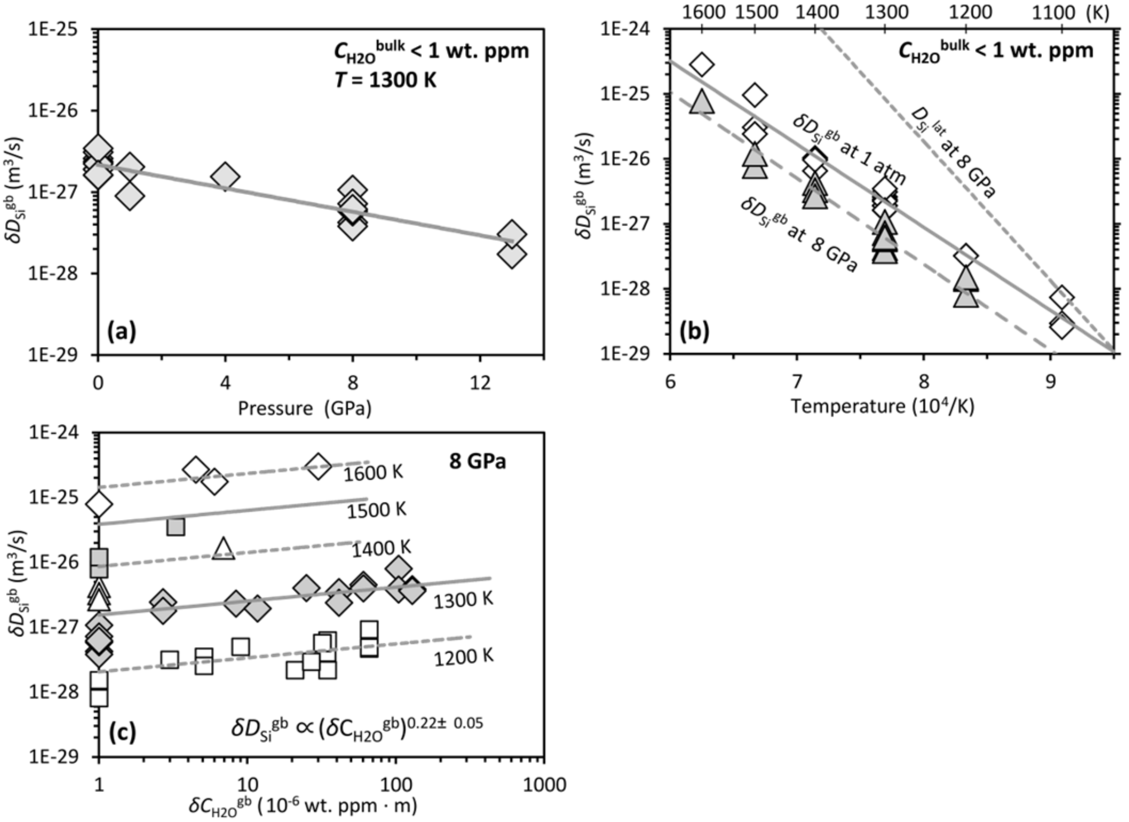

Fig. 3.6-5: Silicon grain-boundary diffusion in forsterite. (a) $\delta D_{\mathrm{Si}}^{\mathrm{gb}}$ against P at 1300 K. (b) $\delta D_{\mathrm{Si}}^{\mathrm{gb}}$ against T. (c) $\delta D_{\mathrm{Si}}^{\mathrm{gb}}$ against $\delta C_{\mathrm{H2O}}^{\mathrm{gb}}$. The data points at $\delta C_{\mathrm{H2O}}^{\mathrm{gb}}$ < 1 wt. ppm · µm are plotted at 1 wt. ppm · µm.

The Coble creep, Nabarro-Herring creep, and dislocation creep rates in the upper mantle calculated from $D_{\mathrm{Si}}^{\mathrm{lat}}$ and $\delta D_{\mathrm{Si}}^{\mathrm{gb}}$ data suggest that dislocation creep should dominate in the asthenosphere and deeper continental lithosphere, whereas diffusion creep dominates in the oceanic and upper part of continental lithosphere (Fig. 3.6-6). The deformation mechanism in the upper mantle is thus opposite as previously considered. The seismic anisotropy jump at mid-lithosphere discontinuity beneath continents and at the Gutenberg discontinuity beneath oceans is caused by the transition from diffusion to dislocation creep. The weak seismic anisotropy in the lithosphere could be interpreted as a fossil anisotropy formed at spreading ridges, which is weakened with time by annealing in diffusion creep and thus old lithosphere has weaker anisotropy than younger lithosphere as seismically observed. The dominance of diffusion creep in the upper lithosphere accounts for the Newtonian rheology suggested by postglacial rebound.

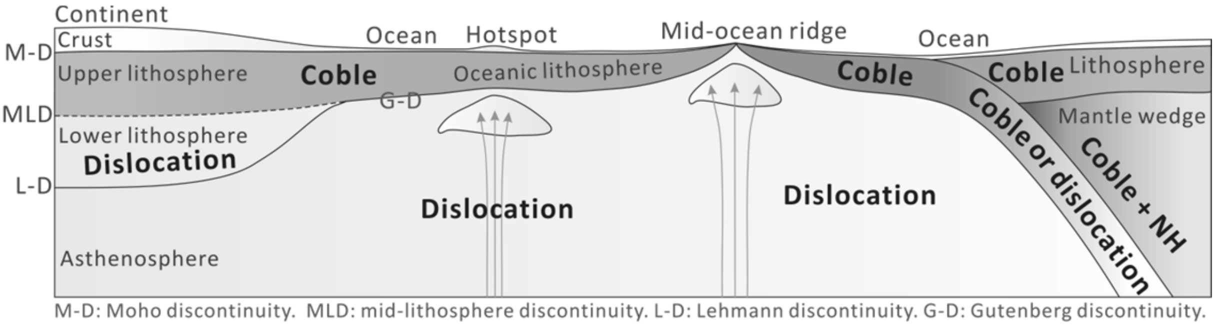

Fig. 3.6-6: Deformation mechanism in the upper mantle. "Coble", "NH", and "dislocation" indicate regions where Coble, Nabarro-Herring, and dislocation creep dominates, respectively.

f. *Dislocation recovery experiment of olivine single crystals and establishment of hydration of olivine single crystals (S. Blaha and T. Katsura)*

Olivine is the most important upper mantle mineral, and is considered to control upper mantle rheology. An open question with olivine rheology is the effect of water on the creep rate of different slip systems. Results of deformation experiments demonstrated that the slip system of [100](010) (A-type) dominates at low water content, but that of [100](001) (E-type), then successively [001](100) (C-type) dominates with increasing water content. If the dominant slip system changes in this way, it is expected that the dislocation creep rate of each slip system increases in the order of A-type, E-type and C-type with increasing water content. In this project, the dislocation mobility of each slip system is measured as a function of water content in order to examine the above hypothesis.

The method adopted in this project is the dislocation recovery experiment. In this technique, an olivine crystal is deformed in particular simple shear geometry to activate a specific slip system. The crystal is then doped with water and annealed under identical experimental conditions. The dislocation densities before and after annealing are measured by the oxidation decoration method to observe the change in dislocation density. The oxidation spots, which are considered to indicate presence of dislocations, are observed with an SEM. The dislocation density was calculated from the BSE image by image processing with a procedure developed in this study.

Before determining the water effect, the reliability of the dislocation recovery experiment was confirmed at 3 GPa practically under dry conditions. Since the dislocation annihilation rate should be proportional to the square of dislocation density, $d\rho/dt = k\rho^2$, where ρ is dislocation density and k is the dislocation mobility, the dislocation density should decrease according to the equation $1/\rho - 1/\rho_\mathrm{i} = kt$, where ρ_i is the initial dislocation density. Hence the reciprocal dislocation density increases linearly with time, and the slope and intercept of this line give the dislocation mobility and reciprocal initial dislocation density. Olivine crystals simple-sheared in the [100] direction on the (010) plane were annealed for duration of 5 to 25 hour at 1600 K, to confirm the above relation (Fig. 3.6-7). We also confirmed that the dislocations formed by simple shear in the [100] and [001] directions on the (010) plane have identical mobility.

In parallel with this confirmation, water doping of olivine crystals was attempted by loading the olivine crystal in a Pt capsule with water and a mixture of talc+brucite. The capsule was welded by cooling using ice frozen by liquid nitrogen. It was confirmed that an olivine single crystal can be doped with 500 ppm of water at 1400 K and 5 GPa. However, a number of inclusions often formed in the crystal. We also found a strong extra peak in FT-IR spectra in addition to usual peaks assigned to OH-streching, which can be assigned to Ti-chlinohumite-defects (Fig. 3.6-8), which are most commonly found in natural olivines.

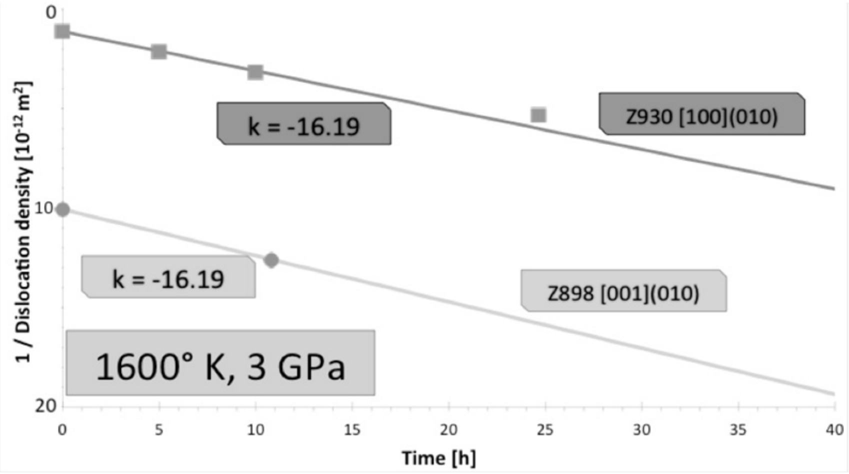

Fig. 3.6-7: Reciprocal dislocation density versus time. The slopes indicate dislocation mobility. The linear trend indicates that the dislocations annihilate by coalescence of two dislocations.

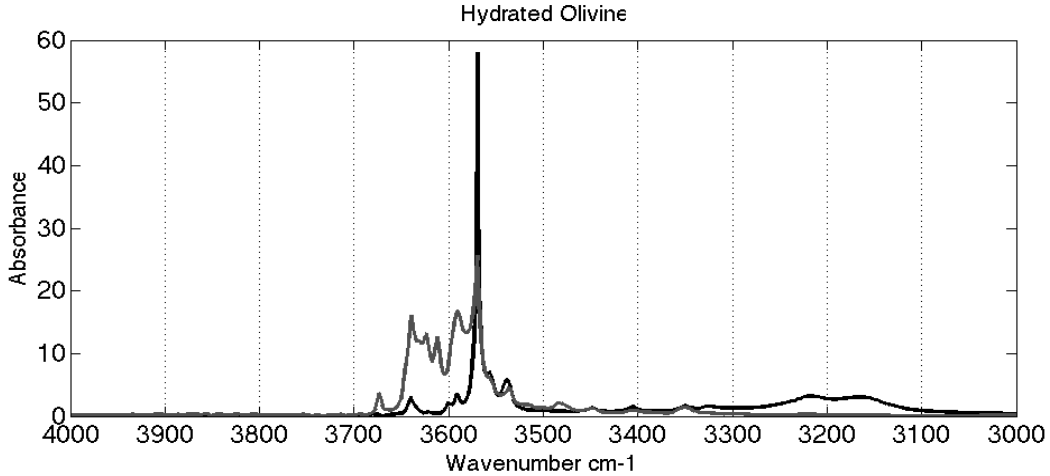

Fig. 3.6-8: Polarized FTIR-measurements in the b-plane of sample Z1061; the highest peak can be assigned to the Ti-clinohumite defect.

g. *Temperature dependence of [100](010) and [001](010) dislocation mobility in natural olivine (L. Wang, S. Blaha, H. Fei, R. Farla, T. Kawazoe, H. Mohseni and T. Katsura)*

Olivine is the most abundant mineral in the upper mantle, and its rheological properties are fundamental to understand mantle dynamics. Knowledge of slip system activation during plastic flow is particularly important to assess flow patterns in the mantle characterized by seismic anisotropy. Natural polycrystalline samples suggest that the most dominant slip system involves dislocation glide in the [100] direction on the (010) plane (A-type), whereas that in the [001] direction on the (010) plane (B-type) seems also activated. Hence an open question is what determines the dominant slip system between these two types.

The dominant slip system is usually determined from deformation experiments on polycrystals. However, stresses and strain rates in deformation experiments are several orders of magnitude higher than those at natural conditions. Therefore, the deformation processes in the deformation experiments could be different from those in the Earth's mantle, if there is a change in deformation mechanism not observed under laboratory conditions. Actually, the stress conditions in the major part of the upper mantle are nearly hydrostatic in the sense of laboratory experiments.

In order to avoid extrapolation in stress, dislocation recovery experiments were conducted in this study in which dislocation mobility is measured under quasi-hydrostatic conditions. The mobilities of dislocations formed by the A- and B-type slip systems were measured as a function of temperature, in order to examine whether temperature is a key parameter for the dominant slip system.

Dislocations were introduced by deformation at 3 GPa and 1600K under simple shear geometry and then several deformed single crystals with suitable high dislocation densities were recovered. The crystals were ideally oriented for activation of dislocation glide in either the [100] or [001] direction on the (010) plane. The deformed crystals were subsequently cut and annealed at temperatures between 1470 and 1770 K at ambient pressure for certain durations.

Dislocations were highlighted using the oxidation-decoration technique. Dislocation densities before and after annealing were imaged and measured using a SEM equipped with a backscatter electron detector. The dislocation mobility (k) was obtained from the following equation, $k = (1/\rho_f - 1/\rho_i)/t$, where ρ_f and ρ_i are dislocation densities after and before annealing respectively, and t is the annealing time.

The dislocation density decreases systematically by annealing (Fig. 3.6-9). A- and B-type slip seem to form predominantly edge and screw dislocation lines elongated in the [001] direction, which are hereafter called A- and B-type dislocations, respectively. The mobilities calculated for A- and B-type dislocations are shown in the Arrhenius plot (Fig. 3.6-10). We observe that the mobilities of these two types of dislocations are almost identical. By fitting the Arrhenius equation, the activation energies for the A- and B-type dislocations are found to be E_A = 390±80 and E_B = 420±120 kJ/mol. Thus, the activation energies of dislocation mobility in these two types of dislocations are also identical within experimental errors.

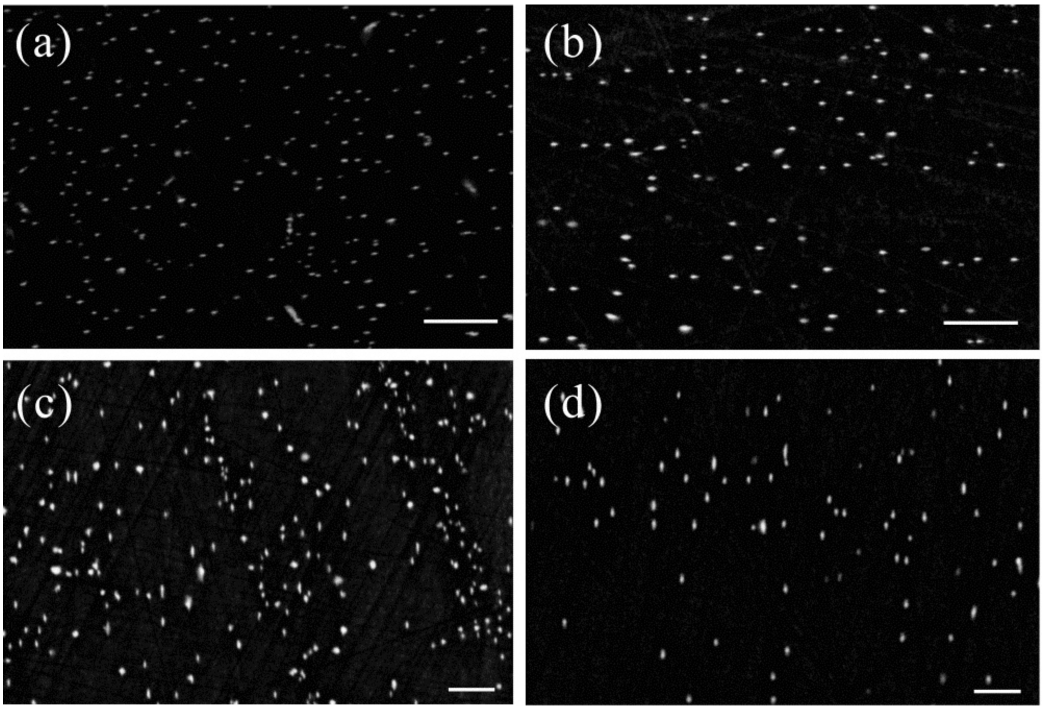

Fig. 3.6-9: Backscattered electron images of the oxidation-decorated olivine. The bright spots are expected to indicate presence of dislocations. The scale bars denote 2 µm. (a) and (b): A-type, (c) and (d): B-type. (a) and (c) are before annealing, whereas (b) and (d) are after annealing at a temperature of 1770 K for 20 and 30 minutes, respectively. Densities of both types of dislocation decreased by the annealing.

The similarity of activation energies suggests that temperature alone does not control activation of a dominant slip system. We note that these activation energies are identical to that of Si self-diffusion (410±30 kJ/mol). This suggests that Si diffusion controls dislocation motion under low-stress conditions.

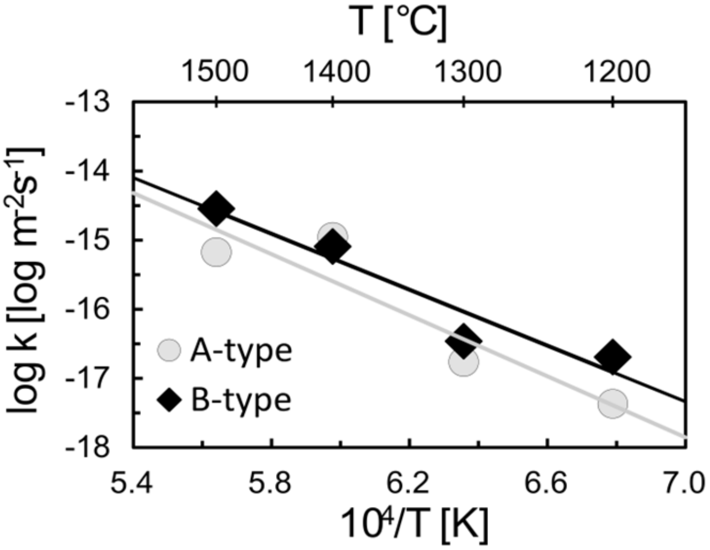

Fig. 3.6-10: Dislocation mobility of A- and B-type dislocations versus the reciprocal temperature. The mobilities of these two types of dislocations are almost identical.

3.7 Materials Science

One of the main goals of experimental geosciences is to model processes and mineral behaviour in the Earth's interior. High-pressure material science and technology apply the same methods and methodologies as experimental geoscientists do but to a much wider class of materials. At the Bayerisches Geoinstitut, unique high-pressure equipment and *in situ* technologies are available that allow sophisticated and challenging research into the physics and chemistry of materials at extreme conditions. In this annual report, we present results of studies of various classes of solids – metal alloys, borides, simple and complex oxides, and oxychlorides.

Although superconductivity was discovered more than 100 years ago, the synthesis of new superconductors based on theoretical predictions has so far remained elusive. In 2010, a new compound, iron tetraboride (FeB_4), has been predicted to be a superconductor with a brand-new crystal structure. This new material, made from cheap and commercially available iron and boron, was successfully synthesised at high pressures and temperatures. Single crystal X-ray diffraction studies reveal that it exhibits the predicted crystal structure. Moreover, it was found to be a superconductor and unexpectedly hard. Iron and manganese tetraborides (other compounds which structure and properties are reported this year) open up a new class of highly desirable materials combining advanced mechanical and electronic or magnetic properties.

Perovskites (general formula ABO_3) are an extremely common class of oxide materials that find applications in almost all spheres of human activities. They demonstrate enormous chemical and structural flexibility and a large variety of physical properties, *e.g.*, ferroelectricity, superconductivity, colossal magnetoresistance, and multiferroicity. The perovskite structure provides two types of sites for metal cations: octahedrally-coordinated *B* sites and *A* sites with variable coordination number. In the overwhelming majority of perovskites, the *A* and *B* cations play different roles in the realisation of the material properties: the octahedrally-coordinated transition metal *B* cations take part in charge transfer and magnetic interactions, whereas the *A* cations remain electronically inactive. For example, one of the most important and industry-relevant sub-classes of perovskites is manganite perovskites, $AMnO_3$, in which the Mn ions exclusively occupy the *B*-sites in the crystal structure. Two new phases of Mn_2O_3, corundum-type and perovskite-type Mn_2O_3, were obtained by high-pressure high-temperature synthesis. The observation of the perovskite structure in simple Mn_2O_3 challenges the main conjecture of perovskite science and technology which so far assumed a strict separation of the *A*- and *B*-sites in the crystal structure, with the former being occupied by electronically inactive (alkali, alkali-earth, rare-earth) metals and the latter by transition metals.

Multiferroic materials are at the focus of intensive scientific research in modern solid state physics and chemistry. Multiferroics demonstrate the coupling of electric and magnetic properties and are important for the development of new electronic devices in which magnetism is controlled by an electric field. A high-pressure study of novel multiferroic compound $PbFe_{0.5}Nb_{0.5}O_3$ at Bayerisches Geoinstitut has revealed a complex behaviour of this material and points towards the possibility of synthesising new polymorphs at elevated pressures.

a. *Pressure-induced phase transitions in transition-metal oxychlorides (M. Bykov and S. van Smaalen/Bayreuth; E. Bykova and L.S. Dubrovinsky; M. Hanfland/Grenoble; H.-P. Liermann/ Hamburg)*

The class of isostructural layered compounds *M*OCl (*M* = Ti, V, Cr, Fe) has been recently studied due to their low-dimensional magnetic properties. It was shown that the different number of *d* electrons on the M^{3+} strongly affects the low-temperature behaviour of *M*OCl and accounts for the entirely different magnetism of these compounds. While FeOCl, VOCl and CrOCl exhibit antiferromagnetic ordering with different types of superstructures at low temperatures, TiOCl undergoes two phase transitions forming a nonmagnetic spin-Peierls state below 67 K. Recently, high-pressure studies on TiOCl have demonstrated the high sensitivity of its electronic and structural properties to the degree of compression. High-pressure structural phase transitions in TiOCl are reminiscent of those at low temperatures, however, a number of discrepancies in the interpretation of high-pressure data still remain. We have discovered pressure-induced phase transitions in FeOCl and CrOCl by means of single-crystal X-ray diffraction in a diamond anvil cell.

*M*OCl structures can be described in terms of *M*-O double layers sandwiched between Cl layers thus forming slabs that are stacked along the crystallographic **c** axis (Fig. 3.7-1). The slabs are formed by sharing O-O and O-Cl edges of the distorted cis-MO_4Cl_2 octahedra and they are connected by weak van der Waals interactions. Due to the layered nature, *M*OCl

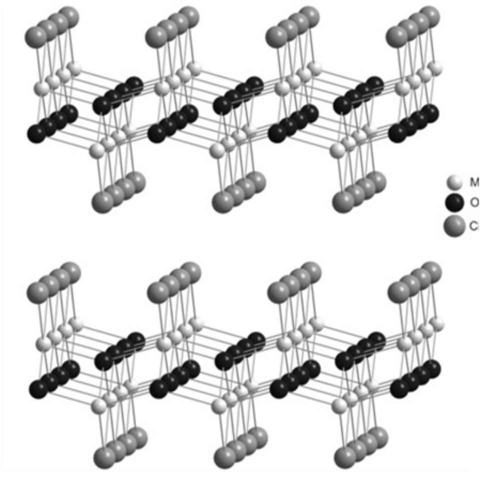

Fig. 3.7-1: Ambient-pressure layered structure of *M*OCl (*M* = Ti, V, Cr, Fe)

structures exhibit a noticeable response to the applied pressure. So, the linear compressibility of the **c** axis (perpendicular to the layers) is several times larger than those of **a** and **b** axes. Highly anisotropic compression of these compounds leads to structural instabilities at high pressure and they undergo phase transitions in the vicinity of 15 GPa, which are accompanied by the formation of $4a \times b \times 2c$ and $7a \times b \times 2c$ superstructures of FeOCl and CrOCl respectively. The high-pressure superstructures reveal an antiphase buckling of the *M*-O bilayers, with a noticeable variation of the interlayer distances (Fig. 3.7-2). We suggest that the phase transitions and resulting structures are controlled by Cl-Cl interactions. At ambient conditions the interlayer Cl-Cl distances are close to the sum of their van der Waals radii, while the intralayer Cl-Cl distances are larger, because they are defined by a rigid *M*-O framework. Therefore, *M*OCl structures are to a certain extent frustrated systems, since an optimal packing of Cl atoms is not realized. Up to 15 GPa, the packing density of chlorine is increased by a large decrease of interlayer Cl-Cl distances. The *M*-O framework is much more rigid, so that the intralayer Cl-Cl van der Waals contacts are hardly affected by pressure.

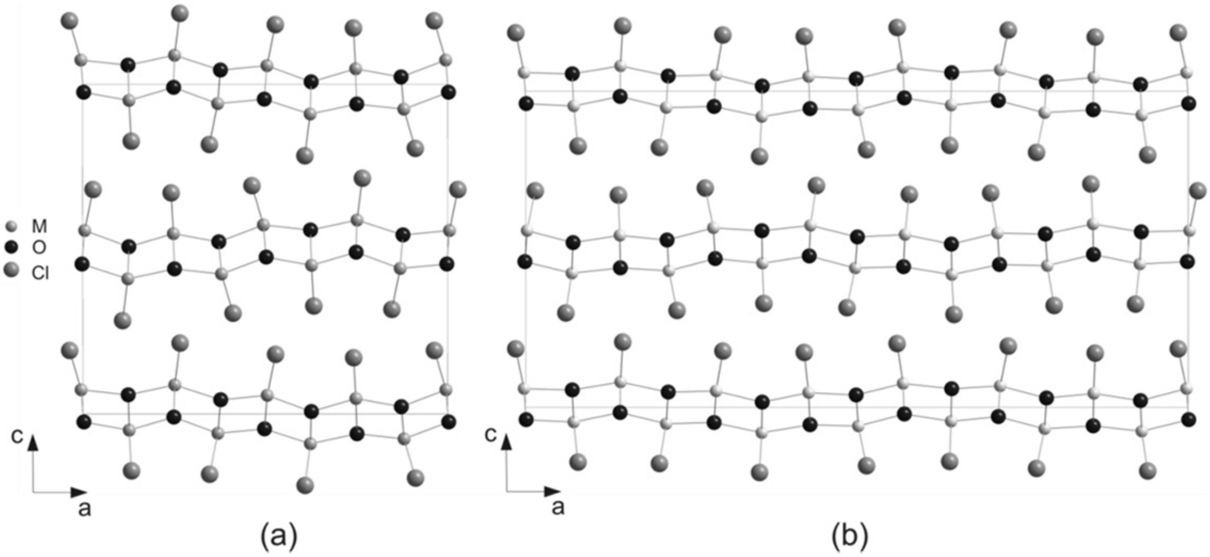

Fig. 3.7-2: High-pressure superstructures of FeOCl (a) and CrOCl (b) at P ≈ 23 GPa

The distortions defining the superstructure of the high-pressure phase allow an increase of both the interlayer and intralayer packing density in two ways. First, regions exist of increased intralayer Cl-Cl distances. This allows for interpenetration of layers and each Cl atom of one layer is exclusively coordinated to Cl atoms of the neighboring layer. Second, within the other regions, the intralayer Cl-Cl distances are decreased, such that their distances are optimized. The antiphase buckling of the layers within the high-pressure phase leads to both types of regions. The proposed mechanism for the high-pressure phase transition of FeOCl and CrOCl is essentially different from the mechanism proposed for TiOCl, where the phase transition is attributed to spin-Peierls-like interactions between Ti^{3+}, followed by the formation of superstructures, involving alternation of Ti-Ti distances. On the other hand, the proposed model of partial interpenetration of chlorine layers may also contribute to the pressure-induced phase transitions in TiOCl. This alternative interpretation of the mechanism of the transition in TiOCl may explain the discrepancies between experimental data on high-pressure behaviour of TiOCl from different sources.

b. *Pressure-induced structural phase transition in multiferroic* $PbFe_{0.5}Nb_{0.5}O_3$ *(D.P. Kozlenko, N.T. Dang, E.V. Lukin and S.E. Kichanov/Dubna; L.S. Dubrovinsky)*

Multiferroic materials are extremely important for development of new electronic devices. They exhibit coupling between electric and magnetic properties, which provides possibilities of controlling their magnetic properties by application of an electric field or vice versa. These materials are at the forefront of extensive scientific research in modern condensed matter physics.

$PbFe_{0.5}Nb_{0.5}O_3$ is a nonconventional multiferroic relaxor with a diffuse transition to ferroelectric state. The polar rhombohedral *R3m* phase is formed in $PbFe_{0.5}Nb_{0.5}O_3$ below T = 354 K, and another intermediate polar tetragonal *P4mm* phase exists in the temperature range 354-383 K.

It is well known that application of high pressure can stabilize novel phases of materials not existing at ambient conditions. In order to search for the structural phase transitions in $PbFe_{0.5}Nb_{0.5}O_3$, Raman spectroscopy and X-ray diffraction experiments were performed at high pressures up to 30 GPa. The Raman spectra obtained at selected pressures, are shown in Fig. 3.7-3. At pressures above 7.5 GPa, an appearance of additional modes at 380 and 760 cm^{-1} were observed, indicating a structural phase transition. From additional XRD experiments performed at P02.2 beamline at Petra-III, DESY, a possible symmetry of the high-pressure phase is established as monoclinic with space group *Pm*. The values of structural parameters are evaluated at P = 27.2 GPa are a = 3.895(3), b = 3.933(3), c = 3.862(3) Å, β = 89.5°.

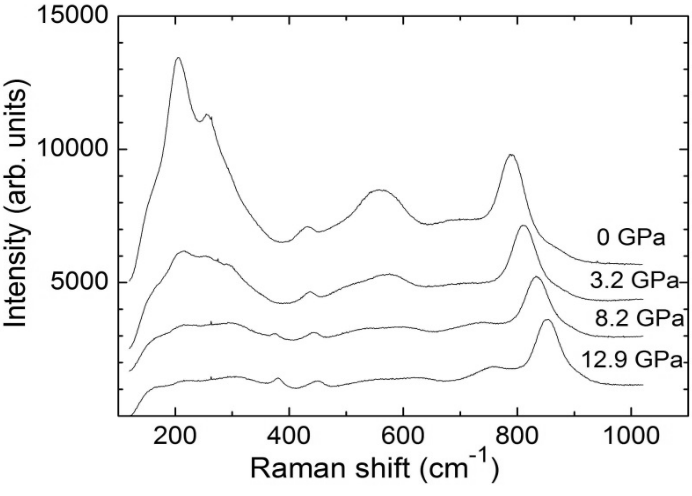

Fig. 3.7-3: The Raman spectra of $PbFe_{0.5}Nb_{0.5}O_3$ obtained at selected pressures

c. *Synthesis and superconductivity of FeB$_4$ (H.Y. Gou; N.A. Dubrovinskaia/Bayreuth; L.S. Dubrovinsky; A.A. Tsirlin, D. Kasinathan and W. Schnelle/Dresden)*

The design of and search for novel superconductive materials have been the subject of active research with both experimental synthesis and first-principles calculations. Despite such efforts, superconductors remain among the most challenging materials to develop. Recently, Kolmogorov *et al.*, using a high-throughput evolutionary algorithm method, predicted a new orthorhombic FeB$_4$ phase with a superconductive temperature of 15-20 K. However, this FeB$_4$ phase has not been synthesized to date and it properties are unknown.

In this study FeB$_4$ was synthesized under high-pressure high-temperature conditions using the piston-cylinder and multianvil apparatus in a pressure range from 3 GPa to 20 GPa at temperatures between 1323 K and 1973 K. A SEM image of a cross-section of a FeB$_4$ sample is shown in Fig. 3.7-4. The morphology and chemical composition of the synthesized samples were studied by means of the scanning electron microscopy (SEM) (LEO-1530). The measurements of magnetic susceptibility were performed in Dresden with the Quantum Design MPMS SQUID magnetometer in the temperature range 2-300 K in applied magnetic fields up to 5 T. The samples were glued on paper using the standard GE varnish. The diamagnetic contribution of the paper and varnish assembly is negligibly small, as checked in an independent measurement run without the sample. Heat capacity was measured by a relaxation technique using the Quantum Design PPMS in the temperature range of 1.8-20 K. Measurements in a broader temperature range are presently impossible owing to the very small size of available samples.

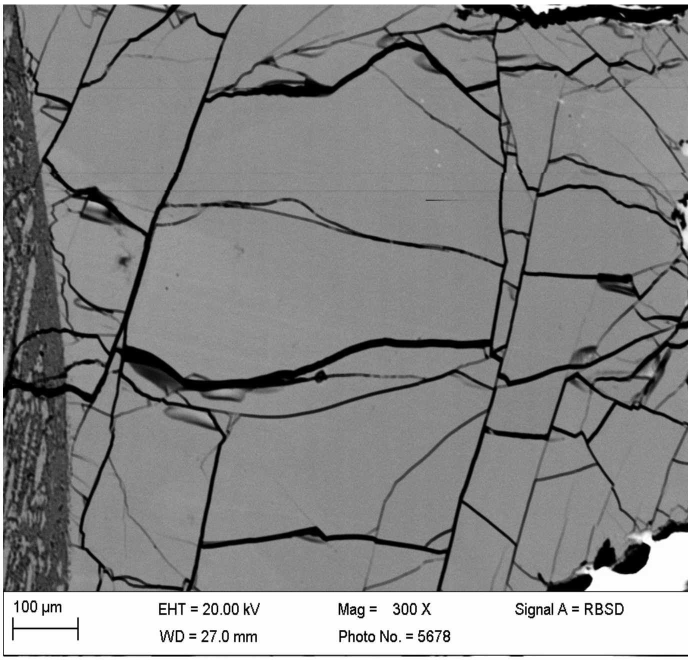

Fig. 3.7-4: A SEM image of a cross-section of the FeB$_4$ sample synthesized at 12 GPa and 1673 K.

Magnetic susceptibility measurements under zero field-cooling (ZFC) conditions reveal a strong diamagnetic response of FeB_4 samples below 3 K (Fig. 3.7-5). Above 3 K, FeB_4 is weakly paramagnetic with a nearly temperature-independent susceptibility above 70 K. Furthermore, we compared samples containing different boron isotopes. The sample enriched with the heavier B isotope shows a lower superconducting transition temperature (T_c = 2.89 K and 2.95 K for the $Fe^{11}B$ and $Fe^{10}B$ samples, respectively), as expected for a phonon-mediated superconductor. Indeed, our tentative estimate of the isotope shift yields $\Delta T_c \sim 0.05$ K in good agreement with $\Delta T_c \sim 0.06$ K, as found experimentally. The bulk nature of superconductivity is also confirmed by heat capacity measurements showing a jump at the superconducting transition around 3 K.

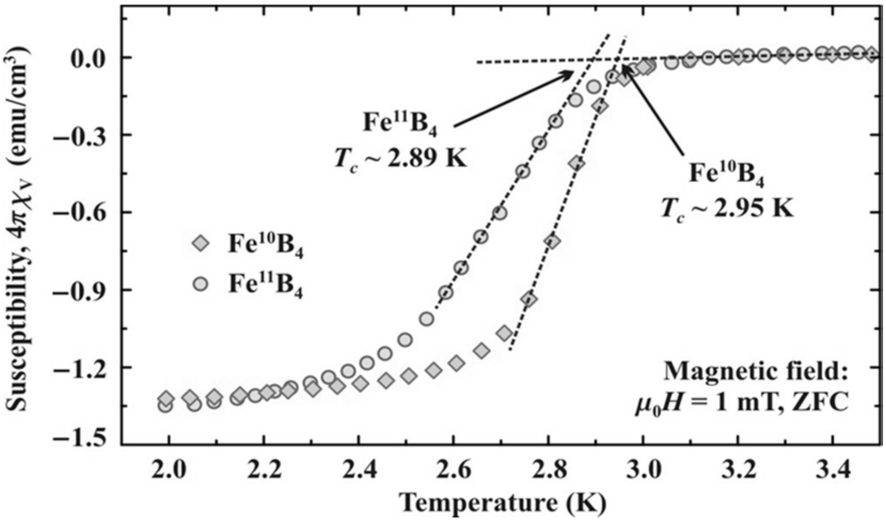

Fig. 3.7-5: Magnetic susceptibility of FeB_4 measured in an applied field of 1 mT zero-field-cooling. Two sets of data were collected on the samples enriched with ^{10}B and ^{11}B isotopes. Dashed lines denote the procedure for determining the onset temperature.

d. *High-pressure synthesis and studies of mechanical properties of MnB_4 (H.Y. Gou, S.V. Ovsyannikov, A. Kurnosov, D.M. Trots and E. Bykova; N.A. Dubrovinskaia/Bayreuth; L.S. Dubrovinsky)*

Synthesis of MnB_4 with a monoclinic *C2/m* structure was previously reported in the literature. However, this monoclinic phase was suggested to be unstable from recent theoretical predictions and instead an orthorhombic FeB_4-type structure for MnB_4 was found to be energetically more favorable. In this study, high-quality single crystals and powders of MnB_4 were produced to verify the structure and measure the mechanical properties of MnB_4.

MnB_4 single crystals and powder samples were synthesized at pressures of 3-12 GPa and temperatures of 1080-1600 °C (heating duration was 1 hour) in the piston-cylinder and the multianvil apparatus using high-pressure assemblies and *h*-BN capsules. Scanning electron microscopy (SEM) images of a cross-section of sintered MnB_4 are shown in Fig. 3.7-6.

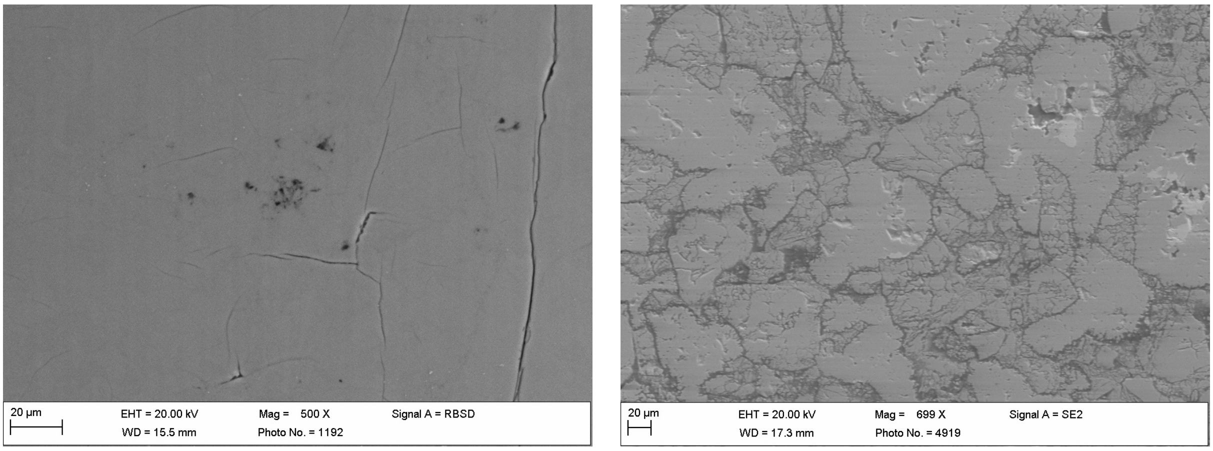

Fig. 3.7-6: SEM images of MnB_4. A single crystal (left) was synthesized at 12 GPa and 1873 K and a polycrystalline sample (right) was synthesized at 3 GPa and 1373 K.

To study the compressibility of MnB_4 by means of *in situ* high-pressure powder X-ray diffraction a piston-cylinder-type diamond anvil cell was used with a culet size of 350 µm and with a rhenium gasket. A powder sample of MnB_4 of ~ 20 µm in size was loaded into a hole of ~ 150 µm in diameter in the rhenium gasket pre-indented to ~ 50 µm. Using a gas-loading apparatus at BGI, the hole was filled with a neon pressure-transmitting medium. The XRD experiments (with the X-ray wavelength of $\lambda = 0.29135$ Å) were carried out at the PETRA III beamline P02.2 at DESY (Hamburg). Pressure values were determined by the shift of the ruby luminescence line. The data were collected using a PerkinElmer XRD1621 detector and then the 2D XRD images were integrated using Fit2D program.

The obtained variations of the volume and lattice parameters of MnB_4 with pressure up to 25 GPa are presented in Fig. 3.7-7. Fitting the *P*-*V* data with the third-order Birch-Murnaghan equation of state (Fig. 3.7-7, left) gives a bulk modulus value of K_0 of ~ 259 GPa at fixed $K' = 4$. This value is almost the same as those reported for FeB_4, 252(5) GPa, SiC, 248 GPa, and Al_2O_3, 252 GPa. The high incompressibility of MnB_4 along the *b* direction (Fig. 3.7-7, right) can be linked to the shorter B-B distances along this direction in the structure, in comparison with the other crystallographic directions. One can also notice that the boron-manganese bonds are parallel to the *b* direction.

The Vickers hardness of monoclinic MnB_4 was found to be 37.4 GPa at a load of 9.8 N and 34.6 GPa at 14.7 N, which is larger than that of 5*d* transition metal borides, WB_4 (28.1 GPa or 31.8 GPa at 4.9N), ReB_2 (18 GPa at 9.8 N, 26.0-32.5 GPa or 26.6 GPa at 4.9N), OsB_2 (19.6 GPa or 16.8 at 4.9 N). Remarkable mechanical properties of MnB_4 may make it potentially interesting for applications as a functional material.

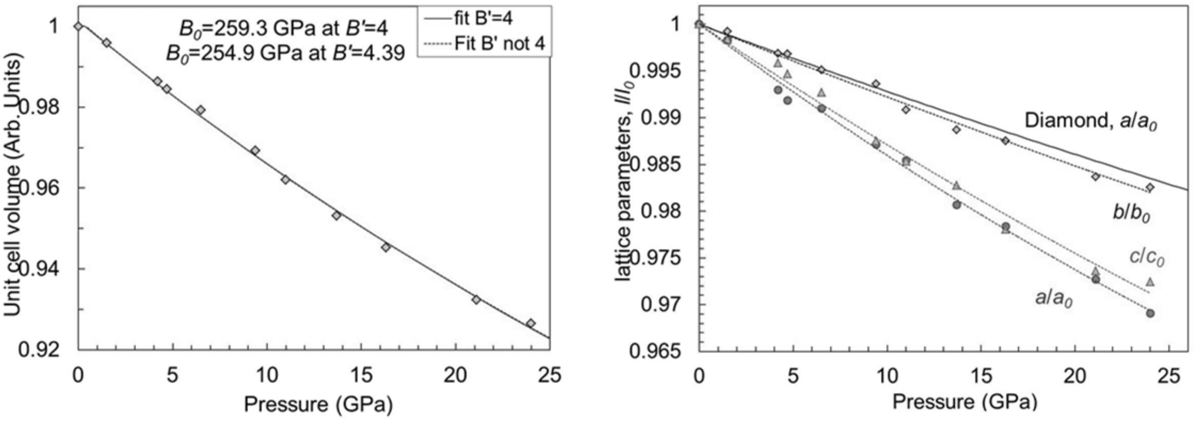

Fig. 3.7-7: The pressure dependence of the unit cell volume (left) and the individual lattice parameters (right) for MnB_4 up to 25 GPa.

e. *High-pressure, high-temperature synthesis and properties of the perovskite phase of Mn_2O_3 (S.V. Ovsyannikov, K.V. Glazyrin and L.S. Dubrovinsky; A.M. Abakumov/Antwerp, A.A. Tsirlin/Dresden, W. Schnelle/Dresden, R. Egoavil/Antwerp, J. Verbeeck/Antwerp, G. Van Tendeloo/Antwerp and M. Hanfland/Grenoble)*

The behaviour of Mn_2O_3 was examined at high-pressure and high-temperature (HP-HT) conditions by sintering the starting pure bixbyite-structured material in a multianvil apparatus and studying the recovered samples *ex situ*. Heating of Mn_2O_3 at temperatures of ~1150–850 K (depending on pressure) and at pressures 10-22 GPa did not result in any transformation. When the material was heated above 1300–1600 K in the same pressure range, it self-reduced to the orthorhombic (space group *Pbcm*) high-pressure phase of Mn_3O_4. Synthesis at temperatures about 1100-1300 K allowed fabrication of two new chemically pure phases of Mn_2O_3, quenchable to ambient conditions. The crystal structures of these phases were solved by using high-quality powder X-ray diffraction (XRD) data collected at ID31 lines at ESRF.

One of the newly synthesized phases has been refined in the corundum-type structure (space group $R\overline{3}c$) with the unit cell parameters as follows: a = 5.0282(9) Å, c = 14.1125(7) Å, and V = 309.01(3) Å^3. This phase is about 1 % denser than the ambient cubic bixbyite-structured Mn_2O_3.

The intensity distribution on the powder XRD patterns of the second HP-HT phase of Mn_2O_3 (Fig. 3.7-8a) is reminiscent of a perovskite structure with a subcell of $a_p \approx 3.67$Å. Electron diffraction (ED) patterns of this phase obtained with a Tecnai G2 microscope suggested a face-centered triclinically distorted supercell with $a = 4a_p \approx 14.7$Å. The perovskite-type structure of ζ-Mn_2O_3 can be directly visualized using annular bright-field scanning transmission electron microscopy (ABF-STEM) (Fig. 3.7-8b). A perovskite octahedral framework with heavily tilted MnO_6 octahedra is clearly marked by the projections of the MnO and O columns on the ABF-STEM image (Fig. 3.7-8b). The crystal structure of the perovskite-type Mn_2O_3 was determined within the $a = 4a_p$ supercell (space group $F\bar{1}$ (no. 2, *P*

$\bar{1}$ in the standard settings), a = 14.6985(2) Å, b = 14.6482(2) Å, c = 14.6705(2) Å, α = 89.2108(8)°, β = 89.2031(9)°, γ = 89.196(1)°, V = 3157.73(9) Å^3, Z = 64 (Fig. 3.7-8). This phase is about 5 % denser than the ambient cubic bixbyite-structured Mn_2O_3. The perovskite structure of Mn_2O_3 (Fig. 3.7-8c) is a distorted variant of $AA'_3B_4O_{12}$ perovskite. Bond valence sums (BVS) analysis found somewhat larger BVS of 3.4 for the Mn_B positions and.strongly underbonded the Mn_A positions with the average BVS of 1.4. Therefore, the valence distribution in the perovskite structure could be as follows: $Mn^{2+}(Mn^{3+})_3(Mn^{3.25+})_4O_{12}$. This distribution has been directly confirmed by electron energy loss spectroscopy (EELS) that found 14(2) % of Mn^{2+}, 72(2) % of Mn^{3+}, and 13(4) % of Mn^{4+}.

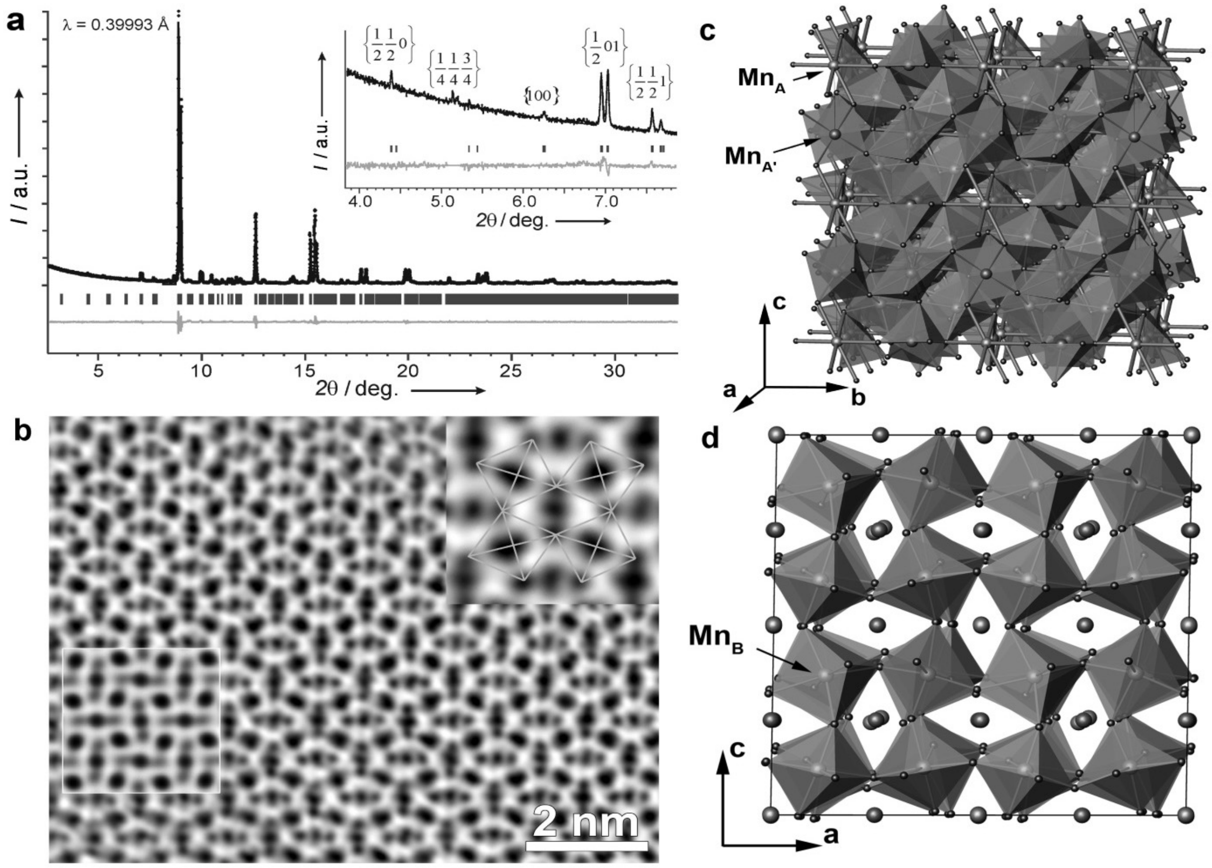

Fig. 3.7-8: Structural characterization of perovskite-type Mn_2O_3 at ambient conditions. (***a***) Rietveld refinement of a high-resolution X-ray diffraction pattern collected at ID31 of ESRF. The inset shows the low-angle part with the superstructure reflections indexed in the a_p perovskite subcell. Vertical bars mark the reflection positions for the triclinic $4a_p \times 4a_p \times 4a_p$ unit cell used in the Rietveld refinement. (***b***) ABF-STEM image taken along the $<100>_p$ perovskite direction (the enlarged part of the image (top right corner) shows the projections of the corner-sharing in-phase tilted MnO_6 octahedra which are traced by the lines), (***c***) the crystal structure of perovskite-type Mn_2O_3. The Mn_B cations are situated in the octahedra, $Mn_{A'}$ cations are at the centres of the tetragonal pyramids and octahedra, Mn_A cations are shown as spheres. Oxygen atoms are shown as small spheres. (***d***) the framework of corner-sharing Mn_BO_6 octahedra demonstrating the in-phase cooperative tilting distortion.

Magnetic susceptibility was measured with the Quantum Design MPMS SQUID magnetometer in the temperature range 2-380 K in applied fields up to 5 T under both field-cooling (FC) and zero-field-cooling (ZFC) conditions. Heat capacity was measured with Quantum Design PPMS in the temperature range 1.8-320 K using the relaxation method. Above 200 K, the magnetic susceptibility (χ) of the perovskite-type Mn_2O_3 follows the Curie-Weiss law $\chi = C/(T-\theta)$ with an effective magnetic moment of 5.5(1) μ_B and a Curie-Weiss temperature of θ = -320(5) K (Fig. 3.7-9). The negative θ value confirms the predominantly antiferromagnetic nature of the perovskite-type Mn_2O_3. At low temperatures, magnetic susceptibility and heat capacity measurements consistently identify two phase transitions at T_1 = 99 K and T_2 = 47 K (Fig. 3.7-9).

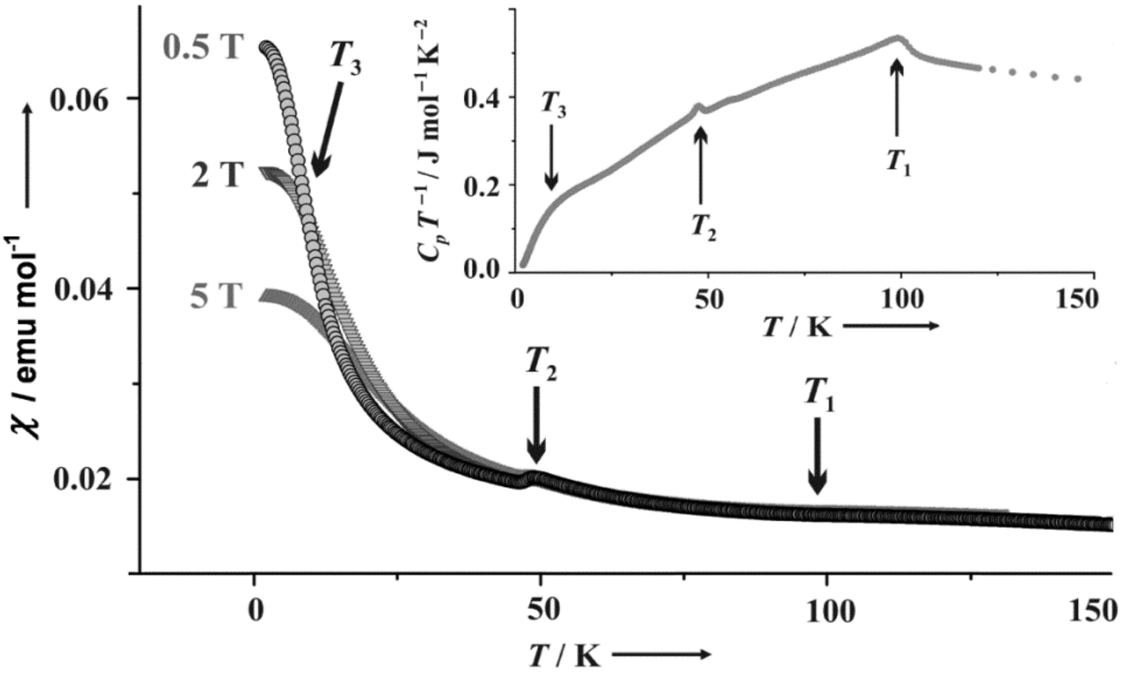

Fig. 3.7-9: Magnetic susceptibility of perovskite-type ζ-Mn_2O_3 measured in applied fields of 0.5-5 T. Zero-field heat capacity is shown as an inset. The characteristic temperatures of T_1 = 99 K, T_2 = 47 K, and T_3 = 12 K are marked with arrows.

Thus, Mn_2O_3 demonstrates an unprecedented example of a binary oxide that can adopt a complex distorted perovskite structure. Since the *A*-type position generally requires a large cation, the respective Mn ions are partially reduced to achieve Mn^{2+} with the higher ionic radius of IR = 0.93 Å. The ions in the *A'*-type positions retain the oxidation state +3 (IR = 0.65 Å), in order to keep the strong Jahn-Teller distortion and the four-fold first coordination sphere. The *B*-type positions can accommodate Mn atoms in different oxidation states and partially host oxidized Mn^{4+} cations (IR = 0.54 Å) that balance the reduction of the Mn ions on the *A* site.

f. *Incompressible alloys under high pressure (K.V. Yusenko/Oslo; E. Bykova; M. Bykov/Bayreuth; L.S. Dubrovinsky)*

Platinum group metals (PGM) and Re are known as chemically stable hard metals with very high melting temperatures. Pure Ir, Os and Re are very incompressible with bulk moduli comparable to diamond. Nevertheless, the experimental data on compressibility of solid solutions of these metals are absent. Information about high-pressure, high-temperature behaviour and mechanical properties of PGM-Re and PGM-Os solid solutions may lead to the discovery of new materials with unique properties for applications at extreme conditions.

In this study, Ir_xOs_{1-x} samples were prepared by thermal decomposition of single-source precursors $(NH_4)_2[Ir_xOs_{1-x}Cl_6]$ in a 10%-H_2/90%-N_2 gas-flow chamber for 0.5 h at 600 °C with further natural cooling to the room temperature for 10 h. 7 samples in the whole range of concentrations were prepared. Four samples with Os concentrations greater than 45 at.% appeared with hcp structure. The hcp-$Ir_{0.55}Os_{0.45}$ and hcp-$Ir_{0.40}Os_{0.60}$ phases have compositions close to limiting stability regions of fcc and hcp phases correspondingly. hcp-$Ir_{0.50}Os_{0.50}$ was in the middle of the miscibility gap between fcc and hcp phases on the experimental phase diagram. Two compositions ($Ir_{0.60}Os_{0.40}$ and $Ir_{0.65}Os_{0.35}$) appeared to be two-phase (fcc+hcp), whilst only a single sample ($Ir_{0.80}Os_{0.20}$) was an fcc single-phase solid solution.

The compressibility of synthetic fcc-$Ir_{0.80}Os_{0.20}$, hcp-$Ir_{0.20}Os_{0.80}$, and hcp-$Ir_{0.55}Os_{0.45}$ solid solutions were investigated at pressures up to 55 GPa, and hcp-$Ir_{0.40}Os_{0.60}$ up to 145 GPa. High-pressure powder X-ray diffraction data on fcc-$Ir_{0.80}Os_{0.20}$, hcp-$Ir_{0.20}Os_{0.80}$, and hcp-$Ir_{0.40}Os_{0.60}$ were collected at room temperature at ID09A beam-line at ESRF (wavelength 0.4145 Å, MAR 555 flat panel detector, beam size 10x15 μm^2), and on hcp-$Ir_{0.55}Os_{0.45}$ at 13-IDD at APS (wavelength 0.31 Å, CCD MAR 345 detector, beam size 2x4 μm^2). Diamond anvil cells with culet sizes of 250 µm (in experiments to 55 GPa) and a diamond anvil cell with a bevelled culet of 120 µm (in experiment with maximum pressure 145 GPa) were used. Rhenium gaskets were pre-indented to a thickness of about 20 µm and holes with a diameter of about one half of the culet size were drilled in the centre of the indentation. Mineral oil was used as pressure transmitting medium in experiments at ESRF, and neon (loaded at pressure 1.3 kbar) was used as a pressure medium in an experiment at APS. Pressure was determined from the lattice parameters of Au, loaded in the pressure chamber as small piece of wire of 5 µm diameter and about 10 µm length, or as a flake of compressed fine powder.

Examples of compressional curves of studied alloys are shown in Fig. 3.7-10. Further analysis is necessary in order to understand peculiarities in the behaviour of each compound. However, preliminary data confirm that all alloys are highly incompressible and no phase transitions were observed at ambient temperature in the studied pressure range. More promising results will be obtained under high-temperature, high-pressure conditions for metastable hcp single phase solid solutions that appear in a two-phase region of the binary phase diagram (hcp-$Ir_{0.40}Os_{0.60}$ and hcp-$Ir_{0.50}Os_{0.50}$) and especially hcp-$Ir_{0.55}Os_{0.45}$, which is close to the maximal solubility of Os in Ir (42 at.%).

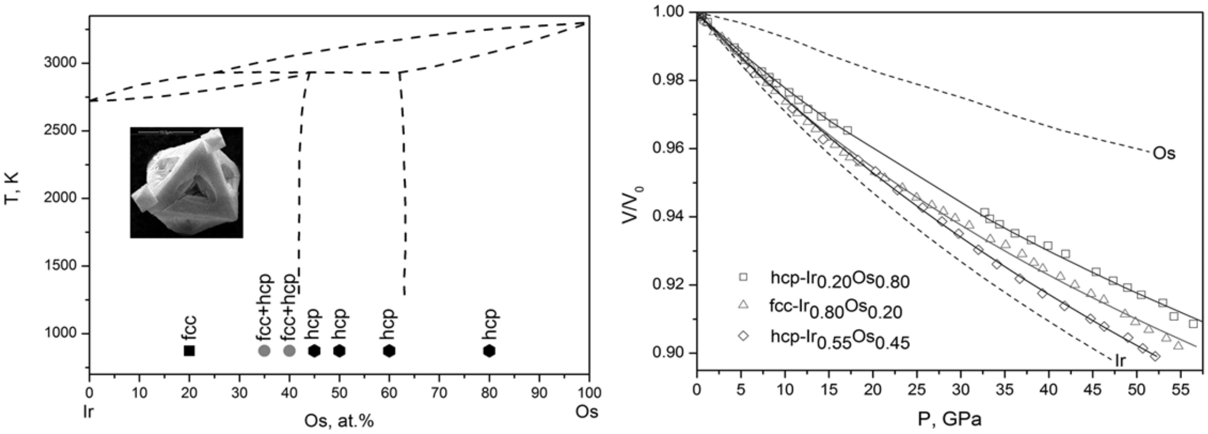

Fig. 3.7-10: Left: existing experimental Ir-Os binary phase diagram (squares and hexagons correspond to fcc and hcp solid solutions; two-phase fcc+hcp samples are shown as circles). Insert shows typical morphology of metallic powders. Right: experimental compressibility curves for three solid solutions (symbols) and calculated curves fitted using the third order Birch-Murnaghan equations of state (lines, data for pure Ir and Os were taken from the literature).

g. *Band gap of Si using a new exchange potential (V. Vlcek and G. Steinle-Neumann; S. Kümmel/Bayreuth)*

In principle, density functional theory (DFT) provides an exact description of the ground state properties of matter. The Kohn-Sham (KS) approach to DFT provides a simplification of the true many-electron problem by substituting the many-body wave function with a set of eigenstates $|\psi_i\rangle$ in an effective KS-potential $\hat{V}$, as

$$\left(\hat{T} + \hat{V}\right)|\psi_i\rangle = \epsilon_i|\psi_i\rangle,$$

with kinetic energy operator $\hat{T}$ and eigenenergy ϵ_i. The K-S potential consists of

$$\hat{V} = \hat{V}_H + \hat{V}_{ext} + \hat{V}_{xc},$$

where $\hat{V}_H$ is the Hartree, $\hat{V}_{ext}$ the external potential, and $\hat{V}_{xc}$ is the exchange and correlation term (xc) that captures the mutual interactions among the electrons. Although both $\hat{V}_H$ and $\hat{V}_{xc}$ are functionals of the charge density, the exact form of $\hat{V}_{xc}$ is not known in general and it has to be approximated while certain conditions (satisfied by an exact functional) are fulfilled.

It is well known that the xc potential can jump discontinuously by a constant Δ upon variation in the number of electrons in the system. In semiconductors and insulators, Δ also contributes to the discontinuous change in the chemical potential upon charge addition and removal and represents a sizable contribution to the fundamental band gap. As most of the commonly used local and semi-local approximations to the xc are smooth functionals of density, they fail to capture Δ and thus incorrectly describe the behaviour of the chemical potential. This leads to the famous "band gap problem" in DFT and a significant underestimation of the fundamental band gaps E_g. Armiento and Kümmel have recently proposed a functional form for generalized-gradient approximation to the exchange functional (AKx) that for finite systems exhibits the discontinuity mentioned. Also, for solid Si at the experimental lattice constant AKx provides a much larger E_g of 1.58 eV while, for instance, the commonly used local density functional gives 0.49 eV.

We have implemented the AKx in an electronic structure code and we here report results obtained for crystalline Si with a lattice constant that minimizes the total energy. In Table 3.7-1 we compare the fundamental band gap E_g, lattice parameters of the primitive cell a_0 and bulk moduli B_0 determined with AKx and with the standard Perdew-Burke-Ernzerhof exchange (PBEx). We also show the results obtained by combining the exchange functionals with PBE correlation, denoted AKx+PBEc and PBExc.

Table 3.7-1: Equation-of-state parameters and band gap E_g of crystalline Si for different approximations to the exchange (x) and correlation (c) potential. E-V results are fit by a third-order finite Eulerian strain expression and equilibrium lattice constants a_0, bulk modulus B_0 and its pressure derivative B_0' are obtained. The band gap E_g is evaluated at the equilibrium lattice constant.

	E_g[eV]	a_0 [Å]	B_0 [GPa]	B_0'
Experiment	1.13	2.72	99	
AKx	0.79	3.04	34	4.5
PBEx	0.98	2.84	64	4.3
AKx+PBEc	1.71	2.91	51	4.5
PBExc	0.63	2.74	88	4.2

Our results show that the AKx and AKx+PBEc functionals tend to overestimate the equilibrium lattice constants and conversely provide very low bulk moduli. Nevertheless, the results for AKx+PBEc indicate that the combination of the new functional with an appropriate correlation term may provide a substantial improvement in *ab initio* electronic structure predictions.

3.8 Methodological Developments

An important goal in both experimental geosciences and material sciences is to develop new experimental techniques as well as improving existing technologies. In order to characterize material properties and behavior under conditions of the Earth's deep mantle and core, an important primary goal is to extend achievable pressure-temperature conditions to higher levels in static experiments performed using multianvil apparatus and diamond anvil cells. High-pressure deformation experiments are used to determine the rheology of the Earth's mantle which is an important parameter that controls large-scale solid state convection and therefore the dynamics of the Earth's interior: in such experiments it is essential to improve methods for characterizing stress and strain rates as well as improving generated pressures and temperatures. An additional goal is to improve methods for measuring *in situ* physical and chemical properties of samples in experiments at high pressures and temperatures. Several contributions in this section describe such developments.

The first contribution describes attempts to reach pressures in the multianvil apparatus that significantly exceed 25 GPa – which is the pressure limit using standard techniques. Although much higher pressures can be reached using sintered diamond anvils, the costs are extremely high (sintered diamond anvils break easily) and achieving high sample temperatures is difficult because diamond is an excellent heat conductor. The approach used here is to utilize tungsten carbide cubes with a specially tapered geometry around the pressure-generating truncated faces. In combination with a reduced sample assembly size, maximum pressures are increased to at least 30 GPa.

The second contribution in this section describes the generation of pressure-temperature conditions (19 GPa and 1800 K) in deformation experiments that are characteristic of the lower part of the transition zone of the Earth's mantle. This development uses the six hydraulic-ram multianvil apparatus at BGI and represents a major advance over previous deformation studies in which maximum pressures were much lower. This opens the possibility for studying rheology of the deep part of the mantle transition zone.

Neutron experiments at high pressures and temperatures give us important information about the behavior of light elements (*e.g.*, H and C) and neighboring elements (*e.g.*, Mg, Al and Si) in crystal structures because neutrons have a scattering cross section that is different from X-rays. The third contribution describes the planning of an efficient detector system that is being combined with the **S**ix **A**nvil **P**ress for **Hi**gh Pressure **R**adiography and Diffraction (SAPHiR) multianvil system at the FRM II neutron source at Garching/Munich. In addition multianvil sample assemblies with large sample volumes and wide anvil gaps are being developed. Both are important for the neutron experiments because of weak neutron signals due to weak neutron-sample interactions.

Gem-quality single crystals of silicate perovskite are essential for studying the elastic properties of the Earth's lower mantle using combined X-ray diffraction and Brillouin spectroscopy at high pressure in a diamond anvil cell. Synthesizing such crystals is very challenging and the current state of progress is described below.

Nickel is an important element in the Earth's deep interior, in particular as a component of the Earth's metallic core. The final contribution in this section describes the characterization of the magnetic and elastic properties of nickel up to 260 GPa using nuclear forward scattering techniques.

a. *Ultrahigh pressure generation in the multianvil cell (R. Myhill, T. Kawazoe and T. Katsura)*

Lower mantle pressures and temperatures are traditionally the reserve of laser-heated diamond anvil cell (LH-DAC) experiments. Despite the enormously valuable contributions made in these studies, experiments are commonly far from thermodynamic equilibrium, and sample volumes are extremely small. Recently, multianvil experiments with sintered diamond anvils have reached pressures corresponding to the lower part of the lower mantle. Multianvil experiments can be performed with larger sample sizes and suffer less from thermal gradients at high temperatures, and as such they represent an potentially valuable alternative to probe changes in mineral behavior in the upper parts of the lower mantle. Relatively little work has been conducted to exploit this possibility.

In this study, we further investigate the use of multianvil experiments with carbide to obtain ultrahigh pressures. We use hard tungsten carbide anvils with truncations of 1.5 mm edge length to compress (Mg,Cr)O octahedral pressure media of 5.3 mm edge length. Each anvil is ground on the three faces adjacent to the truncation to create a 1° taper. This taper imitates the deformation observed in high-pressure experiments, and so increases the efficiency of pressure generation. To reduce deformation of the pressure media and sample, gaskets are shaped to perfectly fill the gaps between the anvils (Fig. 3.8-1).

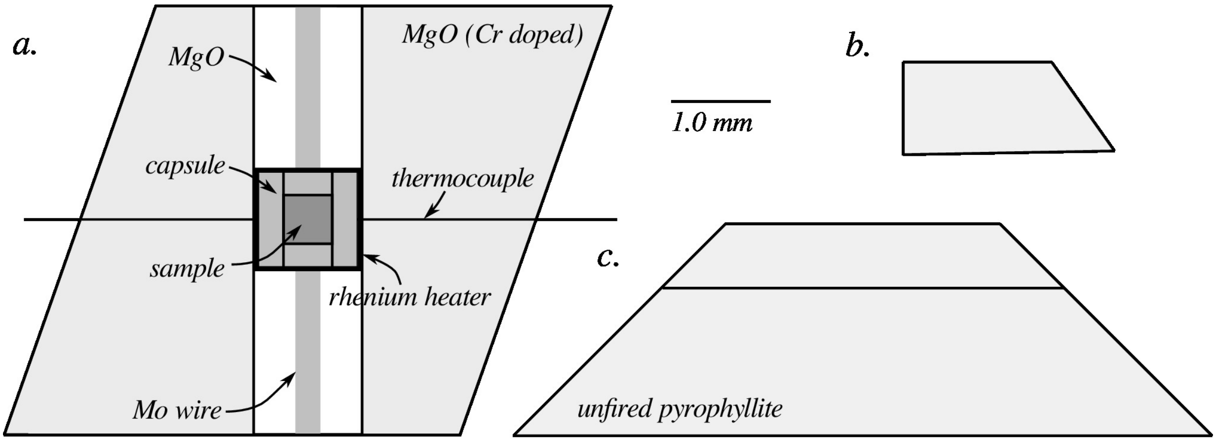

Fig. 3.8-1: HP-HT multianvil assembly design. a) Pressure medium. b) Side view of tapered, truncated gaskets. b) Plan view of gaskets.

For high-temperature experiments, heaters are constructed from rhenium foil. Rhenium foil is very brittle, so to create stable, equally sized heaters, it is necessary to prepare each foil accurately by laser-cutting. Molybdenum wires are inserted along two faces, and thin thermocouple wire is inserted laterally to measure the temperature (Fig. 3.8-1). To estimate pressures obtained by the samples at high temperature, an *in situ* calibrant will be used. This calibrant will take the form of a mineral assemblage with mineral compositions sensitive over the pressure range of interest.

Preliminary pressure calibrations which have been conducted at room temperature to 33 GPa have revealed a high efficiency of pressure generation compared with previous designs (Fig. 3.8-2). These promising results support the continued development of ultrahigh pressure multianvil press techniques.

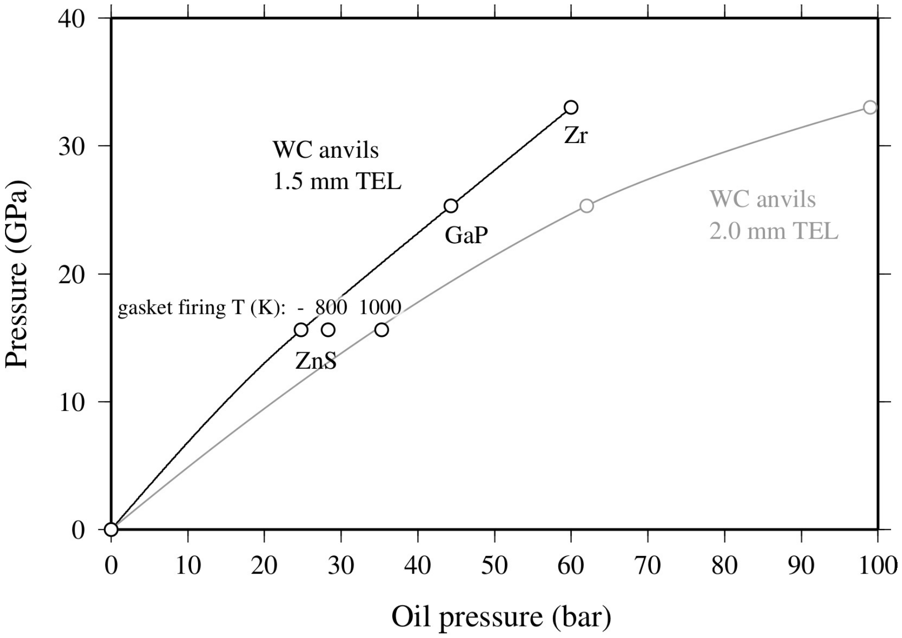

Fig. 3.8-2: High pressure, room temperature pressure-load calibrations with the 5.3/1.5 assembly, compared with the larger 6/2 assembly previously tested in BGI. The three ZnS calibrations were performed with pyrophyllite gaskets fired for 1 hour at different temperatures, to assess the effect of gasket rheology on pressure generation. Gaskets hardened by firing at 800 and 1000 K yield lower sample pressures for a given oil pressure relative to unfired gaskets. This effect is presumably due to the gaskets shielding the pressure medium from the forces exerted by the anvils.

b. *Pressure-temperature generation to 19 GPa and 1800 K in a deformation mode using a six hydraulic-ram multianvil apparatus (T. Kawazoe)*

Deep mantle minerals undergo phase transformations to denser structures at high pressure and temperature, which may result in abrupt changes in rheological properties in the deep parts of the Earth's mantle (*e.g.*, viscosity and crystallographic preferred orientation). Deformation experiments at high pressure and temperature can provide important constraints on such rheological properties of deep mantle minerals, and are accordingly critical for understanding the dynamics of the Earth's deep interior. At the Bayerisches Geoinstitut, deformation experiments have been already succeeded at pressure-temperature conditions of the upper part of the mantle transition zone (to 15 GPa and 1400 K) using a six hydraulic-ram multianvil apparatus. The aim of this project is to extend the pressure-temperature conditions of the deformation experiments with this apparatus to those of the lower part of the mantle transition zone.

Pressure generation experiments were conducted at room temperature and 1800 K to 19 GPa in a deformation mode using the six hydraulic-ram multianvil apparatus combined with a multianvil setup consisting of six inner anvils that compress a cubic sample assembly. I used second-stage tungsten carbide anvils with a truncated edge length of 2.5 mm. Generated pressures were determined using phase transformations of ZnTe, GaAs and $(Mg,Fe)_2SiO_4$. As a result, the present study has extended the pressure range of the deformation experiments in the six hydraulic-ram multianvil apparatus to 19 GPa at 1800 K, which corresponds to conditions of the lower part of the mantle transition zone (Fig. 3.8-3). The present technical development enables us to investigate rheological properties of the deep mantle minerals (*e.g.*, ringwoodite and majorite garnet) under the pressure-temperature conditions of the lower part of the mantle transition zone.

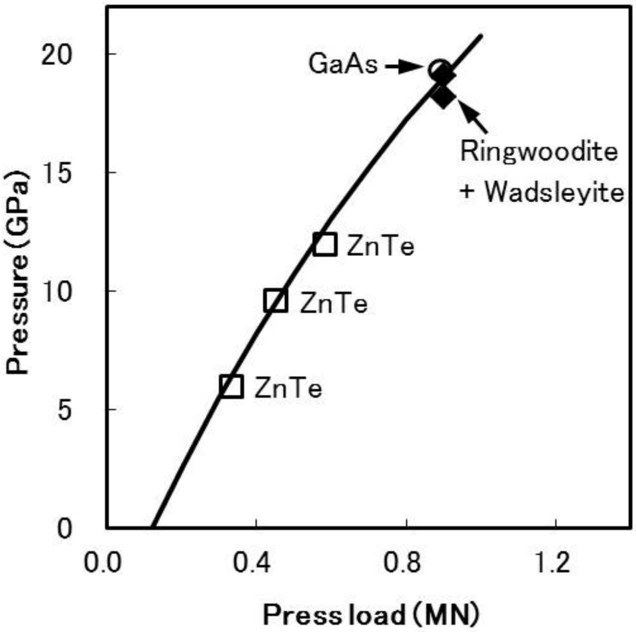

Fig. 3.8-3: Relationship between sample pressure and applied press load. The press load is converted to that of a DIA-type cubic-anvil apparatus.

c. *Development of the neutron radiography and scattering instrument SAPHiR at FRM II (N. Walte and H. Keppler)*

The **S**ix **A**nvil **P**ress for **Hi**gh Pressure **R**adiography and Diffraction (SAPHiR) is an ongoing BMBF funded project to provide an instrument for producing extreme pressure and temperature conditions at the FRM II (*Forschungsreaktor München II*) neutron source in Garching. The six-axis press has been set-up at the end of last year (see 2011 BGI Annual Report) and is the first operating instrument in the new eastern instrument hall (Fig. 3.8-4). In addition to the identical prototype press at the Bayerisches Geoinstitut, an x-y-z-rotation table has been constructed that allows aligning the whole 50 ton press within micron precision in the neutron beam. The second three-year BMBF funding period started this summer and is mainly dedicated to constructing the neutron detectors and to make the instrument fully operational for the FRM II user program. The detector planning and construction is done in collaboration with the FRM II detector group under the leadership of Dr. Karl Zeitelhack.

Since the neutrons can only enter and leave the sample assembly through the gaps of the second stage anvils (Fig. 3.8-5), neutrons can only be detected at an angle of 90° from the

Fig. 3.8-4: The SAPHiR instrument at FRM II in Garching. The large wooden case on the left contains the recently delivered 640 position-sensitive ^{3}He detector tubes. The future neutron beam will come from the right.

incoming beam and in the back- and forward scattering region. Due to this scattering angle limitation the time-of-flight (TOF) scattering method is employed using thermal neutrons with a wavelength range of 1-2.4 Å and the detectors are planned to cover as much of the available space as possible. The detector banks perpendicular to the primary beam and in the forward-scattering area will be equipped with position-sensitive ^{3}He detector tubes, while the backscatter region will be covered with four wavelength-shifting-fiber scintillation detectors. In combination, the TOF detector system will cover a Q-range from below 1 to ca. 10 A^{-1}.

The front and side detector banks will be equipped with 640 position sensitive ^{3}He detector tubes with a diameter of 8 mm each. Earlier tests with prototype tubes with 20 and 30 bar gas pressure at the FRM II instrument TREFF by Dr. Zeitelhack's group resulted in a better suitability of the former type, since a slightly better detection efficiency of the higher gas pressure comes at the cost of a lower ability to discriminate between neutron and gamma events. The recently delivered detector tubes (GE Reuter-Stokes) are currently tested at FRM II. Tests will be completed by the end of 2013, so that the assemblage of the detector banks can commence. The individual banks will consist of the concentrically aligned tubes in front of a neutron shield of BC tiles to reduce background. Electronic modules and the connection wires will be located behind the banks. These units are attached to an aluminium frame that is connected to a larger outer frame by sliding carriage to allow sample replacement and maintenance.

The WLSF detector units have an active area of 35×35 cm each. The working principle is a double layer scintillator sheet that translates incoming neutrons into a photon signal. The photons enter an underlying dense grid of cross-cutting glass fibers that transport the flash to a photo multiplier. This detector type is a new development by the Forschungszentrum Jülich and will be built and installed at SAPHiR by FZ Jülich. The system has a higher position and time resolution than the ^{3}He detectors, thus providing a very good Δd/d resolution at high 2Θ angles.

In addition to the planning of the detector system, the sample environment has been improved. Tests revealed that fired pyrophyllite pressure media combined a higher pressure efficiency with a higher neutron transparency as compared to ZrO_2; external gaskets helped to keep anvil gaps large enough for the neutron beam to reach the sample (2-3 mm, Fig. 3.8-5). Currently favoured assembly configurations are 12/7, 11/6, and 10/6 (cube width/anvil truncation) that currently reach a pressure of > 10-12 GPa. The former two configurations allow including a 3×3 mm sample in a standard Pt or Re tube furnace so that deformation experiments become possible (Fig. 3.8-5). The 10/6 configuration employs a box-furnace geometry for reaching higher pressures at static conditions. According to the current timetable, first neutrons will reach the eastern hall in 2015. Current progress in the detector planning and neutron tube testing make it likely that the instrument SAPHiR will be fully operational by that time.

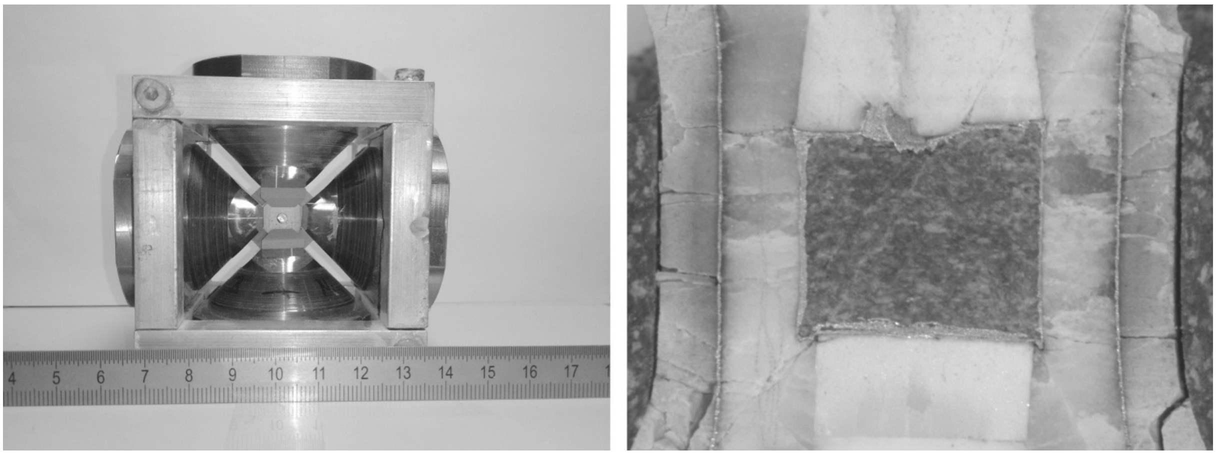

Fig. 3.8-5: Left: A 11/6 assembly setup for neutron measurements. An 11 mm cube of fired pyrophyllite is compressed by secondary anvils with 6 mm anvil truncations. Preformed gaskets, also made of fired pyrophyllite, ensure a good sample alignment and wide anvil gaps for the incoming and scattered neutrons. This assembly reaches pressures of > 10 GPa with large sample volumes and standard Ni-bound secondary anvils. Right: 12 mm assembly containing a large olivine sample (20 mm^3) that was deformed in the SAPHiR press. The originally 4 mm long olivine cylinder was shortened by 30 %.

d. *Synthesis of large gem-quality single crystals of pure, Al-bearing, and (Al, Fe)-bearing* $MgSiO_3$ *perovskite (L. Ziberna, T. Boffa Ballaran and D.J. Frost)*

The determination of the elastic properties of high-pressure mantle minerals is an important step in understanding the structure of the inaccessible Earth's deep mantle. This is a crucial goal of various projects at the BGI (see BGI Annual Reports 2010-2013), and can be achieved by performing *in situ* high-pressure and high-temperature single-crystal X-ray diffraction coupled with Brillouin spectroscopy, using externally heated diamond anvil cells. This technique requires extremely high-quality crystals with at least one dimension on the order of 50-100 µm. However, high-pressure minerals synthesized in large volume multianvil presses often show twins, amorphous or poorly crystalline regions, fluid or other inclusions or major cracks or residual strain. The above mentioned *in situ* techniques cannot be applied on such poor quality crystals and therefore it is necessary to refine the synthesis of high-pressure minerals. To address this issue, we performed a series of multianvil experiments to synthesize large high-quality crystals of both pure, Al-bearing and (Fe, Al)-bearing $MgSiO_3$ perovskite, which will be used for simultaneous single-crystal X-ray diffraction and Brillouin spectroscopy.

All the experiments were performed using Cr_2O_3-doped MgO octahedra of 7 mm edge length in combination with tungsten carbide cubes with 3 mm truncation edge lengths. The cell assembly in the octahedra consisted of a $LaCrO_3$ heater, two Au or Pt capsules (1.3 mm length and 1.0 mm diameter) containing the experimental samples, and MgO sleeves and spacers isolating the capsules from the heater. The temperature was estimated from the electrical power, on the basis of previous calibrations in which type D thermocouples were used. All the experiments were performed at 25 GPa and 1400-2000 °C. To enhance reactions and crystal growth, water was used as a flux material and was loaded either as brucite or as molecular water. In some cases, a step-heating procedure was adopted, which helped to minimize the number of nucleating crystals causing fewer but larger crystals to grow. After sample recovery, crystals with at least two dimensions greater than 50 µm were tested for their quality. This was judged on the basis of the quality of their Bragg reflection intensities and peak profiles using a Huber single-crystal X-ray diffractometer.

Pure $MgSiO_3$ crystals were successfully synthesized from a starting mixture of 50.75 % SiO_2 and 49.25 % $Mg(OH)_2$ by weight, which was kept at 25 GPa and 1700 °C for 30 minutes. High-quality single crystals up to 100 µm were recovered after decompression. Large crystals of $MgSiO_3$ perovskite containing 4 wt.% Al_2O_3 (based on electron microprobe analyses) were synthesized from a stoichiometric mixture of SiO_2, $Mg(OH)_2$ and Al_2O_3. In this case, a step-heating procedure was adopted, with temperature varying between 1400 and 1600 °C. Analyses of their peak profiles, however, revealed the presence of twinning in samples with dimensions greater than 50 µm. Large crystals (up to 150 µm in one dimension) of (Fe, Al)-bearing $MgSiO_3$ perovskite were obtained from a stoichiometric mixture of SiO_2, $Mg(OH)_2$, Al_2O_3 and Fe_2O_3, again adopting a step-heating procedure with temperature varying between 1400 and 1600 °C. The crystals, however, are not of suitable quality, as they show low reflection intensities and broad peak profiles. Further experiments will be performed using the Al- and Fe-bearing compositions, in order to better constrain the processes that are critical to quality crystal synthesis, such as temperature, temperature path and stress conditions.

e. *Hyperfine splitting and room-temperature ferromagnetism of Ni at multi-megabar pressures (L.S. Dubrovinsky; I. Sergueev, A.I. Chumakov, V. Potapkin, I. Kantor, and R. Rüffer/ Grenoble)*

Nickel plays a key role in an astonishingly wide range of fields in physics, spanning from microelectronics to the very interior of Earth. Like iron and cobalt, it is ferromagnetic, with spontaneous ordering of magnetic moments at ambient conditions. In the simple Stoner model, the magnetism of such 3*d*-transition metals is a result of the competition between being itinerant or being localised. Due to the higher Coulomb repulsion between the more localized 3*d*-electrons, correlations between such electrons become important. By arranging the spins in parallel, the Pauli principle will ensure they stay further apart, which lowers the interaction energy, although at the cost of kinetic energy. Depending on the band structure, the balance between these effects may result in fractional spin polarization of the electrons at each structural position, and hence, a net magnetization. Application of pressure broadens the band, thus increasing the kinetic energy. At sufficiently high pressure, kinetic energy will dominate, yielding the Stoner nonmagnetic state without any magnetic moments. It is important to distinguish this non-magnetic state from a paramagnetic state containing disordered local moments without long-range order, which in most magnetic materials is encountered when the temperature exceeds the Curie temperature (T_C). A vanishing net magnetization can thus due either to T_C being below the experimental temperature, or quenching of the local moments. In transition metals, the nature of the magnetic ordering has a critical impact on macroscopic properties, such as chemical phase stability, even below T_C. Applying pressure is the most useful way to study the nature of the magnetic state of transition metals, since the balance between Coulomb and kinetic energy can be tuned. Fe and Co undergo transitions into a nonmagnetic state at about 15 GPa and between 100 and 150 GPa at room temperature, respectively. However, in these cases, the collapse of ferromagnetism is associated with structural transitions of the crystal structure. In Ni, on the other hand, the ground state fcc structure is stable at least up to 200 GPa, as confirmed by X-ray diffraction experiment and it is predicted to be stable up to over 300 GPa. The magnetic moment of Ni has previously been studied by X-ray magnetic circular dichroism up to 200 GPa and indicate only a slight decrease. Extrapolation of the measured magnetic moment to higher pressures implies a non-magnetic phase above 250 GPa. Density functional theory predicts stability of the local magnetic moments up to at least 300 GPa. At the same time, little attention has been paid so far to the stability of the ferromagnetic *order* of the Ni moments at high pressure. Generally, the Curie temperature decreases with pressure, but in Ni it has been shown to increase up to 8 GPa. At still higher pressure, the behavior of T_C is largely unknown. It is thus important to develop new experimental techniques operating at yet higher pressures, in order to investigate the microscopic nature of transition metals, and to complement experiments with theoretical studies for a fundamental understanding of the observed effects. Mossbauer spectroscopy (MS) and its synchrotron radiation counterparts, nuclear forward scattering (NFS) and synchrotron Mossbauer source, are very efficient methods in high-pressure studies of solid state properties as has been demonstrated for iron-bearing compounds. MS can also be performed with the isotope ^{61}Ni, with the nuclear transition energy of 67.4 keV. However, several technical and fundamental problems restrict the applicability of the method, resulting in only few studies of Ni compounds with MS. The NFS method enables one to overcome some of these problems, and its capability for Ni has recently been demonstrated.

We apply NFS to investigate the magnetic and elastic properties of Ni at room temperature up to 260 GPa. The magnetic hyperfine splitting at the Ni site was observed up to 260 GPa, which confirms that Ni remains ferromagnetic up to this pressure, the highest pressure where magnetism in any material has been observed so far. Experimental observations are confirmed by theoretical *ab initio* DFT calculations, which reproduce the peculiar pressure dependence of the hyperfine field, and reveal that it is a clear manifestation of relativistic effects. Moreover, we demonstrate that the Curie temperature of Ni depends on pressure quite weakly, in agreement with the experimental observation of a ferromagnetic state in Ni at multi-megabar pressures and room temperature.

4. Publications, Conference Presentations, Seminars

4.1 Publications (published)

Supplement to **2012** (papers published at the end of 2012):

HARRIES, D.; BERG, T.; LANGENHORST, F.; PALME, H. (2012): Structural clues to the origin of refractory metal alloys as condensates of the solar nebula. Meteoritics and Planetary Science 47(12), 2148-2159

2013

a) Refereed international journals

ABAKUMOV, A.; BATUK, D.; TSIRLIN, A.; PRESCHER, C.; DUBROVINSKY, L.; SHEPTYAKOV, D.; SCHNELLE, W.; HADERMANN, J.; VAN TENDELOO, G. (2013): Frustrated pentagonal Cairo lattice in the non-collinear antiferromagnet $Bi_4Fe_5O_{13}F$. Physical Review B 87, 024423

AUDÉTAT, A. (2013): Origin of Ti-rich rims in quartz phenocrysts from the Upper Bandelier Tuff and the Tunnel Spring Tuff, southwestern USA. Chemical Geology 360-361, 99-104

AUDÉTAT, A.; SIMON, A. (2013): Magmatic controls on porphyry Cu genesis. – In: HEDENQUIST, J.; HARRIS, M.; CAMUS, F. (Eds.) Geology and genesis of major copper deposits and districts of the world: a tribute to Richard Sillitoe. Society of Economic Geologists, Special Publication 16, 553-572

BALI, E.; KEPPLER, H.; AUDETAT, A. (2013): Water and hydrogen are immiscible in Earth's mantle. Nature 495, 220-222

BATUK, D.; BATUK, M.; ABAKUMOV, A.M.; TSIRLIN, A.A.; MCCAMMON, C.; DUBROVINSKY, L.; HADERMANN, J. (2013): Effect of lone electron pair cations on the orientation of crystallographic shear planes in anion-deficient perovskites. Inorganic Chemistry 52(17), 10009-10020

BERNINI, D.; AUDETAT, A.; DOLEJŠ, D.; KEPPLER, H. (2013): Zircon solubility in aqueous fluids at high temperatures and pressures. Geochimica et Cosmochimica Acta 119, 178-187

BERNINI, D.; WIEDENBECK, M.; DOLEJŠ, D.; KEPPLER, H. (2013): Partitioning of halogens between mantle minerals and aqueous fluids: implications for the fluid flow regime in subduction zones. Contributions to Mineralogy and Petrology 165, 117-128

BOFFA BALLARAN, T.; KURNOSOV, A.; TROTS, D. (2013): Single-crystal diffraction at extreme conditions: a review. High Pressure Research 33, 453-465

BOFFA BALLARAN, T. (2013): Diffraction at extreme conditions: a window into the Earth's interior. Rendiconti dei Lincei-Scienze Fisiche e Naturali 24, S47-S54

BYKOV, M.; BYKOVA, E.; VAN SMAALEN, S.; DUBROVINSKY, L.; MCCAMMON, C.; PRAKAPENKA, V.; LIERMANN, H.-P. (2013): High-pressure behavior of FeOCl, Physical Review B 88, 014110

BYKOVA, E.; BYKOV, M.; PRAKAPENKA, V.; KONÔPKOVÁ, Z.; LIERMANN, H.-P.; DUBROVINSKAIA, N.; DUBROVINSKY, L. (2013): Novel high-pressure monoclinic Fe_2O_3 polymorph revealed by single crystal synchrotron X-ray diffraction studies. High Pressure Research 33, 534-545

CHANG, Y.-Y.; JACOBSEN, S.D.; LIN, J.-F.; BINA, C.R.; THOMAS, S.-M.; WU, J.; SHEN, G.; XIAO, Y.; CHOW, P.; FROST, D.J.; MCCAMMON, C.A.; DERA, P. (2013): Spin transition of Fe^{3+} in Al-bearing phase D: an alternative explanation for small-scale seismic scatterers in the mid-lower mantle. Earth and Planetary Science Letters 382, 1-9

CHELAZZI, L.; BOFFA BALLARAN, T.; LEPORE, G.O.; BINDI, L.; BONAZZI, P. (2013): High-pressure behaviour of synthetic $Mn^{2+}{}_2Sb^{5+}{}_2O_7$: an *in situ* single-crystal X-ray study. Solid State Science 21, 85-89

CORDIER, P.; HEIDELBACH, F. (2013): On the origin of twist in quartz crystals from the Alps: a transmission electron microscopy study. European Journal of Mineralogy 25*,* 145-153

DANG, N.T.; KOZLENKO, D.P.; KICHANOV, S.E.; DUBROVINSKY, L.S.; JIRAK, Z.; LEVIN, D.M.; LUKIN, E.V.; SAVENKO, B.N. (2013): Structural and magnetic phase transitions occurring in $Pr_{0.7}Sr_{0.3}MnO_3$ manganite at high pressures. JETP Letters 97, 540-545

DE VRIES, J.; JACOBS, M.H.G.; VAN DEN BERG, A.P.; WEHBER, M.; LATHE, C.; MCCAMMON, C.; VAN WESTRENEN, W. (2013): Thermal equation of state of synthetic orthoferrosilite at lunar pressures and temperatures. Physics and Chemistry of Minerals 40, 691-703

DOBSON, D.P.; MIYAJIMA, N.; NESTOLA, F.; ALVARO, M.; CASATI, N.; LIEBSKE, C.; WOOD, I.G.; WALKER, A.M. (2013): Strong inheritance of texture between perovskite and post-perovskite in the D" layer. Nature Geoscience 6, 575-578

DOMENEGHETTI, M.C.; FIORETTI, A.M.; CÁMARA, F.; MCCAMMON, C.; ALVARO, M. (2013): Thermal history of nakhlites: a comparison between MIL03346 and its terrestrial analogue Theo's flow. Geochimica et Cosmochimica Acta 121, 571-581

DUBROVINSKAIA, N.; DUBROVINSKY, L. (2013): Controversy about ultrahard nanotwinned cBN. Nature 502, E1-E2

DUBROVINSKY, L. (2013): Preface for special journal issue. High Pressure Research 33, 451-452

EL GORESY, A.; GILLET, Ph.; MIYAHARA, M.; OHTANI, E.; OZAWA, S.; BECK, P.; MONTAGNAC, G. (2013): Shock-induced deformation of shergottites: Shock-pressures and perturbations of magmatic ages on Mars. Geochimica et Cosmochimica Acta 101, 233-262

FARLA, R.J.M.; KARATO, S.; CAI, Z. (2013): Role of orthopyroxene in rheological weakening of the lithosphere via dynamic recrystallization. Proceedings of the National Academy of Sciences 110, No. 41, 16355-16360

FEI, H.; WIEDENBECK, M.; YAMAZAKI, D.; KATSURA, T. (2013): Small effect of water on the upper mantle rheology based on Si self-diffusion coefficient. Nature 498, 213-215

GALUSKIN, E.; GALUSKINA, I.; BAILAU, R.; PRUSIK, K.; GAZEEV, V.; ZADOV, A.; PERTSEV, N.; JEZAK, L.; GURBANOV, A.; DUBROVINSKY, L. (2013): Eltyubyuite, $Ca_{12}Fe_{10}^{3+}Si_4O_{32}Cl_6$ – the Fe^{3+} analogue of wadalite: a new mineral from the Northern Caucasus, Kabardino-Balkaria, Russia. European Journal of Mineralogy 25, 221-229

GALUSKINA, I.; GALUSKIN, E.; KUSZ, J.; DZIERZANOWSKI, P.; PRUSIK, K.; GAZEEV, V.; PERTSEV, N.; DUBROVINSKY, L. (2013): Dzhuluite, $Ca_3SloSnFe^{3+}{}_3O_{12}$, a new bitikleite-group garnet from the Upper Chegem Caldera, Northern Caucasus, Kabardino-Balkaria, Russia, European Journal of Mineralogy 25, 231-239

GILLET, Ph; EL GORESY, A. (2013): Shock events in the solar system: The message from minerals in terrestrial planets and asteroids. Annual Reviews of Earth and Planetary Sciences 41, 257-285

GLAZYRIN, K.; POUROVSKII, L.V.; DUBROVINSKY, L.; NARYGINA, O.; MCCAMMON, C.; HEWENER, B.; SCHÜNEMANN, V.; WOLNY, J.; MUFFLER, K.; CHUMAKOV, A.I.; CRICHTON, W.; HANFLAND, M.; PRAKAPENKA, V.; TASNÁDI, F.; EKHOLM, M.; AICHHORN, M.; VILDOSOLA, V.; RUBAN, A.V.; KATSNELSON, M.I.; ABRIKOSOV, I.A. (2013): Importance of correlation effects in hcp iron revealed by a pressure-induced electronic topological transition. Physical Review Letters 110, 117206-1-5

GOU, H.; STEINLE-NEUMANN, G.; BYKOVA, E.; NAKAJIMA, Y.; MIYAJIMA, N.; LI, Y.; OVSYANNIKOV, S.; DUBROVINSKY, L.; DUBROVINSKAIA, N. (2013): Stability of MnB_2 with AlB_2-type structure revealed by first-principles calculations and experiments. Applied Physics Letters 102, 061906

GOU, H.; DUBROVINSKAIA, N.; BYKOVA, E.; TSIRLIN, A.; KASINATHAN, D.; SCHNELLE, W.; RICHTER, A.; MERLINI, M.; HANFLAND, M.; ABAKUMOV, A.; BATUK, D.; VAN TENDELOO, D.; NAKAJIMA, Y.; KOLMOGOROV, A.; DUBROVINSKY, L. (2013): Discovery of a superhard iron tetraboride superconductor. Physical Review Letters 111, 157002

GRIFFIN, J.M.; BERRY, A.J.; FROST, D.J.; WIMPERIS, S.; ASHBROOK, S.E. (2013): Water in the Earth's mantle: a solid-state NMR study of hydrous wadsleyite. Chemical Science 4, 1523-1538

GROAT, L.A.; EVANS, J.; CEMPÍREK, J.; MCCAMMON, C. (2013): As-bearing and Fe-rich vesuvianite and wiluite from Kozlov, Czech Republic. American Mineralogist 98, 1330-1337

GU, T.; WU, X.; QIN, S.; MCCAMMON, C.; DUBROVINSKY, L. (2013): Probing nonequivalent sites in iron phosphide Fe_2P and its mechanism of phase transition. European Physics Journal B 86: 311, 1-6

HARRIES, D.; POLLOK, K.; LANGENHORST, F. (2013): Oxidative dissolution of 4C- and NC-pyrrhotite: Intrinsic reactivity differences, pH dependence, and the effect of anisotropy. Geochimica et Cosmochimica Acta 102, 23-44

HEIDELBACH, F.; TERRY, M.P. (2013): Inherited fabric in an omphacite symplectite: reconstruction of plastic deformation under ultra-high pressure conditions. Microscopy and Microanalysis 19, 942-949

KAWAZOE, T.; OHUCHI, T.; NISHIHARA, Y.; NISHIYAMA, N.; FUJINO, K.; IRIFUNE, T. (2013): Seismic anisotropy in the mantle transition zone induced by shear deformation of wadsleyite. Physics of the Earth and Planetary Interiors 216, 91-98

KOZLENKO, D.P.; KICHANOV, S.E.; LUKIN, E.V.; DANG, N.T.; DUBROVINSKY, L.S.; BYKOVA, E.A.; KAMENEV, K.V.; LIERMANN, H.-P.; MORGENROTH, W.; SHAPIRO, A.Ya.; SAVENKO, B.N. (2013): Effect of high pressure on the crystal structure, magnetic, and vibrational properties of multiferroic $RbFe(MoO_4)_2$. Physical Review B 87, 014112 (1-6)

KOZLENKO, D.P.; DANG, N.T.; KICHANOV, S.E.; LUKIN, E.V.; KNIZEK, K.; JIRAK, Z.; DUBROVINSKY, L.S.; VORONIN, V.I.; SAVENKO, B.N. (2013): Pressure-induced structural transformations, orbital order and antiferromagnetism in $La_{0.75}Ca_{0.25}MnO_3$. The European Physical Journal B 86, 360 (1-8)

KULARATNE K.; AUDÉTAT A. (2013): Rutile solubility in hydrous rhyolite melts at 750-900 °C and 2 kbar, with application to titanium-in-quartz (TitaniQ) thermobarometry. Geochimica et Cosmochimica Acta 125, 196-209

LERCHBAUMER, L.; AUDÉTAT, A. (2013): The metal content of silicate melts and aqueous fluids in sub-economically Mo-mineralized granites: implications for porphyry Mo genesis. Economic Geology 108, 987-1013

LI, Y.; AUDÉTAT, A. (2013): Gold solubility and partitioning between sulfide liquid, monosulfide solid solution, and hydrous mantle melts: Implications for the formation of Au-rich magmas and crust-mantle differentiation. Geochimica et Cosmochimica Acta 118, 247-262

LI, Y.; WIEDENBECK, M.; SHCHEKA, S.; KEPPLER, H. (2013): Nitrogen solubility in upper mantle minerals. Earth and Planetary Science Letters 377-378, 311-323

LIU, X.; XIONG, X.; AUDÉTAT, A.; LI, Y.; SONG, M.; SUN, W.; DING, X. (2013): Partitioning of copper between olivine, orthopyroxene, clinopyroxene, spinel, garnet and silicate melts at upper mantle conditions. Geochimica et Cosmochimica Acta 125, 1-22

MANGHNANI, M.H.; HUSHUR, A.; SMYTH, J.R.; NESTOLA, F.; DERA, P.; SEKAR, M.; AMULELE, G.; FROST, D.J (2013): Compressibility and structural stability of two variably hydrated olivine samples ($Fo_{97}Fa_3$) to 34 GPa by X-ray diffraction and Raman spectroscopy. American Mineralogist 98, 1972-1979

MANTHILAKE, M.A.G.M.; MIYAJIMA, N.; HEIDELBACH, F.; SOUSTELLE, V.; FROST, D.J. (2013): The effect of aluminum and water on the development of deformation fabrics of orthopyroxene. Contributions to Mineralogy and Petrology 165, 495-505

MCCAMMON, C.; GLAZYRIN, K.; KANTOR, A.; KANTOR, I.; KUPENKO, I.; NARYGINA, O.; POTAPKIN, V.; PRESCHER, C.; SINMYO, R.; CHUMAKOV, A.; RÜFFER, R.; SERGUEEV, I.; SMIRNOV, G.; DUBROVINSKY, L. (2013): Iron spin state in silicate perovskite at conditions of the Earth's deep interior. High Pressure Research 33 (3), 663-672, doi: 10.1080/08957959.2013.805217

MOLLO, S.; HEAP, M.J.; DINGWELL, D.B.; HESS, K.-U.; IEZZI, G.; MASOTTA, M.; SCARLATO, P.; VINCIGUERRA, S. (2013): Decarbonation and thermal microcracking under magmatic $P\text{-}T\text{-}f\mathrm{CO_2}$ conditions: the role of skarn substrata in promoting volcanic instability. Geophysical Journal International 195, 369-380

MONDAL, S.; VAN SMAALEN, S.; PARAKHONSKIY, G.; PRATHAPA, S.; NOOHINEJAD, L.; BYKOVA, E.; DUBROVINSKAIA, N.; CHERNYSHOV, D.; DUBROVINSKY, L. (2013): Experimental evidence of orbital order in alpha-B-12 and gamma-B-28 polymorphs of elemental boron. Physical Review B 88, 024118

MORISHIMA, R.; GOLABEK, G.; SAMUEL, H. (2013): N-body simulations of oligarchic growth of Mars: Implications for Hf-W chronology. Earth and Planetary Science Letters 366, 6-13

MROSKO, M.; LENZ, S.; MCCAMMON, C.A.; TARAN, M.; WIRTH, R.; KOCH-MÜLLER, M. (2013): Hydrogen incorporation and the oxidation state of iron in ringwoodite – a spectroscopic study. American Mineralogist 98, 629-636

MUSSI, A.; CORDIER, P.; FROST, D.J. (2013): Transmission electron microscopy characterization of the dislocations and slip systems of the dense hydrous magnesium silicate superhydrous B. European Journal of Mineralogy 25, 561-568

MYHILL, R. (2013): Slab buckling and its effect on the distributions and focal mechanisms of deep-focus earthquakes. Geophysical Journal International 192, no. 2, 837-853

NI, H.; KEPPLER, H. (2013): Carbon in silicate melts. Reviews in Mineralogy and Geochemistry 75, 251-287

NORRBY, N.; LIND, H.; PARAKHONSKIY, G.; JOHANSSON, M.P.; TASNADI, F.; DUBROVINSKY, L.; DUBROVINSKAIA, N.; ABRIKOSOV, I.; ODEN, M. (2013): High pressure and high temperature stabilization of cubic AlN in $Ti_{0.60}Al_{0.40}N$. Journal of Applied Physics 113, 053515

OTSUKA, K.; LONGO, M.; MCCAMMON, C.A.; KARATO, S.-I. (2013): Ferric iron content of ferropericlase as a function of composition, oxygen fugacity, temperature and pressure: Implications for redox conditions during diamond formation in the lower mantle. Earth and Planetary Science Letters 365, 7-16

OVSYANNIKOV, S.V.; ABAKUMOV, A.M.; TSIRLIN, A.A.; SCHNELLE, W.; EGOAVIL, R.; VERBEECK, J.; VAN TENDELOO, G.; GLAZYRIN, K.V.; HANFLAND, M.; DUBROVINSKY, L. (2013): Perovskite-like Mn_2O_3: A path to new manganites. Angewandte Chemie International Edition 52, 1494-1498

OVSYANNIKOV, S.V.; GOU, H.; MOROZOVA, N.V.; TYAGUR, I.; TYAGUR, Y.; SHCHENNIKOV, V.V. (2013): Raman spectroscopy of ferroelectric $Sn_2P_2S_6$ under high pressure up to 40 GPa: phase transitions and metallization. Journal of Applied Physics 113, 013511

OVSYANNIKOV, S.V.; ZAINULIN, Y.G.; KADYROVA, N.I.; TYUTYUNNIK, A.P.; SEMENOVA, A.S.; KASINATHAN, D.; TSIRLIN, A.A.; MIYAJIMA, N.; KARKIN, A.E. (2013): New antiferromagnetic perovskite $CaCo_3V_4O_{12}$ prepared at high-pressure and high-temperature conditions. Inorganic Chemistry 52, 11703-11710

OVSYANNIKOV, S.V.; TROTS, D.M.; KURNOSOV, A.V.; MORGENROTH, W.; LIERMANN, H.-P.; DUBROVINSKY, L. (2013): Anomalous compression and new high-pressure phases of vanadium sesquioxide, V_2O_3. Journal of Physics: Condensed Matter 25, 385401

OVSYANNIKOV, S.V.; WU, X.; GARBARINO, G.; SHCHENNIKOV, V.V.; KHMELEVA, J.A.; KARKIN, A.E.; DUBROVINSKAIA, N.; DUBROVINSKY, L. (2013): High-pressure behavior of structural, optical and electronic transport properties of the golden Th_2S_3-type Ti_2O_3. Physical Review B 88, 184106

PANERO, W.R.; SMYTH, J.R.; PIGOTT, J.S.; LIU, Z.X.; FROST, D.J. (2013): Hydrous ringwoodite to 5 K and 35 GPa: Multiple hydrogen bonding sites resolved with FTIR spectroscopy. American Mineralogist 98, 637-642

PARAKHONSKIY, G.; VTECH, V.; DUBROVINSKAIA, N.; CARACAS, R.; DUBROVINSKY, L. (2013): Raman spectroscopy investigation of alpha boron at elevated pressures and temperatures. Solid State Communications 154, 34-39

PARAKHONSKIY, G.; DUBROVINSKAIA, N.; BYKOVA, E.; WIRTH, R.; DUBROVINSKY, L. (2013): High pressure synthesis and investigation of single crystals of metastable boron phases. High Pressure Research 33, 673-683

POTAPKIN, V.; MCCAMMON, C.; GLAZYRIN, K.; KANTOR, A.; KUPENKO, I.; PRESCHER, C.; SINMYO, R.; SMIRNOV, G.V.; CHUMAKOV, A.I.; RÜFFER, R.; DUBROVINSKY, L. (2013): Effect of iron oxidation state on the electrical conductivity of the Earth's lower mantle. Nature Communications 4, 1427, 1-6

POUROVSKII, L.V.; MIYAKE, T.; SIMAK, S.I.; RUBAN, A.V.; DUBROVINSKY, L.; ABRIKOSOV, I.A. (2013): Electronic properties and magnetism of iron at the Earth's inner core conditions. Physical Review B 87, 115130

REICHMANN, H.J.; JACOBSEN, S.D.; BOFFA BALLARAN, T. (2013): Elasticity of franklinite and trends for transition-metal oxide spinels. American Mineralogist 98, 601-608

ROBINSON, P.; FABIAN, K.; MCENROE, S.A.; HEIDELBACH, F. (2013): Influence of lattice-preferred orientation with respect to magnetizing field on intensity of remanent magnetization in polycrystalline hemo-ilmenite. Geophysical Journal International 192, 514-536

SAMUEL, H. (2013): A level set two-way wave equation approach for Eulerian interface tracking. Journal of Computational Physics 259, 617-635

SANLOUP, C.; CRÉPISSON, C.; KONO, Y.; PARK, C.; DREWITT, J.W.E.; MCCAMMON, C. (2013): Structure and density of molten fayalite at high pressure. Geochimica et Cosmochimica Acta 118, 118-128

SERGUEEV, I.; DUBROVINSKY, L.; EKHOLM, M.; VEKILOVA, O.; CHUMAKOV, A.; ZAJAC, M.; POTAPKIN, V.; KANTOR, I.; BORNEMANN, S.; EBERT, H.; SIMAK, S.; ABRIKOSOV, I.; RÜFFER, R. (2013): Hyperfine splitting and room-temperature ferromagnetism of Ni at multimegabar pressure. Physical Review Letters 111, 157601

SHATSKIY, A.; LITASOV, K.D.; BORZDOV, Y.M.; KATSURA, T.; YAMAZAKI, D.; OHTANI, E. (2013): Silicate diffusion in alkali-carbonatite and hydrous melts at 16.5 and 24 GPa: Implication for the melt transport by dissolution-precipitation in the transition zone and uppermost lower mantle. Physics of the Earth and Planetary Interiors 225, 1-11

SHCHENNIKOV, V.V.; SHCHENNIKOV, Vs.V.; STRELTSOV, S.V.; KOROBEINIKOV, I.A.; OVSYANNIKOV, S.V. (2013): Thermoelectric power of different phases and states of silicon at high pressure. Journal of Electronic Materials 42, 2249-2256

SHIREY, S.B; CARTIGNY, P.; FROST, D.J.; KESHAV, S.; NESTOLA, F.; NIMIS, P.; PEARSON, D.G.; SOBOLEV, N.V.; WALTER, M.J. (2013) Diamonds and the geology of mantle carbon. Reviews in Mineralogy and Geochemistry 75, 355-421

SHUSHAKOVA, V.; FULLER, E.R.; HEIDELBACH, F.; MAINPRICE, D.; SIEGESMUND, S. (2013): Marble decay induced by thermal strains: simulations and experiments. Environmental Earth Sciences 69, 1281-1297

SIMON, R.E.; SERGUEEV, I.; PERSSON, J.; MCCAMMON, C.A.; HATERT, F.; HERMANN, R.P. (2013): Nuclear forward scattering by the 68.7 keV state of ^{73}Ge in $CaGeO_3$ and GeO_2. Europhysics Letters 104, 17006-1-6

SINMYO, R.; HIROSE, K. (2013): Iron partitioning in pyrolitic lower mantle. Physics and Chemistry of Minerals 40, 107-113

SOLOPOVA, N.A.; DUBROVINSKAIA, N.; DUBROVINSKY, L. (2013): Raman spectroscopy of glassy carbon up to 60 GPa. Applied Physics Letters 102, 121909

SORBADERE, F.; SCHIANO, P.; MÉTRICH, N. (2013): Constraints on the origin of silica-undersaturated magmas in islands arcs inferred from olivine-hosted melt inclusion compositions. Journal of Petrology 54, 215-233

SORBADERE, F.; SCHIANO, P.; MÉTRICH, N.; BERTAGNINI, A. (2013): Small scale coexistence of Island Arc- and enriched MORB-type basalts in the Central Vanuatu Arc. Contributions to Mineralogy and Petrology 166, 1305-1321

SORBADERE, F.; MÉDARD, E.; LAPORTE, D.; SCHIANO. P. (2013): Experimental melting of hydrous peridotite-pyroxenite mixed sources: Constraints on the genesis of silica-undersaturated magmas beneath volcanic arcs. Earth and Planetary Science Letters 384, 42-46

SPECKBACHER, R.; STIPP, M.; BEHRMANN, J.H.; HEIDELBACH, F. (2013): Fluid-assisted fracturing, cataclasis, and resulting plastic flow in mylonites from the Moresby Seamount detachment, Woodlark Basin. Journal of Structural Geology 56, 156-171

STAGNO, V.; OJWANG, D.O.; MCCAMMON, C.A.; FROST, D.J. (2013): The oxidation state of the mantle and the extraction of carbon from Earth's interior. Nature 493, 84-88

TROTS, D.M.; KURNOSOV, A.; BOFFA BALLARAN, T.; TKACHEV, S.; ZHURAVLEV, K.; PRAKAPENKA, V.; BERKOWSKI, M.; FROST, D.J. (2013): The Sm:YAG primary fluorescence pressure scale. Journal of Geophysical Research – Solid Earth 118, 5805-5813

TROTS, D.M.; KURNOSOV, A.; MANTHILAKE, M.A.G.M.; OVSYANNIKOV, S.V.; AKSELRUD, L.G.; HANSEN, T.; SMYTH, J.R.; FROST, D.J. (2013): The determination of hydrogen positions in superhydrous phase B. American Mineralogist 98, 1688-1692

TROTS, D.M.; KURNOSOV, A; BOFFA BALLARAN, T.; TKACHEV, S.; PRAKAPENKA, V.; BERKOWSKI, M.; FROST, D.J. (2013): The Sm:YAG primary fluorescence pressure scale. Journal of Geophysical Research – Solid Earth 118, 5805-5813, doi: 10.1002/2013JB010519

TSUNO, K.; FROST, D.J.; RUBIE, D.C. (2013): Simultaneous partitioning of silicon and oxygen into the Earth's core during early Earth differentiation. Geophysical Research Letters 40, 66-71

VAN MIERLO, W.L.; LANGENHORST, F.; FROST, D.J.; RUBIE, D.C. (2013): Stagnation of subducting slabs in the transition zone due to slow diffusion in majoritic garnet. Nature Geoscience 6, 400-403

WEHINGER, B.; BOSAK, A.; CHUMAKOV, A.; MIRONE, A.; WINKLER, B.; DUBROVINSKY, L.; DUBROVINSKAIA, N.; BRAZHKIN, V.; DYUZHEVA, T.; KRISCH, M. (2013): Lattice dynamics of coesite. Journal of Physics: Condensed Matter 25, 275401

WOODLAND, A.B.; SCHOLLENBRUCH, K.; KOCH, M.; BOFFA BALLARAN, T.; ANGEL, R.J.; FROST, D.J. (2013): Fe_4O_5 and its solid solutions in several simple systems. Contributions to Mineralogy and Petrology 166, 1677-1686

XU, W.M.; GREENBERG, E.; ROZENBERG, G.Kh.; PASTERNAK, M.P.; BYKOVA, E.; BOFFA BALLARAN, T.; DUBROVINSKY, L.; PRAKAPENKA, V.; HANFLAND, M.; VEKILOVA, O.Yu.; SIMAK, S.I.; ABRIKOSOV, I.A. (2013): Pressure-induced hydrogen bond symmetrization in iron oxyhydroxide. Physical Review Letters 111, 175501

YE, Y.; SMYTH, J.R.; JACOBSEN, S.D.; PANERO, W.R.; BROWN, D.A.; KATSURA, T.; CHANG, Y.-Y.; TOWNSEND, J.P.; DERA, P.; TKACHEV, S.; UNTERBORN, C.; LIU, Z.; GOUJON, C. (2013): Crystal structure, Raman and FTIR spectroscopy, and equations of state of OH-bearing $MgSiO_3$ akimotoite. Contributions to Mineralogy and Petrology 166(5), 1375-1388

YOSHINO, T.; KATSURA, T. (2013): Electrical conductivity of mantle minerals: Role of water in conductivity anomalies. – In: JEANLOZ, R. (Ed.): Annual Review of Earth and Planetary Sciences 41, 605-628

YOSHIASA, A.; NAKATSUKA A., OKUBE M., KATSURA, T. (2013): Single-crystal metastable high-temperature C2/c clinoenstatite quenched rapidly from high temperature and high pressure. Acta Crystallographica Section B – Struct. Sci. 69, 541-546, doi: 10.1107/ s2052519213028248

ZIBERNA, L.; NIMIS, P.; ZANETTI, A.; MARZOLI, A; SOBOLEV; N.V. (2013): Metasomatic processes in the central Siberian cratonic mantle: evidence from garnet xenocrysts from the Zagadochnaya kimberlite. Journal of Petrology 54, 2379-2409

ZIBERNA, L.; KLEMME, S.; NIMIS, P. (2013): Garnet and spinel in fertile and depleted mantle: insights from thermodynamic modeling. Contributions to Mineralogy and Petrology 166, 411-421

b) Books

KEPPLER, H. (2013): Volatiles under high pressure. – In: KARATO, S. (Ed.): Physics and Chemistry of the Deep Earth. Wiley, Chichester, 1-37

c) Popular scientific magazines

KEPPLER, H.; WALTE, N. (2013): Hochdruckforschung mit Neutronen – ein neues Fenster zum Erdinnern. Akademie Aktuell 2013, 2, 34-37

4.2 Publications (submitted, in press)

AUDÉTAT, A.; LOWENSTERN, J.B.: Melt inclusions. – In: SCOTT, S.D. (Ed.): Geochemistry of Mineral Deposits. Treatise on Geochemistry, 2nd Edition (in press)

BYKOVA, E.A.; BOBROV, A.V.; SIROTKINA, E.A.; BINDI, L.; OVSYANNIKOV, S.V.; DUBROVINSKY, L.S.; LITVIN, Y.A.: X-ray single-crystal and Raman study of knorringite, $Mg_3(Cr_{1.58}Mg_{0.21}Si_{0.21})Si_3O_{12}$, synthesized at 16 GPa and 1,600 °C. Physics and Chemistry of Minerals (accepted)

CARLSON, R.W.; GARNERO, E.; HARRISON, T.M.; LI, J.; MANGA, M.; MCDONOUGH, W.F.; MUKHOPADHYAY, S.; ROMANOWICZ, B.; RUBIE, D.C.; WILLIAMS, Q.; ZHONG, S.: How did early Earth become our modern world? Annual Review of Earth and Planetary Science (submitted)

ČERNOK, A.; BOFFA BALLARAN, T.; CARACAS, R.; MIYAJIMA, N.; BYKOVA, E.; PRAKAPENKA, V.; LIERMANN, H.-P.; DUBROVINSKY, L.: Pressure-induced phase transitions in coesite. American Mineralogist (submitted)

CHEMIA, Z.; DOLEJŠ, D.; STEINLE-NEUMANN, G.: Thermal effects of variable material properties and metamorphic reactions in a three-component subducting slab. Geophysical Journal International (submitted)

DEMOUCHY, S.; TOMMASI, A.; BOFFA BALLARAN, T.; CORDIER, P.: Low strength of Earth's uppermost mantle inferred from tri-axial deformation experiments on dry olivine crystals. Physics of the Earth and Planetary Interiors (in press)

FEI, H.; WIEDENBECK, M.; YAMAZAKI, D.; KATSURA, T.: Water has no significant effect on oxygen self-diffusion rate in forsterite. Physics of the Earth and Planetary Interiors (submitted)

GIANNINI, M.; BOFFA BALLARAN, T.; LANGENHORST, F.: Crystal chemistry of synthetic Ti-Mg bearing hibonites: A single crystal X-ray study. American Mineralogist (submitted)

GLAZYRIN, K.; BOFFA BALLARAN, T.; FROST, D.J.; MCCAMMON, C.; KANTOR, A.; MERLINI, M.; HANFLAND, M.; DUBROVINSKY, L.: Effect of iron oxidation state on the bulk sound velocity of the Earth's lower mantle. Earth and Planetary Science Letters (submitted)

GLAZYRIN, K.; MIYAJIMA, N.; SMITH, J.; LEE, K.K.M.: Stress- and pressure-induced iron spin-state crossover in lower mantle minerals. Journal of Geophysical Reasearch (submitted)

JACOBSON, S.A.; SCHEERES, D.J.; MCMAHON, J.: The formation of the wide asynchronous binary asteroid population. Astrophysical Journal (in press)

JACOBSON, S.A.; MORBIDELLI, A.: Constraints on terrestrial planet formation from the Moon, Earth and Mars. Philosophical Transactions A (submitted)

JACOBSON, S.A.; MORBIDELLI, A.; RAYMOND, S.N.; O'BRIEN, D.P.; WALSH, K.J.; RUBIE, D.C.: Highly siderophile elements in the Earth's mantle as a clock for the Moon-forming impact. Nature (submitted)

JACOBSON, S.A.; MARZARI, F.; ROSSI, A.; SCHEERES, D.J.; DAVIS, D.R.: Effect of rotational disruption on the size-frequency distribution of the Main Belt asteroid population. Monthly Notices of the Royal Astronomical Society Letters (submitted)

KONSCHAK, A.; KEPPLER, H.: The speciation of carbon dioxide in silicate melts. Contributions to Mineralogy and Petrology (submitted)

KUPENKO, I.; MCCAMMON, C.; SINMYO, R.; PRESCHER, C.; CHUMAKOV, A.I.; KANTOR, A.; RÜFFER, R.; DUBROVINSKY, L.: Electronic spin state of Fe,Al-containing $MgSiO_3$ perovskite at lower mantle conditions. Lithos, DOI: 10.1016/j.lithos.2013.10.022

LI, Y.; KEPPLER, H.: Nitrogen speciation in mantle and crustal fluids. Geochimica et Cosmochimica Acta (submitted)

LIN, Y.; EL GORESY, A.; HU, S.; ZHANG, J.; GILLET, Ph.; XU, Y.; YANG, W.; FENG, L.; ZHAO, X.; OZAWA, S.: Organic carbon from the Tissint Martian meteorite: Hints at past existence of life on Mars. Astrobiology (submitted)

MOOKHERJEE, M.; KEPPLER, H.; MANNING, C.E.: Aluminium speciation in aqueous fluids at deep crustal pressure and temperature. Geochimica et Cosmochimica Acta (in press)

MASOTTA, M.; MOLLO, S.; FREDA, C.; MOORE, G.M.; GAETA, M.: Clinopyroxene-liquid thermometers and barometers specific for alkaline differentiated magmas. Contributions to Mineralogy and Petrology (in press)

MASOTTA, M.; NI, H.; KEPPLER, H.: *In situ* observations of bubble growth in basaltic, andesitic and rhyodacitic melts. Contributions to Mineralogy and Petrology (accepted)

MIYAGI, L.; AMULELE, G.; OTSUKA, K.; DU, Z.; FARLA, R.J.M.; KARATO, S.: Plastic anisotropy and slip systems in ringwoodite deformed to high shear strain in the Rotational Drickamer Apparatus. Physics of the Earth and Planetary Interiors (in press)

MIYAHARA, M.; OHTANI, E.; EL GORESY, A.; LIN, Y.; FENG, L.; ZHANG, J.-C.; GILLET, Ph.; NAGASE, T.; MUTO, J.; NISHIJIMA, M.: Diamond mine in the solar system. Proceedings of the National Academy of Sciences (submitted)

NI, H.; KEPPLER, H.; WALTE, N.; SCHIAVI, F.; CHEN, Y.; MASOTTA, M.; LI, Z.: First *in situ* observation of olivine growth in an alkali basalt melt and the development of crystal size distribution in igneous rocks. Contributions to Mineralogy and Petrology (submitted)

NISHIHARA, Y.; OHUCHI, T.; KAWAZOE, T.; SPENGLER, D.; TASAKA, M.; KIKEGAWA, T.; SUZUKI, A.; OHTANI, E.: Rheology of fine-grained forsterite aggregate at deep upper mantle conditions. Journal of Geophysical Research (submitted)

NOVELLA, D.; FROST, D.J. (2013): The composition of hydrous partial melts of garnet peridotite at 6 GPa: implications for the origin of group II kimberlites. Journal of Petrology (submitted)

PAMATO, M.G.; KURNOSOV, A.; BOFFA BALLARAN, T.; TROTS, D.M.; CARACAS, R.; FROST, D.J.: Crystal structure refinement and elasticity of $Na_{1.07}Mg_{1.58}Al_{4.91}Si_{1.26}O_{12}$ NAL phase. American Mineralogist (submitted)

PRESCHER, C.; WEIGEL, C.; MCCAMMON, C.; NARYGINA, O.; POTAPKIN, V.; KUPENKO, I.; GLAZYRIN, K.; SINMYO, R.; CHUMAKOV, A.I.; DUBROVINSKY, L.: Iron spin state in silicate glass at high pressure: implications for melts in the Earth's lower mantle. Earth and Planetary Science Letters (in press)

RUBIE, D.C.; NIMMO, F.; MELOSH, H.J.: Formation of the Earth's core. – In: STEVENSON, D.J. (Ed.): Treatise on Geophysics 2nd Edition, Vol. 9: Evolution of the Earth. Elsevier, Amsterdam (submitted)

SCHMAUSS, D.; KEPPLER, H.: Adsorption of sulfur dioxide on volcanic ashes. American Mineralogist (submitted)

SINMYO, R.; BYKOVA, E.; MCCAMMON, C.; KUPENKO, I.; POTAPKIN, V.; DUBROVINSKY, L.: Crystal chemistry of Fe^{3+}-bearing (Mg,Fe)SiO_3 perovskite: A single-crystal X-ray diffraction study. Physics and Chemistry of Minerals (in press)

SINMYO, R.; GLAZYRIN, K.; MCCAMMON, C.; KUPENKO, I.; KANTOR, A.; POTAPKIN, V.; CHUMAKOV, A.I.; RÜFFER, R.; DUBROVINSKY, L.: The influence of solid solution on elastic wave 1 velocity determination in (Mg,Fe)O using nuclear inelastic scattering. Physics of the Earth and Planetary Interiors (submitted)

SINMYO, R.; PESCE, G.; GREENBERG, E.; MCCAMMON, C.; DUBROVINSKY, L.: Lower mantle electrical conductivity based on measurements of Al, Fe-bearing perovskite under lower mantle conditions. Earth and Planetary Science Letters (submitted)

SOUSTELLE, V.; TOMMASI, A.; DEMOUCHY, S.; FRANZ, L.: Melt-rock interactions, deformation, hydration and seismic properties in the sub-arc lithospheric mantle inferred from xenoliths from seamounts near Lihir, Papua New Guinea. Tectonophysics, doi: 10.1016/j.tecto.2013.09.024 (in press)

SOUSTELLE, V.; WALTE, N.P.; MANTHILAKE, M.A.G.M.; FROST, D.J.: Melt migration and melt-rock reactions in the deforming Earth's upper mantle: Experiments at high pressure and temperature. Geology, doi: 10.1130/G34889.1 (in press)

STAGNO, V.; FROST, D.J.; MCCAMMON, C.A.; FEI, Y.: The oxygen fugacity of graphite and diamond bearing eclogites in equilibrium with carbonate-rich melts. Implications for oxy-thermobarometry of eclogite rocks. Contributions to Mineralogy and Petrology (submitted)

SUN, W.; AUDÉTAT, A.; DOLEJŠ, D.: Solubility of molybdenite in hydrous haplogranite melts at 800 °C, 100-200 MPa. Geochimica et Cosmochimica Acta (submitted)

WANG, J.; BASS, J.D.; KATSURA, T.: Elastic properties of iron-bearing wadsleyite to 17.7 GPa: implications for mantle mineral model. Physics of the Earth and Planetary Interiors (in press)

YANG, X.; KEPPLER, H.; DUBROVINSKY, L.; KURNOSOV, A.: *In situ* infrared spectra of hydroxyl in wadsleyite and ringwoodite at high pressure and high temperature. American Mineralogist (submitted)

4.3 Presentations at scientific institutions and at congresses

BEYER, C.; FROST D.J.: 25.-30.08.2013, Goldschmidt 2013, Florence, Italy: "Experimental calibration of a garnet-clinopyroxene geobarometer for mantle eclogites", Mineralogical Magazine, 77(5), 698

BLAHA, S.; KATSURA, T.: 07.-12.04.2013, European Geosciences Union General Assembly, Vienna, Austria: "Annealing of deformed olivine single-crystals under 'dry' conditions", Geophysical Research Abstracts 15, EGU2013-9010, 2013

BOFFA BALLARAN, T.; KULARATNE, K.; KURNOSOV, A.; TRØNNES, R.G.: 19.-22.03.2013, 21th Annual Meeting of the German Crystallographic Society (DGK), Freiberg, Germany: "High-pressure structural behaviour of $CaIrO_3$ perovskite"

BYKOVA, E.; GOU, H.; DUBROVINSKAIA, N.; DUBROVINSKY, L.; MERLINI, M.; HANFLAND, M.: 19.-22.03.2013, 21th Annual Meeting of the German Crystallographic Society (DGK), Freiberg, Germany: "Compressibility of orthorhombic FeB_4 studied on a single crystal sample"

BYKOVA, E.; GOU, H.; HANFLAND, M.; ABAKUMOV, A.; DUBROVINSKAIA, N.; DUBROVINSKY, L.: 07.-12.07.2013, APS-SCCM & AIRAPT-24 Joint Conference, Seattle, USA: "Novel metal borides: structure, high-pressure behavior and properties"

BYKOVA, E.; BYKOV, M.; PRAKAPENKA, V.; KONÔPKOVÁ, Z.; LIERMANN, H.-P.; DUBROVINSKAIA, N.; DUBROVINSKY, L.: 08.-11.09.2013, 2013 Workshop of the IUCr Commission on High Pressure 'Advances in Static and Dynamic High-Pressure Crystallography', DESY, Hamburg, Germany: "Novel high-pressure Fe_2O_3 polymorph"

BYKOVA, E.; BYKOV, M.; PRAKAPENKA, V.; KONÔPKOVÁ, Z.; LIERMANN, H.-P.; DUBROVINSKAIA, N.; DUBROVINSKY, L.: 27.09.-01.10.2013, 3rd International Conference on Crystallogenesis and Mineralogy, Novosibirsk, Russia: "Novel high-pressure Fe_2O_3 polymorph"

CERANTOLA, V.; MCCAMMON, C.; DUBROVINSKY, L.: 07.-12.04.2013, European Geosciences Union General Assembly, Vienna, Austria: "Investigations on the fate of subducted carbonates", Geophysical Research Abstracts 15, EGU2013-8982, 2013

CERANTOLA, V.; MCCAMMON, C.; DUBROVINSKY, L.: 16.-19.09.2013, DMG & GV Joint Annual Meeting 2013, Tübingen, Germany: "Fe-bearing carbonates in the Earth's lower mantle"

CERANTOLA, V.; MCCAMMON, C.A.; DUBROVINSKY, L.S.; KUPENKO, I.; KANTOR, A.; SPIVAK, A.; POTAPKIN, V.; KANTOR, I.; CHUMAKOV, A.; SOLOPOVA, N.: 09.-13.12.2013, AGU Fall Meeting, San Francisco, USA[*B]: "Stability of Fe-bearing carbonates in the Earth's lower mantle", Abstract MR11B-03, 2013

ČERNOK, A.; BOFFA BALLARAN, T.; CARACAS, R.; MIYAJIMA, N.; BYKOVA, E.; PRAKAPENKA, V.; LIERMANN, H.-P.; DUBROVINSKY, L.: 25.-30.08.2013, Goldschmidt 2013, Florence, Italy: "Pressure-induced phase transitions in coesite", Mineralogical Magazine, 77(5), 844

CHUST, T.; STEINLE-NEUMANN; G.; BUNGE, H.-P.: 07.-12.04.2013, European Geosciences Union General Assembly, Vienna, Austria: "A computational framework for mineralogical thermodynamics", Geophysical Research Abstracts 15, EGU-2013-3225, 2013

COBIC, A.; MCCAMMON, C.; BERMANEC, V.: 26.05.-02.06.2013, 6th International Symposium on Granitic Pegmatites, Bartlett, USA: "Preliminary ^{57}Fe Mössbauer spectroscopy study of metamict allanite-(Ce) from granitic pegmatite, Fone, Aust-Agder, Norway"

DAUPHAS, N.; ROSKOSZ, M.; LIN, J.-F.; LIU, J.; NEUVILLE, D.R.; ALP, E.E.; HU, M.; ZHAO, J.; MCCAMMON, C.A.; OKUCHI, T.; TOMIOKA, N.; SIO, C.K.I.; TISSOT, F.; TISSANDIER, L.; MEDARD, E.; CORDIER, C.: 09.-13.12.2013, AGU Fall Meeting, San Francisco, USA*B: "Controls on iron isotopic fractionation in igneous rocks", Abstract MR52A-03, 2013

DE VRIES, J.; NIMMO, F.; MELOSH, H.J.; RUBIE, D.C.: 08.-13.09.2013, Earth and Planetary Science Congress, London, U.K.: "Melting during planetary collisions: Influence of target and impactor size"

DE VRIES, J.; NIMMO, F.; MELOSH, H.J.; RUBIE, D.C.: 21.-23.10.2013, Paneth Kolloquium, Nördlingen, Germany*A: "Melting during planetary collisions: Influence of target and impactor size"

EL GORESY, A.; GILLET, Ph.; MIYAHARA, M.; OHTANI, E.; OZAWA, S.; LIN, Y.; FENG, L.; ESCERIG, S.: 18.-22.03.2013, 44th Lunar and Planetary Science Conference, The Woodlands, Houston, USA: "Multiple shock events and diamond formation on Mars", Abstract 1037

EL GORESY, A.; GILLET, Ph.; MIYAHARA, M.; OHTANI, E.: OZAWA, S.; LIN Y.; FENG, L; ESCERIG, S: 19.-24.05.2013, Japan Geoscience Union Meeting, Makuhari, Chiba, Japan: "Tissint is a Rosetta stone deciphering Noachian magmatic activities and dynamic events in Mars' young history"

EL GORESY, A.; GILLET, Ph.; MIYAHARA, M.; OHTANI, E.; OZAWA, S.; BECK, P.; MONTAGNAC, G.: 31.05.2013, Tohoku University, Institute of Mineralogy, Petrology and Mineral Deposits, Sendai, Japan: "Shock-induced deformation of Shergottites: Shock-pressures and perturbations of magmatic ages on Mars"

EL GORESY, A.: 29.07.-02.08.2013, 76th Annual Meeting of the Meteoritical Society, Edmonton, Canada *(Leonard Medal Lecture)*: "Detailed petrography combined with careful isotopic studies versus intuitive interpretation of meteoritic evolution history"

FARLA, R.J.M.; AMULELE, G.; GIRARD, J.; MIYAJIMA, N.; KARATO, S.: 16.-18.09.2013, 19th International Conference on Deformation Mechanisms, Rheology and Tectonics, KU Leuven, Belgium: "High pressure (~ 19 GPa) and temperature (~ 2000-2200 K) deformation experiments on polycrystalline wadsleyite in the rotational Drickamer apparatus"

FEI, H.: 26.09.2013, Nanjing University, School of Earth Sciences and Engineering, Nanjing, China: "Silicon diffusion in forsterite and deformation mechanism in the Earth's upper mantle"

FISCHER, R.A.; CAMPBELL, A.J.; FROST, D.J.; HARRIES, D.; LANGENHORST, F.; MIYAJIMA, N.; POLLOK, K.; RUBIE, D.C.: 17.-20.06.2013, COMPRES Annual Meeting, Lake Geneva, USA: "High pressure metal-silicate partitioning of Co, Ni, Si, V, Cr, and O"

FISCHER, R.A.; CAMPBELL, A.J.; FROST, D.J.; HARRIES, D.; LANGENHORST, F.; MIYAJIMA, N.; POLLOK, K.; RUBIE, D.C.: 09.-13.12.2013, AGU Fall Meeting, San Francisco, USA*B: "Metal-silicate partitioning of Co, Ni, V, Cr, Si, and O up to 100 GPa and 5500 K: Implications for core formation", Abstract V33D-2798, 2013

FROST, D.J.: 09.09.2013, Centre for Earth Evolution and Dynamics (CEED), University of Oslo, Norway: "The redox state of the Earth's interior and its influence on the deep carbon and water cycle"

FROST, D.J.: 25.11.2013, GeoZentrum Nordbayern, FAU Erlangen-Nürnberg: "Diamonds, windows onto the Earths deep interior and the carbon cycle"

FROST, D.J.: 28.11.2013, Universitätsverein Bayreuth e.V., KSB Pegnitz: "Diamanten – Fenster in das tiefe Erdinnere und den Kohlenstoffkreislauf der Erde"

FROST, D.J.; MYHILL, R.; ZIBERNA, L.: 09.-13.12.2013, AGU Fall Meeting, San Francisco, USA^{*B}: "The distribution of ferric iron within the Earth's interior and evolution in the mantle's redox state", Abstract V41E-04, 2013

FROST, D.J.; NOVELLA, D.; MYHILL, R.; LIEBSKE, C.; TRØNNES, R.G.: 25.-30.8.2013, Goldschmidt 2013, Florence, Italy: "Experimental efforts to understand deep mantle melting", Mineralogical Magazine, 77(5), 1115

FROST, D.J.; STAGNO, V.; MCCAMMON, C.; FEI, Y.: 25.-30.08.2013, Goldschmidt 2013, Florence, Italy: "The stability of carbonate melt in eclogite rocks with respect to oxygen fugacity", Mineralogical Magazine, 77(5), 1116

GIANNINI, M.; BOFFA BALLARAN, T.; LANGENHORST, F.: 21.-23.10.2013, Paneth Kolloquium, Nördlingen, Germany^{*A}: "Ti^{3+} in hibonite - fingerprint of oxygen fugacity or crystal chemistry?"

GLAZYRIN, K.; MIYAJIMA, N.; SMYTH, J.; LEE, K.K.M.: 09.-13.12.2013, AGU Fall Meeting, San Francisco, USA^{*B}: "Stress- and pressure-induced iron spin-state crossover in lower mantle minerals", Abstract MR21A-2307, 2013

HEIDELBACH, F.: 10.-15.03.2013, DPG Spring Meeting of the Condensed Matter Section, Regensburg, Germany: "Recent developments in characterization of ultra-fine grained materials by EBSD"

IIZUKA, R.; SOUSTELLE, V.; WALTE, N.; FROST, D.J.; YAGI, T.: 09.-13.12.2013, AGU Fall Meeting, San Francisco, USA^{*B}: "Preferred orientation of lawsonite determined by deformation experiments at high pressure and temperature: Implications for low velocity layers in subduction zones", Abstract T43G-03, 2013

JACOBSON, S.A.: 13.11.2013, Solar, Stellar, and Planetary Sciences Seminar, Center for Astrophysics, Harvard University, Cambridge, USA: "Terrestrial planet formation in the age of the truncated disk"

JACOBSON, S.A.; MORBIDELLI, A.; WALSH, K.J.; O'BRIEN, D.P.; RAYMOND, S.N.; RUBIE, D.C.: 06.-11.10.2013, American Astronomical Society, 45th Annual Meeting, Division of Planetary Sciences, Denver, USA: "Getting down to brass tacks' in the Grand Tack scenario: matching important accretion and timing constraints", Meeting Abstracts 45, 503.02

JACOBSON, S.A.; MORBIDELLI, A.; WALSH, K.J.; O'BRIEN, D.P.; RAYMOND, S.N.; RUBIE, D.C.: 23.-26.09.2013, Royal Society Satellite Meeting: Origin of the Moon – Challenges and Prospects, London, UK: "Moon formation in the Grand Tack Scenario"

JACOBSON, S.A.; MORBIDELLI, A.; WALSH, K.J.; O'BRIEN, D.P.; RAYMOND, S.N.: 15.-20.07.2013, Protostars & Planets VI, Heidelberg, Germany: "Tactful accretion: considering constraints in the Grand Tack model", 2H024

JACOBSON, S.A.; MORBIDELLI, A.; WALSH, K.J.; O'BRIEN, D.P.; RAYMOND, S.N.: 23.-28.06.2013, Gordon Research Conference 'Origins of Solar Systems', South Hadley, USA: "Last giant (Moon forming) impacts in the Grand Tack paradigm"

KATSURA, T.; FEI, H.; WIEDENBECK, M.; YAMAZAKI, D.: 04.-06.03.2013, 3rd Global-COE International Symposium on Deep Earth Mineralogy, Ehime University, Matsuyama, Japan (*invited*): "Small effect of water on upper mantle rheology based on Si self-diffusion coefficients"

KATSURA, T.: 08.-11.09.2013, Workshop of the IUCr Commission on High Pressure, DESY, Hamburg: "Defect chemistry and Si-diffusion in forsterite"

KATSURA, T.; FEI, H.; KOIZUMI, S.; HIRAGA, T.; SAKAMOTO, N.; HASHIGUCHI, M.; YURIMOTO, H.; YAMAZAKI, D.: 09.-13.12.2013, AGU Fall Meeting, San Francisco, USA^{*B}: "Si grain-boundary diffusion in forsterite as a function of pressure, temperature and water content", Abstract MR41A-2354, 2013

KATSURA, T.; FEI, H.; WIEDENBECK, M.; YAMAZAKI, D.: 07.-12.04.2013, European Geosciences Union General Assembly, Vienna, Austria: "Si and O self-diffusion coefficient of forsterite as a function of water content", Geophysical Research Abstracts 15, EGU2013-2326, 2013

KAWAZOE, T.; NISHIHARA, Y.; OHUCHI, T.; MARUYAMA, G.; HIGO, Y.; FUNAKOSHI, K.; IRIFUNE, T.: 08.-11.09.2013, 2013 Workshop of the IUCr Commission on High Pressure 'Advances in Static and Dynamic High-Pressure Crystallography', DESY, Hamburg, Germany: "*In situ* stress-strain measurements on ringwoodite at 18 GPa and 1700 K using a deformation-DIA apparatus combined with synchrotron radiation"

KAWAZOE, T.; NISHIHARA, Y.; OHUCHI, T.; MARUYAMA, G.; HIGO, Y.; FUNAKOSHI, K.; IRIFUNE, T.: 09.-13.12.2013, AGU Fall Meeting, San Francisco, USA^{*B}: "*In situ* creep strength measurements on ringwoodite at 18 GPa and 1700 K using a deformation-DIA apparatus combined with synchrotron radiation", Abstract MR33C-02, 2013

KEPPLER, H.: 11.-12.07.2013, Universität Köln, DFG Rundgespräch 'From asteroids towards the first oceans: building a habitable planet', Köln, Germany: "Carbon and nitrogen on the early Earth"

KULARATNE, K.; AUDÉTAT, A.: 25.-30.08.2013, Goldschmidt 2013, Florence, Italy: "New experimental data on TiO_2 solubility in hydrous rhyolite melts: implications for TitaniQ", Mineralogical Magazine, 77(5), 1521

KUPENKO, I.; MCCAMMON, C.A.; SINMYO, R.; CERANTOLA, V.; POTAPKIN, V.; CHUMAKOV, A.; KANTOR, A.; RÜFFER, R.; DUBROVINSKY, L.S.: 09.-13.12.2013, AGU Fall Meeting, San Francisco, USA^{*B}: "Electronic spin state of lower mantle perovskite at conditions of the deep Earth's interior from *in situ* high P,T nuclear resonance measurements", Abstract MR21A-2309, 2013

KURNOSOV, A.; TROTS, D.; BOFFA BALLARAN, T.; FROST, D.: 25.-30.08.2013, Goldschmidt 2013, Florence, Italy: "Single-crystal elastic properties of $Fe_{0.04}Mg_{0.96}SiO_3$ – perovskite at high pressure" Mineralogical Magazine, 77(5), 1526

KURNOSOV, A.; TROTS, D.M.; BOFFA BALLARAN, T.; FROST, D.J.: 27.09.-01.10.2013, 3rd International Conference on Crystallogenesis and Mineralogy, Novosibirsk, Russia: "Single-crystal elastic properties of $(Mg,Fe)SiO_3$ – perovskites at high pressure"

KURNOSOV, A.: 02.-06.10.2013, Post-Conference Workshop for Students and Young Scientists 'Frontiers of Crystallography', Novosibirsk State University, Novosibirsk, Russia (*invited*): "High pressure X-ray diffraction combined with Brillouin spectroscopy"

KURNOSOV, A.; BOFFA BALLARAN, T.; TROTS, D.M.; FROST, D.J.: 09.-13.12.2013, AGU Fall Meeting, San Francisco, USA*B: "High pressure single crystal elasticity of $MgSiO_3$ and $(Mg,Fe)SiO_3$ perovskite", Abstract MR31A-2272, 2013

LAURENZ, V.; RUBIE, D.C.; FROST, D.J.: 21.-23.10.2013, Paneth Kolloquium, Nördlingen, Germany*A: "Metal-silicate partitioning of HSE in S-bearing systems-Implications for Earth's core formation"

LAURENZ, V.; RUBIE, D.C.; FROST, D.J.: 25.-30.08.2013, Goldschmidt 2013, Florence, Italy: "Metal-silicate partitioning of the HSE at high pressures and temperatures in S-bearing systems", Mineralogical Magazine, 77(5), 1554

LAURENZ, V.; RUBIE, D.C.; FROST, D.J.: 23.-28.06.2013, Gordon Research Conference 'Origins of Solar Systems', South Hadley, USA: "Metal-silicate partitioning of the HSE at high pressures and high temperatures in S-bearing systems"

LIN, Y.; EL GORESY, A.; HU, S.; ZHANG, J.; GILLET, Ph.; XU, Y.; HAO, J.; MIYAHARA, M.; OYANG, Z.; OHTANI, E.; XU, L.; YANG, W.; FENG, L.; ZHAO, X.; YANG, J.; OZAWA, S.: 18.-22.03.2013, 44th Lunar and Planetary Science Conference, The Woodlands, Houston, USA: "NanoSIMS analyses of organic carbon from Mars: Evidence for biogenic origin", Abstract 1476

MASOTTA, M.; NI, H.; KEPPLER, H.: 09.-13.12.2013, AGU Fall Meeting, San Francisco, USA*B: "*In situ* observations of bubble growth in basaltic, andesitic and rhyodacitic melts", Abstract V13H-04, 2013

MCCAMMON, C.; POTAPKIN, V.; GLAZYRIN, K.; KANTOR, A.; KUPENKO, I.; PRESCHER, C.; SINMYO, R.; SMIRNOV, G.; CHUMAKOV, A.; RÜFFER, R.; DUBROVINSKY, L.: 11.-12.01.2013, 7th North American Mössbauer Symposium, Austin, USA: "Mössbauer spectroscopy along the geotherm"

MCCAMMON, C.: 07.-12.04.2013, European Geosciences Union General Assembly, Vienna, Austria: "Iron matters: Its influence on what we think we know about the deep Earth's interior", Geophysical Research Abstracts 15, EGU2013-13917, 2013

MCCAMMON, C.: 21.05.2013, Australian National University, Canberra, Australia: "Iron matters and how it influences what we think we know about the deep Earth's interior"

MCCAMMON, C.: 24.05.2013, University of New South Wales at Australian Defence Force Academy, Canberra, Australia: "What we think we know about the deep Earth's interior"

MCCAMMON, C.: 27.-28.05.2013, Macquarie University, Sydney, Australia: "Short Course on Oxygen Fugacity"

MIYAHARA. M.; OHTANI, Y.; EL GORESY, A.; LIN, Y.; FENG, L.; ZHANG, J.; GILLET, Ph.; NAGASE, T.; MUTO, J.; NISHIJIMA, M.: 44th Lunar and Planetary Science Conference, The Woodlands, Houston, USA: "A huge single diamond in Almahata Sitta coarse-grained ureilite", Abstract 1425

MIYAJIMA, N.: 19.-24.05.2013, Japan Geoscience Union Meeting, Makuhari, Chiba, Japan: "Al, Si interdiffusion in majoritic garnet and the dislocation microstructures"

MYHILL, R.; NOVELLA, D.; FROST, D.J.: 02.-07.06.2013, Gordon Research Conference 'Interior of the Earth', South Hadley, USA: "Melting in the MgO-SiO_2-H_2O-CO_2 system to 20 GPa"

MYHILL, R.; FROST, D.J.: 20.-22.11.2013, Network Meeting of the Alexander von Humboldt Foundation, Jena, Germany: "The oxidation state of Earth's upper mantle"

NISHIHARA, Y.; OHUCHI, T.; KAWAZOE, T.; MARUYAMA, G.; HIGO, Y.; FUNAKOSHI, K.; SETO, Y.; IRIFUNE, T.: 04.-06.03.2013, GCOE-TANDEM International Symposium 2013, Matsuyama, Japan: "Lattice preferred orientation of hcp-iron induced by shear deformation"

NOVELLA D.; FROST D.J.; HAURI; E.H.: 25.-30.08.2013, Goldschmidt 2013, Florence, Italy: "The formation of low degree hydrous melts in the Earth's upper mantle"

NOVELLA D.: 20.11.2013, Laboratoire Magmas et Volcans, Clermont-Ferrand, France, "The interaction between silicate minerals and C-O-H bearing melts in the Earth's mantle"

OVSYANNIKOV, S.V.; TSIRLIN, A.A.; KARKIN, A.E.; SHCHENNIKOV, V.V.; BYKOVA, E.; TROTS, D.M.; KURNOSOV, A.V.; EGOAVIL, R.; VERBEECK, J.; ABAKUMOV, A.M., GOU, H.; MCCAMMON, C.; DUBROVINSKY, L.: 01.-06.09.2013, 51nd European High-Pressure Research Group Conference (EHPRG), London, U.K.: "High-pressure high-temperature synthesis and properties of Fe_4O_5"

OVSYANNIKOV, S.V.; TROTS, D.M.; KURNOSOV, A.V.; MORGENROTH, W.; LIERMANN, H.-P.; DUBROVINSKY, L.: 01.-06.09.2013, 51nd European High-Pressure Research Group Conference (EHPRG), London, U.K.: "High-pressure behaviour and new high-pressure phases of vanadium sesquioxide, V_2O_3"

PAMATO, M.G.; KURNOSOV, A.; BOFFA BALLARAN, T.; TROTS, D.M.; FROST, D.J.: 19.-22.03.2013, 21th Annual Meeting of the German Crystallographic Society (DGK), Freiberg, Germany: "Single crystal elasticity of $Na_{1.07}Mg_{1.58}Al_{4.91}Si_{1.26}O_{12}$ NAL phase at high-pressure and temperature"

PAMATO, M.G.; KURNOSOV, A.; BOFFA BALLARAN, T.; TROTS, D.M.; CARACAS, R.; FROST, D.J.: 25.-30.08.2013, Goldschmidt 2013, Florence, Italy: "Single crystal elasticity of the $Na_{1.07}Mg_{1.58}Al_{4.91}Si_{1.26}O_{12}$ NAL phase and seismic heterogeneity in the deep mantle", Mineralogical Magazine, 77(5), 1916

PAMATO, M.G.; KURNOSOV, A.; BOFFA BALLARAN, T.; FROST, D.J.; ZIBERNA, L.; GIANNINI, M.; TROTS, D.M.; TKACHEV, S.N.; ZHURAVLEV, K.K.; PRAKAPENKA, V.B.: 09.-13.12.2013, AGU Fall Meeting, San Francisco, USA*B: "Single crystal elasticity of majoritic garnet at high pressure and temperature, Abstract MR31A-2277, 2013

POSNER, E.S.; GANGULY, J.; HERVIG, R.: 18.-22.03.2013, 44th Lunar and Planetary Science Conference, The Woodlands, Houston, USA: "Cr diffusion in spinel: Experimental studies and applications to cooling rate recorded by chevron zoned Cr spinel in Allende and Mn-Cr cosmochronology", Abstract 1419

POSNER, E.S.; FROST, D.J.; RUBIE, D.C.: 23.-28.06.2013, Gordon Research Conference 'Origins of Solar Systems', South Hadley, USA: "Si diffusion in liquid Fe: Implications for the basal region of a magma ocean and planetary core-mantle boundaries"

POSNER, E.S.; FROST, D.J.; RUBIE, D.C.: 25.-30.08.2013, Goldschmidt 2013, Florence, Italy: "Silicon diffusion in liquid iron: Kinetic implications for metal-silicate equilibration"

POSNER, E.S.; RUBIE, D.C.; FROST, D.J.: 21.-23.10.2013, Paneth Kolloquium, Nördlingen, Germany^{*A}: "Chemical evolution of planetesimal cores during the early history of the solar system"

POTAPKIN, V.; DUBROVINSKY, L.; MCCAMMON, C.; KANTOR, A.; KUPENKO, I.; GLAZYRIN, K.; CHUMAKOV, A.I.; RÜFFER, R.; SINMYO, R.; PRESCHER, C.; SMIRNOV, G.V.: 01.-06.09.2013, International Conference on the Applications of the Mössbauer Effect 2013, Opatija, Croatia: "No spin transitions of ferric iron in lower mantle silicate perovskite"

PRESCHER, C.; BYKOVA, E.; KUPENKO, I.; GLAZYRIN, K.; KANTOR, A.; MCCAMMON, C.A.; MOOKHERJEE, M.; MIYAJIMA, N.; CERANTOLA, V.; NAKAJIMA, Y.; PRAKAPENKA, V.; RÜFFER, R.; CHUMAKOV, A.; DUBROVINSKY, L.S.: 09.-13.12.2013, AGU Fall Meeting, San Francisco, USA^{*B}: "Elastic properties and phase transitions of Fe_7C_3 and new constraints on the light element budget of the Earth's inner core", Abstract MR11B-04, 2013

ROBERGE, M.; BUREAU, H.; BOLFAN-CASANOVA, N.; FROST, D.; RAEPSAET, C.; SURBLE, S.; KHODJA, H.; FIQUET, G.: 25.-30.08.2013, Goldschmidt 2013, Florence, Italy: "F and Cl solubilities in wadsleyite and ringwoodite", Mineralogical Magazine, 77(5), 2068

RUBIE, D.C.: 30.-31.01.2013, ACCRETE Group Meeting, Bayerisches Geoinstitut, Bayreuth, Germany: "Combining models of accretion and core formation"

RUBIE, D.C.: 23.-28.06.2013, Gordon Research Conference 'Origins of Solar Systems', South Hadley, USA: "Terrestrial planet formation in the context of giant planet formation"

RUBIE, D.C.; O'BRIEN, D.P.; MORBIDELLI, A.; JACOBSON, S.A.; YOUNG, E.D.; 25.-30.08.2013, Goldschmidt 2013, Florence, Italy: "Accretion and chemical evolution of the terrestrial planets" Mineralogical Magazine, 77(5), 2094

RUBIE, D.C.; YOUNG, E.D.; JACOBSON, S.A.; MORBIDELLI, A.; O'BRIEN, D.P.: 25.-26.09.2013, Royal Society Meeting 'Origin of the Moon – Challenges and propects', Chicheley Hall, Buckinghamshire, U.K.: "Oxygen isotope evolution during accretion of the terrestrial planets"

RUBIE, D.C.; YOUNG, E.D.; JACOBSON, S.A.; MORBIDELLI, A.; O'BRIEN, D.P.: 21.-23.10.2013, Paneth Kolloquium, Nördlingen, Germany^{*A}: "Oxygen isotope evolution in the early Solar System"

SHCHEKA, S.; KEPPLER, H.: 10.10.2013, Centre de Recherche Pétrographiques et Géochimiques, Nancy, France: "Noble gas solubility in $MgSiO_3$-perovskite and the origin of the terrestrial noble gas signature"

SINMYO, R.; GLAZYRIN, K.; MCCAMMON, C.A.; KUPENKO, I.; KANTOR, A.; POTAPKIN, V.; CHUMAKOV, A.; RÜFFER, R.; DUBROVINSKY, L.S.: 09.-13.12.2013, AGU Fall Meeting, San Francisco, USA^{*B}: "The influence of solid solution on elastic wave velocity determination in (Mg,Fe)O using nuclear inelastic scattering", Abstract MR21A-2313, 2013

SMYTH, J.R.; JACOBSEN, S.D.; HUSS, G.R.; MIYAJIMA, N.; PAMATO, M.G.: 09.-13.12.2013, AGU Fall Meeting, San Francisco, USA^{*B}:"Hydrogen incorporation in aluminous $MgSiO_3$-perovskite", Abstract MR12A-06, 2013

SORBADERE, F.; SCHIANO, P.; MÉTRICH, N.; MÉDARD, E.; LAPORTE, D.: 09.-13.12.2013, AGU Fall Meeting, San Francisco, USA^{*B} (*invited*): "Constraints on the origin of silica-undersaturated arc magmas inferred from melt inclusions and experimental melting of peridotite – pyroxenite mixed source", Abstract V23D-04, 2013

SORBADERE, F.; FROST, D.; MCCAMMON, C.: 09.-13.12.2013, AGU Fall Meeting, San Francisco, USA^{*B}: "Determination of the ferric iron (Fe^{3+}) behaviour during MORB petrogenesis", Abstract V33A-2717, 2013

SOUSTELLE V.; WALTE, N.P.; MANTHILAKE, M.A.G.M.; FROST, D.J.: 04.-06.03.2013, 3rd Global-COE International Symposium on Deep Earth Mineralogy, Ehime University, Matsuyama, Japan: "Interactions between deformation and reactive melt percolation in the upper mantle: simple-shear deformation experiment at high pressure and temperature"

SPICE, H.; SANLOUP, C.; DREWITT, J.; GROUCHY, C.D.; CREPISSON, C.; KONO, Y.; PARK, C.; MCCAMMON, C.: 25.-30.08.2013, Goldschmidt 2013, Florence, Italy: "Viscosity and structure of fayalite liquid at high pressure up to 9 GPa", Mineralogical Magazine, 77(5), 2247

STEINLE-NEUMANN, G.; DE KOKER, N.; VLČEK, V.: 07.-12.04.2013, European Geosciences Union General Assembly, Vienna, Austria (*invited*): "Electrical and thermal conductivity of liquid iron and iron alloys at core conditions", Geophysical Research Abstracts 15, EGU2013-3473, 2013

STEINLE-NEUMANN, G.: 23.-25.10.2013, Joint Workshop on High Pressure, Planetary, and Plasma Physics in Berlin, Germany: "High values of thermal conductivity for Fe in planetary cores: the puzzle pieces and what they mean for planetary dynamos"

STEINLE-NEUMANN, G.: 04.-07.11.2013, Workshop on Computational exploration of atomistic structures and their interrelation with physical properties, IFW Dresden, Germany (*invited*): "Magnetism in iron at high pressure"

VOGEL, A.K.; RUBIE, D.C.; FROST, D.J.; PALME, H., AUDÉTAT, A.: 30.-31.01.2013, ACCRETE Group Meeting, Bayerisches Geoinstitut, Bayreuth, Germany: "The partitioning behaviour of volatile elements at high pressures and temperatures"

VOGEL, A.K.; RUBIE, D.C.; FROST, D.J.; AUDÉTAT, A.; PALME, H.: 25.-30.08.2013, Goldschmidt 2013, Florence, Italy: "The dependence of siderophile element partitioning on pressure, temperature, fO_2 and S-content", Mineralogical Magazine, 77(5), 2423

VOGEL, A.K.; RUBIE, D.C.; FROST, D.J.; AUDÉTAT, A.; PALME, H.: 21.-23.10.2013, Paneth Kolloquium, Nördlingen, Germany^{*A}: "The dependence of siderophile element partitioning on pressure, temperature, fO_2, and Si- and S-contents"

VOGEL, A.K.; RUBIE, D.C.; FROST, D.J.; PALME, H.; AUDÉTAT, A.: 23.-28.06.2013, Gordon Research Conference 'Origins of Solar Systems', South Hadley, USA: "The dependence of siderophile element partitioning on pressure, temperature, oxygen fugacity and sulfur content"

YOUNG, E.D.; RUBIE, D.C.; O'BRIEN, D.P.: 18.-22.03.2013, 44th Lunar and Planetary Science Conference, The Woodlands, Houston, USA: "Oxygen isotope consequences of giant planet migration", Abstract 1794

ZIBERNA; L.; KLEMME, S.; NIMIS, P.: 25.-30.08.2013, Goldschmidt 2013, Florence, Italy: "Garnet and spinel in the upper mantle: Results from thermodynamic modeling in fertile and depleted compositions", Mineralogical Magazine, 77(5), 2618

*A **Joint meeting 'Paneth Kolloquium', 'The first 10 million years of the solar system' (DFG SPP 1385), 21.-23.10.2013, Nördlingen, Germany**

*B **AGU: American Geophysical Union Fall Meeting, 09.-13.12.2013, San Francisco, USA**

4.4 Lectures and seminars at Bayerisches Geoinstitut

ANGEL, R., Università degli Studi di Padova, Dipartimento di Geoscienze, Padova, Italy: "Structure and function: Why are feldspars so anisotropic?", 27.06.2013

BEYER, C., Bayerisches Geoinstitut, Bayreuth, Germany: "Experimental calibration of a garnet-clinopyroxene geobarometer for mantle eclogites", 07.11.2013

BOLLINGER, C., Université Lille 1, UMET - Unité Matériaux et Transformation, CNRS, Villeneuve d'Ascq, France: "Experimental study of the rheology of polycristalline olivine under upper mantle conditions with the Deformation-DIA", 19.07.2013

BOTCHARNIKOV, R., Leibniz Universität Hannover, Institut für Mineralogie, Hannover, Germany: "Mobilization and transport of volatiles and metals in magmatic systems", 07.01.2013

BOULARD, E., Stanford University, Department of Geological and Environmental Sciences, Stanford, USA: "Investigation of C-rich phases at lower mantle conditions", 21.11.2013

BYKOVA, E., Bayerisches Geoinstitut, Bayreuth, Germany: "High pressure behavior of Fe_2O_3", 06.06.2013

CERANTOLA, V., Bayerisches Geoinstitut, Bayreuth, Germany: "Fe-bearing carbonates in the Earth's lower mantle", 14.11.2013

CHANG, Y.-Y., Northwestern University, Department of Earth and Planetary Sciences, Evanston, USA: "Elastic properties of Earth and applied materials: the influence of defects", 12.09.2013

CHEN, J., Florida International University, Mechanical and Materials Engineering Departement, Miami, USA: "Water is needed in the mantle from both rheological and elastic perspectives", 08.08.2013

CHEN, J., Florida International University, Mechanical and Materials Engineering Departement, Miami, USA: "Strengths of mantle dominant minerals and their possible implications to understanding of deep earthquakes", 19.09.2013

CHUST, T., Bayerisches Geoinstitut, Bayreuth, Germany: "A computational framework for mineralogical thermodynamics", 02.05.2013

CLESI, V., Ecole Normale Supérieure de Lyon, France: "Phase stability of the tetragonal almandine pyrope phase (TAPP)", 13.06.2013

FEDORTCHOUK, Y., Department of Earth Sciences, Dalhousie University, Halifax, Nova Scotia, Canada: "Look into the composition of mantle fluid from diamond resorption", 22.10.2013

FEI, H., Bayerisches Geoinstitut, Bayreuth, Germany: "Small effect of water on upper mantle rheology", *Academy Commission Business Meeting*, 25.04.2013

FEI, H., Bayerisches Geoinstitut, Bayreuth, Germany: "Silicon grain-boundary diffusion in forsterite and deformation mechanism in Earth's upper mantle", 19.09.2013

FRIGO, C., Bayerisches Geoinstitut, Bayreuth, Germany: "Oxidation-hydration relations in eudialyte from the Ilímaussaq complex, Greenland", 25.07.2013

FROST, D., Bayerisches Geoinstitut, Bayreuth, Germany: "Carbon in the Earth's interior", *Academy Commission Business Meeting*, 25.04.2013

GOU, H., Bayerisches Geoinstitut, Bayreuth, Germany: "Realizations of novel boron-based materials at extreme conditions", 16.05.2013

KLIMM, K., Johann Wolfgang Goethe-Universität, Institut für Geowissenschaften, Facheinheit Mineralogie, Frankfurt/M., Germany: "REE & S in slab melts: Insights into the thermal structure and redox state of subduction zones", 17.01.2013

KOLESNIKOV, A., Carnegie Institution of Washington, Geophysical Laboratory, Washington DC, USA: "Chemistry of hydrocarbons under extreme pressures and temperatures", 24.05.2013

KULARATNE, K., Bayerisches Geoinstitut, Bayreuth, Germany: "High pressure structural evolution of $CaIrO_3$ perovskite", 01.08.2013

KURNOSOV, A., Bayerisches Geoinstitut, Bayreuth, Germany: "Elastic properties of $(Mg,Fe)SiO_3$-perovskites at high pressures. Simoultaneous Brillouin scattering and XRD measurements", 28.11.2013

LAUMONIER, M., UMR 7327 – CNRS/Université d'Orléans, Institut des Sciences de la Terre d'Orléans, France: "Magma mixing at HP-HT", 24.07.2013

LE ROUX, V., Woods Hole Oceanographic Institution, Woods Hole, USA: "Melting, erupting, receyling: Where and how to probe the Earth's mantle", 23.01.2013

LI, Y., Bayerisches Geoinstitut, Bayreuth, Germany: "An experimental study of deep nitrogen geochemistry", 20.06.2013

LIERMANN, H.-P., Deutsches Elektronen Synchrotron DESY, PETRA III, P02 Hard X-Ray Diffraction Beamline, Hamburg, Germany: "Extreme conditions research at DESY: Tools to explore high-pressure and planetary physics", 14.10.2013

LIN, Y., Chinese Academy of Sciences, Institute of Geology and Geophysics, Beijing, China: "NanoSIMS analysis of organic carbon from the Tissint Martian meteorite: Evidence for biogenic origin", 03.09.2013

MALFAIT, W., ETH Zürich, Institute of Geochemistry and Petrology, Zürich, Switzerland: "Structure and properties of magmatic liquids: From molecular species to supervolcanoes", 08.01.2013

MARQUARDT, H., GeoForschungsZentrum Potsdam, Germany: "Elasticity and structure of geomaterials at extreme conditions", 17.10.2013

MARQUARDT, K., GeoForschungsZentrum Potsdam, Germany: "Grain boundaries in Earth sciences: Structures, properties and processes", 15.08.2013

MUGNAIOLI, E., Johannes Gutenberg-Universität Mainz, Institut für Physikalische Chemie, Mainz, Germany: "Structure characterization of nanocrystalline materials by HRTEM and electron diffraction tomography", 01.07.2013

NEMETH, P., Arizona State University, School of Earth and Space Exploration, Tempe, USA: "TEM - our window into minerals at the atomic scale", 03.07.2013

NOVELLA, D., Universitè Blaise Pascal, Laboratoire Magmas et Volcans, Clermont-Ferrand, France: "The interaction between silicate minerals and C-O-H bearing melts in the Earth's mantle", 31.10.2013

OHUCHI, T., Ehime University, Geodynamics Research Center, Matsuyama, Japan: "*In situ* shear deformation of olivine and its implications for the mechanism of fabric developments", 13.09.2013

OJWANG', D.O., Bayerisches Geoinstitut, Bayreuth, Germany: "Fe_4O_5: a new iron oxide phase", 28.02.2013

SANCHEZ VALLE, C., ETH Zürich, Institute of Geochemistry and Petrology, Zürich, Switzerland: "Fluids and mass transfer mechanisms in subduction zones", 15.01.2013

SANTAMARIA PÉREZ, D., Universidad Complutense de Madrid, Departamento de Química-Física I, Madrid, Spain: "Towards the understanding of the structure of solids", 21.01.2013

SAVCHUK, O., Bayerisches Geoinstitut, Bayreuth, Germany: "Pressure effect on thermocouple electro-motive force (EMF)", 18.07.2013

SCHIANO, P., Universitè Blaise Pascal, Laboratoire Magmas et Volcans, Clermont-Ferrand, France: "Melt inclusions preserved in minerals as natural experimental environments", 26.09.2013

SHARP, Z., University of New Mexico, Department of Earth & Planetary Sciences, Albuquerque, USA: "A hydrogen reduction method relevant to planetary formation", 28.05.2013

TROTS, D., Bayerisches Geoinstitut, Bayreuth, Germany: "The determination of hydrogen positions in high-pressure silicates by neutron diffraction", 23.05.2013

VOGEL, A., Bayerisches Geoinstitut, Bayreuth, Germany: "The dependence of siderophile element partitioning on pressure, temperature, fO_2 and Si- and S-contents", 11.11.2013

VLCEK, V., Bayerisches Geoinstitut, Bayreuth, Germany: "Electronic transport properties in liquid Al at high pressure", *Academy Commission Business Meeting*, 25.04.2013

WEBSTER, J., American Museum of Natural History, Department of Earth & Planetary Sciences, New York, USA: "Volatile components, magma evolution, and eruptive behaviors of Augustine Volcano, Alaska", 12.09.2013

ZIBERNA, L., Bayerisches Geoinstitut, Bayreuth, Germany: "What garnet and clinopyroxene can tell us about the evolution of sub-cratonic mantle sections: A case study of the Zagadochnaya kimberlite (Yakutia)", 18.04.2013

4.5 Conference organization

25.-30.08.2013, Goldschmidt 2013, Florence, Italy: Theme 22 "The Cutting Edge in Mineralogy and Mineral Physics" (C. MCCAMMON; R. OBERTI)

25-30.08.2013, Goldschmidt 2013, Florence, Italy: Session 07e "Vapor phase mobility in arc volcanic systems" (A. KENT; A. AUDÉTAT; M. ROWE)

16.-19.09.2013, DMG & GV Joint Annual Meeting, Tübingen, Germany: Sessions T5S2 & T5S3 Earth Mantle, Solids, Liquids and Gases Parts A & B (C. MCCAMMON; M. WILKE; R. ALMEEV)

02.-06.12.2013, 12th Freiburg Short Course in Economic Geology: "Granite-related mineral systems" (A. AUDÉTAT; R.E. BOTCHARNIKOV; D.B. CLARKE; F. HOLTZ; J.-L. VIGNERESSE)

09.-13.12.2013, American Geophysical Union Fall Meeting, San Francisco, USA: Session V52B "Footprints of Magma Chamber Dynamics in Eruptive Products" (S. MOLLO; K. PUTIRKA; M. MASOTTA; P. GIACOMONI)

23.-25.10.2013, Joint Workshop on High Pressure, Planetary, and Plasma Physics, DLR Institute of Planetary Research, Berlin, Germany (F. SOHL; H.-P. LIERMANN; R. REDMER; G. STEINLE-NEUMANN; T. TSCHENTSCHER; F.W. WAGNER)

5. Visiting scientists

5.1 Visiting scientists funded by the Bayerisches Geoinstitut

BOLLINGER, C., Université Lille 1, UMET - Unité Matériaux et Transformation, CNRS, Villeneuve d'Ascq, France: 17.-19.07.2013
BOTCHARNIKOV, R., Leibniz Universität Hannover, Institut für Mineralogie, Hannover, Germany: 07.-09.01.2013
BOULARD, E., Stanford University, Department of Geological and Environmental Sciences, Stanford, USA: 20.-22.11.2013
CHANG, Y.-Y., Northwestern University, Department of Earth and Planetary Sciences, Evanston, USA: 10.-14.09.2013
CHEN, J., Florida International University, Mechanical and Materials Engineering Department, Miami, USA: 27.07.-23.09.2013
CLESI, V., Ecole Normale Supérieure de Lyon, France: 11.01.-30.06.2013
DOBSON, D., University College London, Department of Earth Sciences, London, U.K.: 29.-31.10.2013
DOLEJŠ, D., Charles University, Institute of Petrology and Structural Geology, Prague, Czech Republic: 11.-15.02.2013, 14.-16.04.2013
FEDORTCHOUK, Y., Department of Earth Sciences, Dalhousie University, Halifax, Nova Scotia, Canada: 21.-23.10.2013
HELFFRICH, G., Bristol University, School of Earth Sciences, Bristol, U.K.: 03.-06.12.2013
KLIMM, K., Johann Wolfgang Goethe-Universität, Institut für Geowissenschaften, Facheinheit Mineralogie, Frankfurt/M., Germany: 16.-18.01.2013
LAUMONIER, M., UMR 7327 – CNRS/Université d'Orléans, Institut des Sciences de la Terre d'Orléans, France: 24.-26.07.2013
LE ROUX, V., Woods Hole Oceanographic Institution, Woods Hole, USA: 22.-26.01.2013
LI, W., China University of Geosciences, Wuhan, China: 14.-18.04.2013, 01.11.-31.12.2013
LIERMANN, H.-P., Deutsches Elektronen Synchrotron DESY, PETRA III, P02 Hard X-Ray Diffraction Beamline, Hamburg, Germany: 14.10.2013
LIN, Y., Chinese Academy of Sciences, Institute of Geology and Geophysics, Beijing, China: 02.-04.09.2013
MALFAIT, W., ETH Zürich, Institute of Geochemistry and Petrology, Zürich, Switzerland: 07.-10.01.2013
MARQUARDT, H., GeoForschungsZentrum Potsdam, Germany: 16.-17.10.2013
MARQUARDT, K., GeoForschungsZentrum Potsdam, Germany: 14.-16.08.2013
MUGNAIOLI, E., Johannes Gutenberg-Universität Mainz, Institut für Physikalische Chemie, Mainz, Germany: 30.06.-03.07.2013
NEMETH, P., Arizona State University, School of Earth and Space Exploration, Tempe, USA: 02.-07.07.2013
SANCHEZ VALLE, C., ETH Zürich, Institute of Geochemistry and Petrology, Zürich, Switzerland: 14.-16.01.2013

SANTAMARIA PÉREZ, D., Universidad Complutense de Madrid, Departamento de Química-Física I, Madrid, Spain: 20.-24.01.2013

SCHIANO, P., Université Blaise Pascal, Laboratoire Magmas et Volcans, Clermont-Ferrand, France: 24.-28.09.2013

SEIFERT, F., Berlin, Germany: 30.-31.01.2013

SHARP, Z., University of New Mexico, Department of Earth & Planetary Sciences, Albuquerque, USA: 27.-29.05.2013

SIERSCH, N.-C., Universität Tübingen, Germany: 18.02.-28.03.2013

WEBSTER, J., American Museum of Natural History, Department of Earth & Planetary Sciences, New York, USA: 11.-14.09.2013

5.2 Visiting scientists supported by other externally funded BGI projects

CAMPBELL, A., University of Chicago, Department of Geophysical Sciences, Chicago, USA: 28.01.-03.02.2013 (ERC *A)

CARACAS, R., Laboratoire de Sciences de la Terre, CNRS UMR5570, Ecole Normale Supérieure de Lyon, France: 28.01.-08.02.2013 (ERC *A)

CHEMIA, Z., University of Copenhagen, Department of Geography and Geology, Copenhagen, Denmark: 14.-16.04.2013 (DFG *B)

FISCHER, R., University of Chicago, Department of Geophysical Sciences, Chicago, USA: 25.01.-08.02.2013, 13.-25.07.2013 (ERC *A)

KOLESNIKOV, A., Carnegie Institution of Washington, Geophysical Laboratory, Washington DC, USA: 21.-24.05.2013 (DFG *B)

MANTHILAKE, G., Université Blaise Pascal, Laboratoire Magmas et Volcans, Clermont-Ferrand, France: 13.-19.06.2013 (ERC *A)

MORBIDELLI, A., Observatoire de la Cote d'Azur, Nice, France: 27.01.-01.02.2013 (ERC *A)

O'BRIEN, D.P., Planetary Science Institute, Tucson, USA: 27.01.-01.02.2013 (ERC *A)

PALME, H., Köln, Germany: 30.-31.01.2013 (ERC *A)

ROSE WESTON, L., Thunder Bay, Ontario, Canada: 30.06.-08.07.2013 (ERC *A)

SOLFERINO, G., Mount Royal University, Earth Science Department, Calgary, Canada: 03.-17.11.2013 (DFG *B/Core Facility)

WANG, Z., Beijing University of Technology, China: 21.-25.04.2013 (DFG *B)

WOODLAND, A., Johann Wolfgang Goethe-Universität, Physikalisch-Chemische Mineralogie, Frankfurt/M., Germany: 09.-20.09.2013 (DFG *B/Core Facility)

ZHANG, X., China University of Geosciences, Wuhan, China: 14.-18.04.2013 (DFG *B)

ZHAO, C., University of Science & Technology, Department of Earth & Space Science, Hefei, China: 13.-16.05.2013 (DFG *B)

***A) ERC: European Research Council**

***B) DFG: Deutsche Forschungsgemeinschaft**

5.3 Visitors (externally funded)

ANGEL, R., Università degli Studi di Padova, Dipartimento di Geoscienze, Padova, Italy: 17.-28.06.2013

BUREAU, H., Institut de Minéralogie et de Physique des Milieux Condensés, Paris, France: 20.10.-02.11.2013

DOLEJŠ, D., Charles University, Institute of Petrology and Structural Geology, Prague, Czech Republic: 13.-14.05.2013

GAUTIER, F., Université de Toulouse, Laboratoire de Chimie de Coordination, Toulouse, France: 15.-17.01.2013

GOTOU, H., The University of Tokyo, Institute for Solid State Physics, Chiba, Japan: 09.09.2013

GREENBERG, Y., Tel Aviv University, Israel: 20.02.2013

GUO, X., University of Science and Technology of China, Hefei, China: 30.08.-28.09.2013

HESSE, K., Friedrich-Alexander-Universität Erlangen-Nürnberg, Germany: 24.10.2013

IIZUKA, R., Ehime University, Geodynamics Research Center, Matsuyama, Japan: 04.02.-21.03.2013, 08.07.-24.12.2013

KESHAV, S., Université Montpellier 2, Géosciences, Montpellier, France: 07.12.-31.12.2013

KING, S., Virginia Polytechnic Institute and State University, Department of Geosciences, Blacksburgh, USA: 03.-28.06.2013

KOZLENKO, D., Frank Laboratory of Neutron Physics, Joint Institute for Nuclear Research, Dubna, Russia: 24.06.-04.07.2013

LEROY, C., Institut de Minéralogie et de Physique des Milieux Condensés, Paris, France: 20.-26.10.2013

LITVIN, Y., Institute of Experimental Mineralogy, Chernogolovka, Moscow region, Russia: 13.-23.04.2013

LUKIN, E., Frank Laboratory of Neutron Physics, Joint Institute for Nuclear Research, Dubna, Russia: 31.07.-03.08.2013

MARQUARDT, K., GeoForschungsZentrum Potsdam, Germany: 12.-13.09.2013

MELCHIOR, A., Tel Aviv University, Israel: 20.02.2013

MERLINI, M., Università degli Studi di Milano, Dipartimento di Scienze della Terra, Milano, Italy: 15.-16.05.2013

MILANI, S., Università degli Studi di Padova, Dipartimento di Geoscienze, Padova, Italy: 25.02.-01.03.2013

NI, H., University of Science and Technology of China, Hefei, China: 30.08.-28.09.2013

NOVELLA, D., Université Blaise Pascal, Laboratoire Magmas et Volcans, Clermont-Ferrand, France: 28.-31.10.2013

OHUCHI, T., Ehime University, Geodynamics Research Center, Matsuyama, Japan: 12.-15.09.2013

POMMIER, A., Arizona State University, School of Earth and Space Exploration, Tempe, USA: 01.-31.07.2013

POTAPKIN, V., European Synchrotron Radiation Facility, Grenoble, France: 10.-15.06.2013

SECLAMAN, A., Ecole Normale Supérieure de Lyon, France: 22.09.-22.12.2013

SMYTH, J.R., University of Colorado at Boulder, Department of Geological Sciences, Boulder, USA: 13.05.-14.06.2013

SOUTHWORTH, R., University College London, Department of Earth Sciences, London, U.K.: 25.02.-01.03.2013

SPIVAK, A., Institute of Experimental Mineralogy, Chernogolovka, Moscow region, Russia: 03.06.-31.07.2013

STENETEG, P., Linköping University, Department of Physics, Chemistry and Biology, Linköping, Sweden: 13.-16.02.2013

STERER, E., Tel Aviv University, Israel: 20.02.2013

TRØNNES, R., University of Oslo, Natural History Museum, Oslo, Norway: 19.06.-25.07.2013, 17.09.-05.10.2013

UENVER-THIELE, L., Johann Wolfgang Goethe-Universität, Physikalisch-Chemische Mineralogie, Frankfurt/M., Germany: 09.-20.09.2013

YANG, X., Nanjing University, School of Earth Sciences and Engineering, Nanjing, China: 29.04.-27.05.2013

ZAKHARCHENKO, E., Institute of Experimental Mineralogy, Chernogolovka, Moscow region, Russia: 03.06.-31.07.2013

6. Additional scientific activities

6.1 Theses

Ph.D. theses

FEI, Hongzhan: Silicon and oxygen self-diffusion in forsterite and implications to upper-mantle rheology.

LI, Yuan: An experimental study of deep nitrogen geochemistry.

NOVELLA, Davide: The interaction between silicate minerals and C-O-H bearing melts in the Earth’s mantle.

PARAKHONSKIY, Gleb: Synthesis and investigation of boron phases at high pressures and temperatures.

PRESCHER, Clemens: Iron spin crossovers at high pressures and temperatures and their effects on materials relevant to the Earth's lower mantle and core.

M.Sc. theses

FRIGO, Corinne: Oxidation-hydration relations in eudialyte from the Ilimaussaq complex, Greenland.

KULARATNE, Kanchana: High pressure structural evolution of $CaIrO_3$ perovskite.

OJWANG', Dickson: The stability field and microstructures of Fe_4O_5 and effects of oxygen fugacity.

SAVCHUK, Oles: Pressure effect on electromotive force.

6.2 Honours and awards

El GORESY, Ahmed	2013 Leonard Medal of the Meteoritical Society, Edmonton, Canada
MCCAMMON, Catherine	2013 Robert Wilhelm Bunsen Medal of the Geochemistry, Mineralogy, Petrology & Volcanology Division of the European Geosciences Union
BYKOWA, ELENA	Student Travel Scholarschip Award for the 2013 Joint APS-SCCM/AIRAPT Conference in Seattle/USA
LAURENZ, Vera	EAG/GS Outstanding Student Poster Award, Goldschmidt Conference, Florence, Italy

6.3 Editorship of scientific journals

KATSURA, Tomoo	Associate Editor "Reviews of Geophysics"
KEPPLER, Hans	Editorial Advisory Board "Elements" Editorial Board "Contributions to Mineralogy and Petrology"
MCCAMMON, Catherine	Chief Editor "Physics and Chemistry of Minerals" Advisory Editor "Springer Briefs in Earth Sciences"
RUBIE, David	Editorial Board "Physics of the Earth and Planetary Interiors" Editorial Board "Progress in Earth and Planetary Science"

6.4 Membership of scientific advisory bodies

BOFFA BALLARAN, Tiziana	Member of the Peer Review Panel 6 of Diamond Light Source
DUBROVINSKY, Leonid	Co-Chair of SIG "Crystallography at extreme conditions" of the European Crystallography Union Member, Editorial Board of the Journal of High Pressure Research Member, Review Panel for allocation of beam-time at ESRF Member, Review Panel of Canadian Light Source Member, Review Panel of SPRING8 Chair, Subcomission on Spectroscopy, Diffraction, and new Instrumentations in Mineral Physics of the International Mineralogical Association Member, Deep Carbon Observatory Scientific Steering Committee
FROST, Dan	Member of the council of the European Association of Geochemistry (EAG) - (Chair of the communications committee) Member, Geochemical Fellows Selection Committee (EAG-GSA
KEPPLER, Hans	Member, Research Council of the German Mineralogical Society (Forschungskollegium Mineralogie der DMG) Member, Abraham Gottlob Werner Medal Committee, German Mineralogical Society (DMG) Chair, American Geophysical Union Fellow Committee (VGP section)

	Member, Commission for Research of Bayreuth University (Präsidialkommission für Forschung und wissenschaftlichen Nachwuchs) Member, German National Academy of Sciences (Leopoldina) Member, Bavarian Academy of Sciences Member, Deep Carbon Observatory Scientific Steering Committee Member, Alexander von Humboldt Foundation Selection Panel for Humboldt Awardees Member, Commision for Research Infrastructures, Wissenschaftsrat (German Council of Science and Humanities)
MCCAMMON, Catherine	President, Volcanology, Geochemistry & Petrology Section of the American Geophysical Union Member, Council of the American Geophysical Union Member, Bunsen Medal Committee, European Geosciences Union Chair, Sub-committee "Earth’s Deep Interior" of the Commission of the Physics of Minerals, International Mineralogical Association IAVCEI representative, Inter-Association Commission for Physics and Chemistry of Earth Materials
RUBIE, David	Member of Houtermans Award Committee, European Association of Geochemistry

7. Scientific and Technical Personnel

Name		Position	Duration in 2013	Funding source
AUDÉTAT, Andreas	Dr.	Akad. Rat		BGI
BEYER, Christopher	M.Sc.	Wiss. Mitarbeiter		EU
BLAHA, Stephan	M.Sc.	Wiss. Mitarbeiter	to 25.06.	BGI
			from 26.06.	DFG
BÖHM, Ulrich		Mechaniker		BGI
BOFFA BALLARAN, Tiziana	Dr.	Akad. Oberrätin		BGI
BUCHERT, Petra		Fremdsprachensekretärin		BGI
BYKOVA, Elena	Dipl. Chem.	Wiss. Mitarbeiter	from 01.02.	BMBF
CERANTOLA, Valerio	M.Sc.	Wiss. Mitarbeiter	to 30.04.	EU
		Stipendiat,	from 01.05.	UB e.V.
		Wiss. Hilfskraft		EU, DFG
CERNOK, Ana	M.Sc.	Wiss. Mitarbeiterin		BMBF
CHUST, Thomas	Dipl. Geophys.	Wiss. Mitarbeiter		DFG
DE VRIES, Jellie	Dr.	Wiss. Mitarbeiterin		EU
DINIUS, Ganna	Mag.	Verw. Angestellte	to 30.09.	BGI
DUBROVINSKY, Leonid	Apl. Prof. Dr.	Akad. Direktor		BGI
EL GORESY, Ahmed	Prof. Dr.			BGI/VP[1]
EVONUK, Martha	Dr.	Wiss. Mitarbeiterin		DFG
FARLA, Robert	Dr.	Wiss. Mitarbeiter	from 01.05.	BGI/VP
FEI, Hongzhan	B.Sc./ Dr.	Wiss. Mitarbeiter	to 30.11.	BGI/VP
FISCHER, Heinz		Mechaniker		BGI
FISCHER, Nicole	ROI	Verwalt. Beamtin		BGI
FROST, Daniel	Prof. Dr.	Stellvertr. Leiter	from 01.04.	BGI
GIANNINI, Mattia	M.Sc.	Wiss. Mitarbeiter	to 31.10.	DFG
GOLLNER, Gertrud		Chem.-Techn. Assistentin		BGI
GOU, Huiyang	Dr.	Forschungsstipendiat	to 31.08.	AvH
HEIDELBACH, Florian	Dr.	Wiss. Mitarbeiter	from 01.04.	DFG
JACOBSON, Seth	Ph.D.	Wiss. Mitarbeiter	from 18.01.	EU
KANTOR, Anastasia	Dr.	Wiss. Mitarbeiterin	to 30.06.	BMBF
KATSURA, Tomoo	Prof. Dr.	Leiter	from 01.04.	BGI
KAWAZOE, Takaaki	Dr.	Akad. Rat	from 01.02.	BGI
KEPPLER, Hans	Prof. Dr.	Professor		BGI
KEYSSNER, Stefan	Dr.	Akad. Oberrat		BGI
KISON-HERZING, Lydia		Sekretärin		BGI

KLASINSKI, Kurt	Dipl.-Ing. (FH)	Techn. Angestellter		BGI
KRAUßE, Detlef	Dipl.-Inform. (FH)	Techn. Angestellter		BGI
KRIEGL, Holger		Haustechniker		BGI
KULARATNE, Kanchana	M.Sc.	Wiss. Mitarbeiterin	from 01.12.	DFG
KURNOSOV, Alexander	Dr.	Wiss. Mitarbeiter		EU
LAURENZ, Vera	Dr. rer. nat.	Wiss. Mitarbeiterin		EU
LI, Yuan	M.Sc.	Wiss. Mitarbeiter	to 31.08.	DFG
LINHARDT, Sven		Elektrotechniker		BGI
MARQUARDT, Katharina	Dr.	Akad. Rätin	from 16.12.	BGI
MASOTTA, Matteo	Dr.	Wiss. Mitarbeiter	to 28.07.	BGI/VP
		Forschungsstipendiat	from 29.07.	AvH
MCCAMMON, Catherine	Dr.	Akad. Oberrätin		BGI
MIYAJIMA, Nobuyoshi	Dr.	Akad. Rat		BGI
MYHILL, Robert	Dr.	Forschungsstipendiat		AvH
NJUL, Raphael		Präparator		BGI
NOVELLA, Davide	M.Sc.	Wiss. Mitarbeiter	to 31.07.	BGI
OUSSADOU, Mezhoura	M.Sc.	Wiss. Mitarbeiterin	to 31.01.	DFG
OVSYANNIKOV, Sergey	Dr.	Wiss. Mitarbeiter	to 14.07.	DFG
			from 15.07.	BGI/VP
			from 01.09.	DFG
PAMATO, Martha	M.Sc.	Stipendiatin,	to 30.04.	UB e.V.
		wiss. Hilfskraft		DFG
		Wiss. Mitarbeiterin	from 01.05.	EU
			from 01.12.	DFG
PETIGIRARD, Sylvain	Ph.D.	Wiss. Mitarbeiter	from 14.01.	EU
		Forschungsstipendiat	from 01.10.	AvH
POSNER, Esther	M.Sc.	Wiss. Mitarbeiterin	from 14.01.	EU
POTZEL, Anke		Chem.-Techn. Assistentin		BGI
RAMMING, Gerd		Elektroniker		BGI
RAUSCH, Oliver		Mechaniker		BGI
ROSENTHAL, Anja	Dr.	Wiss. Mitarbeiterin		EU
RUBIE, David C.	Prof. Dr.	Professor		EU
SCHULZE, Hubert		Präparator		BGI
SHCHEKA, Svyatoslav	Dr.	Wiss. Mitarbeiter		DFG
SINMYO, Ryosuke	Dr.	Forschungsstipendiat		AvH
SOLOPOVA, Natalia	M.Sc.	Wiss. Mitarbeiterin	to 07.09.	DFG
SORBADERE, Fanny	Dr.	Wiss. Mitarbeiterin	from 15.04.	BGI/VP
SOUSTELLE, Vincent	Dr.	Forschungsstipendiat		AvH
STEINLE-NEUMANN, Gerd	Dr.	Akad. Rat		BGI

STROHM, Cornelius	Dr.	Wiss. Mitarbeiter	from 15.10.	BMBF
TRENZ, Ulrike		Biol.-Techn. Assistentin		BGI
TROTS, Dmytro	Dr.	Wiss. Mitarbeiter		EU
			from 01.11.	BGI/VP
ÜBELHACK, Stefan		Mechaniker		BGI
VLCEK, Vojtech	M.Sc.	Wiss. Mitarbeiter		DFG
VOGEL, Antje	Dipl.-Min.	Wiss. Mitarbeiterin		DFG
WALTE, Nicolas	Dr.	Wiss. Mitarbeiter		BMBF
ZIBERNA, Luca	Ph.D.	Wiss. Mitarbeiter	from 01.03.	EU
			from 01.11.	BGI/VP

Abbreviations/explanations:

AvH	Alexander von Humboldt Foundation
BGI	Staff Position of Bayerisches Geoinstitut
BGI/VP	Visiting Scientists' Program of Bayerisches Geoinstitut
BMBF	Federal Ministry of Education and Research
DFG	German Science Foundation
EU	European Union
UB e.V.	Universität Bayern e.V.

---

[1] partially funded by the Visiting Scientists' Program of Bayerisches Geoinstitut

Index